

AD_____

Award Number: W81XWH-04-1-0559

TITLE: Concurrent MR-NIR Imaging for Breast Cancer Diagnosis

PRINCIPAL INVESTIGATOR: Birsen Yazici, Ph.D.

CONTRACTING ORGANIZATION: Rensselaer Polytechnic Institute
Troy, NY 12180

REPORT DATE: June 2006

TYPE OF REPORT: Annual

PREPARED FOR: U.S. Army Medical Research and Materiel Command
Fort Detrick, Maryland 21702-5012

DISTRIBUTION STATEMENT: Approved for Public Release;
Distribution Unlimited

The views, opinions and/or findings contained in this report are those of the author(s) and should not be construed as an official Department of the Army position, policy or decision unless so designated by other documentation.

REPORT DOCUMENTATION PAGE				Form Approved OMB No. 0704-0188	
Public reporting burden for this collection of information is estimated to average 1 hour per response, including the time for reviewing instructions, searching existing data sources, gathering and maintaining the data needed, and completing and reviewing this collection of information. Send comments regarding this burden estimate or any other aspect of this collection of information, including suggestions for reducing this burden to Department of Defense, Washington Headquarters Services, Directorate for Information Operations and Reports (0704-0188), 1215 Jefferson Davis Highway, Suite 1204, Arlington, VA 22202-4302. Respondents should be aware that notwithstanding any other provision of law, no person shall be subject to any penalty for failing to comply with a collection of information if it does not display a currently valid OMB control number. PLEASE DO NOT RETURN YOUR FORM TO THE ABOVE ADDRESS.					
1. REPORT DATE (DD-MM-YYYY) 01-06-2006		2. REPORT TYPE Annual		3. DATES COVERED (From - To) 1 Jun 2005 - 31 May 2006	
4. TITLE AND SUBTITLE Concurrent MR-NIR Imaging for Breast Cancer Diagnosis				5a. CONTRACT NUMBER	
				5b. GRANT NUMBER W81XWH-04-1-0559	
				5c. PROGRAM ELEMENT NUMBER	
6. AUTHOR(S) Birsen Yazici, Ph.D. E-Mail: yazici@ecse.rpi.edu				5d. PROJECT NUMBER	
				5e. TASK NUMBER	
				5f. WORK UNIT NUMBER	
7. PERFORMING ORGANIZATION NAME(S) AND ADDRESS(ES) Rensselaer Polytechnic Institute Troy, NY 12180				8. PERFORMING ORGANIZATION REPORT NUMBER	
9. SPONSORING / MONITORING AGENCY NAME(S) AND ADDRESS(ES) U.S. Army Medical Research and Materiel Command Fort Detrick, Maryland 21702-5012				10. SPONSOR/MONITOR'S ACRONYM(S)	
				11. SPONSOR/MONITOR'S REPORT NUMBER(S)	
12. DISTRIBUTION / AVAILABILITY STATEMENT Approved for Public Release; Distribution Unlimited					
13. SUPPLEMENTARY NOTES					
14. ABSTRACT: The primary objective of this research program is to investigate concurrent near infrared (NIR) optical and magnetic resonance (MR) imaging for breast cancer diagnosis. The NIR diffuse optical imaging offers novel criteria for cancer differentiation with the ability to measure (in vivo) oxygenation and vascularization state, the uptake and release of contrast agents and chromophore concentrations with high sensitivity. However, NIR diffuse optical tomography is inherently a low spatial resolution imaging modality due to diffuse nature of light photons. Alternatively, MRI provides high spatial resolution with excellent tissue discrimination, but has limited ability to monitor hemoglobin dynamics and other contrast mechanisms that optical imaging provides. Therefore, concurrent MRI-NIR optical imaging brings together the most advantageous aspects of the two imaging modalities for breast cancer diagnosis.					
15. SUBJECT TERMS					
16. SECURITY CLASSIFICATION OF:			17. LIMITATION OF ABSTRACT	18. NUMBER OF PAGES	19a. NAME OF RESPONSIBLE PERSON
a. REPORT	b. ABSTRACT	c. THIS PAGE			USAMRMC
U	U	U	UU	151	19b. TELEPHONE NUMBER (include area code)

Table of Contents

Cover.....	
SF 298.....	2
Introduction.....	4
Body.....	6
Key Research Accomplishments.....	24
Reportable Outcomes.....	24
Conclusions.....	25
References.....	26
Appendices.....	28

Concurrent MR-NIR Imaging for Breast Cancer Diagnosis

Birsen Yazici

I. INTRODUCTION

Near infrared (NIR) diffuse optical imaging provides quantitative functional information from breast tissue that can not be obtained by conventional radiological methods. NIR techniques can provide *in vivo* measurements of oxygenation and vascularization state, the uptake and release of molecular contrast agents and chromophore concentrations with high sensitivity. There is considerable evidence that tumor growth is dependent on angiogenesis [8]- [10], and that tumor aggressiveness can be assessed from its increased number of new vessels and reduced oxygenation state relative to normal breast tissue and benign breast lesions [11]- [13]. NIR diffuse optical tomographic (DOT) methods has the potential to characterize angiogenesis related vessel density as it measures the total hemoglobin concentration and provide the ability to differentiate between benign and malignant lesions based on oxygen saturation. Furthermore, NIR methods are non-ionizing, relatively inexpensive and can be made portable.

The diagnosis and management of cancer involves several stages where magnetic resonance (MR) plays a valuable and growing role. MRI of the breast is now a routine part of the clinical care in many centers [16]- [18]. Magnetic Resonance imaging (MRI) is indicated in patients with inconclusive clinical and/or mammographic examinations. Patients that may benefit include women with radiographically dense breasts, and high risk potential population [19]- [20]. MRI possesses less than 10% contrast for soft tissue pathology [21]. Gadolinium (Gd) enhanced MRI offers much better contrast and is specific for tumor vessel imaging. However, the signal in the Gd-MRI arises from the larger vessels as the contrast agent is flushed out of the vascular bed of the tumor [22]. In comparison, NIR measurements of absorption have extremely high contrast. It was reported that 5% change in vascular density as measured histologically in ductal carcinomas leads to approximately 300% contrast in NIR absorption coefficients [14]. Furthermore, there are studies suggesting that the kinetics of contrast enhanced optical spectroscopy provides information about the cellular spaces [15]. On the other hand, NIR DOT suffers from poor spatial resolution and as such, it is unlikely that NIR imaging will be a stand-alone screening method in the general

population. Therefore, we believe that the concurrent MR and NIR imaging brings together the most advantageous aspects of the two imaging modalities (structural and functional). In the future, we envision that this multimodality imaging approach will lead to high resolution hemoglobin tomography and comprehensive quantitative functional tissue characterization to differentiate malignant and benign tumors.

In this project, the clinical studies are performed using the novel MR-NIR hybrid time-resolved spectroscopy (TRS) imager and fast Indocynine Green (ICG) enhanced spectroscopic imager developed by Dr. Chance, a Co-PI of this proposal, at the University of Pennsylvania (UPenn), Biophysics Department, Diffuse Optical Imaging and Spectroscopy Laboratory.

The central hypothesis of this project is that the concurrent MR-NIR diffuse optical tomographic methods coupled with fast contrast enhanced NIR spectroscopic methods provide fundamentally new quantitative functional and structural information for breast cancer tumor characterization and detection. This new information can be obtained by novel modeling, analysis and data fusion methods from the tomographic, temporal and cellular-based contrast measurements, which exploit fast imaging techniques together with TRS tomographic methods. In this project, we investigate new methods for multi-modality high spatial resolution hemoglobin tomography, pharmacokinetic modeling of molecular contrast agents based on fast NIR spectroscopy and analysis of structural and functional information provided by MR and NIR imaging methods for breast cancer detection based on receiver operating characteristics methodology. Specific aims of the project are as follows:

- Aim 1: Utilize a priori anatomical information provided by MRI, to reconstruct 3D high resolution hemoglobin, water and lipid concentration, and oxygen saturation images directly from 6 wavelength time resolved optical measurements. Evaluate improvements in image reconstruction between that of stand-alone NIR and concurrent MR-NIR measurements using water and lipid images obtained from MRI.
- Aim 2: Develop a compartmentalized pharmacokinetic modeling of ICG, optical contrast agent, and extract quantitative parameters that can characterize tumor metabolism and angiogenesis. Compare ICG kinetics with the Gadolinium, MR contrast agent, kinetics and biopsy findings.
- Aim 3: Evaluate accuracy of breast cancer diagnosis based on the quantitative functional information extracted from stand-alone NIR system. This information includes hemoglobin, water and lipid concentration, optical scatter power and oxygen saturation images, and ICG pharmacokinetic parameters. Evaluate the added value of ICG kinetic parameters in breast cancer diagnosis.
- Aim 4: Combine NIR based breast cancer diagnosis features with the systematic MR breast architecture and kinetics interpretation model developed by Dr. Nunes, M.D, Co-PI of this proposal, to evaluate the sensitivity and specificity of concurrent MR-NIR imaging method. Compare results with that of stand-alone MR and NIR

results.

In the following sections, we will provide detailed description of our current research in line with the statement of work (SOW) and the aims outlined above. For the period of June 1st, 2005 to May 31st 2006, SOW includes only the first two aims of the project.

II. BODY

In the year 2 of the project, SOW includes tasks related to Aim 2 and 3 of the project. Below, we describe the works that has been performed towards the Aim 2, Task 3 and Aim 3 Tasks 1 and 2. We also improved upon the Task 1 of Aim 1.

A. AIM 2 - Tasks 3

- Task 3. Extract kinetic parameters from *in vivo* NIR measurements. 9-18th month

1) *Pharmacokinetic Modeling and Compartmental Model Analysis*: In general, the continuous time state-space representation for an n -compartment model is given by

$$\dot{\mathbf{C}}(t) = \mathbf{K}(\boldsymbol{\alpha}_n)\mathbf{C}(t) \quad (1)$$

$$m(t) = \mathbf{V}(\boldsymbol{\alpha}_n)\mathbf{C}(t) \quad (2)$$

where $\mathbf{C}(t)$ denotes the concentration vector whose elements are the concentrations of the fluorescence agents in different compartments, and $\dot{\mathbf{C}}(t)$ denotes its time derivative. $m(t)$ is the bulk fluorescence concentration, n is the number of compartments, $\boldsymbol{\alpha}_n$ is the parameter vector whose elements are the pharmacokinetic rate constants and volume fractions. $\mathbf{K}(\boldsymbol{\alpha}_n)$ is the system matrix with entries being the pharmacokinetic rates, and $\mathbf{V}(\boldsymbol{\alpha}_n)$ is the vector containing the volume fractions [3].

Although the formulation for the direct reconstruction of pharmacokinetic rate images can be applicable for n -compartment models, here the two-compartment model for ICG pharmacokinetics will be our running example [5], [6]. Based on a two-compartment model for ICG kinetics, as shown in Figure 1, the ICG transition between the two compartments can be modeled by two coupled differential equations

$$\frac{dC_e(t)}{dt} = -k_{out}C_e(t) + k_{in}C_p(t), \quad (3)$$

$$\frac{dC_p(t)}{dt} = -(k_{in} + k_{elm})C_p(t) + k_{out}C_e(t). \quad (4)$$

Here, $\mathbf{C}(t)$ in (1) and (2) includes, $C_p(t)$ and $C_e(t)$, representing the ICG concentrations in the plasma and extracellular extravascular space (EES), respectively. The parameter vector, α_2 , includes, k_{in} , k_{out} , k_{elm} , v_p , and v_e ;

$$\alpha_2 = [k_{in} \quad k_{out} \quad k_{elm} \quad v_p \quad v_e]^T \quad (5)$$

where k_{in} and k_{out} are the pharmacokinetic rates that govern the leakage into and the drainage out of the EES, k_{elm} describes the ICG elimination from the body through kidneys and livers, and v_p and v_e are the plasma and EES volume fractions, respectively.

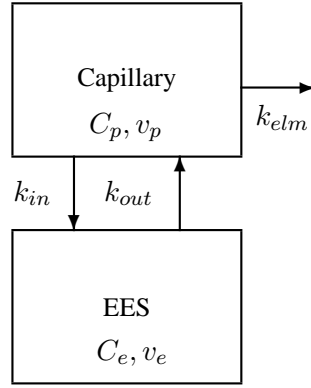


Fig. 1. Block diagram of the two-compartment model for ICG pharmacokinetics.

Here, to obtain 2-D images of pharmacokinetic rates and fluorescence agent concentrations in different compartments, we extend the compartmental model equation, (1) and (2) to spatially resolved model as follows:

$$\begin{bmatrix} \dot{\mathbf{C}}(r_1, t) \\ \vdots \\ \dot{\mathbf{C}}(r_N, t) \end{bmatrix} = \begin{bmatrix} \mathbf{K}(\alpha_n(r_1)) & 0 & 0 \\ 0 & \ddots & 0 \\ 0 & 0 & \mathbf{K}(\alpha_n(r_N)) \end{bmatrix} \begin{bmatrix} \mathbf{C}(r_1, t) \\ \vdots \\ \mathbf{C}(r_N, t) \end{bmatrix} + \boldsymbol{\omega}(\mathbf{r}, t) \quad (6)$$

where $\boldsymbol{\omega}(\mathbf{r}, t)$ is uncorrelated zero mean Gaussian processes with covariance matrix \mathbf{Q} , representing the small deviations resulting from model mismatch. $\mathbf{r} = [r_1 \ r_2 \dots r_N]$, and r_j is the location of the j^{th} voxel for $j = 1, 2, 3 \dots N$, N being the number of total voxels in the discretized domain.

$$\begin{bmatrix} m(r_1, t) \\ \vdots \\ m(r_N, t) \end{bmatrix} = \begin{bmatrix} \mathbf{V}(\alpha_n(r_1)) & 0 & 0 \\ 0 & \ddots & 0 \\ 0 & 0 & \mathbf{V}(\alpha_n(r_N)) \end{bmatrix} \begin{bmatrix} \mathbf{C}(r_1, t) \\ \vdots \\ \mathbf{C}(r_N, t) \end{bmatrix} + \boldsymbol{\eta}(\mathbf{r}, t) \quad (7)$$

where $\boldsymbol{\eta}(\mathbf{r}, t)$ is a zero mean Gaussian process with covariance matrix \mathbf{R} presenting the noise in the measurements.

The implicit form of (6) and (7) can be expressed as

$$\dot{\mathbf{C}}(\mathbf{r}, t) = \mathbf{K}(\boldsymbol{\alpha}_n(\mathbf{r}))\mathbf{C}(\mathbf{r}, t) + \boldsymbol{\omega}(\mathbf{r}, t) \quad (8)$$

$$\mathbf{m}(\mathbf{r}, t) = \mathbf{V}(\boldsymbol{\alpha}_n(\mathbf{r}))\mathbf{C}(\mathbf{r}, t) + \boldsymbol{\eta}(\mathbf{r}, t). \quad (9)$$

The quantity we wish to reconstruct is the spatially varying pharmacokinetic rate parameters instead of the absorption coefficient of the fluorescence agent as is commonly the case in fluorescence diffuse optical tomography (FDOT) [1]. To do this, we first need to develop a mapping which relates the boundary flux measurements to the bulk fluorescence agent concentrations in tissue. This mapping can be obtained by using FDOT forward model which will be explained in the next section.

2) *Fluorescence Diffuse Optical Tomography*: We used a coupled system of diffusion equations to model fluorescence light propagation in tissue [1]. Based on the coupled diffusion equations, the forward model for FDOT can be expressed as:

$$\boldsymbol{\Psi}(\mathbf{r}, t) = f(\boldsymbol{\mu}_{af}(\mathbf{r}, t)), \quad (10)$$

where $\boldsymbol{\mu}_{af}(\mathbf{r}, t) = [\mu_{af}(r_1, t), \dots, \mu_{af}(r_N, t)]$ is the time dependent absorption coefficient of the fluorescence agent, $\boldsymbol{\Psi}(\mathbf{r}, t) = [\Psi(r_1, t), \dots, \Psi(r_N, t)]$ is the time-dependent boundary flux measurements, and f is a nonlinear function defined by the coupled diffusion equation. Under the assumption that the exogenous optical properties has no effect on endogenous optical properties, (10) can be linearized to obtain

$$\boldsymbol{\Psi}(\mathbf{r}, t) = \mathbf{W}\boldsymbol{\mu}_{af}(\mathbf{r}, t), \quad (11)$$

where \mathbf{W} is the weight matrix relating the absorption coefficients to the boundary measurements. This map can be numerically calculated using finite elements methods (FEM) or finite difference methods (FDM) [4].

The absorption coefficient of the fluorescence agents is related to the bulk fluorescence agent concentration as follows:

$$\boldsymbol{\mu}_{af}(\mathbf{r}, t) = \epsilon \mathbf{m}(\mathbf{r}, t) \quad (12)$$

where ϵ is the extinction coefficient of the fluorescence agent at the excitation wavelength.

3) *Pharmacokinetic Rate to Measurement Map for Fluorescence Agents*: To derive a complete formulation to reconstruct the pharmacokinetic parameters and concentrations in different compartments using the photon flux measurements, we combined the FDOT forward problem equations, (10) or (11) with the compartmental model equations.

Combining (9) and (10), with the knowledge of the linear relationship between the absorption coefficient and the bulk fluorescence concentration, (12), nonlinear FDOT forward problem is related to the bulk fluorescence agent concentration as:

$$\Psi(\mathbf{r}, t) = g(\mathbf{m}(\mathbf{r}, t)) \sim g(\mathbf{V}(\boldsymbol{\alpha}_n(\mathbf{r}))\mathbf{C}(\mathbf{r}, t)) \quad (13)$$

where g is the non-linear function which relates the bulk fluorescence agent concentrations to the boundary flux measurements.

The linearized version of (11) is given as:

$$\begin{aligned} \Psi(\mathbf{r}, t) &= \epsilon \mathbf{W} \mathbf{m}(\mathbf{r}, t) \\ &= \epsilon \mathbf{W} \mathbf{V}(\boldsymbol{\alpha}_n(\mathbf{r})) \mathbf{C}(\mathbf{r}, t) + \epsilon \mathbf{W} \boldsymbol{\eta}(\mathbf{r}, t) \\ &= \Gamma \mathbf{C}(\mathbf{r}, t) + \epsilon \mathbf{W} \boldsymbol{\eta}(\mathbf{r}, t), \end{aligned} \quad (14)$$

where \mathbf{W} , \mathbf{V} and $\boldsymbol{\eta}(\mathbf{r}, t)$ are defined above and $\Gamma = \epsilon \mathbf{W} \mathbf{V}(\boldsymbol{\alpha}_n(\mathbf{r}))$.

The equations (8) and (13), which combine the FDOT forward problem with the compartment model equations constitute the set of equations which will be used for the direct reconstruction of pharmacokinetic rates, volume fractions, and fluorescence concentrations in different compartments.

4) *Discretization of the Compartmental Model Equations and a Dynamic Model for System Parameters:* The source detector measurements in (9) are collected at discrete time instances, $t = kT$, $k = 0, 1, \dots$, where T is the sampling period. Therefore, the continuous model described in (8) and (14) has to be discretized. To simplify our notation, we shall use $\mathbf{C}(\mathbf{r}, k) = \mathbf{C}(\mathbf{r}, kT)$ and $\Psi(\mathbf{r}, k) = \Psi(\mathbf{r}, kT)$.

Let $\boldsymbol{\theta}_n$ denote the discrete-time parameter vector of the pharmacokinetic rates and volume fractions. The parameter vector $\boldsymbol{\theta}_n(\mathbf{r})$ can be either time dependent or time independent. The formulation given in this work can be used for both cases. In our case, the pharmacokinetic rates and the volume fractions are time independent. However, in order to estimate $\boldsymbol{\theta}_n$ within the EKF framework, the following dynamic model is introduced:

$$\boldsymbol{\theta}_n(\mathbf{r}, k+1) = \boldsymbol{\theta}_n(\mathbf{r}, k) + \boldsymbol{\varsigma}(\mathbf{r}, k), \quad (15)$$

where $\boldsymbol{\varsigma}(\mathbf{r}, k)$ is a zero mean white noise process with covariance matrix \mathbf{S} . The details of the dynamic model introduced for the joint estimation of the system parameters and the states can be found in [5].

5) *A priori information for Pharmacokinetic Rates and Volume Fractions:* To improve the robustness of estimates of the parameters we impose *a priori* information on pharmacokinetic parameters and volume fractions. Here, we assume that there is no information about the tumor structure and used a 4-pixel neighborhood model.

Using the 4-pixel neighbor model with equal weights β , the random process, $\theta_n(\mathbf{r}, k)$, can be modeled as:

$$\theta_n(r_j, k+1) = \beta\theta_n(r_j, k) + \beta \sum_{i=1}^4 \theta_n(r_{ji}, k) + \varsigma(\mathbf{r}, k). \quad (16)$$

6) *Extended Kalman Filter (EKF) Formulation:* In our state-space model, (8) and (9), both the states (concentrations) and system parameters (pharmacokinetic rates and volume fractions) are unknown. In this case, the state-space model can be regarded as a non-linear model in which system parameters and states are combined to form the new states of the non-linear model. This system is then linearized and solved for the unknown states using EKF framework [5]. To solve for the concentrations and the unknown parameters, the parameter vector $\theta_n(\mathbf{r}, k)$ is inserted into the concentration vector $\mathbf{C}(\mathbf{r}, k)$ as:

$$\begin{bmatrix} \mathbf{C}(\mathbf{r}, k+1) \\ \theta_n(r_j, k+1) \end{bmatrix} = \begin{bmatrix} \mathbf{K}(\theta_n(\mathbf{r}, k))\mathbf{C}(\mathbf{r}, k) \\ \beta\theta_n(r_j, k) + \beta \sum_{i=1}^4 \theta_n(r_{ji}, k) \end{bmatrix} + \begin{bmatrix} \omega(\mathbf{r}, k) \\ \varsigma(\mathbf{r}, k) \end{bmatrix}. \quad (17)$$

The measurement equation for the non-linear case is given as:

$$\Psi(\mathbf{r}, k) = \begin{bmatrix} g(\mathbf{V}(\alpha_n(\mathbf{r}))\mathbf{C}(\mathbf{r}, k)) & 0 \end{bmatrix} \begin{bmatrix} \mathbf{C}(\mathbf{r}, k) \\ \theta_n(\mathbf{r}, k) \end{bmatrix} + \eta(\mathbf{r}, k). \quad (18)$$

Without explicit proof, the extended Kalman filtering algorithm for simultaneous estimation of concentrations and parameters for the nonlinear case, (13), is given follows:

$$\begin{bmatrix} \hat{\mathbf{C}}(\mathbf{r}, 0) \\ \hat{\theta}_n(\mathbf{r}, 0) \end{bmatrix} = \begin{bmatrix} E(\mathbf{C}(\mathbf{r}, 0)) \\ \hat{\theta}_n(\mathbf{r}, 0) \end{bmatrix} \quad (19)$$

$$\mathbf{P}_{0,0} = \begin{bmatrix} Var(\mathbf{C}(\mathbf{r}, 0)) & 0 \\ 0 & \mathbf{S}_d \end{bmatrix}, \quad (20)$$

where E denotes the expected value of $\mathbf{C}(\mathbf{r}, 0)$, \mathbf{P} is the error covariance matrix, and \mathbf{S}_d is the preassigned covariance matrix of the unknown system parameters.

The following equations describe how the concentration estimates and error covariance matrix are updated at the k^{th} time instant given all the measurements up to $(k-1)^{th}$ time instant. For $k = 1, 2, \dots$,

$$\begin{bmatrix} \hat{\mathbf{C}}(\mathbf{r}, k|k-1) \\ \hat{\theta}_n(r_j, k|k-1) \end{bmatrix} = \begin{bmatrix} \mathbf{K}(\hat{\theta}_n(r, k-1))\hat{\mathbf{C}}(\mathbf{r}, k-1) \\ \beta\hat{\theta}_n(r_j, k-1) + \beta \sum_{i=1}^4 \hat{\theta}_n(r_{ji}, k) \end{bmatrix} \quad (21)$$

$$\mathbf{P}_{k|k-1} = \mathbf{J}(k-1)\mathbf{P}_{k-1,k-1}\mathbf{J}^T(k-1) + \begin{bmatrix} \mathbf{Q}_d & 0 \\ 0 & \mathbf{S}_d \end{bmatrix}, \quad (22)$$

where \mathbf{J} is the Jacobian matrix given by

$$\mathbf{J}(k) = \begin{bmatrix} \mathbf{K}(\hat{\boldsymbol{\theta}}_n(\mathbf{r}, k)) & \frac{\partial}{\partial \boldsymbol{\theta}} [\mathbf{K}(\hat{\boldsymbol{\theta}}_n(\mathbf{r}, k)) \hat{\mathbf{C}}(\mathbf{r}, k)] \\ \frac{\partial}{\partial \mathbf{C}} \hat{\boldsymbol{\theta}}_n(\mathbf{r}, k) & \frac{\partial}{\partial \boldsymbol{\theta}} \hat{\boldsymbol{\theta}}_n(\mathbf{r}, k) \end{bmatrix}. \quad (23)$$

$$\mathbf{G}_k = \mathbf{P}_{k,k-1} \boldsymbol{\Lambda}^T [\boldsymbol{\Lambda} \mathbf{P}_{k,k-1} \boldsymbol{\Lambda}^T + \mathbf{R}]^{-1}, \quad (24)$$

where \mathbf{G}_k is the recursive Kalman gain, \mathbf{R} is the covariance matrix of the measurements and $\boldsymbol{\Lambda}$ is:

$$\boldsymbol{\Lambda} = \begin{bmatrix} \frac{\partial}{\partial \mathbf{C}} g(\mathbf{V}(\boldsymbol{\theta}_n(\mathbf{r}, k|k-1) \mathbf{C}(\mathbf{r}, k|k-1))) \\ \vdots \\ \frac{\partial}{\partial \boldsymbol{\theta}} \left(\frac{\partial}{\partial \mathbf{C}} g(\mathbf{V}(\boldsymbol{\theta}_n(\mathbf{r}, k|k-1) \mathbf{C}(\mathbf{r}, k|k-1))) \right) \end{bmatrix}^T, \quad (25)$$

$$\mathbf{P}_{k,k} = [\mathbf{I} - \mathbf{G}_k \boldsymbol{\Lambda}] \mathbf{P}_{k,k-1}. \quad (26)$$

where \mathbf{I} is the identity matrix.

$$\begin{bmatrix} \hat{\mathbf{C}}(\mathbf{r}, k) \\ \hat{\boldsymbol{\theta}}_n(\mathbf{r}_j, k) \end{bmatrix} = \begin{bmatrix} \hat{\mathbf{C}}(\mathbf{r}, k|k-1) \\ \beta \hat{\boldsymbol{\theta}}_n(r_j, k|k-1) + \beta \sum_{i=1}^4 \hat{\boldsymbol{\theta}}_n(r_{ji}, k|k-1) \end{bmatrix} \\ + \mathbf{G}_k (\boldsymbol{\Psi}(\mathbf{r}, k) - g(\mathbf{V}(\boldsymbol{\theta}_n(\mathbf{r}, k|k-1) \mathbf{C}(\mathbf{r}, k|k-1))).$$

B. Clinical Results

1) *Apparatus:* We used the data collected with a continuous wave (CW) NIR imaging apparatus. The apparatus has 16 light sources, which are tungsten bulbs with less than 1 watt of output energy. They are located on a circular holder at an equal distance from each other with 22.5 degree apart. Sixteen detectors, namely, silicon photodiodes, are situated in the same plane. The breast is arranged in a pendular geometry with the source-detector probes gently touching its surface. Figure 2 illustrates the configuration of the apparatus and the configuration of the detectors and the sources in a circular plane. A band pass filter at 805nm, the absorption peak of ICG, is placed in front of the sources to select the desired wavelength. A set of data for one source is collected every 500 ms. The total time for a whole scan of the breast including 16 sources and 16 detectors is 8.8 seconds. The detectors use the same positions as the sources to collect the light originating from one source at a time. Only the signals from the farthest 11 detectors are used in the analysis. For example, when Source 1 is on, the data is collected using detectors 4 to 14. A more detailed explanation of the apparatus and the data collection procedure can be found in [7].

2) *Protocol:* Patients with suspicious breast tumors were enrolled for this study. ICG was injected intravenously by bolus with a concentration of 0.25 mg per kg of body weight. Diagnostic information is obtained using biopsy results. Since biopsy modifies the blood volume and blood flow around the tumor region, measurements were made before the biopsy. Data acquisition started before the injection of ICG and continued for 10 minutes.

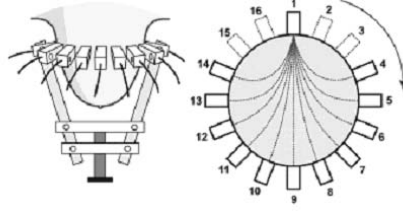


Fig. 2. The cut section of the 16 light source-detector device, holding a human breast inside. The diameter can be fitted easily. The 16 light source-detector combinations in each arm are located equal distance, but when the device fits the breast, only the diameter changes.

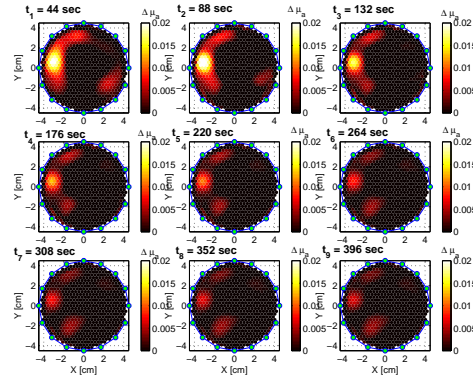


Fig. 3. Differential absorption reconstruction images for a set of time instants for Case 1.

3) *Tumor Information:* Three different patients with different tumor types are included in this study. First case, Case 1, is fibroadenoma, which corresponds to a mass estimated to be 1–2 cm in diameter within a breast of 9 cm diameter. Second case, Case 2, is adenocarcinoma corresponding to a tumor estimated to be 2–3 cm in diameter within a breast of 7.7 cm diameter. The third case, Case 3, is invasive ductal carcinoma, which corresponds to a mass estimated to be 3–4 cm in diameter.

4) *ICG Concentration Measurements for Pharmacokinetic Parameter Estimations:* Using the CW imager described above, for each patient, sufficient number of source detector readings were collected from different angles. Reconstruction of differential absorption images using the source-detector readings was discussed in Intes et al. [2]. A sample set of reconstructed differential absorption images for Case 1, Case 2, and Case 3 for 9 selected time instants are shown in Figure 3, 4, and 5, respectively.

Using the linear relationship between ICG concentration and absorption coefficient, we obtained ICG concentration images from differential absorption images for each case. A sample set of ICG concentration images for the selected time instants is shown in Figure 6, 7, and 8 for Cases 1, 2 and 3, respectively. Here, the concentration images represent bulk ICG concentration in the tissue, not specifically in plasma or the EES.

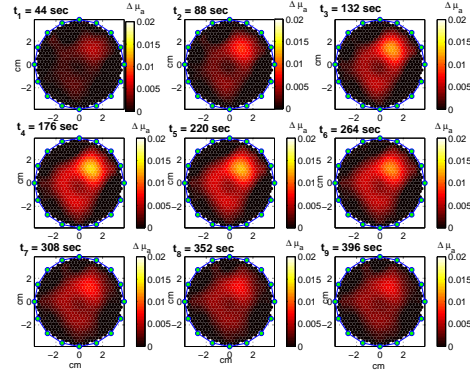


Fig. 4. Differential absorption reconstruction images for a set of time instants for Case 2.

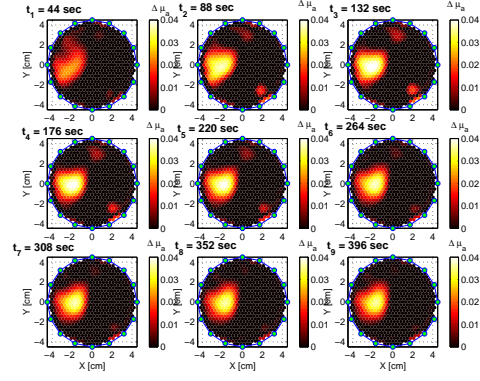


Fig. 5. Differential absorption reconstruction images for a set of time instants for Case 3.

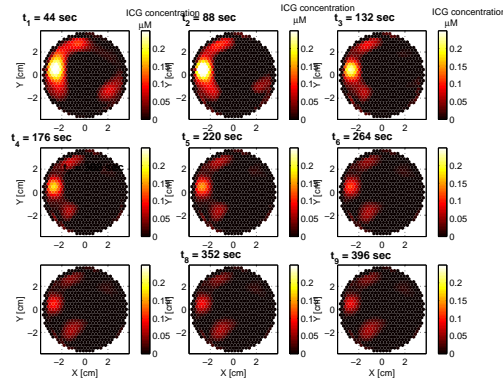


Fig. 6. 2-D ICG concentration images for a set of time instants for Case 1.

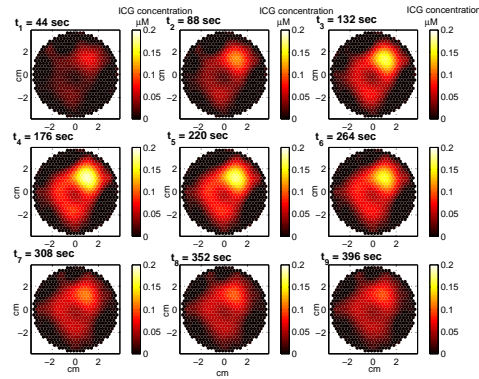


Fig. 7. 2-D ICG concentration images for a set of time instants for Case 2.

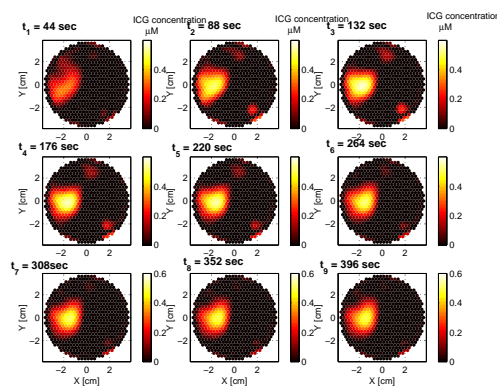


Fig. 8. 2-D ICG concentration images for a set of time instants for Case 3.

Using the ICG concentration curves, we estimated the pharmacokinetic parameters for each pixel based on the two-compartment model. We then constructed 2-D permeability rate images using values of these parameters. 2-D images for k_{in} , k_{out} for two-compartmental model for each case are shown in Figures 9 (a), (b), 10 (a), (b), and 11 (a), (b), respectively. We also analyzed whether the kinetic rates are statistically different or not for the inside and outside the tumor region. The k_{in} and k_{out} values from inside and outside the tumor region are statistically different with a p-value of less than 0.0001 for all cases.

We constructed 2-D ICG concentration images for plasma and the EES. Figures 12-17 show the ICG concentration in the EES and plasma for 3 different time instants for Case 1, 2, 3, respectively. We observed that ICG concentrations in plasma and the EES compartments are higher around the tumors agreeing with the hypothesis that around tumor region ICG may act as a diffusible extravascular flow in leaky capillary of cancer vessels.

C. AIM 3 - Tasks 1 and 2

The SOW with regard to Aim 3 includes the following specific tasks:

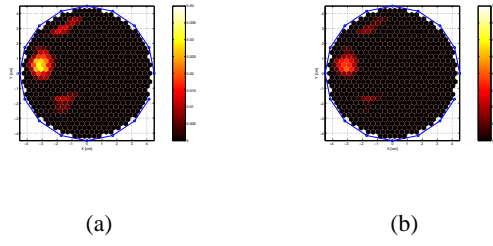


Fig. 9. 2-D images for pharmacokinetic rates k_{in} and k_{out} for Case 1.

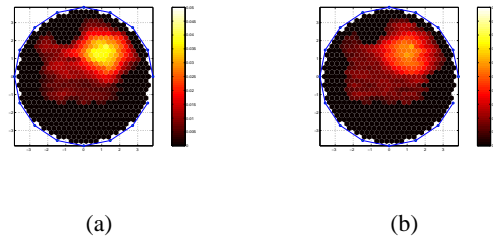


Fig. 10. 2-D images for pharmacokinetic rates k_{in} and k_{out} for Case 2.

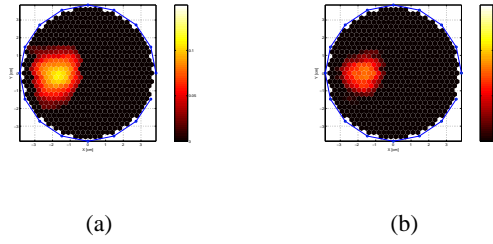


Fig. 11. 2-D images for pharmacokinetic rates k_{in} and k_{out} for Case 3.

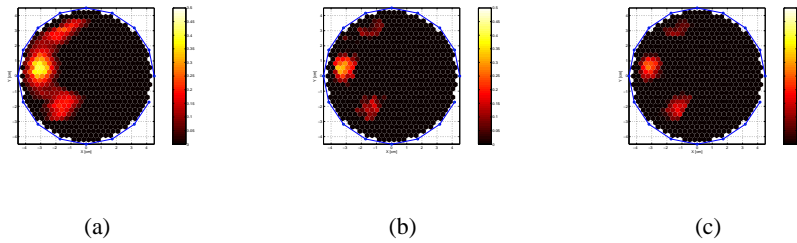


Fig. 12. 2-D ICG concentration images in plasma for Case 1 for the 246.4^{th} , 334.4^{th} , and 422.4^{th} seconds.

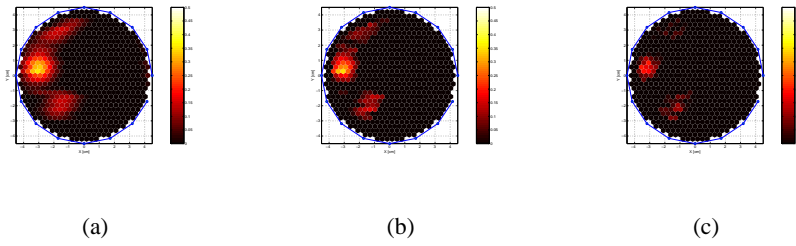


Fig. 13. 2-D ICG concentration images in the EES for Case 1 for the 246.4^{th} , 334.4^{th} , and 422.4^{th} seconds.

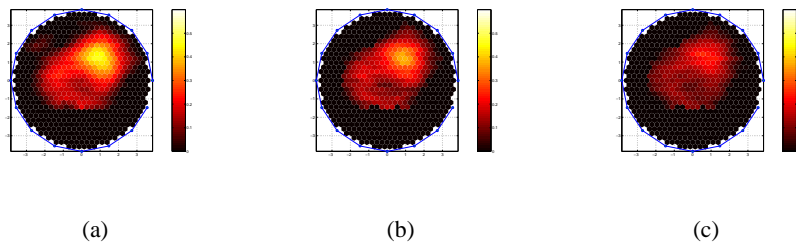


Fig. 14. 2-D ICG concentration images in plasma for Case 2 for the 228.8^{th} , 316.8^{th} , and 404.8^{th} seconds.

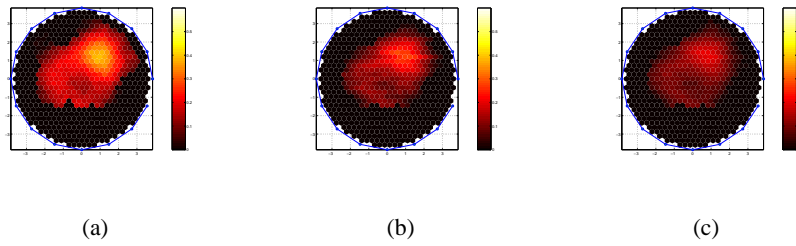


Fig. 15. 2-D ICG concentration images in the EES for Case 2 for the 228.8^{th} , 316.8^{th} , and 404.8^{th} seconds.

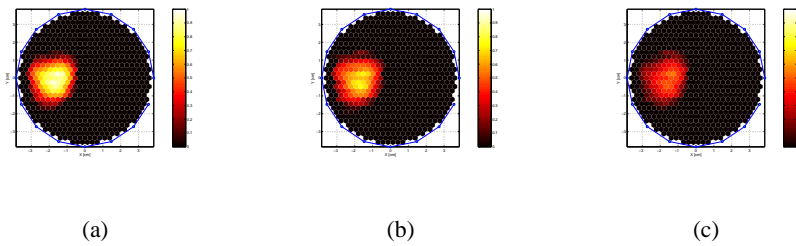


Fig. 16. 2-D ICG concentration images in plasma for Case 3 for the 246.4^{th} , 378.4^{th} , and 510.4^{th} seconds.

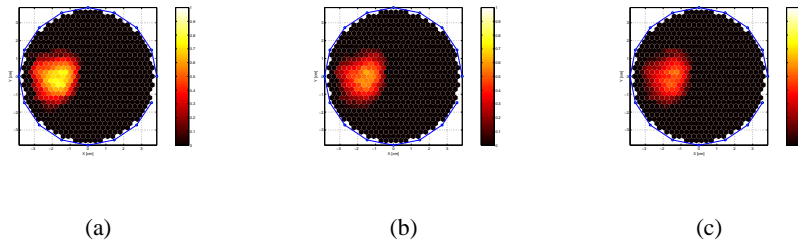


Fig. 17. 2-D ICG concentration images in the EES for Case 3 for the 246.4th, 378.4th, and 510.4th seconds.

- Task 1. Determine statistical variability of each NIR feature inside and outside the suspected tumor in an individual and evaluate the statistical significance of the measured difference with the instrumentation precision.

12-18th month

- Task 2. Design statistical classifiers to determine the ROC of each NIR feature for an individual. *18-24th month*
- Task 3. Evaluate the ROC, positive predicted value (PPV) and negative predicted value (NPV) of various combinations of the NIR features for an individual. *24-27th month*
- Task 4. Investigate the significance of the measured difference between malignant and benign tumor patient groups for single and combined NIR features. *27-30th month*

Year 2 tasks involve Task 1 and 2.

- Task 1 and 2. The evaluation of ICG related parameter is partly addresses in Task 3 of Aim 2.

This work describes the characterization efficiency of incremental biochemical and physiological properties of breast tumors [23]. In this work an NIR method which is capable of rapidly acquiring data from the human breast with a handheld spectroscopy apparatus is used. The device measures relative increases of tumor hemoglobin concentration and relative hemoglobin desaturation, all data being taken on a relative basis using generally the mirror image site on the contralateral breast, substantially mitigating the multiple effects of variable demographic and structural features of the human breast by measuring relative hemoglobin concentration and oxygenation compared to a normal breast within subjects. In analyzing relative hemoglobin concentration against relative saturation, a nomogram display conveniently segregates verified cancers from cancer-free breasts over a wide range of tumor sizes and types.

1) Apparatus: In this study, a continuous wave (CW) near infra red spectrometer (NIRS) is used (Fig. 1) [23]. In the center of the probe there is a 3-wavelength LED. The LED intensity is low, 10-15 mA. The probe consisted of one multi-wavelength LED as a light source and 8 silicon diodes as detectors (Fig. 2). These 8 detectors surround the LED at 4 cm distance, so that 8 locations over a 9 cm diameter area from a breast can be measured. The

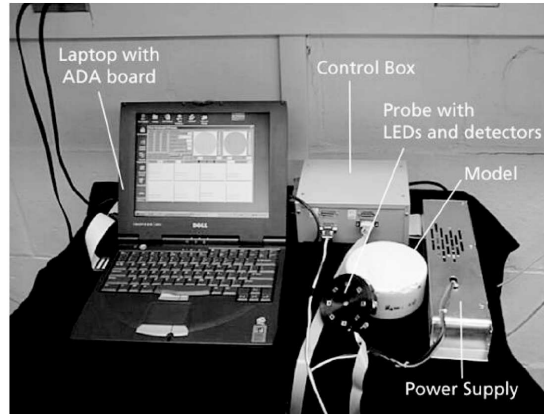


Fig. 18. A photograph of the whole apparatus (Fig. 1A) illustrates the handheld puck or probe, the coupling to the circuit box which contains the drivers for the LED, the amplifiers for the OPTI-101s, the digitally controlled gain adjustment amplifier, the electronic switch which decodes the light pulses and stores the information in a memory capacitor, the second set of switches which sample the memory capacitor at a rate compatible with the computer ADC, the software for computing blood concentration and blood saturation and the display on the computer which serves to normalize the signals through the digitally controlled amplifier.

light sources are flashed alternately 100 times per second and electronic circuits are designed to amplify and time separate the signals in a sample and hold circuit which integrates the signals over an interval of a few seconds sufficiently rapidly to follow the movements of the sensor over the breast, allowing usually 10 seconds for any particular sensor position. The data are then digitized and presented as a running time display so that the operator can be sure that stable readings are reached at each position of the sensor. The light intensity from the 8 detectors were adjusted to be near 1 volt by gains set and calibrated with a phantom with known absorption and scattering coefficients ($\mu_a = 0.04$ to 0.07 and $\mu'_s = 8 \text{ cm}^{-1}$). The puck (Fig. 2) is then transferred to the contralateral breast to include the mirror image location of the suspected cancer. The signal outputs from all source detector combinations are recorded. The probe is then moved from the contralateral breast to the ipsilateral breast suspected of cancer. The sensors giving the largest changes with respect to the mirror image position on the contralateral breast are related to the suspected cancer. The procedure requires less than 10 minutes.

2) *Subjects*: This study includes two Clinical Centers: the Abramson Family Cancer Research Institute/Department of Radiology of the Hospital of University of Pennsylvania (HUP), and the Department of Gynecology of Leipzig University. The population targeted at HUP are those who have come for possible biopsy and for radiology. The second group has come to the Breast Cancer Clinic at Leipzig. HUP and Leipzig provided 24 and 20 cancer patients, respectively, and 64 and 8 non cancer disease patients, respectively. Skill has been required in order to ensure all sensors were pressed upon the breast with equal pressure ($\sim 3 \text{ mmHg}$). Patients were lying on their backs and the

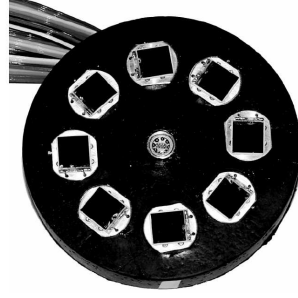


Fig. 19. The near infrared probe which 8 sources and 8 detectors.

puck was placed on the breast in such a way that coronal breast scan data is acquired (perpendicular to gravity).

3) *Feature Extraction*: The features that is used for tumor characterization may be computed using $\Delta\varepsilon \approx 1\text{cm}^{-1}$ and $\Delta L = 4\text{cm} \times 5$ for pathlength factors of 5, $\Delta OD = \Delta\varepsilon \cdot \Delta C \cdot \Delta L$ where OD is the optical density, ε is the extinction coefficient, C is blood concentration, and L is the mean pathlength of photons.

Then relative blood concentration, ΔBV and oxygen saturation, $\Delta Deoxy$, can be approximated at two different wavelengths by

$$\Delta BV \propto 0.3\Delta OD_{730} + \Delta OD_{850} \quad (27)$$

$$\Delta Deoxy \propto 1.3\Delta OD_{730} - \Delta OD_{850} \quad (28)$$

The concentrations of Hb (hemoglobin), HbO_2 (oxy hemoglobin) were calculated by a modified Beer-Lambert Law where I is light intensity after absorption and scattering and using known extinction coefficients of Hb , HbO_2 and differential pathlength factors [24].

ΔBV and $\Delta Deoxy$ can be calculated by using

$$\Delta BV \propto \Delta[Hb] + \Delta[HbO_2] \quad (29)$$

$$\Delta Deoxy \propto \Delta[HbO_2] - \Delta[Hb] \quad (30)$$

Here it is important to note that ΔBV and $\Delta Deoxy$ were based on a lipid blood oxygen model. Thus the increments of BV and $Deoxy$ are relative to the contralateral breast:

$$\Delta BV = \Delta BV_{tumor} - \Delta BV_{contra} \quad (31)$$

$$\Delta Deoxy = \Delta Deoxy_{tumor} - \Delta Deoxy_{contra} \quad (32)$$

where ΔBV_{tumor} , ΔBV_{contra} are ΔBV in the tumor breast and the mirror image position of the contralateral breast, respectively, and $\Delta Deoxy_{tumor}$, $\Delta Deoxy_{contra}$ are $\Delta Deoxy$ in the tumor breast and the mirror image position of the contralateral breast, respectively.

4) *Feature Analysis and Classification for Cancer Characterization*: In this subsection, we present the set of tumor classification features and the malignancy differentiation criteria. F1 denotes ΔBV , F2 denotes $\Delta Deoxy$, and F3 denotes, S , size of the tumor. We evaluate the malignancy differentiation capability of the individual features and various combinations of the these features.

As a malignancy differentiation criterion, we used the Neyman-Pearson hypothesis testing method [25]. Neyman-Pearson decision rule maximizes true positive rate subject to a given false positive rate. True positive rate is defined as the ratio between the number of correct malignant decisions and total number of malignant cases. False positive rate is the ratio between the number of incorrect malignant decisions and total number of benign cases.

Let F be a set of features chosen from F1 - F3. The Neyman-Pearson statistics is given by the following likelihood ratio:

$$\frac{P(F | H_1)}{P(F | H_0)} = l(F) \quad (33)$$

where $P(F | H_0)$ is the conditional probability of F given that the tumor is benign, and $P(F | H_1)$ is the conditional probability of F given that the tumor is malignant. In Neyman-Pearson likelihood ratio test; a threshold value τ_α is chosen so that the false positive probability is equal to α , i.e.,

$$\alpha = P(l(F) > \tau_\alpha | H_0) \quad (34)$$

This results in the following malignancy differentiation criteria :

$$\begin{aligned} H_0 : \quad l(F) < \tau_\alpha &\implies \text{Benign tumor} \\ H_1 : \quad l(F) > \tau_\alpha &\implies \text{Malignant tumor} \end{aligned}$$

Neyman-Pearson test is implemented using various classifiers, namely, k-nearest neighbor classifier (KNNC), Parzen density based classifier (PAR), Automatic neural network classifier (NEURC), Normal densities based linear classifier (LDC), Nearest mean classifier (NMC), Scaled nearest mean classifier (NMSC), Normal densities based quadratic (multi-class) classifier (QDC), Uncorrelated normal densities based quadratic classifier (UDC). The more details information on these classifiers can be found in [26].

We evaluated the malignancy differentiation capability of the following individual and combined features:

F1: ΔBV

F2 : $\Delta Deoxy$

F3 : Tumor Size, (S)

F1-F2: ΔBV and $\Delta Deoxy$

F1-F2-F3: ΔBV , $\Delta Deoxy$, and S

TABLE I

AUC VALUES FOR DIFFERENT CLASSIFIERS FOR F1-F2-F3: ΔBV , $\Delta Deoxy$, S

Type	NMSC	PAR	LDC	UDC	NEURC	QDC	NMC	KNNC
AUC	0.9098	0.9041	0.9017	0.8984	0.8864	0.8843	0.8807	0.8752

TABLE II

AUC VALUES FOR DIFFERENT CLASSIFIERS FOR F1-F2: ΔBV , $\Delta Deoxy$

Type	NMSC	PAR	LDC	UDC	NEURC	QDC	NMC	KNNC
AUC	0.9001	0.8993	0.8930	0.8908	0.8992	0.8821	0.8782	0.8645

The evaluation is based on receiver operating characteristics (ROC) methodology. The ROC curve is obtained by plotting the probability of false positive versus the probability of detection. The evaluation of the classification methods is based on the area under the ROC curve (AUC). The best performing feature set is the combination of the three features. Table 1 gives the AUC values for 8 different classifiers for all three features. The scaled nearest mean classifier has the best performance in terms of classification with a AUC value of 0.9098. Table 2 gives the AUC values for 8 different classifiers for the features ΔBV and $\Delta Deoxy$. The scaled nearest mean classifier has the best performance in terms of classification with a AUC value of 0.9001. Table 3 gives the AUC values for 8 different classifiers for the feature ΔBV . The nearest mean classifier has the best performance in terms of classification with a AUC value of 0.8832. Table 4 gives the results 8 different classifiers for the feature $\Delta Deoxy$. The nearest mean classifier has the best performance in terms of classification with a AUC of 0.8790.

Figures 3 and 4 show the distribution of features ΔBV and $\Delta Deoxy$ extracted from benign and malignant tumors. The thresholds computed using scaled nearest mean classifier and Parzen classifiers. In Fig. 5, ROC curves

TABLE III

AUC VALUES FOR DIFFERENT CLASSIFIERS FOR F1: ΔBV

Type	NMSC	PAR	LDC	UDC	NEURC	QDC	NMC	KNNC
AUC	0.8817	0.8764	0.8807	0.8779	0.8513	0.8778	0.8832	0.8302

TABLE IV

AUC VALUES FOR DIFFERENT CLASSIFIERS FOR F2: $\Delta Deoxy$

Type	NMSC	PAR	LDC	UDC	NEURC	QDC	NMC	KNNC
AUC	0.8787	0.8764	0.8776	0.8711	0.8491	0.8613	0.8790	0.8331

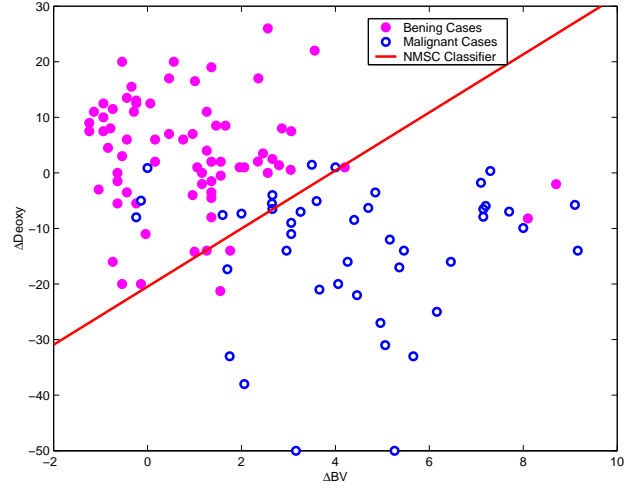


Fig. 20. Scaled Nearest Mean Classifier and F1-F2 2-D data clustering.

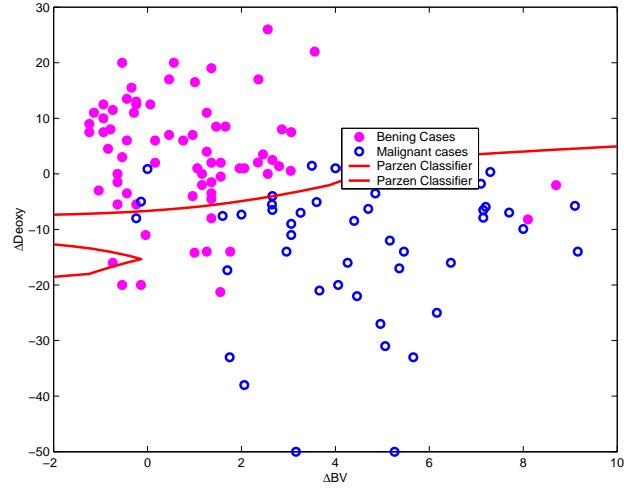


Fig. 21. Parzen and F1-F2 2-D data clustering.

for all of the features and the best two features, namely, $\Delta Deoxy$ and ΔBV are plotted using scaled nearest mean classifier. The observed area under the ROC curve for all the features and F1-F2 are 0.9098 and 0.9001, respectively. In Fig. 6, ROC curves for individual features are plotted using nearest mean classifier. The observed area under the ROC curve for $\Delta Deoxy$ and ΔBV are 0.8832 and 0.8790, respectively.

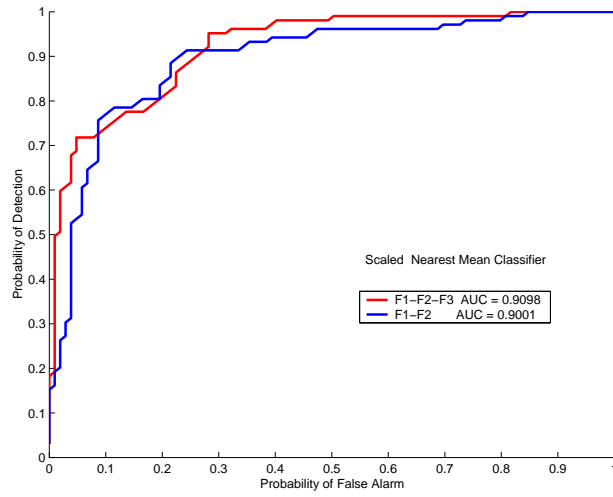


Fig. 22. ROC curves for F1-F2-F3 and F1-F2 using NMSC Classifier.

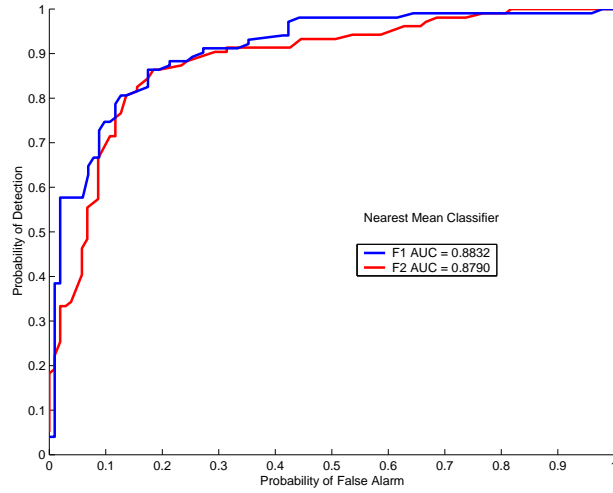


Fig. 23. ROC curves for F1 and F2 using NMC Classifier.

III. KEY RESEARCH ACCOMPLISHMENTS

- 1) We developed a new adaptive discretization method based on MR a priori information for diffuse optical image reconstruction.
- 2) Born approximation based linearization is widely used in practical NIR image reconstruction algorithms. We derived the Born expansion and Frechet derivatives of the coefficient-to-measurement map in diffuse optical tomography and we analyzed the error due to m^{th} order Born expansion in diffuse optical tomography.
- 3) We completed the work on two-level domain decomposition methods for diffuse optical tomography and submitted as a journal paper. The work is accepted to appear in *Inverse Problems*, and Institute of Physics Journal.
- 4) We developed a direct reconstruction method for spatially resolved pharmacokinetic rate images of indocyanine green and applied this method to human breast data. This work is now being prepared as a journal publications.
- 5) We performed an ROC analysis of NIR parameters collected from 116 patients using a handheld NIR spectroscopy instrument and compared the discrimination capability of different NIR parameters using various statistical classifiers and ROC methodology. This work is now being prepared as a journal publication.
- 6) We collected concurrent MR-NIR tomographic data and ICG data from 10 patients. We are currently processing this data.

IV. REPORTABLE OUTCOMES

Complete list of reportable outcomes is given below:

- 1) B. Alacam, B. Yazici, X. Intes, B. Chance, "Extended Kalman filtering for the modeling and analysis of ICG pharmacokinetics in cancerous tumors using NIR optical methods," to appear in *IEEE Transactions in Biomedical Engineering*.
- 2) B. Alacam, B. Yazici, X. Intes, B. Chance, "Analysis of ICG pharmacokinetics in cancerous tumors using NIR optical methods" in *Proc. of EMBS-27th Anniversary Conference*, September, 2005, Shanghai, China, pp. 62 - 65.
- 3) B. Alacam, B. Yazici, X. Intes, S. Nioka, B. Chance, "Spatially resolved pharmacokinetic rate images of ICG using Near Infrared optical methods", *Proc. of 2006 SPIE Photonic West*, San Jose, California USA, 21- 26 January 2006, vol. 6088. pp. 455-464.
- 4) B. Alacam, B. Yazici, X. Intes, S. Nioka, B. Chance, "Direct reconstruction of pharmacokinetic rate Images of Indocyanine Green in fluorescence molecular tomography" *Proceedings of Biomedical Optics Topical Meeting*, Fort Lauderdale, Florida, USA , 19-22 March, 2006, In print.

- 5) B. Alacam, B. Yazici, A. Serdaroglu, X. Intes, B. Chance, "Reconstruction of spatially resolved pharmacokinetic rate images of fluorescence agents in FDOT" to appear in *Proc. of EMBS-28th Anniversary Conference*, September, 2006, New York.
- 6) B. Alacam, B. Yazici, X. Intes, B. Chance, "Direct reconstruction of spatially resolved pharmacokinetic rate images of fluorescence agents" to be submitted to *IEEE Transactions in Medical Imaging*.
- 7) K. Kwon and B. Yazici, "Two-level domain decomposition methods for diffuse optical tomography," to appear in *Inverse Problems*.
- 8) M. Guven, B. Yazici, K. Kwon, E. Giladi, X. Intes, "Effect of Discretization error in diffuse optical absorption imaging," submitted to *Inverse Problems*.
- 9) K. Kwon and B. Yazici, "Born expansion and Frechet derivatives in diffuse optical tomography," submitted to *Inverse Problems*.
- 10) M. Guven, B. Yazici, K. Kwon, E. Giladi, X. Intes, "Effect of Born Approximation in diffuse optical absorption imaging," in preparation.
- 11) M. Guven, B. Yazici, X. Intes, B. Chance, "A hierarchical Bayesian formulation for diffuse optical tomography with a priori anatomical information", in the proceedings of ASILOMAR Conference, Pacific Grove, October 30-November 2, 2005.
- 12) M. Guven, B. Yazici, X. Intes, B. Chance, "Diffuse optical tomography with a priori anatomical information", in the proceedings of Applied Imagery Pattern Recognition (AIPR) Workshop Emerging Technologies and Applications for Imagery Pattern Recognition, Washington, DC, USA, October 19-21.
- 13) M. Guven, K. Kwon, B. Yazici, E. Giladi, X. Intes, "A Priori Interpolation Error Based Mesh Generation for Diffuse Optical Tomography" in the proceedings of Applied Imagery Pattern Recognition (AIPR) Workshop Emerging Technologies and Applications for Imagery Pattern Recognition, Washington, DC, USA, October 19-21.

V. CONCLUSIONS

In the last 12 months, our collaborator, Dr. Britton Chance at University of Pennsylvania has provided 116 patient data collected using the handheld spectrometers. This data set is not tomographic, however, it is sufficiently informative in understanding the value of the stand alone NIR features for breast cancer diagnosis. We have analyzed this data using the ROC methodology and demonstrated that stand-alone NIR features yield a high AUC (0.9 or above) for cancer diagnosis. We are in the process of documenting our results as a journal paper.

We have developed a direct pharmacokinetic rate imaging method for ICG. We have reported our research in

three conference papers. We are currently in the process of documenting our research as a journal paper.

We have extended the two level domain decomposition methods and published it as a journal article. We have developed adaptive discretization methods for diffuse optical tomography based on a priori information provided by MR images and submitted this work as a journal paper. In practice, diffuse optical image reconstruction is performed typically using linear forward model based on Born approximation. We analyzed the error in diffuse optical image reconstruction due to Born approximation and submitted our results as a journal paper.

Dr. Chance has also collected MR-NIR concurrent tomographic data and ICG data from 10 patients. We are currently in the process of processing this data. We plan to reconstruct diffuse optical tomographic images with MR a priori information. We will also apply our direct reconstruction method to obtain IG pharmacokinetic rate images. In the upcoming 12 months, we expect to collect more patient data and perform an ROC study on NIR features extracted from tomographic images.

REFERENCES

- [1] E. M. Sevick-Muraca et al., "Fluorescence and absorption contrast mechanisms for biomedical optical imaging using frequency-domain techniques," *Photochem. Photobiol.*, Vol.66, pp. 55, 1997.
- [2] X. Intes, J. Ripoll, Y. Chen, S. Nioka, A. G. Yodh, B. Chance, "In vivo continuous-wave optical breast imaging enhanced with Indocyanine Green," *Med. Phys.*, vol. 30-6, pp.1039-1047, June 2003.
- [3] C. Cobelli, D. Foster, and G. Toffolo, *Tracer Kinetics in Biomedical Research*, Kluwer Academic/Plenum, New York, c2000.
- [4] S. C. Brenner, and L. R. Scott, *The mathematical theory of finite element methods*, Springer, Berlin, 1994.
- [5] B. Alacam, B. Yazici, X. Intes, B. Chance "Extended Kalman Filtering for the Modeling and Analysis of ICG Pharmacokinetics in Cancerous Tumors using NIR Optical Methods", *Transactions in IEEE Biomedical Engineering*, Accepted, In Press.
- [6] D.J. Cuccia, F. Bevilacqua, A. J. Durkin, S. Merritt, B. J. Tromberg, G. Gulsen, H. Yu, J. Wang, and O. Nalcioglu, "In vivo quantification of optical contrast agent dynamics in rat tumors by use of diffuse optical spectroscopy with magnetic resonance imaging coregistration," *Applied Optics*, vol. 42, no. 1, pp. 2940-2950, June 2003.
- [7] S. Nioka, Y. Yung, M. Schnall, S. Zhao, S. Orel, C. Xie, B. Chance, and S. Solin, "Optical imaging of breast tumor by means of continuous waves," *Adv. Exp. Med. Biol.*, 411, 227-232, 1997.
- [8] Folkman, J., Tumor angiogenesis: therapeutic implications. *N. Engl. J. Med.*, 1971. 285(21): p. 1182-6.
- [9] Folkman, J., What is the evidence that tumors are angiogenesis dependent? *J. Natl. Cancer inst.*, 1990. 82(1): p. 4-6.
- [10] Blood, C. H. and B. R. Zetter, Tumor interactions with the vasculature: angiogenesis and tumor metastasis. *Biochem. Biophys. Acta*, 1990. 1032(1): p. 89-118.
- [11] Vaupel, P., et al., Current status of knowledge and critical issues in tumor oxygenation. Results from 25 years research in tumor pathophysiology. *Adv. Exp. Med. Biol.*, 1998. 454: p. 591-602.
- [12] Vaupel, P., et al., Oxygenation of human tumors: evaluation of tissue oxygen distribution in breast cancers by computerized O₂ tension measurements. *Cancer Res.*, 1991. 51(12): p. 3316-22.
- [13] Runkel, S., et al., Oxygenations of mammary tumors as evaluated by ultrasound-guided computerized-pO₂-histography. *Adv. Exp. Med. Biol.*, 1994. 345: p. 451-8.

- [14] Pogue, B. W., et al., Quantitative hemoglobin tomography with diffuse near-infrared spectroscopy: pilot results in the breast. *Radiology*, 2001. 218(1): 261–6.
- [15] Gurfinkel M et al 2000 Pharmacokinetics of ICG and HPPH-car for the detection of normal and tumour tissue using fluorescence, near-infrared reflectance imaging: a case study *Photochem. Photobiol.* 72 94-102
- [16] Harms S E. Breast magnetic resonance imaging. *Seminars in Ultrasound, CT & MR* 1998; 19:104-120.
- [17] Harms SE, Flamig DP, Hesley KL, et al. MR imaging of the breast with rotating delivery of excitation off resonance: clinical experience with pathologic correlation. *Radiology* 1993; 187:493-501.
- [18] Williams MB, Pisano ED, Schnall MD, Fajardo LL. Future directions in imaging of breast diseases. *Radiology* 1998; 206:297-300.
- [19] Swift M, Morrell D, Massey RB, Chase CL. Incidence of cancer in 161 families affected by ataxia-telangiectasia. *New England Journal of Medicine* 1991; 325:1831-1836.
- [20] Esserman L, Hylton N, Yassa L, et al. Utility of magnetic resonance imaging in the management of breast cancer: Evidence for improved preoperative staging. *J Clin Oncol* 1999; 17:110-119.
- [21] Robinson, K. J., C. J. Kotre and K. Faulkner. "The use of contrast-detail test objects in the optimization of optical density in mammography." *Br. J. Radiol.* 68: 277-282, 1995.
- [22] Moran, G. R. and F. S. Prato. "Modeling tissue contrast agent concentration: a solution to the tissue homogeneity model using a simulated arterial input function." *Mag. Res. Med.* 45:42-45, 2001.
- [23] Chance B, Nioka S, Zhang J, Conant EF, Hwang E, Briest S, Orel SG, Schnall MD, Czerniecki BJ., "Breast cancer detection based on incremental biochemical and physiological properties of breast cancers: a six-year, two-site study," *Academic Radiology*, Vol. 12, Issue 8 pp. 925-933, August 2005.
- [24] Fantini S, Hueber D, Franceschini MA, Gratton E, Rosenfeld W, Stubblefield PG, Maulik D, Stankovic MR., "Non-invasive optical monitoring of the newborn piglet brain using continuous-wave and frequency-domain spectroscopy," *Phys. Med. Biol.*, Vol. 44, pp. 1543-1563, 1999.
- [25] Fukunaga K. *Introduction to Statistical Pattern Recognition*, New York:Academic Press, 1990.
- [26] Duda RO, Hart PE, Stork DG. *Pattern Classification*. New York: Wiley-Interscience, 2000.

Appendix

Key Publications

Extended Kalman Filtering for the Modeling and Analysis of ICG Pharmacokinetics in Cancerous Tumors using NIR Optical Methods

Burak Alacam, *Member, IEEE*, Birsen Yazici*, *Member, IEEE*, Xavier Intes, Britton Chance

Abstract—Compartmental modeling of indocyanine green (ICG) pharmacokinetics, as measured by near infrared (NIR) techniques, has the potential to provide diagnostic information for tumor differentiation. In this paper, we present three different compartmental models to model the pharmacokinetics of ICG in cancerous tumors. We introduce a systematic and robust approach to model and analyze ICG pharmacokinetics based on the extended Kalman filtering (EKF) framework. The proposed EKF framework effectively models multiple-compartment and multiple-measurement systems in the presence of measurement noise and uncertainties in model dynamics. It provides simultaneous estimation of pharmacokinetic parameters and ICG concentrations in each compartment. Moreover, the recursive nature of the Kalman filter estimator potentially allows real time monitoring of time varying pharmacokinetic rates and concentration changes in different compartments. Additionally, we introduce an information theoretic criteria for the best compartmental model order selection, and residual analysis for the statistical validation of the estimates. We tested our approach using the ICG concentration data acquired from four Fischer rats carrying adenocarcinoma tumor cells. Our study indicates that, in addition to the pharmacokinetic rates, the EKF model may provide parameters that may be useful for tumor differentiation.

Index Terms—Extended Kalman filter, indocyanine green, compartmental analysis, pharmacokinetics, tumor characterization.

I. INTRODUCTION

NEAR infrared (NIR) diffuse optical imaging and spectroscopy methods provide quantitative functional information that cannot be obtained by the conventional radiological methods [1]–[3]. NIR techniques can provide *in vivo* measurements of the oxygenation and vascularization states, uptake and release of optical contrast agents, and chromophore concentrations with high sensitivity. In particular, NIR diffuse

optical techniques in conjunction with optical contrast agents have the potential to characterize angiogenesis, and to differentiate between malignant and benign tumors [4]–[7].

At present, indocyanine green (ICG) is the only NIR optical agent approved for human use. In NIR measurements, the presence of ICG within an imaging volume results in an increased signal that can be observed over the course of the experiment. Study of the time kinetics of ICG concentration curves may provide physiologically relevant information for tumor differentiation. Specifically, cancerous tissue types are expected to show high and fast uptake due to the proliferation of "leaky" angiogenic microvessels, while normal and fatty tissue show little uptake.

A number of research groups reported compartmental modeling of ICG time-kinetic measurements using NIR methods for tumor diagnosis in animal and human subjects [8]–[10]. A compartmental model is a mathematical description of the concentrations of contrast agents in which each compartment represents a kinetically distinct tissue type. It consists of a set of coupled ordinary differential equations (ODE) and a measurement model. Coefficients of the ODE's are the physiological parameters of interest that represent rates of exchange between different compartments. These parameters are non-linearly related to the total concentration of ICG measured by NIR methods. Furthermore, concentration of ICG in each compartment cannot be directly measured non-invasively by NIR techniques, making the pharmacokinetic parameter estimation a highly non-linear problem.

Current methods of ICG compartmental modeling involve curve fitting methods and various techniques for solving differential equations. Gurfinkel et al. presented a two-compartment model for ICG kinetics and estimated model parameters [8]. The measurements were obtained using a frequency domain photon migration system coupled with a charge-coupled device. The pharmacokinetic parameters were estimated for each pixel based on a curve fitting method. This study indicated that model parameters show no difference in the ICG uptake rates between normal and diseased tissue. Cuccia et al. presented a study of the dynamics of ICG in an adenocarcinoma rat tumor model [9]. A two-compartment model describing the ICG dynamics was used to quantify physiologic parameters related to capillary permeability. The ICG concentration curves were fitted to the compartmental model using a non-linear least squares Levenberg-Marquart algorithm. It was shown that different tumor types have different capillary permeability rates. Intes et al. presented the uptake of ICG by breast tumors

Manuscript received April 7, 2005; revised February 4, 2006. This work was supported by U.S. Army Medical Research Acquisition Activity under grant W81XWH-04-1-0559, and Office of Naval Research under grant N000014-04-1-0694, and partly supported by CenSSIS under the Engineering Research Centers Program of National Science Foundation under grant EEC-9986821. X. Intes acknowledges partial support from the National Institute of Health grant No: CA110173. Asterisk indicates corresponding author.

Burak Alacam, and *Birsen Yazici are with Department of Electrical, Computer, and Systems Engineering, Rensselaer Polytechnic Institute, Troy, NY, USA (e-mail: yazici@ecse.rpi.edu). Xavier Intes is with Advanced Research Technologies Inc., Saint-Laurent, Quebec, CANADA. Britton Chance is with Department of Biochemistry and Biophysics, University of Pennsylvania, Philadelphia, PA, USA.

Copyright (c) 2006 IEEE. Personal use of this material is permitted. However, permission to use this material for any other purposes must be obtained from the IEEE by sending an email to pubs-permissions@ieee.org.

using a continuous wave diffuse optical tomography apparatus [10]. A two-compartment model was used to analyze the pharmacokinetics of ICG. A curve fitting algorithm, namely the non-linear Nelder-Mead simplex search, was used to estimate the pharmacokinetic parameters. This study showed that the malignant cases exhibit slower rate constants (uptake and outflow) as compared to healthy tissue.

While the studies described above demonstrate the feasibility of the ICG pharmacokinetics in tumor characterization; due to the highly non-linear nature of the pharmacokinetic parameter estimation, variation in parameter values from one subject to another, and sparse data available in clinical and laboratory settings, a *systematic and robust* approach is needed to model, estimate and analyze ICG pharmacokinetics. Such an approach must include: *i)* a method for compartmental model order selection, *ii)* a robust method of estimating ICG pharmacokinetic parameters, and *iii)* a method of validating the selected model and the estimation results.

In this paper, we present three different compartmental models for the ICG pharmacokinetics in cancerous tumors and propose an extended Kalman filtering (EKF) framework to estimate the model parameters. The models capture the transportation of ICG between the vascular and extravascular compartments, including interstitial fluid region, parenchymal cell, intracellular binding site, and extravascular, extracellular spaces (EES). The extended Kalman filter (EKF) is a recursive modeling and estimation method with numerous advantages in ICG pharmacokinetic modeling. These include: *i)* effective modeling of multiple compartments, and multiple measurement systems governed by coupled ordinary differential equations, in the presence of measurement noise and uncertainties in the compartmental model dynamics; *ii)* simultaneous estimation of pharmacokinetic model parameters and ICG concentrations in each compartment, which are not accessible *in vivo* by means of NIR techniques; *iii)* recursive estimation of time-varying pharmacokinetic model parameters; *iv)* statistical validation of estimated concentrations and error bounds on the pharmacokinetic parameter estimates; *v)* incorporation of available a priori information about the initial conditions of the permeability rates into the estimation procedure; *vi)* potential real-time monitoring of ICG pharmacokinetic parameters and ICG concentrations in different compartments due to the recursive nature of the EKF estimation method. Additionally, we present a method for selecting the optimal compartmental model order based on a Bayesian information criterion, and a statistical validation method based on residual analysis.

We test our approach using the ICG concentration data acquired from four Fisher rats carrying adenocarcinoma tumor cells. Two-, three- and four-compartment models are fitted to data and pharmacokinetic model parameters and concentrations in different compartments are estimated using the EKF framework. The Bayesian information criterion suggests that the two-compartment model provides a sufficient fit for our data. The estimated model order and the model parameters are further validated by residual analysis. The model parameters are used to differentiate between two types of cancerous tumors. Our study suggests that the permeability rates out of the vasculature are higher in edematous tumors as compared

to necrotic tumors. Additionally, we observe that in the two-compartment model, the ICG concentration curve is higher in the EES compartment in edematous tumors. This suggests that the ratio of the peak value of the ICG concentrations in different compartments may be a useful parameter to differentiate tumors.

The paper is organized as follows: In Section II, we present the two-, three- and four-compartment models for ICG pharmacokinetics in tissue. In Section III, we present the state-space representation of the compartmental models; estimation of ICG pharmacokinetic parameters and ICG concentrations in the EKF framework; and an optimal model order selection criterion. In Section IV, we present the experimental results obtained from Fischer rat data. Section V summarizes our results and conclusion. Appendix I includes the derivation of the likelihood function used in the Bayesian information criterion.

II. ICG PHARMACOKINETIC MODELING USING NIR MEASUREMENTS

A. Indocyanine Green

ICG is an optical dye commonly used in retinopathy and hepatic diagnostics. Given its low toxicity and FDA approval, it has recently been utilized as a blood pooling agent for the detection and diagnosis of cancerous tumors by means of NIR optical methods. The absorption peak of ICG is 805 nm and the fluorescence peak is at 830 nm. ICG has strong affinity for blood proteins. In plasma, ICG is near-completely bound, primarily to albumin. As a result, its *in vivo* kinetics are similar to those of a 70 kD molecule, although it has a molecular weight of about 700 D [11]–[15].

ICG is eliminated from the body primarily through the bile. Outside of the circulatory system, it is not available for removal until it returns to the system. The kinetics of this transition offers a potential means of non-invasively assessing the leakiness of large molecules from the microvasculature; this permeability is a characteristic of the poorly developed vasculature observed in angiogenesis. The increase in local microvasculature density is also expected to induce increased perturbation in the optical signal from intercapillary ICG.

There are some differences in the delivery of ICG between normal and cancerous vasculature. In normal tissue, ICG acts as a blood flow indicator in tight capillaries of normal vessels. However in tumors, ICG may act as a diffusible (extravascular) flow in the leaky capillary of cancer vessels. To investigate the validity of this hypothesis, one has to employ at least a two-compartment model composed of plasma and EES. Additionally, the permeability rate is expected to increase as the malignancy advances [9], [10]. Fig. 1 (a) and (b) illustrates the ICG flow for healthy and malignant tissue, respectively.

B. Compartmental Analysis of ICG Pharmacokinetics

Compartmental modeling allows relatively simple and effective mathematical representation of complex biological responses due to contrast agents. A region of interest is assumed to consist of a number of compartments, generally representing a volume or a group of similar tissues into which the contrast

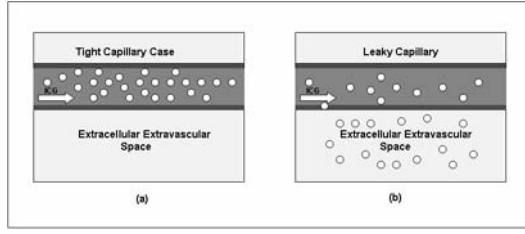


Fig. 1. An illustration of the ICG flow (a) in tight capillary of normal vessel, (b) in permeable capillary of tumor tissue.

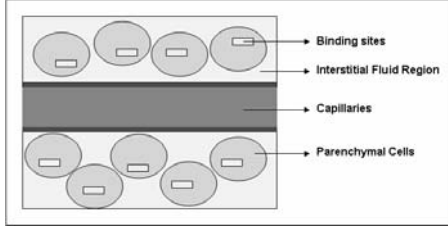


Fig. 2. A simple illustration of the capillary extracapillary structure.

agent is distributed. The concentration change in a specific compartment is modeled as a result of the exchange of contrast agent between connected compartments. These changes are modeled by a collection of coupled ODEs; each equation describing the time change dictated by the biological laws that govern the concentration exchanges between the interacting compartments [16]–[19]. In this work, we investigate three different compartmental models for the ICG kinetics and determine the optimal model order based on Bayesian information criteria.

1) *The four-compartment model:* Fig. 2 illustrates the capillary and extracapillary space relevant to the four compartment model. The four-compartment model includes capillary region, interstitial fluid region, parenchymal cell region and intracellular binding site as compartments [20]. The ICG, injected intravenously into the subject, can pass from the capillary into the reversible binding site inside the cell through the interstitial fluid region and the parenchymal cell region [20]–[22]. Moreover, in advanced tumor stages, the leakiness around the tumor vessels is expected to increase, resulting in higher permeability rates during the transportation of ICG into the compartments. A block diagram of the four-compartment transport and chemical model of ICG delivery is shown in Fig. 3(a).

Let C_p , C_i , C_{pc} , C_b denote the ICG concentrations in plasma, the interstitial fluid region, the parenchymal cell region and the intracellular binding site, respectively; and let $k_{out}^{(4)}$, $k_a^{(4)}$, $k_b^{(4)}$, $k_c^{(4)}$, $k_d^{(4)}$, $k_e^{(4)}$ and $k_f^{(4)}$ be the constants used as equilibrium coefficients as shown in Fig. 3(a). Then the set of differential equations representing the ICG transition between the four compartments is given as follows:

The leakage into and the drainage out of plasma:

$$\frac{dC_p(t)}{dt} = k_b^{(4)} C_i(t) - k_a^{(4)} C_p(t) - k_{out}^{(4)} C_p(t). \quad (1)$$

The leakage into and the drainage out of the interstitial fluid

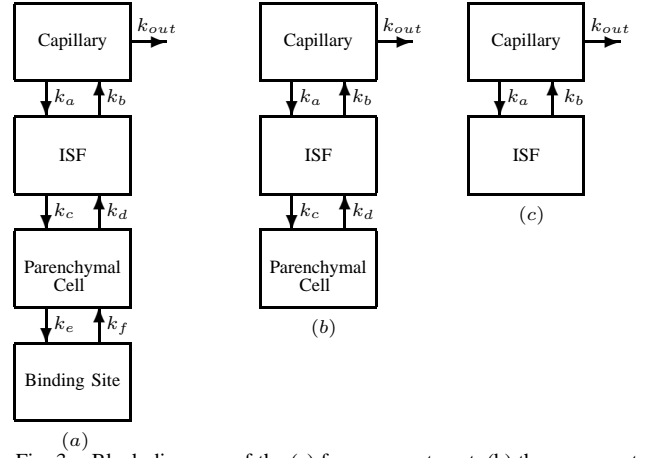


Fig. 3. Block diagrams of the (a) four-compartment, (b) three-compartment, (c) two-compartment models for the ICG pharmacokinetics.

region:

$$\frac{dC_i(t)}{dt} = k_a^{(4)} C_p(t) - k_b^{(4)} C_i(t) - k_c^{(4)} C_i(t) + k_d^{(4)} C_{pc}(t). \quad (2)$$

The leakage into and the drainage out of the parenchymal cell:

$$\frac{dC_{pc}(t)}{dt} = k_c^{(4)} C_i(t) - k_d^{(4)} C_{pc}(t) - k_e^{(4)} C_{pc}(t) + k_f^{(4)} C_b(t). \quad (3)$$

The leakage into and the drainage out of the intracellular binding site:

$$\frac{dC_b(t)}{dt} = k_e^{(4)} C_{pc}(t) - k_f^{(4)} C_b(t). \quad (4)$$

Physiologically, the equilibrium constants are defined by the permeability surface area products given as $PS\rho$, where P is the capillary permeability constant, S is the capillary surface area, and ρ is the tissue density. $k_{out}^{(4)}$ is proportional to the flow rate into and out of the capillary and $k_a^{(4)}$, $k_b^{(4)}$, $k_c^{(4)}$, $k_d^{(4)}$, $k_e^{(4)}$, and $k_f^{(4)}$ represent intra-tissue physiologic effects during ICG delivery from the capillary to the binding site. Note that the superscript denotes the order of the compartmental model.

The actual bulk ICG concentration in the tissue measured by NIR spectroscopy, $m(t)$, is a linear combination of the ICG concentrations in the four different compartments.

$$m(t) = v_p^{(4)} C_p(t) + v_i^{(4)} C_i(t) + v_{pc}^{(4)} C_{pc}(t) + v_b^{(4)} C_b(t), \quad (5)$$

where $v_p^{(4)}$, $v_i^{(4)}$, $v_{pc}^{(4)}$, $v_b^{(4)}$, are volume fractions of plasma, the interstitial fluid region, the parenchymal cell region and the intracellular binding site, respectively.

2) *The three-compartment model:* In this model, the parenchymal cell and intracellular binding site compartments are combined to form a single compartment called parenchymal cell. This amounts to the assumptions that the transport of ICG into the intracellular binding site is negligible as compared to the other compartments, and therefore omitted from the model. A block diagram of the three-compartment transport and chemical model of ICG delivery is shown in Fig. 3(b). The three-compartment transport equations are given as follows:

The leakage into and the drainage out of plasma:

$$\frac{dC_p(t)}{dt} = k_b^{(3)}C_i(t) - k_a^{(3)}C_p(t) - k_{out}^{(3)}C_p(t) \quad (6)$$

The leakage into and the drainage out of the interstitial space:

$$\frac{dC_i(t)}{dt} = k_a^{(3)}C_p(t) - k_b^{(3)}C_i(t) - k_c^{(3)}C_i(t) + k_d^{(3)}C_{pc}(t) \quad (7)$$

The leakage into and the drainage out of the parenchymal cell:

$$\frac{dC_{pc}(t)}{dt} = k_c^{(3)}C_i(t) - k_d^{(3)}C_{pc}(t) \quad (8)$$

The total ICG concentration measured by NIR:

$$m(t) = v_p^{(3)}C_p(t) + v_i^{(3)}C_i(t) + v_{pc}^{(3)}C_{pc}(t) \quad (9)$$

where $v_p^{(3)}$, $v_i^{(3)}$, $v_{pc}^{(3)}$ and C_p , C_i , C_{pc} are as defined in the four-compartment model.

3) *The two-compartment model:* In the two-compartment model, the tumor region is assumed to be composed of two compartments, namely the plasma and the extra-cellular extra-vascular space (EES) [9], [23], [24]. The EES is defined as the region that lies outside of both the vascular region and the tumor cells. The transport of the ICG to the third and fourth compartments are assumed to be negligible. Therefore the last two compartments in the four compartment model is omitted. We consider transcapillary leakage to occur only at the tumor site. We also assume that a small perturbation of the global plasma concentration does not affect the bulk removal. Fig. 3(c) shows the block diagram of the two-compartment model for the ICG kinetics. Let C_p and C_e denote the ICG concentrations in plasma and the EES, respectively. Then the two-compartment ICG chemical transport equations are given as follows:

The leakage into and the drainage out of plasma:

$$\frac{dC_p(t)}{dt} = k_b^{(2)}C_e(t) - k_a^{(2)}C_p(t) - k_{out}^{(2)}C_p(t). \quad (10)$$

The leakage into and the drainage out of the EES:

$$\frac{dC_e(t)}{dt} = k_a^{(2)}C_p(t) - k_b^{(2)}C_e(t). \quad (11)$$

The parameters $k_a^{(2)}$ and $k_b^{(2)}$ govern the leakage into and the drainage out of the EES, respectively. The parameter $k_{out}^{(2)}$ describes the ICG elimination from the body through kidneys and liver.

Actual bulk ICG concentration in the tissue measured by NIR is a linear combination of plasma and EES ICG concentrations given by:

$$m(t) = v_p^{(2)}C_p(t) + v_e^{(2)}C_e(t), \quad (12)$$

where the parameters $v_p^{(2)}$ and $v_e^{(2)}$ denote the plasma and EES volume fractions, respectively.

III. EXTENDED KALMAN FILTERING FOR THE ICG PHARMACOKINETICS

For the rest of our discussion, we shall use the explicit form of the two-compartment model as a running example to clarify our notation. Note that for the rest of the paper, all matrices and vectors will be in boldface and scalar quantities will be in non-boldface notation.

A. State-space Representation of the ICG Pharmacokinetics

Coupled differential equations resulting from the two-compartment modeling of the ICG pharmacokinetics can be expressed in state-space representation as follows:

$$\begin{bmatrix} dC_e(t) \\ dC_p(t) \end{bmatrix} = \begin{bmatrix} -k_b^{(2)} & k_a^{(2)} \\ k_b^{(2)} & -(k_a^{(2)} + k_{out}^{(2)}) \end{bmatrix} \begin{bmatrix} C_e(t) \\ C_p(t) \end{bmatrix} + d\mathbf{B}(t), \quad (13)$$

$$m(t) = \begin{bmatrix} v_e^{(2)} & v_p^{(2)} \end{bmatrix} \begin{bmatrix} C_e(t) \\ C_p(t) \end{bmatrix} + \eta(t)$$

where $d\mathbf{B}(t)$ is the Wiener process increment, $d\mathbf{B}(t) = \boldsymbol{\omega}(t)dt$. Here, $\boldsymbol{\omega}(t)$ and $\eta(t)$ can be thought of as uncorrelated zero mean Gaussian processes with covariance matrix \mathbf{Q} , and variance σ^2 , respectively.

In vector-matrix notation, the continuous time state-space representation for the n -compartment model is given by:

$$d\mathbf{C}(t) = \boldsymbol{\kappa}(\boldsymbol{\alpha}_n)\mathbf{C}(t)dt + d\mathbf{B}(t),$$

$$m(t) = \mathbf{V}(\boldsymbol{\alpha}_n)\mathbf{C}(t) + \eta(t). \quad (14)$$

In (14), $\mathbf{C}(t)$ denotes the concentration vector; $\boldsymbol{\kappa}(\boldsymbol{\alpha}_n)$ is the system matrix, $\mathbf{V}(\boldsymbol{\alpha}_n)$ is the measurement matrix and $\boldsymbol{\alpha}_n$ is the parameter vector whose elements are the pharmacokinetic constants and the volume fractions for the n -compartment model. For example the parameter vector $\boldsymbol{\alpha}_2$ for the two-compartment model is given by

$$\boldsymbol{\alpha}_2 = [k_a^{(2)} \quad k_b^{(2)} \quad k_{out}^{(2)} \quad v_e^{(2)} \quad v_p^{(2)}]. \quad (15)$$

The ICG measurements in (14) are collected at discrete time instances, $t = kT$, $k = 0, 1, \dots$, where T is the sampling period. Therefore, the continuous model described in (14) has to be discretized. To simplify our notation, we shall use $\mathbf{C}(k) = \mathbf{C}(kT)$ and $m(k) = m(kT)$. The discrete state space system and the measurement models are given as follows:

$$\mathbf{C}(k+1) = \boldsymbol{\kappa}_d(\boldsymbol{\alpha}_n)\mathbf{C}(k) + \boldsymbol{\omega}(k)$$

$$m(k) = \mathbf{V}_d(\boldsymbol{\alpha}_n)\mathbf{C}(k) + \eta(k), \quad (16)$$

where $\boldsymbol{\kappa}_d(\boldsymbol{\alpha}_n) = e^{\boldsymbol{\kappa}(\boldsymbol{\alpha}_n)T}$ is the discrete-time system matrix and $\mathbf{V}_d(\boldsymbol{\alpha}_n) = \mathbf{V}(\boldsymbol{\alpha}_n)$ is the discrete-time measurement matrix. $\boldsymbol{\omega}(k)$ and $\eta(k)$ are zero mean Gaussian white noise processes with covariance matrix \mathbf{Q}_d and variance σ_d^2 , respectively. Discretization of state-space models can be found in various system theory books, see for example [25].

An explicit form of the discrete state space model for the two-compartment case is given as follows:

$$\begin{bmatrix} C_e(k+1) \\ C_p(k+1) \end{bmatrix} = \begin{bmatrix} \tau_{11} & \tau_{12} \\ \tau_{21} & \tau_{22} \end{bmatrix} \begin{bmatrix} C_e(k) \\ C_p(k) \end{bmatrix} + \boldsymbol{\omega}(k) \quad (17)$$

$$m(k) = \begin{bmatrix} v_e^{(2)} & v_p^{(2)} \end{bmatrix} \begin{bmatrix} C_e(k) \\ C_p(k) \end{bmatrix} + \eta(k),$$

where τ_{ij} is the i^{th} row and j^{th} column entry of the system matrix $\boldsymbol{\kappa}_d(\boldsymbol{\alpha}_2)$. Note that the matrix entry τ_{ij} is an exponential function of the parameters $k_a^{(2)}$, $k_b^{(2)}$ and $k_{out}^{(2)}$.

To simplify the estimation process, we shall first estimate the matrix entries, τ_{ij} , of the discrete-time system matrix $\kappa_d(\alpha_n)$ and then compute the pharmacokinetic parameters for each compartmental model.

B. Modeling of ICG Pharmacokinetic Parameters and Concentrations in an Extended Kalman Filter Framework

The Kalman filter provides a recursive method to estimate the states in state-space models, in which the states are driven by noise, and the measurements are collected in the presence of measurement noise [26]–[28]. In the case of non-linear state-space models, the extended Kalman filter linearizes the model around the current state estimate, and then applies the KF to the resulting linear model. The EKF framework is also utilized for the joint estimation of the unknown system and/or measurement parameters and states. In a linear state-space model when both states and system parameters are unknown, the linear state-space model can be regarded as a non-linear model in which the linear system parameters and states are combined to form the new states of the non-linear model. This system is then linearized and solved for the unknown states using the KF estimator. We consider a linear Taylor approximation of the non-linear model. The details of the linearization procedure and a general discussion on EKF can be found in [27], [29]–[31].

In our problem, the objective is to simultaneously estimate the states, i.e., the ICG concentrations in each compartment, and the system and measurement parameters, i.e., the pharmacokinetic parameters and the volume fractions. Let θ_n denote the discrete-time parameter vector of the pharmacokinetic rates and volume fractions. For example, in the two-compartment model, θ_2 is given by

$$\theta_2 = \begin{bmatrix} \tau_{11} & \tau_{12} & \tau_{21} & \tau_{22} & v_e^{(2)} & v_p^{(2)} \end{bmatrix}^T. \quad (18)$$

Note that the parameter vector θ_n , derived from the state space model (17), is time independent. In order to estimate θ_n within the EKF framework, the following dynamic model is introduced:

$$\theta_n(k+1) = \theta_n(k) + \varsigma(k), \quad (19)$$

where $\varsigma(k)$ is a zero mean white noise process with covariance matrix S_d [27]. Here, $\theta_n(k)$ can be thought of as the k^{th} update of the parameter rather than its value at time k .

We append the parameter vector $\theta_n(k+1)$ to the ICG concentration vector $C(k+1)$ to form the new non-linear state-space model given by

$$\begin{bmatrix} C(k+1) \\ \theta_n(k+1) \end{bmatrix} = \begin{bmatrix} K(\theta_n)C(k) \\ \theta_n(k) \end{bmatrix} + \begin{bmatrix} \omega(k) \\ \varsigma(k) \end{bmatrix} \quad (20)$$

$$m(k) = \begin{bmatrix} V_d(\theta_n) & 0 \end{bmatrix} \begin{bmatrix} C(k) \\ \theta_n(k) \end{bmatrix} + \eta(k),$$

where $K(\theta_n) = \kappa_d(\alpha_n)$.

C. EKF Joint Estimation of ICG Concentrations, Pharmacokinetic Parameters, and Volume Fractions

In this section we will summarize the major steps of the EKF estimator for the joint estimation of ICG concentrations and compartmental model parameters.

Let the subscript $k|t$ denote the estimate at time k given all the measurements up to time t . Then the 1-step ahead prediction of the ICG concentrations and the compartmental model parameters are given as follows:

$$\begin{bmatrix} \hat{C} \\ \hat{\theta}_n \end{bmatrix}_{k|k-1} = \begin{bmatrix} K(\hat{\theta}_n)\hat{C} \\ \hat{\theta}_n \end{bmatrix}_{k-1|k-1}. \quad (21)$$

For the two-compartment model, (21) becomes

$$\begin{bmatrix} \hat{C}_e \\ \hat{C}_p \\ \hat{\theta}_2 \end{bmatrix}_{k|k-1} = \begin{bmatrix} \hat{\tau}_{11}\hat{C}_e + \hat{\tau}_{12}\hat{C}_p \\ \hat{\tau}_{21}\hat{C}_e + \hat{\tau}_{22}\hat{C}_p \\ \hat{\theta}_2 \end{bmatrix}_{k-1|k-1}. \quad (22)$$

The error covariance matrix, $P_{k|k-1}$, of the 1-step ahead predictions is given as follows:

$$P_{k|k-1} = J_{k-1}P_{k-1|k-1}J_{k-1}^T + \begin{bmatrix} Q_d & 0 \\ 0 & S_d \end{bmatrix}, \quad (23)$$

where J_k is the Jacobian of the non-linear EKF system function at time k . Explicitly, it is given by:

$$J_k = \begin{bmatrix} K(\hat{\theta}_n) & \frac{\partial}{\partial \theta_n}[K(\hat{\theta}_n)\hat{C}] \\ \mathbf{0} & \mathbf{I} \end{bmatrix}_{k|k}, \quad (24)$$

where $\mathbf{0}$ and \mathbf{I} denote zero and identity matrices, respectively. The Jacobian matrix for the two-compartment model becomes

$$J_k = \begin{bmatrix} \begin{pmatrix} \hat{\tau}_{11} & \hat{\tau}_{12} \\ \hat{\tau}_{21} & \hat{\tau}_{22} \end{pmatrix} & \begin{pmatrix} \hat{C}_e & \hat{C}_p & 0 & 0 & 0 & 0 \\ 0 & 0 & \hat{C}_e & \hat{C}_p & 0 & 0 \end{pmatrix} \\ \mathbf{0}_{(6 \times 2)} & \mathbf{I}_{(6 \times 6)} \end{bmatrix}_{k|k}, \quad (25)$$

where $\mathbf{0}_{(6 \times 2)}$ is a 6×2 zero matrix, and $\mathbf{I}_{(6 \times 6)}$ is a 6×6 identity matrix.

The 1-step ahead predictions are updated to the k^{th} -step estimates by means of the Kalman gain matrix which is given by

$$G_k = P_{k|k-1}\Lambda^T[\Lambda P_{k|k-1}\Lambda^T + \sigma_k^2]^{-1}, \quad (26)$$

where Λ is the following vector

$$\begin{bmatrix} V_d(\hat{\theta}) & \frac{\partial}{\partial \theta}[V_d(\hat{\theta})\hat{C}] \end{bmatrix}_{k|k-1}. \quad (27)$$

For the two-compartment model the Λ vector becomes

$$\begin{bmatrix} \hat{v}_e^{(2)} & \hat{v}_p^{(2)} & 0 & 0 & 0 & 0 & \hat{C}_e & \hat{C}_p \end{bmatrix}_{k|k-1}. \quad (28)$$

The k^{th} -step estimate of the concentrations and the parameters are obtained recursively using

$$\begin{bmatrix} \hat{C} \\ \hat{\theta} \end{bmatrix}_{k|k} = \begin{bmatrix} \hat{C} \\ \hat{\theta} \end{bmatrix}_{k|k-1} + G_k(m(k) - [V_d(\hat{\theta})\hat{C}]_{k|k-1}). \quad (29)$$

For the two-compartment case, the k^{th} -step estimate of the concentrations and the parameters is

$$\begin{bmatrix} \hat{C}_e \\ \hat{C}_p \\ \hat{\theta}_2 \end{bmatrix}_{k|k} = \begin{bmatrix} \hat{C}_e \\ \hat{C}_p \\ \hat{\theta}_2 \end{bmatrix}_{k|k-1} + \mathbf{G}_k [m(k) - (\hat{v}_e^{(2)} \hat{C}_e - \hat{v}_p^{(2)} \hat{C}_p)_{k|k-1}] \quad (30)$$

The error covariance matrix, $\mathbf{P}_{k|k}$, of the k^{th} -step estimates is updated as

$$\mathbf{P}_{k|k} = [\mathbf{I} - \mathbf{G}_k \mathbf{A}] \mathbf{P}_{k|k-1}, \quad (31)$$

where \mathbf{I} is the identity matrix.

In general, the convergence of EKF depends on proper choices of the initial values of the parameters, θ , initial values of the concentrations, \mathbf{C} , and proper selection of the noise covariance matrices \mathbf{S}_d , \mathbf{Q}_d , and the variance σ_d^2 [33]. The parameter σ_d^2 controls the convergence of the Kalman gain \mathbf{G}_k . To ensure stability, we set σ_d^2 much higher than the $\mathbf{A} \mathbf{P}_{k|k-1} \mathbf{A}^T$ term in (26). However, setting very high values of σ_d^2 leads to slow convergence of the Kalman gain \mathbf{G}_k . The main cause of divergence in EKF can be tracked down to the fact that a change in the parameter vector has no direct effect on the Kalman gain; in other words, there is no coupling term between the Kalman gain and the parameter vector [34]. Based on this observation, we improved the convergence of the EKF by modifying the term $\mathbf{J}(1, 2) = \frac{\partial}{\partial \theta} \mathbf{K}(\theta) \hat{\mathbf{C}}$ in (24), as described in [34].

It has been shown that if \mathbf{Q}_d , \mathbf{S}_d and σ_d^2 are selected less than the actual values, it leads to overconfidence in the accuracy of the estimates of the error covariance matrix [32]. Therefore, we regarded these matrices as tuning parameters and not as the estimates of the true covariance matrices, as suggested in [32].

Theoretically, the state estimates can be initialized at the expected value of the ICG concentrations, i.e. $E[\mathbf{C}(0)]$. One approach to the initialization of the parameters is to utilize the state-space presentation given in (16). Since $E(m(0)) = \mathbf{V}_d(\theta_n(0))E[\mathbf{C}(0)]$, $m(0) - \mathbf{V}_d(\theta_n(0))E[\mathbf{C}(0)]$ is a zero mean random variable. If we express the variance of the measurement $m(0)$ in terms of the variance of $\mathbf{C}(0)$ using the measurement model in (16), and solve for θ_n , we get the estimate $\hat{\theta}_n(0)$ as the most appropriate value for initialization. The details of the selection of the initial values for the parameters can be found in [27].

The initialization of the error covariance matrix is also important for the performance of the EKF. The error covariance matrix is the matrix which provides information about the error bounds for the estimates. Theoretically, the initial error covariance matrix is a diagonal matrix where the diagonal entries are the initial estimates of the variance of concentrations and pharmacokinetic parameters, i.e.

$$\mathbf{P}_{0|0} = \begin{bmatrix} Cov(\mathbf{C}(0)) & 0 \\ 0 & \mathbf{S}_d \end{bmatrix}. \quad (32)$$

In depth discussion on the convergence properties of the EKF can be found in [27], [32]–[34].

D. Compartmental Model Order Selection

We adopted the Bayesian information criterion (BIC) for the optimal model order selection. BIC is a well known information theoretic criterion, in which the optimal model order is selected by minimizing a cost function to avoid overfitting. The cost function depends on the number of observations, the number of unknown parameters to be estimated and the likelihood function. A detailed discussion of the BIC can be found in [35]–[37].

In order to calculate the BIC for different compartmental models, we first derived a likelihood function for the extended Kalman filter. The derivation is based on maximum likelihood estimation of the parameters in the Kalman filtering framework given as in [38], [39]. We then modified this likelihood function for the extended Kalman filter estimator for the joint estimation of compartmental model parameters and concentrations. The details of the derivation is provided in the Appendix I.

IV. EXPERIMENTAL RESULTS - ICG PHARMACOKINETICS IN FISCHER RAT DATA

We applied the proposed EKF framework to the pharmacokinetic analysis of ICG data obtained from four Fischer rats with adenocarcinoma. R3230ac adenocarcinoma cells were injected below the skin into four Fischer rats 3 weeks prior to measurements. The tumor size for the rats varies in diameter from 5 to 30 mm. Measurements were conducted with a combined frequency-domain and steady-state optical technique that facilitates rapid measurement of tissue absorption. Frequency domain measurements were obtained at 674, 800, 849, 898, and 915 nm, modulated at frequencies from 50 to 601 MHz, sweeping a total of 233 frequencies. Tumors were also imaged by use of contrast-enhanced magnetic resonance imaging and coregistered with the location of the optical probe. In addition, a broadband continuous wave reflectance measurement spanning the range 650-1000 nm was performed with a spectrometer. With the reduced-scattering coefficient spectrum and diffusion theory, the broadband reflectance spectra were converted to absorption coefficient spectra. The absolute concentration of ICG, together with oxy-hemoglobin, deoxy-hemoglobin, and water were calculated by using multiple linear regressions of ICG extinction coefficient spectra to the calculated absorption spectrum at approximately every second for ten minutes. A detailed discussion of the measurement process and apparatus can be found in [40], [41].

Fig. 4 presents the ICG concentrations (μM) from four different rats. Tumors in Rat 1 and 2 are classified as necrotic because of their low tissue oxy-hemoglobin, low total hemoglobin, and low gadolinium-diethylene-triamine penta-acetic acid (Gd-DTPA) enhancement levels. Tumors in Rat 3 and 4 are classified as edematous due to their high water content [42]. It can be observed from Fig. 4 that the necrotic cases display low peak ICG concentration values and slowly rising slopes unlike the edematous cases with high peak values and sharp rising slopes.

We estimated the pharmacokinetic rates for the four-, three- and two-compartment models. Each data set has 504 mea-

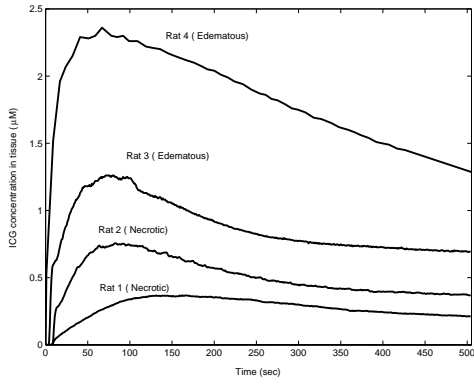


Fig. 4. ICG concentrations measured in tissue for four different rats.

measurements. The reported parameter estimates are the asymptotic values obtained when the extended Kalman filter has converged. In other words, the predicted parameter values corresponding to the final estimate, i.e., $k_a^2 = k_a^2, (k=504)$. The results are given in Tables I, II, and III, respectively. The error bounds on the estimates are derived from the covariance matrix of the EKF estimator. The estimated pharmacokinetic rates for all compartmental models indicate that the exchange rates between the capillary and the adjacent compartment (ISS or EES), $k_a^n, k_b^n, n = 2, 3, 4$, are significantly different for the necrotic and edematous tissue. We observe that for the four- and three-compartment models, the estimated exchange rates between the ISS and parenchymal cell compartments, $k_c^n, k_d^n, n = 3, 4$, are comparable. Similarly, the estimated rate of drainage out of the plasma, $k_{out}^n, n = 2, 3, 4$, are consistent for all models.

Based on the model parameter estimates, we computed the BIC values for each rat data to reveal overfitting. The BIC values and the number of unknown parameters for each rat data are tabulated in Table IV. The BIC suggests that the two-compartment model is sufficient for all four measurement sets.

We further analyze the goodness-of-fit of the compartmental models by means of residual analysis. The basic idea of residual analysis is to compare the actual measurements $m(k)$ with their 1-step ahead predictions, $\hat{m}(k)_{k|k-1}$, based on the estimated parameters. A detailed discussion on residual analysis can be found in [26], [43]. The mean and variance of the residual error for the four-, three- and two-compartmental models are tabulated in Table 5. To normalize the error with respect to the magnitude of the actual measurements, we calculated the signal-to-noise ratio (SNR) using the median value of the measurements and the mean of the residual errors for each rat data. As seen from the results in Table 6, the SNR values are higher for the two-compartment case for all data sets. These results show that the two-compartment model provides the minimum bias and the best statistical efficiency. Fig. 5 shows the measured total concentration data and its 1-step ahead prediction based on the two-compartment model for each rat data. Clearly, there is a good agreement between the actual and the predicted values.

Based on the BIC and residual analysis, we conclude that the two-compartment model provides the best statistical fit for

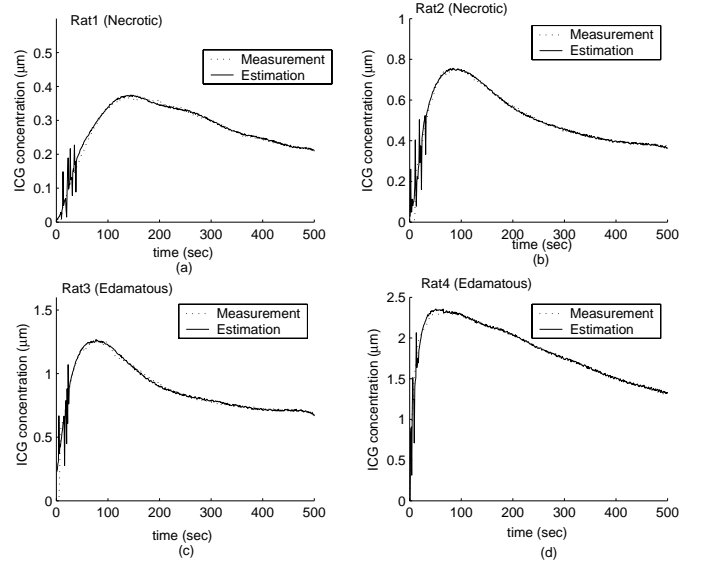


Fig. 5. ICG concentration measurement data and 1-step prediction of the measurements for four different rats.

the rat data and investigate the estimated model parameters in more detail.

In the two-compartment model, the rate of leakage into the EES from the capillary, $k_a^{(2)}$, range from 0.0247 to 0.0840 sec^{-1} and the rate of drainage out of the EES and into the capillary, $k_b^{(2)}$, range from 0.0106 to 0.0777 sec^{-1} . Note that the permeability rates for the necrotic cases are lower than the ones observed for the edematous cases. Additionally, the estimated values for the pharmacokinetic rates are much higher than the normal tissue values due to the increased leakiness of the blood vessels around the tumor region [9], [44]. The estimated plasma volume fractions agrees with the values reported earlier [9], and the values presented in the literature [45], [46]. These results confirm that $v_p^{(2)}$ can be large in tumors and that its magnitude varies with respect to the stage of the tumor [24]. The estimated values of the EES volume fraction, $v_e^{(2)}$, range from 0.218 to 0.53, in agreement with the 0.2 to 0.5 range reported earlier [23]. Note that these results are valid only for the ICG pharmacokinetics in tumor cells R3230ac, adenocarcinoma and may not be generalized for other types of contrast agents or tumor types.

Fig. 6 shows the estimated ICG concentrations in plasma and the EES compartments for the two-compartment model for Rats 1 to 4. Note that the concentration curves in Fig. 5 and Fig. 6 follow a similar time course since the curves

TABLE IV
TEST FOR MODEL ORDER SELECTION FOR THREE DIFFERENT
COMPARTMENTAL MODELS FOR FOUR DIFFERENT DATA SETS

		Rat1	Rat2	Rat3	Rat4
Model	p	$\phi_{BIC}(p)$	$\phi_{BIC}(p)$	$\phi_{BIC}(p)$	$\phi_{BIC}(p)$
Two-comp. Model	7	-178.24	-198.36	-202.81	-172.09
Three-comp. Model	11	-71.62	-83.85	-92.18	-63.91
Four-comp. Model	15	-39.72	-45.12	-56.34	-30.02

TABLE I
FOUR-COMPARTMENT MODEL: ESTIMATED PHARMACOKINETIC PARAMETERS USING EKF ALGORITHM

	$k_a^{(4)}$ ($\text{sec}^{-1}10^{-2}$)	$k_b^{(4)}$ ($\text{sec}^{-1}10^{-2}$)	$k_c^{(4)}$ ($\text{sec}^{-1}10^{-2}$)	$k_d^{(4)}$ ($\text{sec}^{-1}10^{-2}$)	$k_e^{(4)}$ ($\text{sec}^{-1}10^{-2}$)	$k_f^{(4)}$ ($\text{sec}^{-1}10^{-2}$)	$k_{out}^{(4)}$ ($\text{sec}^{-1}10^{-3}$)
Rat 1 (Necrotic)	1.45±0.013	1.22±0.019	1.86±0.017	2.02±0.026	2.74±0.041	2.41±0.051	4.05±0.059
Rat 2 (Necrotic)	3.48±0.048	2.77±0.034	4.28±0.048	4.33±0.040	2.98±0.048	3.03±0.061	4.76±0.062
Rat 3 (Edematous)	4.94±0.052	5.16±0.067	4.22±0.052	4.13±0.067	4.14±0.070	4.27±0.078	5.39±0.085
Rat 4 (Edematous)	5.25±0.053	5.31±0.063	5.07±0.068	5.22±0.063	4.43±0.075	4.03±0.072	3.85±0.056

TABLE II
THREE-COMPARTMENT MODEL: ESTIMATED PHARMACOKINETIC PARAMETERS USING EKF ALGORITHM

	$k_a^{(3)}$ ($\text{sec}^{-1}10^{-2}$)	$k_b^{(3)}$ ($\text{sec}^{-1}10^{-2}$)	$k_c^{(3)}$ ($\text{sec}^{-1}10^{-2}$)	$k_d^{(3)}$ ($\text{sec}^{-1}10^{-2}$)	$k_{out}^{(3)}$ ($\text{sec}^{-1}10^{-3}$)
Rat 1 (Necrotic)	1.93±0.061	1.28±0.049	1.82±0.032	2.02±0.041	3.89±0.052
Rat 2 (Necrotic)	4.41±0.074	2.48±0.067	4.87±0.066	5.03±0.057	5.45±0.071
Rat 3 (Edematous)	4.71±0.085	3.88±0.077	4.95±0.059	4.68±0.050	4.42±0.040
Rat 4 (Edematous)	5.29±0.091	6.48±0.096	4.48±0.062	4.20±0.048	5.01±0.055

TABLE III
TWO-COMPARTMENT MODEL: ESTIMATED PHARMACOKINETIC PARAMETERS AND VOLUME FRACTIONS USING EKF ALGORITHM

	$k_a^{(2)}$ ($\text{sec}^{-1}10^{-2}$)	$k_b^{(2)}$ ($\text{sec}^{-1}10^{-2}$)	$k_{out}^{(2)}$ ($\text{sec}^{-1}10^{-3}$)	$v_e^{(2)}$ (10^{-2})	$v_p^{(2)}$ (10^{-2})
Rat 1 (Necrotic)	2.47±0.043	1.06±0.052	4.61±0.073	21.8±1.92	1.41±0.053
Rat 2 (Necrotic)	3.54±0.082	2.98±0.086	4.83±0.092	25.4±3.49	2.42±0.088
Rat 3 (Edematous)	6.90±0.101	4.93±0.072	3.95±0.048	30.4±2.81	4.84±0.120
Rat 4 (Edematous)	8.40±0.114	7.77±0.091	4.02±0.068	53.0±4.73	7.03±0.321

TABLE V

THE MEAN AND VARIANCE OF THE ERROR BETWEEN THE ESTIMATES AND MEASUREMENTS

	Four-compartment		Three-compartment		Two-compartment	
	Mean	Variance	Mean	Variance	Mean	Variance
Rat1	0.0987	7.6e-004	0.0605	4.7e-004	0.0072	2.5e-005
Rat2	0.1043	9.1e-004	0.0767	3.0e-004	0.0057	4.8e-005
Rat3	0.1204	8.9e-004	0.0883	4.9e-004	0.0041	3.0e-005
Rat4	0.0904	5.9e-004	0.0589	6.8e-004	0.0076	8.6e-005

TABLE VI

SNR VALUES FOR THREE DIFFERENT COMPARTMENTAL MODELS FOR FOUR DIFFERENT DATA SETS

	Rat1	Rat2	Rat3	Rat4
Model	SNR (dB)	SNR	SNR	SNR
Two-compartment Model	73.2	68.1	108.3	107.9
Three-compartment Model	30.7	36.1	23.9	47.0
Four-compartment Model	20.8	29.9	27.7	18.4

in Fig. 6 is a linear combination of the curves in Fig. 5. Note that initial estimates of concentrations are noisy due to the limited data used in the recursive EKF estimation. This can be improved by Kalman backward smoothing [47]. The peak values of the plasma concentration, C_p , range from 2.72 μM to 4.28 μM . The absolute value of the concentrations may not be very useful. However, concentration of ICG in a compartment relative to the one in another compartment may

provide useful information. We consider the ratio of the peak concentrations in plasma and the EES as a potential parameter to discriminate different tumors. The peak C_p/C_e ratio for Rats 1 to 4 is 0.551, 0.593, 0.787, 1.151, respectively. This ratio is higher in edematous cases consistent with the fact that ICG-albumin leaks more into the EES in edematous tumors. Additionally, the ICG concentration in plasma decays faster than the ICG concentration in the EES due to its elimination through the liver and kidneys.

V. CONCLUSION

In this paper we present three different compartmental models, an extended Kalman filtering framework for the modeling, and estimation of ICG pharmacokinetics in cancerous tumors based on NIR measurements. Additionally, we introduce an information theoretic criterion and residual analysis for model selection and statistical validation. The proposed compartmental models are fit to data obtained from Fischer rats with adenocarcinoma cells. The pharmacokinetic rates and volume fractions are estimated for all models. The estimated rates for all compartmental models indicate that the exchange rates between the capillary and the adjacent compartment (ISS or EES) are significantly larger for the edematous tissue as compared to the necrotic cases. Based on the BIC and residual analysis, we conclude that the two-compartment model provides the best statistical fit for the rat data and ICG pharmacokinetics. Parameters of this model indicate that the permeability rates are higher for edematous

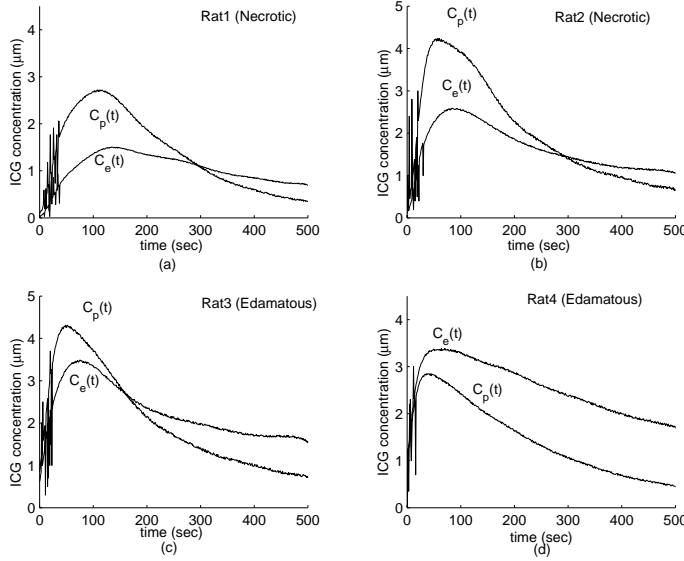


Fig. 6. ICG concentrations in plasma, $C_p(t)$ and EES, $C_e(t)$, for four different rats. (a) Rat1, (b) Rat2, (c) Rat3, and (d) Rat4.

cases as compared to the necrotic tumors. Additionally, we estimated the ICG concentrations in different compartments. The concentrations in different compartments may provide additional parameters for tissue characterization.

While our study indicates that the two-compartment model provides the best fit for the ICG pharmacokinetics, the three- or four-compartment models may be advantageous for modeling the pharmacokinetics of functionalized optical contrast agents that actively accumulate or activate in diseased tissue [48]–[50]. In the near future, we plan to analyze the pharmacokinetics of optical agents within the framework of EKF using data sets collected from animals and human subjects.

VI. ACKNOWLEDGMENT

The authors would like to thank Dr. Bruce Tromberg and Dr. David Cuccia for providing the rat data used in our study.

APPENDIX I

The cost function for the BIC is given by

$$\phi_{BIC}(p) = p \ln N - 2 \ln L(\theta_p, m(1), \dots, m(N)), \quad (33)$$

where p is the dimension of θ_p , which is related to the number of compartments in the model, N is the data length, and $L(\theta, m(1), m(2), \dots, m(N))$ is the likelihood function. The likelihood function for the EKF is given by

$$L(\theta, m(1), \dots, m(N)) = -\frac{1}{2} \sum_{k=1}^N \ln[\det(\mathbf{H}_k)] - \frac{1}{2} \sum_{k=1}^N \mathbf{A}_k^T \mathbf{H}_k^{-1} \mathbf{A}_k, \quad (34)$$

where the matrix \mathbf{H} is defined as:

$$\mathbf{H}_k = \Lambda \mathbf{P}_{k|k-1} \Lambda^T + \sigma_k^2, \quad (35)$$

and σ_k^2 , Λ , and $\mathbf{P}_{k|k-1}$ are as defined in Section III.C. The vector \mathbf{A} is defined as:

$$\mathbf{A}_k = m(k) - [\mathbf{V}_d(\hat{\theta})\hat{\mathbf{C}}]_{k|k-1}, \quad (36)$$

where $m(k)$ is the ICG concentration data collected from Fisher rats at time k , and $[\mathbf{V}_d(\hat{\theta})\hat{\mathbf{C}}]_{k|k-1}$ is the 1-step ahead estimate of the volume fractions and concentrations. The explicit form of the likelihood function for BIC calculation is given by

$$L(\theta, m(1), \dots, m(N)) = -\frac{1}{2} \sum_{k=1}^N \ln[\det(\Lambda \mathbf{P}_{k|k-1} \Lambda^T + \sigma_k^2)] - \frac{1}{2} \sum_{k=1}^N [m(k) - [\mathbf{V}_d(\hat{\theta})\hat{\mathbf{C}}]_{k|k-1}]^T [\Lambda \mathbf{P}_{k|k-1} \Lambda^T + \sigma_k^2]^{-1} \cdot [m(k) - [\mathbf{V}_d(\hat{\theta})\hat{\mathbf{C}}]_{k|k-1}]. \quad (37)$$

where all the parameters and matrices are as defined in Section III.C.

REFERENCES

- [1] A. Yodh and B. Chance, "Spectroscopy and imaging with diffusing light," *Phys. Today* Vol. 48-3, pp. 34-40, 1995.
- [2] X. Intes and B. Chance, "Non-PET functional imaging techniques: optical," *Radiol. Clin. N Am.*, vol.43, pp.221-234, 2005.
- [3] D. Boas, D. Brooks, E. Miler, C. DiMarzio, M. Kilmer, R. Gaudette, "Imaging the body with diffuse optical tomography," *IEEE Signal Processing Magazine*, vol. 18, pp. 57-74, 2001.
- [4] D. Hawrysz and E. Sevick-Muraca, "Developments toward diagnostic breast cancer imaging using Near-Infrared optical measurements and fluorescent contrast agents," *Neoplasia* vol.2, pp. 388-417, 2000.
- [5] Furukawa, K., D. H. Crean, T. S. Mang, H. Kato and T. J. Dougherty (1995) "Fluorescence detection of premalignant, malignant, and micrometastatic disease using hexylpyropheophorbide," *Proc. SPIE* vol. 2371, pp. 510-514.
- [6] Y. Chen, Q. Liu, P. Huang, S. Hyman, X. Intes, W. Lee, and B. Chance, "Assessment of tumor angiogenesis using fluorescence contrast agents," *Proc. of the SPIE*, vol. 5254, no.1, pp. 296-301, 2003.
- [7] A. Becker, G. Schneider, B. Riefke, K. Licha, and W. Semmler, "Localization of near-infrared contrast agents in tumors by intravital microscopy," *Proc. SPIE* vol. 3568, pp. 112-118.
- [8] M. Gurfinkel, A. B. Thompson, W. Ralston, T. L. Troy, A. L. Moore, T. A. Moore, J. D. Gust, D. Tatman, J. S. Reynolds, B. Muggenburg, K. Nikula, R. Pandey, R. H. Mayer, D. J. Hawrysz, and E. M. Sevick-Muraca, "Pharmacokinetics of ICG and HPPH-car for the detection of normal and tumor tissue using fluorescence, near-infrared reflectance imaging: a case study," *Photochem. Photobiol.*, vol. 72, pp. 94-102, 2000.
- [9] D.J. Cuccia, F. Bevilacqua, A. J. Durkin, S. Merritt, B. J. Tromberg, G. Gulsen, H. Yu, J. Wang, and O. Nalcioglu, "In vivo quantification of optical contrast agent dynamics in rat tumors by use of diffuse optical spectroscopy with magnetic resonance imaging coregistration," *Applied Optics*, vol. 42, no. 1, pp. 2940-2950, June 2003.
- [10] X. Intes, J. Ripoll, Y. Chen, S. Nioka, A. G. Yodh, B. Chance, "In vivo continuous-wave optical breast imaging enhanced with Indocyanine Green," *Med. Phys.*, vol. 30-6, pp.1039-1047, June 2003.
- [11] D. Hansen, A. Spence, T. Carski, and M. Berger, "Indocyanine green (ICG) staining and demarcation of tumor margins in a rat glioma model," *Surg. Neurol.*, vol. 40, pp. 451-456, 1993.
- [12] H. Shinohara, A. Tanaka, T. Kitai, N. Yanabu, T. Inomoto, S. Satoh, Hatano, Y. Yamaoka, and K. Hirao, "Direct measurement of hepatic Indocyanine Green clearance with near-infrared spectroscopy: separate evaluation of uptake and removal," *Hepatology*, vol. 23, pp. 137-144, 1996.
- [13] A. ElDeosky, A. Seifalian, M. Cope, D. Delpy, and B. Davidson, "Experimental study of liver dysfunction evaluated by direct Indocyanine green clearance using near infrared spectroscopy," *Br. J. Surg.*, vol. 86, pp. 1005-1011, 1999.
- [14] X. Li, B. Beauvoit, R. White, S. Nioka, B. Chance, and A. Yodh, "Tumor localization using fluorescence of Indocyanine Green (ICG) in rat models," *Proc. SPIE*, vol. 2389, pp. 789-797, 1995.

- [15] M. S. Yates, C. J. Bowmer, and J. Emmerson, "The plasma clearance of indocyanine green in rats with acute renal failure: effect of dose and route of administration," *Biochem. Pharmacol.*, vol. 32, pp. 3109-3114, 1983.
- [16] C. W. Tornøe, "Grey-Box PK/PD Modeling of Insulin," M.S. Thesis, June 28, 2002.
- [17] D. H. Anderson, *Lecture Notes in Biomathematics: Compartmental Modeling and Tracer Kinetics*, Springer-Verlag, Berlin, 1983.
- [18] J. A. Jacquez, *Compartmental Analysis in Biology and Medicine: Kinetics of Distribution of Tracer-labeled Materials*, Elsevier Pub. Co., New York, 1972.
- [19] C. Cobelli, D. Foster, and G. Toffolo, *Tracer Kinetics in Biomedical Research: from Data to Model*, Kluwer Academic/Plenum, New York, c2000.
- [20] P. Huang, X. Intes, B. Chance, S. Nioka, "Simulation of delivery of indocyanine green injected intravenously into the human subject for breast cancer detection," *Proceedings of SPIE*, vol. 4949, pp. 450-459, 2003.
- [21] S. Mordon, J. M. Devoisselle, S. Soulie-Begu, T. Desmettre, "Indocyanine Green: Physicochemical Factors Effecting Its Fluorescence in vivo," *Microvascular Research*, vol. 55, pp. 146-152, 1998.
- [22] S. Fickweiler, R. M. Szeimies, W. Baumlner, P. Steinbach, S. Karrer, A. E. Goetz, C. Abels, F. Hofstadler, M. Landthaler, "Indocyanine Green: Intracellular Uptake and Phototherapeutic effects in vitro," *Jour. Photochem. Photobio. B: Biology*, vol. 38, pp. 178-183, 1997.
- [23] P. S. Tofts, DPhil, G. Brix, D. L. Buckley, J. L. Evelhoch, E. Henderson, M. V. Knopp, H. B.W. Larsson, T. Lee, N. A. Mayr, G. J.M. Parker, R. E. Port, J. Taylor, and R. M. Weisskoff, "Estimating Kinetic Parameters From Dynamic Contrast-Enhanced T1-Weighted MRI of a Diffusible Tracer: Standardized Quantities and Symbols," *Jour. Mag. Res. Ima.*, vol. 10, pp. 223-232, 1999.
- [24] P. S. Tofts, "Modeling tracer kinetics in dynamic Gd-DTPA MR imaging," *J. Magn. Reson. Imag.*, vol. 7, pp. 91-101, 1997.
- [25] C. Chen, *Linear System Theory and Design*, Oxford University Press, New York, 1999.
- [26] P. Zarchan, *Fundamentals of Kalman Filtering : a Practical Approach*, American Institute of Aeronautics and Astronautics, Reston, 2000.
- [27] C.K.Chui, G. Chen, *Kalman Filtering with real time applications*, Springer, Berlin, 1999.
- [28] C. E. Catlin, *Estimation, Control, and the Discrete Kalman Filter*, Springer, New York, 1989.
- [29] L. Ljung, "Asymptotic Behavior of the Extended Kalman Filter as a Parameter Estimator for Linear Systems," *IEEE Tran. Automa. Control*, vol. AC-24, no. 1, pp. 36-50, Feb 1979.
- [30] R. Togneri, and L. Deng, "Joint State and Parameter Estimation for a Target-Directed Nonlinear Dynamic System Model," *IEEE Tran. on Sig. Proc.*, vol. 51, no. 12, pp. 3061-3070, Dec 2003.
- [31] L. Nelson, and E. Stear, "The Simultaneous On-Line Estimation of Parameters and States in Linear Systems," *IEEE Tran. on Auto. Control*, vol.21, pp. 94-98, Feb 1976.
- [32] B. F. La Scala, and R. R. Bitmead, "Design of an extended Kalman filter frequency tracer," *IEEE Tran. on Sig. Proc.*, vol. 44, no. 3, pp. 739-742, March 1996.
- [33] M. Boutayeb, H. Rafaralahy, M. Darouach, "Convergence analysis of the Extended Kalman Filter used as an observer for nonlinear deterministic discrete-time systems," *IEEE Transactions on Automatic Control*, vol. 42, no. 4, pp. 581-586, 1997.
- [34] B. J. Schnekenburger, "An extended Kalman filter as a parameter estimator for linear discrete time systems" M.S. thesis, University of NJIT, Newark, NJ, USA, 1988.
- [35] G. Schwarz, "Estimating the dimensions of a model," *Annals. of Statistics*, vol. 6, pp. 461-464, 1978.
- [36] G.E.P. Box, G.M. Jenkins, and G.C. Reinsel, *Time Series Analysis: Forecasting and Control*, Third edition, Prentice Hall, 1994.
- [37] H. Akaike, "Likelihood and the Bayes Procedure," *Bayesian Statistics*, Univ. Press, Valencia, Spain, 1980.
- [38] A. Harvey, *Time Series Models*, MIT Press, 1993.
- [39] W.M. Sallas and D.A. Harville, "Noninformative Priors and Restricted Maximum Likelihood Estimation in the Kalman Filter", in J.C. Spall (Ed.), *Bayesian Analysis of Time Series and Dynamic Models*, New York: Marcel-Dekker, Inc., 1988.
- [40] F. Bevilacqua, A. J. Berger, A. E. Cerussi, D. Jakubowski, and B. J. Tromberg, "Broadband absorption spectroscopy in turbid media by combined frequency-domain and steady-state methods," *Appl. Opt.*, vol. 39, pp. 6498-6507, 2000.
- [41] D. J. Jakubowski, "Development of broadband quantitative tissue optical spectroscopy for the non-invasive characterization of breast disease," Beckman Laser Institute, University of California, Irvine, Irvine, Calif., 2002.
- [42] S. Merritt, F. Bevilacqua, A. J. Durkin, D. J. Cuccia, R. Lanning, B. J. Tromberg, G. Gulsen, H. Yu, J. Wang, and O. Nalcioglu, "Monitoring tumor physiology using near-infrared spectroscopy and MRI coregistration," *Appl. Opt.*, vol. 42, pp. 2951-2959, 2003.
- [43] L.M. Gray, L.D. Davisson, *An Introduction to Statistical Signal Processing*, Cambridge University Press, Boston, 2004.
- [44] M. Y. Su, A. Muhler, X. Lao, and O. Nalcioglu, "Tumor characterization with dynamic contrast-enhanced MRI using MR contrast agents of various molecular weights," *Magn. Reson. Med.*, vol. 39, pp. 259-269, 1998.
- [45] J. B. Fishkin, O. Coquoz, E. Anderson, M. Brenner, and B. J. Tromberg, "Frequency-domain photon migration measurements of normal and malignant tissue optical properties in a human subject," *Appl. Opt.*, vol. 36, pp. 10-20, 1997.
- [46] D. L. Buckley, "Uncertainty in the analysis of tracer kinetics using dynamic contrast-enhanced T1-weighted MRI," *Magn. Reson. Med.*, vol. 47, pp. 601-606, 2002.
- [47] A. Gelb, *Applied Optimal Estimation*, M.I.T. Press, Cambridge, 1989.
- [48] K. Licha, "Contrast agents for optical imaging," *Topics in Current Chemistry*, vol.222, pp.1-29, 2002.
- [49] Y. Chen, G. Zheng, Z. Zhang, D. Blessington, M. Zhang, H. Li, "Metabolism Enhanced Tumor Localization by Fluorescence Imaging: In Vivo Animal Studies," *Optics Letters*, vol. 28, pp. 2070-2072, 2003.
- [50] R. Weissleder, C. H. Tung, U. Mahmood, A. Bogdanov, "In vivo imaging with protease-activated near-infrared fluorescent probes," *Nat. Biotech.*, vol. 17, pp. 375-378, 1999.



Burak Alacam received his M.S. degree in Electrical, and Computer Engineering Department of Drexel University, Philadelphia, USA in 2003. He is currently a Ph.D. candidate in Electrical, Computer, and Systems Engineering Department of Rensselaer Polytechnic Institute, Troy, NY, USA. His research areas are biomedical signal and image processing, time series analysis, estimation and detection, inverse problems and image reconstruction. His current research focuses on compartmental modeling of pharmacokinetics of fluorescence agents.



Birsan Yazici received MS and Ph.D. degrees from Mathematics and Electrical Engineering in 1990 and 1994, respectively both from Purdue University, W. Lafayette, IN. From 1994 until 2000, she was a research scientist at the General Electric Company Research Center, Schenectady NY. During her tenure in industry, she worked on radar, industrial and medical imaging systems. From January 2001 to 2003, she was with Drexel University Electrical and Computer Engineering Department. She joined Rensselaer Polytechnic Institute, Electrical, Computer and Systems Engineering Department in August 2003. Her research interests include inverse problems in medical imaging and radar, applied harmonic analysis, X-ray imaging, diffuse optical tomography, biomedical optics, synthetic aperture radar and waveform design. She holds 12 patents.

Xavier Intes received a Ph.D. degree in 1998 in physics from the University of Bretagne Occidentale (France). He then joined Prof Chance laboratory in 1999 as a postdoctoral fellow at the University of Pennsylvania. In 2001, he acted as the Director of Research of the Medical Diagnostic Research Foundation, and the Director of Research of Optical Devices Inc., Philadelphia, USA. In 2003 he joined Advanced Research Technologies Inc as a Senior Staff Scientist and later acted as ARTs Chief Scientist. Dr. Intes's research is focused on application of optical techniques for biomedical imaging of small animal and in clinical settings.



Britton Chance received his Ph.D. in Chemistry(1940), University of Pennsylvania, his second Ph.D. in Biology(1942), Cambridge University. He got his D. Sc. degree(1952) from Cambridge University. Britton Chance is Eldridge Reeves Johnson University Professor Emeritus of Biochemistry and Biophysics and Physical Chemistry and Radiologic Physics, School of Medicine, University of Pennsylvania, and President, Medical Diagnostic Research Foundation (MDRF), Philadelphia, Pennsylvania.

Spatially Resolved Pharmacokinetic Rate Images of ICG using Near Infrared Optical Methods

Burak Alacam^a, Birsen Yazıcı^a, Xavier Intes^b, Shoko Nioka^c, and Britton Chance^c

^aElectrical, Computer and Systems Engineering Dept., Rensselaer Polytechnic Institute, USA

^bART Advanced Research Technologies Inc., Canada

^cDepartment of Biochemistry and Biophysics, University of Pennsylvania, USA

ABSTRACT

In this work, we present spatially resolved pharmacokinetic rate images of indocyanine green (ICG) obtained from three breast cancer patients using near infrared imaging methods. We used a two-compartment model, namely, plasma and extracellular extravascular (EES), to model ICG kinetics around the tumor region. We introduced extended Kalman filtering (EKF) framework to estimate the ICG pharmacokinetic rate images. The EKF framework allows simultaneous estimation of pharmacokinetic rates and the ICG concentrations in each compartment. Based on the pharmacokinetic rate images, we observed that the rates from inside and outside the tumor region are statistically different with a p-value of 0.0001 for each patient. Additionally, we observed that the ICG concentrations in plasma and the EES compartments are higher around the tumors agreeing with the hypothesis that ICG may act as a diffusible extravascular flow in leaky capillary of cancer vessels. Our study shows that spatially resolved pharmacokinetic rate images can be potentially useful for breast cancer screening and diagnosis.

Keywords: extended Kalman filter, indocyanine green, pharmacokinetic analysis, breast cancer.

1. INTRODUCTION

Near Infrared (NIR) optical imaging has recently emerged as a potential diagnostic tool for breast cancer. NIR imaging has several advantages over existing imaging modalities. It is easy to use, minimally invasive, relatively inexpensive and can be made portable. More importantly, in conjunction with molecular imaging probes, NIR imaging techniques can provide cellular, molecular level information, which can be used for cancer imaging. In particular, dynamic tomographic imaging methods can produce absorption images which can be used to derive kinetics of molecular probes. The kinetic rates can then be used as potential detection and diagnosis tools.

Presently, ICG is the only FDA approved fluorescent agent for human use. It is hypothesized that ICG may act as a blood flow indicator in tight capillaries of normal vessels and as a diffusible (extravascular) flow in leaky capillary of cancer vessels.^{1,4} A number of studies using compartmental modeling were reported to show the feasibility of using ICG pharmacokinetics in tumor characterization.¹⁻⁵ Parameters related to capillary permeability were used as malignancy indicators. Gurfinkel et. al.³ presented *in vivo* fluorescent, NIR reflectance images of ICG to discriminate spontaneous canine adenocarcinoma from normal mammary tissue using a two compartmental model. It was claimed that the model parameters show no difference in the ICG uptake rates between normal and diseased tissue. Cuccia et al.⁴ presented a study of the dynamics of ICG in an adenocarcinoma rat tumor model. A two-compartment model describing ICG dynamics was used to quantify physiologic parameters related to capillary permeability. It was shown that different tumor types have different capillary permeability rates. Intes et. al.⁵ presented the uptake of ICG by breast tumors using a continuous wave diffuse optical tomography apparatus. A two-compartment model was used to analyze the pharmacokinetics of ICG. It was shown that the malignant cases exhibit slower rate constants (uptake and outflow) compared to healthy tissue.

The studies above demonstrate the feasibility of the ICG pharmacokinetics in tumor characterization. However, estimation of pharmacokinetic parameters is a challenging problem, because it is a highly non-linear estimation problem with sparse data available in clinical setting. Furthermore, parameter values show variation from

Further author information: Send correspondence to Birsen Yazıcı, e-mail: yazici@ecse.rpi.edu

one subject to another. To address these issues, we recently introduced a systematic and robust approach to model, estimate and analyze the ICG pharmacokinetics based on extended Kalman filtering framework.^{1,2} We introduced Bayesian Information Criteria to choose best statistical model fit. EKF based approach can be also utilized to estimate time-dependent pharmacokinetic rates. We tested three different compartmental models for ICG pharmacokinetics using NIR data collected from Fischer rats with cancerous tumors. Our study showed that the permeability rates out of the vasculature are higher in edematous tumors as compared to necrotic tumors.

In this paper, our objective is to obtain spatially resolved pharmacokinetic rate images of ICG, using NIR data acquired from three breast cancer patients. We first develop a set of temporally resolved 2-D ICG concentration images based on linearized diffusion equation. We then estimate the ICG pharmacokinetic rates and the concentrations in each compartment for each pixel based on the EKF framework for the two-compartment model. Reconstructed 2-D pharmacokinetic rate images of the three patient show that the rates from inside and outside the tumor region are statistically different with a p-value of 0.0001. Additionally, the ICG concentrations in plasma and the EES compartments are higher around the tumor agreeing with the hypothesis that around the tumor region ICG may act as a diffusible extravascular flow in leaky capillary of cancer vessels.

The rest of the paper is organized as follows: In Section II, we present the reconstruction of differential absorption and ICG concentration images. In Section III, we present the two-compartment model for ICG. In Section IV, we present the EKF based estimation of ICG pharmacokinetic parameters. In Section V, we present the clinical results obtained from breast cancer patients. Finally, Section VI summarizes our results and conclusion.

2. DIFFUSE OPTICAL TOMOGRAPHY (DOT) USING ICG

2.1. Reconstruction of Bulk ICG Concentration Images

The propagation of light in soft tissue is modeled by diffusion approximation.⁶ In the forward model, the analytical solutions of the heterogenous diffusion equation given in⁵ is derived using first order Rytov approximation. The sample volume is divided into a set of voxels and the measurements are related to the relative absorption coefficients of each voxel by a system of linear equations. The shape of the breast was approximated as a cylinder and the Kirchhoff approximation^{7,8} for diffuse waves was used to model the interaction of light with boundaries. In order to account for the biological noise, the forward model was implemented with coupling coefficient technique.⁹ The inverse problem was addressed by using singular value decomposition of the Moore-Penrose generalized system. Tikhinov regularization was used to stabilize the inversion procedure. The L-curve method was applied to an experimental model reconstruction and the best regularization parameter was derived using a curvature function which was employed in.¹⁰ A detailed discussion of the forward and inverse models used for the reconstruction of differential absorption coefficients can be found in.⁵

We used the linear relationship between the differential absorption coefficients and concentrations given by the following equation to reconstruct a set of temporally resolved 2-D ICG concentration images.¹¹

$$\Delta\mu_a = e C \ln 10 = 2.303 e C \quad (1)$$

where $\Delta\mu_a$ denotes the differential absorption coefficient, and C denotes the concentration of ICG, and e is the extinction coefficient of ICG at wavelength 805nm. Using the linear relationship above, we get 2-D images of ICG concentrations in tissue from differential absorption images reconstructed at different time instants on a pixel by pixel basis. In the following Sections, we will discuss the two-compartment model, and the estimation of pharmacokinetic rates.

3. ICG PHARMACOKINETICS AND THE TWO-COMPARTMENT MODELING

3.1. Compartmental Analysis of ICG Pharmacokinetics

In this paper, we assume that the tumor region is composed of two compartments; namely plasma and the EES.^{1,4} Figure 1 shows the two-compartment model for ICG kinetics. C_p and C_e represent the ICG concentrations in plasma and the EES, respectively. The parameters k_{in} and k_{out} govern the leakage into and the drainage out

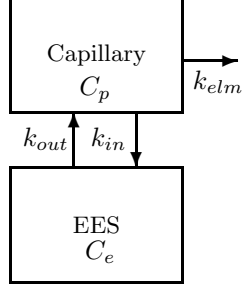


Figure 1. Block diagram of the two-compartment model for ICG pharmacokinetics.

of the EES. The parameter k_{elm} describes the ICG elimination from the body through kidneys and livers. The parameters v_p and v_e are plasma and the EES volume fractions, respectively.

The leakage into and the drainage out of the EES is given by:

$$\frac{dC_e(t)}{dt} = -k_{out}C_e(t) + k_{in}C_p(t). \quad (2)$$

The leakage into and the drainage out of plasma is given by:

$$\frac{dC_p(t)}{dt} = -(k_{in} + k_{elm})C_p(t) + k_{out}C_e(t). \quad (3)$$

The parameters k_{in} , k_{out} , and k_{elm} have a unit of sec^{-1} . They are defined as the permeability surface area products given by $PS\rho$, where P is the capillary permeability constant, S is the capillary surface area, and ρ is the tissue density. We consider transcapillary leakage to occur only at the tumor site.

Actual bulk ICG concentration in the tissue measured by NIR spectroscopy is a linear combination of plasma and the EES ICG concentrations:

$$m(t) = v_p C_p(t) + v_e C_e(t), \quad (4)$$

where v_p , v_e , C_e , and C_p are as defined above, and $m(t)$ denotes the bulk ICG concentration.

Here, we consider transcapillary leakage to occur only at the tumor site. We also assume that a small perturbation of the global plasma concentration does not affect the bulk removal.

4. EXTENDED KALMAN FILTERING FOR THE ESTIMATION OF ICG PHARMACOKINETICS

Coupled differential equations resulting from the two-compartment model of the ICG pharmacokinetics can be expressed in state-space representation as follows:

$$\begin{bmatrix} \dot{C}_e(t) \\ \dot{C}_p(t) \end{bmatrix} = \begin{bmatrix} -k_{out} & k_{in} \\ k_{out} & -(k_{in} + k_{elm}) \end{bmatrix} \begin{bmatrix} C_e(t) \\ C_p(t) \end{bmatrix} + \boldsymbol{\omega}(t), \quad (5)$$

$$m(t) = \begin{bmatrix} v_e & v_p \end{bmatrix} \begin{bmatrix} C_e(t) \\ C_p(t) \end{bmatrix} + \eta(t)$$

where $\boldsymbol{\omega}(t)$ and $\eta(t)$ are uncorrelated zero mean Gaussian processes with covariance matrix \mathbf{Q} , and variance σ^2 , respectively.

In matrix-vector notation, the state-space representation is given by:

$$d\mathbf{C}(t) = \mathbf{K}(\boldsymbol{\alpha})\mathbf{C}(t)dt + \boldsymbol{\omega}(t)dt, \quad (6)$$

$$m(t) = \mathbf{V}(\boldsymbol{\alpha})\mathbf{C}(t) + \eta(t).$$

where $\mathbf{C}(t)$ denotes the concentration vector with elements $C_e(t)$, and $C_p(t)$; $\mathbf{K}(\boldsymbol{\alpha})$ is the 2×2 system matrix, $\mathbf{V}(\boldsymbol{\alpha})$ is the 1×2 measurement matrix as defined in equation (5) and $\boldsymbol{\alpha}$ is the parameter vector given by

$$\boldsymbol{\alpha} = [k_{out} \quad k_{in} \quad k_{elm} \quad v_e \quad v_p]. \quad (7)$$

The ICG measurements in equation (6) are collected at discrete time instances, $t = kT$, $k = 0, 1, \dots$, where T is the sampling period. Therefore, the continuous model given in Equation (6) has to be discretized. To simplify our notation, we shall use $\mathbf{C}(k) = \mathbf{C}(kT)$ and $m(k) = m(kT)$. The corresponding discrete state-space model is given by:

$$\mathbf{C}(k+1) = \mathbf{K}_d(\boldsymbol{\alpha})\mathbf{C}(k) + \boldsymbol{\omega}(k) \quad (8)$$

$$m(k) = \mathbf{V}_d(\boldsymbol{\alpha})\mathbf{C}(k) + \eta(k),$$

where $\mathbf{K}_d(\boldsymbol{\alpha}) = e^{\mathbf{K}(\boldsymbol{\alpha})}$ is the discrete time system matrix and $\mathbf{V}_d(\boldsymbol{\alpha}) = \mathbf{V}(\boldsymbol{\alpha})$ is the discrete measurement matrix. $\boldsymbol{\omega}(k)$ and $\eta(k)$ are zero mean Gaussian white noise processes with covariances matrix \mathbf{Q}_d and variance σ_d^2 , respectively.

An explicit form for the discrete time state-space model is given as follows:

$$\begin{bmatrix} C_e(k+1) \\ C_p(k+1) \end{bmatrix} = \begin{bmatrix} \tau_{11} & \tau_{12} \\ \tau_{21} & \tau_{22} \end{bmatrix} \begin{bmatrix} C_e(k) \\ C_p(k) \end{bmatrix} + \boldsymbol{\omega}(k) \quad (9)$$

$$m(k) = \begin{bmatrix} v_e & v_p \end{bmatrix} \begin{bmatrix} C_e(k) \\ C_p(k) \end{bmatrix} + \eta(k),$$

where τ_{ij} is the i^{th} row and j^{th} column entry of the system matrix $\mathbf{K}_d(\boldsymbol{\alpha})$. The matrix entry τ_{ij} is an exponential function of the parameters k_{in} , k_{out} and k_{elm} . To simplify the estimation process, we shall first estimate τ_{ij} 's and then compute the pharmacokinetic parameters k_{in} , k_{out} and k_{elm} .

We use the EKF algorithm for the joint estimation of the unknown pharmacokinetic parameters, k_{in} , k_{out} , and k_{elm} , volume fractions, v_e , and v_p , and ICG concentrations in plasma and the EES, C_p , and C_e . In a linear state-space model when both states (ICG concentrations) and system parameters (pharmacokinetic rates and volume fractions) are unknown, the linear state-space model can be regarded as a non-linear model in which the linear system parameters and states are combined to form the new states of the non-linear model. This system is then linearized and solved for the new unknown states using the EKF estimator. A detailed discussion of the Kalman filtering algorithm for joint estimation of the pharmacokinetic parameters and ICG concentrations in different compartments can be found in.^{1, 2}

5. CLINICAL RESULTS

5.1. Apparatus

In this work, we used the data collected with a continuous wave (CW) NIR imaging apparatus. The apparatus has 16 light sources, which are tungsten bulbs with less than 1 watt of output energy. They are located on a circular holder at an equal distance from each other with 22.5 degree apart. Sixteen detectors, namely, silicon photodiodes, are situated in the same plane. The breast is arranged in a pendular geometry with the source-detector probes gently touching its surface. Figure 2 illustrates the configuration of the apparatus and the configuration of the detectors and the sources in a circular plane. A band pass filter at 805nm, the absorption peak of ICG, is placed in front of the sources to select the desired wavelength. A set of data for one source is collected every 500 ms. The total time for a whole scan of the breast including 16 sources and 16 detectors is 8.8 seconds. The detectors use the same positions as the sources to collect the light originating from one source at a time. Only the signals from the farthest 11 detectors are used in the analysis. For example, when Source 1 is on, the data is collected using detectors 4 to 14. A more detailed explanation of the apparatus and the data collection procedure can be found in.¹²

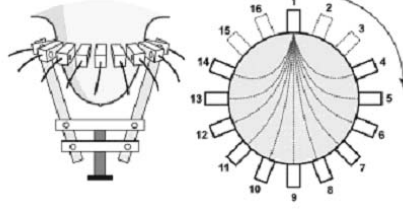


Figure 2. The cut section of the 16 light source-detector device, holding a human breast inside. The diameter can be fitted easily. The 16 light source-detector combinations in each arm are located equal distance, but when the device fits the breast, only the diameter changes.

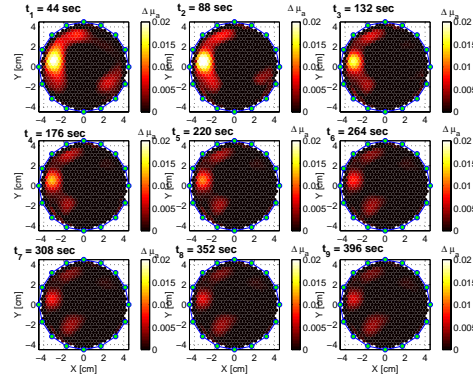


Figure 3. Differential absorption reconstruction images for a set of time instants for Case 1.

5.2. Protocol

Patients with suspicious breast tumors were enrolled for this study. ICG was injected intravenously by bolus with a concentration of 0.25 mg per kg of body weight. Diagnostic information is obtained using biopsy results. Since biopsy modifies the blood volume and blood flow around the tumor region, measurements were made before the biopsy. Data acquisition started before the injection of ICG and continued for 10 minutes.

5.3. Tumor Information

Three different patients with different tumor types are included in this study. First case, Case 1, is fibroadenoma, which corresponds to a mass estimated to be 1–2 cm in diameter within a breast of 9 cm diameter. Second case, Case 2, is adenocarcinoma corresponding to a tumor estimated to be 2–3 cm in diameter within a breast of 7.7 cm diameter. The third case, Case 3, is invasive ductal carcinoma, which corresponds to a mass estimated to be 3–4 cm in diameter.

5.4. ICG Concentration Measurements for Pharmacokinetic Parameter Estimations

Using the CW imager described above, for each patient, sufficient number of source detector readings were collected from different angles. Reconstruction of differential absorption images using the source-detector readings was discussed in Intes et al.⁵ A sample set of reconstructed differential absorption images for Case 1, Case 2, and Case 3 for 9 selected time instants are shown in Figure 3, 4, and 5, respectively. Although only 9 reconstructions are displayed, there are approximately 50 reconstructions, each corresponding to a different time instant for each patient. Here, each 2-D image is composed of 649 pixels.

Using the linear relationship between ICG concentration and absorption coefficient, we obtained ICG concentration images from differential absorption images for each case. A sample set of ICG concentration images for the selected time instants is shown in Figure 6, 7, and 8 for Cases 1, 2 and 3, respectively. Here, the concentration images represent bulk ICG concentration in the tissue, not specifically in plasma or the EES.

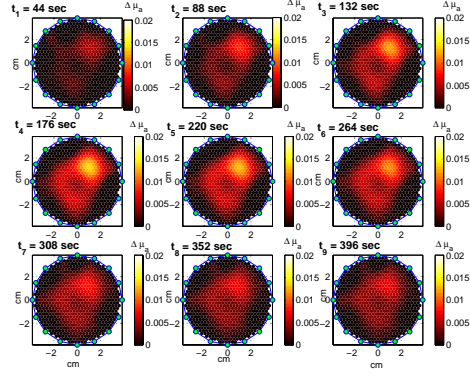


Figure 4. Differential absorption reconstruction images for a set of time instants for Case 2.

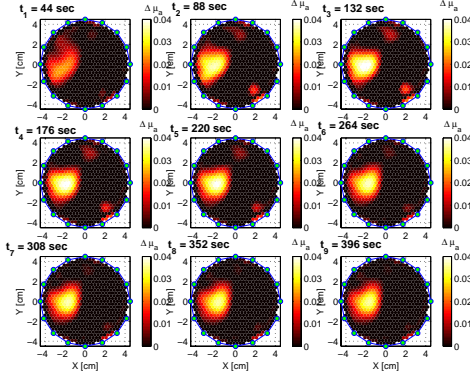


Figure 5. Differential absorption reconstruction images for a set of time instants for Case 3.

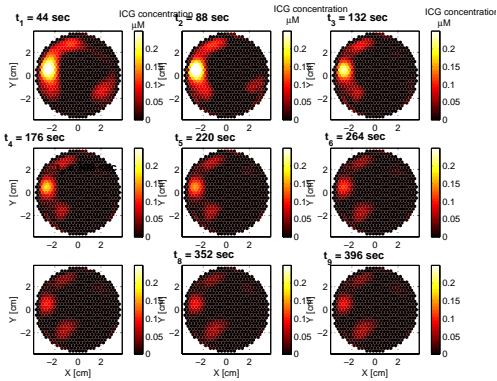


Figure 6. 2-D ICG concentration images for a set of time instants for Case 1.

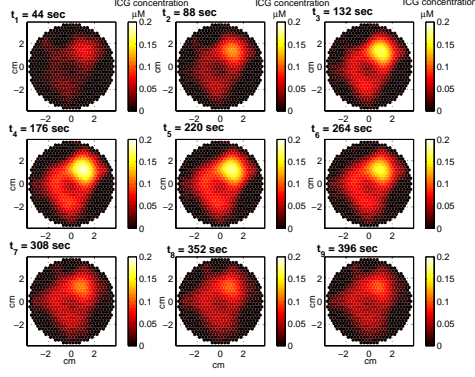


Figure 7. 2-D ICG concentration images for a set of time instants for Case 2.

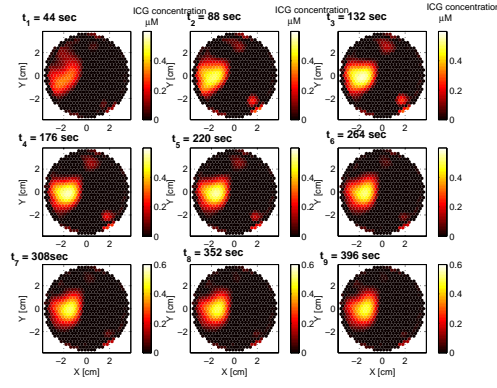


Figure 8. 2-D ICG concentration images for a set of time instants for Case 3.

Using the ICG concentration curves, we estimated the pharmacokinetic parameters for each pixel based on the two-compartment model. We then constructed 2-D permeability rate images using values of these parameters. 2-D images for k_{in} , k_{out} for two-compartmental model for each case are shown in Figures 9 (a), (b), 10 (a), (b), and 11 (a), (b), respectively. We also analyzed whether the kinetic rates are statistically different or not for the inside and outside the tumor region. The k_{in} and k_{out} values from inside and outside the tumor region are statistically different with a p-value of less than 0.0001 for all cases.

We constructed 2-D ICG concentration images for plasma and the EES. Figures 12-17 show the ICG concentration in the EES and plasma for 3 different time instants for Case 1, 2, 3, respectively. We observed that ICG concentrations in plasma and the EES compartments are higher around the tumors agreeing with the hypothesis that around tumor region ICG may act as a diffusible extravascular flow in leaky capillary of cancer vessels.

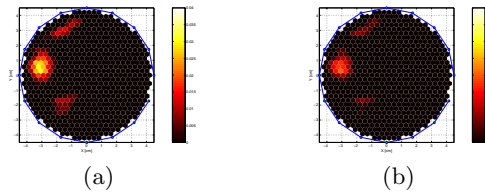


Figure 9. 2-D images for pharmacokinetic rates k_{in} and k_{out} for Case 1.

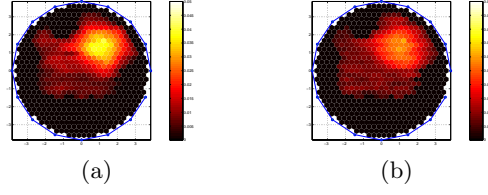


Figure 10. 2-D images for pharmacokinetic rates k_{in} and k_{out} for Case 2.

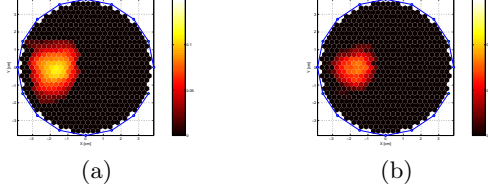


Figure 11. 2-D images for pharmacokinetic rates k_{in} and k_{out} for Case 3.

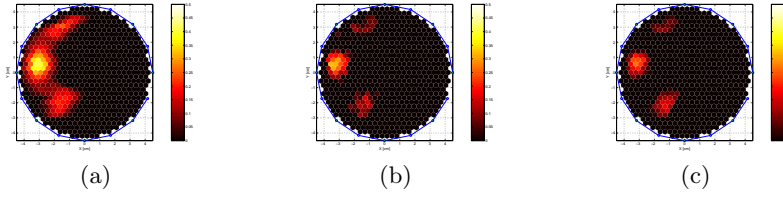


Figure 12. 2-D ICG concentration images in plasma for Case 1 for the 246.4th, 334.4th, and 422.4th seconds.

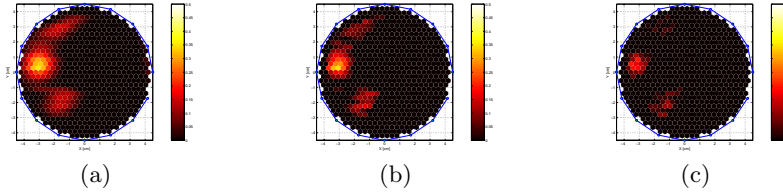


Figure 13. 2-D ICG concentration images in the EES for Case 1 for the 246.4th, 334.4th, and 422.4th seconds.

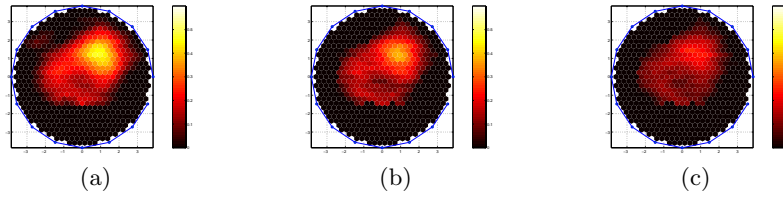


Figure 14. 2-D ICG concentration images in plasma for Case 2 for the 228.8th, 316.8th, and 404.8th seconds.

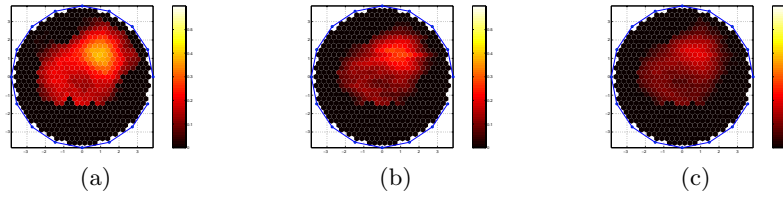


Figure 15. 2-D ICG concentration images in the EES for Case 2 for the 228.8th, 316.8th, and 404.8th seconds.

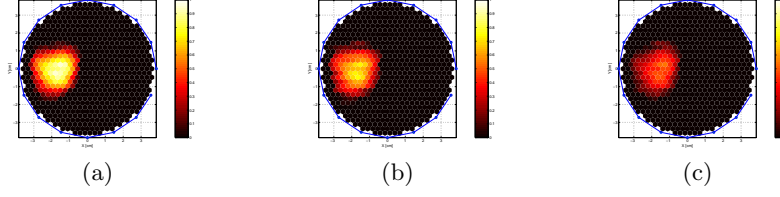


Figure 16. 2-D ICG concentration images in plasma for Case 3 for the 246.4th, 378.4th, and 510.4th seconds.

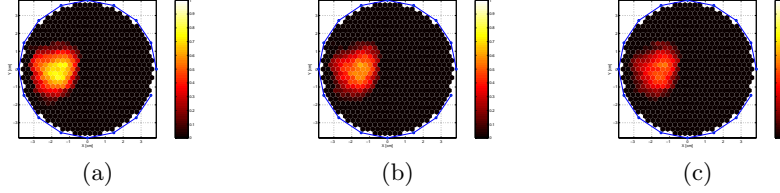


Figure 17. 2-D ICG concentration images in the EES for Case 3 for the 246.4th, 378.4th, and 510.4th seconds.

6. CONCLUSION

In this study, we presented spatially resolved ICG pharmacokinetic images together with the ICG concentrations in plasma and the EES using NIR data obtained from three breast cancer patients. We observed that the pharmacokinetic rates are higher inside the tumor region compared to the outer region; and the ICG concentrations in plasma and the EES are higher around the tumor region. Our study indicates that pharmacokinetic images can be potentially useful to characterize tumor metabolism and angiogenesis. In the near future, we plan to model gadolinium kinetics and compare with ICG kinetics and biopsy findings.

REFERENCES

1. B. Alacam, B. Yazici, X. Intes, B. Chance "Extended Kalman Filtering Framework for the Modeling and Analysis of ICG Pharmacokinetics," *Proc. Of 2005 SPIE Photonic West*, San Jose, California USA, 22 - 27 January 2005, vol. 5693. pp. 17-27.
2. B. Alacam, B. Yazici, X. Intes, B. Chance "Analysis of ICG Pharmacokinetics in Cancerous Tumors using NIR Optical Methods," *Proc. of EMBS – 27th Anniversary Conference*, Shanghai, China, September 2005.
3. M. Gurfinkel, A. B. Thompson, W. Ralston, T. L. Troy, A. L. Moore, T. A. Moore, J. D. Gust, D. Tatman, J. S. Reynolds, B. Muggenburg, K. Nikula, R. Pandey, R. H. Mayer, D. J. Hawrysz, and E. M. Sevick-Muraca, "Pharmacokinetics of ICG and HPPH-car for the detection of normal and tumor tissue using fluorescence, near-infrared reflectance imaging: a case study," *Photochem. Photobiol.*, Vol. 72, 2000, pp. 94-102.
4. D.J. Cuccia, F. Bevilacqua, A. J. Durkin, S. Merritt, B. J. Tromberg, G. Gulsen, H. Yu, J. Wang, and O. Nalcioglu, "In vivo quantification of optical contrast agent dynamics in rat tumors by use of diffuse optical spectroscopy with magnetic resonance imaging coregistration," *Applied Optics*, Vol. 42, No 1, June 2003.
5. X. Intes, J. Ripoll, Y. Chen, S. Nioka, A. G. Yodh, B. Chance, "In vivo continuous-wave optical breast imaging enhanced with Indocyanine Green," *Med. Phys.* Vol. 30-6, June 2003.
6. A. Yodh and B. Chance, "Spectroscopy and imaging with diffusing light," *Phys. Today* 48(3), 3440, 1995.
7. J. Ripoll, V. Ntziachristos, R. Carminati, and M. Nieto-Vesperinas, "Kirchhoff approximation for diffusive waves," *Phys. Rev. E* 64, 051917, 2001.
8. J. Ripoll, V. Ntziachristos, J. P. Culver, D. N. Pattanayak, A. G. Yodh, and M. Nieto-Vesperinas, "Recovery of optical parameters in multilayered diffusive media: theory and experiments," *J. Opt. Soc. Am. A* 18, 821830, 2001.
9. D. Boas, T. Gaudette, and S. Arridge, "Simultaneous imaging and optode calibration with diffuse optical tomography," *Opt. Express* 8, 263270, 2001.
10. P. Hansen and D. OLeary, "The use of the L-curve in the regularization of discrete ill-posed problems," *SIAM J. Sci. Comput.*, 14, 1487 1503, 1993.

11. M. L. J. Landsman, G. Kwant, G. A. Mook, W. G. Zijlstra, "Light- absorbing properties, stability, and spectral stabilization of indocyanine green," *J. Appl. Physiol.*, 40, 575-583, 1976.
12. S. Nioka, Y. Yung, M. Schnall, S. Zhao, S. Orel, C. Xie, B. Chance, and S. Solin, "Optical imaging of breast tumor by means of continuous waves," *Adv. Exp. Med. Biol.*, 411, 227232, 1997.

Two-level domain decomposition methods for diffuse optical tomography

Kiwoon Kwon, Birsen Yazıcı and Murat Guven

Electrical, Computer, and Systems Engineering, Rensselaer Polytechnic Institute,
110 8th St, Troy, NY 12180, USA

E-mail: yazici@ecse.rpi.edu

Received 26 March 2006, in final form 16 June 2006

Published DD MMM 2006

Online at stacks.iop.org/IP/22/1

Abstract

Diffuse optical tomography (DOT) in the near infrared involves the reconstruction of spatially varying optical properties of turbid medium from boundary measurements based on a forward model of photon propagation. Due to the nonlinear nature of DOT, high quality image reconstruction is a computationally demanding problem which requires repeated use of forward and inverse solvers. Therefore, it is desirable to develop methods and algorithms that are computationally efficient. In this paper, we develop two-level overlapping multiplicative Schwarz-type domain decomposition (DD) algorithms to address the computational complexity of the forward and inverse DOT problems. We use frequency domain diffusion equation to model photon propagation and consider a nonlinear least-squares formulation with a general Tikhonov-type regularization for simultaneous reconstruction of absorption and scattering coefficients. In the forward solver, a two-grid method is used as a preconditioner to DD to enhance convergence. In the inverse solver, DD is initialized with a coarse grid solution to achieve local convergence. We show the strong local convexity of the nonlinear objective functional resulting from the inverse problem formulation and prove the local convergence of the DD algorithm for the inverse problem. We provide the computational cost analysis of the forward and inverse solvers and demonstrate their performance in numerical simulations.

1. Introduction

Diffuse optical image reconstruction based on the diffusion equation is a nonlinear ill-posed problem that calls for the use of nonlinear minimization methods with regularization to stabilize the solution [1].

Due to lack of analytical solutions for practical applications with arbitrary geometries, DOT image reconstruction is often posed as an optimization problem involving two coupled

steps, namely forward and inverse problems. Each step consists of an iterative solver whose solution is used as an input to the other solver. More precisely, the forward solver computes the photon density and its Jacobian with respect to the current optical coefficient estimates, and the inverse solver updates the optical coefficients based on the output of the forward step. The updated coefficients are then used in the forward solver to recompute the photon density and its Jacobian. As a result, the computational complexity of DOT image reconstruction quickly grows with the number of unknowns and dimension. Thus, real time computation of DOT requires numerical techniques to reduce the complexity of the problem.

In this paper, we develop two-level domain decomposition (DD) algorithms to address the computational complexity of the forward and inverse problems. More specifically, we develop an overlapping multiplicative Schwarz-type DD algorithm equipped with a two-grid preconditioner to solve the forward problem resulting from the finite element discretization of the frequency-domain diffusion equation. For simultaneous absorption and scattering coefficients reconstruction, we consider a nonlinear least-squares formulation with a general Tikhonov-type regularization. To solve the resulting optimization problem, we develop a two-level overlapping multiplicative Schwarz-type DD algorithm, where we use a trust region method for minimization. Finally, under the conditions that lead to the local strong convexity of the nonlinear objective functional considered for the inverse problem formulation, we prove the local convergence of the DD algorithm developed for the inverse problem.

DD methods originate from the Schwarz alternating procedure, which is known to be the first DD method applied for solving partial differential equations (PDEs) [32]. In the last two decades, motivated by the need for fast and efficient algorithms for solving large-scale, three-dimensional problems, DD methods have been extensively developed and applied in the area of numerical solution of PDEs [31, 33]. DD methods involve partitioning of bounded domains into two or more sub-domains, thereby dividing the original problem into a series of smaller sized sub-problems defined on the sub-domains. As a result, DD methods allow the parallel solution of the resulting sub-problems, making the computation extremely efficient.

Owing to the computational advantages they offer, DD methods have been applied to inverse problems as well. In [4–6, 36, 38], DD methods were applied to constrained convex minimization problems arising from variational inequalities, where the term ‘space decomposition’ was introduced for DD methods in the context of optimization problems. In [5, 36, 38], the convergence of DD methods has been shown for convex optimization problems. DD methods have also been applied to a number of application specific inverse problems, including radon transform inversion in radar and x-ray tomography [8, 9], geophysics [14], parameter estimation problems [37], inverse heat conduction problem [29] and welding and metal cutting problems [23, 28]. In the area of DOT, a ‘data driven zonation’ method coupled with extended Kalman filtering was applied in conjunction with a DD method [15], where the convergence of the DD algorithm was shown empirically. In this work [15]; instead of partitioning the main inverse problem formulation, independent local inverse problems were formulated on each non-overlapping sub-domain, using the measurement data due to the source-detector pairs that were physically present in the sub-domain. In the same work, a multi-grid algorithm was used to accelerate the finite difference solution of the forward problem; however, DD methods were not used. A similar multi-grid-based approach for the forward problem was also presented in [30]. Multi-grid algorithms in the context of optimization have been proposed for the solution of the inverse DOT problem as well [26, 40], however in both of these studies [26, 40], multi-grid was used as an iterative solver and DD methods were not considered. In [16, 17], a fast adaptive composite-grid (FAC) algorithm was proposed for the linearized DOT inverse problem, which can be viewed as a fully overlapping Schwarz-type domain decomposition algorithm [13], to provide enhanced spatial resolution

in a region of interest. Most recently in [34], a multi-level overlapping Schwarz-type domain decomposition algorithm was proposed for the linearized inverse DOT problem, which was posed as a linear least-squares problem without regularization. In all these studies [16, 17, 34], DD methods were not pursued for the solution of the forward problem and convergence of the proposed algorithms was presented empirically.

In this work, we consider an overlapping partitioning of the optical domain to convert the finite element formulation of the frequency-domain diffusion equation into a number of smaller-sized sub-problems and use a multiplicative Schwarz-type DD algorithm. For the numerical solution of elliptic PDEs such as the frequency-domain diffusion equation, it has been shown that one-level domain decomposition methods are not efficient in conveying the information on one sub-domain to the others, which is attributed to the rapid decay of Green's function of these PDEs and the dependence of the solution on the boundary conditions [33]. An effective way to address this issue is to use multi-grid methods [33]. Therefore, we employ a two-grid preconditioner to enhance the global communication of the multiplicative Schwarz-type DD algorithm applied on the fine resolution level. We note that the multiplicative nature of the Schwarz algorithm provides higher convergence rate as compared to that of the additive Schwarz algorithms (section 3.3). We refer to [10, 33] for a detailed discussion about the convergence analysis of DD methods with multi-grid preconditioners for the numerical solution of elliptic PDEs. For the inverse problem, we consider a nonlinear optimization problem resulting from the nonlinear least-squares formulation with a general Tikhonov-type regularization. Unlike the approach in [15], we formulate a single inverse problem on the whole domain using the boundary measurements due to all source-detector pairs. Then, we apply a two-level Schwarz-type multiplicative DD algorithm coupled with a trust region method to successively minimize the resulting objective functional on each overlapping sub-domain. In this case, the coarse level serves to provide a good initial guess for the fine level, where the inverse problem is formulated. Under some mild conditions, we show the local strong convexity of the nonlinear objective functional. Then, we prove the local convergence of the DD algorithm for the nonlinear inverse DOT problem by using the local strong convexity property of the nonlinear inverse problem formulation. In this context, the coarse-level solution used as the initial guess to the fine level is crucial in achieving the convergence. Note that we show the convergence properties of the DD algorithm for the inverse problem, independent of the optimization method. Therefore, the convergence properties do not change if the trust region method is replaced by another optimization method. We perform two sets of experiments to show the computational savings provided by the proposed DD algorithms as compared to non-DD algorithms.

The rest of the paper is organized as follows: in section 2, we define the forward problem and formulate the inverse problem, respectively. In section 3, we present the DD algorithms developed for the solution of the forward and inverse problems, and discuss the convergence properties and computational complexity of the proposed algorithms. Section 4 presents the numerical simulations and section 5 summarizes our results and conclusions. The paper includes an appendix for the proof of the local convergence of the DD algorithm developed for the inverse problem.

2. Diffuse optical tomography

2.1. Photon diffusion equation in frequency domain

We model the propagation of light in biological tissue by the diffusion equation with Robin boundary conditions [1]. In frequency domain, the photon diffusion equation is given as

follows:

$$\begin{aligned} -\nabla \cdot (\kappa \nabla \Phi) + \left(\mu_a + \frac{i\omega}{c} \right) \Phi &= q & \text{in } \Omega \\ \Phi + 2a\kappa \frac{\partial \Phi}{\partial \nu} &= 0 & \text{on } \partial\Omega \end{aligned} \quad (2.1)$$

where Ω is a Lipschitz domain in \mathbb{R}^n , $n = 2, 3$; $\partial\Omega$ is its boundary, Φ is the photon density, c is the speed of light, ω is the angular frequency of the source q , ν is the unit outward normal vector on the boundary, a is a parameter to account for the the refraction index mismatch at the boundary, and μ_a , μ'_s and $\kappa = \frac{1}{3(\mu_a + \mu'_s)}$ are the absorption, reduced scattering and isotropic diffusion coefficients, respectively. For the general anisotropic material, see [19].

The unique identification of the optical coefficients μ_a and κ in (2.1) when Dirichlet-to-Neumann map is given (or when infinite sources and infinite detectors are given) can be easily shown by using the uniqueness results for the isotropic case [35]. For the uniqueness of the optical coefficients when κ has anisotropic anomalous region contained in a known background, see [18, 20, 22].

In [2, 3], numerical examples show that the Rytov approximation provides better DOT images as compared to the Born approximation. Therefore, we use the Rytov measurements [27] on the boundary:

$$\Gamma = \log \left(-\kappa \frac{\partial \Phi}{\partial \nu} \right) \quad (2.2a)$$

$$= \log \left(\frac{1}{2a} \Phi \right). \quad (2.2b)$$

Then, the Jacobian of Γ with respect to μ_a and μ'_s is given as follows:

$$\frac{\partial \Gamma}{\partial \mu_a}(r) = -\frac{1}{2a\Phi(r)} \int_{\Omega} [-3\kappa(r')^2 \nabla G(r, r') \nabla \overline{\Phi(r')} + G(r, r') \overline{\Phi(r')}] dr', \quad (2.3a)$$

$$\frac{\partial \Gamma}{\partial \mu'_s}(r) = -\frac{1}{2a\Phi(r)} \int_{\Omega} -3\kappa(r')^2 \nabla G(r, r') \nabla \overline{\Phi(r')} dr' \quad (2.3b)$$

where $r \in \partial\Omega$, $\overline{\Phi}$ is the complex conjugate of Φ , and G is Green's function of (2.1).

2.2. Discretization and finite element method

Suppose that there are N_s sources located at r_j , $j = 1, \dots, N_s$; and N_d detectors located on the boundary of Ω , at r_{i+N_s} , $i = 1, \dots, N_d$. Let Φ_j be the solution of (2.1) for the point source $q^j(r) = \delta(r - r_j)$. Define

$$\Gamma_{i,j} = \log(\Phi_j(r_{i+N_s})), \quad (2.4)$$

for the i th detector and the j th source.

Consider the finite element space spanned by the bases u_k , $k = 1, \dots, N_n$. Note that for piecewise bilinear element, N_n is the same as the number of nodes. Let T_m denote the elements for $m = 1, \dots, N_e$, where N_e is the number of the elements. Then, the finite element formulation for (2.1) in this finite element space for the point source q^j located at r_j , is given as follows:

$$\left[K + C + \frac{1}{2a} A \right] \Phi_j = f^j, \quad (2.5)$$

where K, C, A are $N_n \times N_n$ matrices and f^j is a $N_n \times 1$ column vector given by

$$\begin{aligned} K_{kl} &= \int_{\Omega} \kappa \nabla u_k \nabla u_l \\ C_{kl} &= \int_{\Omega} \left(\mu_a + i \frac{\omega}{c} \right) u_k u_l \\ A_{kl} &= \int_{\partial\Omega} u_k u_l \\ f_l^j &= \begin{cases} 1 & \text{if } l = j \\ 0 & \text{Otherwise,} \end{cases} \end{aligned}$$

for $k, l = 1, \dots, N_n$.

Next, we define the following function spaces:

$$V^y = \{\eta \in L^2(\Omega) | L^y \leq |\eta(r)|_{r \in \Omega} \leq U^y\}, \quad (2.6a)$$

$$V_{N_e}^y = \{\eta \in V^y | \eta \text{ is constant at each } T_m, m = 1, \dots, N_e\}, \quad (2.6b)$$

where y is either μ_a or μ'_s , and L^y and U^y are positive constants. Note that we can choose different values for L^y and U^y depending on μ_a and μ'_s . Let $\eta \in V_{N_e}^y$ be $\eta = (\eta_1, \dots, \eta_{N_e})$, then we define the norms in V^y and $V_{N_e}^y$ as follows:

$$\begin{aligned} \|\eta\|_{V^y} &= \|\eta\|_{L^2(\Omega)} \text{ for } \eta \in V^y, \\ \|\eta\|_{V_{N_e}^y} &= \sqrt{\sum_{m=1}^{N_e} \frac{\eta_m^2}{|T_m|}} \text{ for } \eta = (\eta_1, \dots, \eta_{N_e}) \in V_{N_e}^y, \end{aligned}$$

where $|T_m|$ is the area of T_m .

Assume that $\mu_a \in V_{N_e}^{\mu_a}$, $\mu'_s \in V_{N_e}^{\mu'_s}$. Let $\Phi_j(k)$ be the value of Φ_j at the k th node point, $G(k : j)$ be the value of Green's function at the k th node point due to the j th point source, and $\kappa(m)$ be the value of κ at the m th element T_m . By discretizing (2.3a), we obtain the value of the Jacobian of $\Gamma_{i,j}$ at the m th element as follows:

$$\frac{\partial \Gamma_{i,j}}{\partial \mu_a}(m) = -\frac{1}{2a\Phi_j(i)} \sum_{k,l=1}^{N_n} G(i : k) [-3\kappa(m)^2 E_m(k, l) + F_m(k, l)] \Phi_j(l), \quad (2.7a)$$

$$\frac{\partial \Gamma_{i,j}}{\partial \mu'_s}(m) = -\frac{1}{2a\Phi_j(i)} \sum_{k,l=1}^{N_n} G(i : k) [-3\kappa(m)^2 E_m(k, l)] \Phi_j(l), \quad (2.7b)$$

where

$$E_m(k, l) = \int_{T_m} \nabla u_k \nabla u_l, \quad (2.8a)$$

$$F_m(k, l) = \int_{T_m} u_k u_l. \quad (2.8b)$$

We note that in most practical applications, computing $G(i : k)$ for each point source located at the k th node and evaluating at the i th detector location is not feasible. Instead, we consider the adjoint problem associated with (2.1) [1], with the adjoint point source located at the i th detector position. Then, the solution $G^*(k : i)$ to the adjoint problem at the k th node for the adjoint source at the i th detector location satisfies $G^*(k : i) = G(i : k)$.

2.3. DOT as a nonlinear ill-posed optimization problem and the trust region method

Although the unique determination of μ_a and μ'_s from the measurement Γ at the boundary is possible for infinite sources and detectors when $\omega \neq 0$ and κ is known near the boundary [1], the unique solvability of inverse DOT problem for finite sources and detectors is not known. In addition, when the number of measurements is less than the total number of unknowns in the discretized inverse problem, the underdetermined problem challenges the determination of the optical coefficients. However, even in the overdetermined case, the inevitable ill posedness of the inverse problem may result in large perturbations in the reconstructed optical coefficients due to small amount of noise in the measurements. In order to address the ill posedness, we use general Tikhonov-type regularization and consider the following nonlinear minimization problem:

$$(\mu_a, \mu'_s) = \underset{(\eta, v) \in V_{N_e}^{\mu_a} \times V_{N_e}^{\mu'_s}}{\operatorname{argmin}} F(\eta, v), \quad (2.9)$$

where

$$F(\eta, v) = \frac{1}{2} \sum_{j=1}^{N_s} \sum_{i=1}^{N_d} (\Gamma_{i,j}(\eta, v) - \mathcal{M}_{i,j})^2 + \alpha \Lambda(\eta, v). \quad (2.10)$$

In (2.10), $\mathcal{M}_{i,j}$ denotes the measurement at the i th detector due to the j th source, Λ is a non-negative operator from $V_{N_e}^{\mu_a} \times V_{N_e}^{\mu'_s}$ into non-negative real numbers $\mathbb{R}^+ \cup \{0\}$, and $\alpha > 0$ is the regularization parameter. For example, Λ can be chosen as follows:

$$\Lambda(\eta, v) = \|L_1(\eta - \eta^*)\|_{V_{N_e}^{\mu_a}}^2 + \|L_2(v - v^*)\|_{V_{N_e}^{\mu'_s}}^2, \quad (2.11)$$

where $(\eta^*, v^*) \in V_{N_e}^{\mu_a} \times V_{N_e}^{\mu'_s}$ is a given prior for the optical coefficients, and L_1 and L_2 are $N_e \times N_e$ matrices. Note that depending on the choice of L_1 and L_2 , (2.11) can be either zeroth- or first-order Tikhonov regularizer. For other regularization methods, see [19].

Note that (2.10) can be extended in a straightforward manner to include multi-frequency measurements. However, to simplify our notation, we will present the rest of our development for the single frequency measurements.

The optimization problem in (2.9) is composed of two steps; the step to determine the minimizing direction at the current coefficients (μ_a, μ'_s) ; and the step to perform line search on those minimizing directions. In the Newtonian method, the minimizing direction is $-(F'')^{-1} F'$, where F' and F'' are the Jacobian and the Hessian of F with respect to (μ_a, μ'_s) , respectively.

In this paper, we adopted the trust region method [12], one of the Newtonian approaches, which updates (μ_a, μ'_s) in (2.9) iteratively as

$$(\mu_a, \mu'_s) \leftarrow (\mu_a, \mu'_s) + (\delta\mu_a, \delta\mu'_s),$$

by solving the following quadratic minimization problem formulated at the previous update of (μ_a, μ'_s) :

$$\begin{aligned} (\delta\mu_a, \delta\mu'_s) &= \arg \min_{x \in K} \left\{ \frac{1}{2} x^t F''(\mu_a, \mu'_s) x + x^t F'(\mu_a, \mu'_s) \right\}, \\ &\text{subject to } \|Dx\| \leq T. \end{aligned} \quad (2.12)$$

In (2.12), D is a scaling matrix, T is a trust region parameter and K is a subspace of $V^{\mu_a} \times V^{\mu'_s}$. The scaling matrix D is used to handle the constraints for the minimization. To stabilize the minimization, we control the trust region parameter T , similar to the way the parameter λ in the Levenberg–Marquardt method is controlled [7, 24, 25]. To avoid extensive computation,

the subspace K is chosen as the two-dimensional subspace composed of the gradient direction and the approximate Newton direction. This makes the trust region method suitable for large-scale constrained optimization problems like the one in (2.9).

Note that F' and F'' for a given (μ_a, μ'_s) in (2.12) are given as follows:

$$F' = J^t b + \alpha \Lambda', \quad (2.13a)$$

$$F'' = J^t J + H b + \alpha \Lambda'', \quad (2.13b)$$

where $b = \Gamma_{i,j}(\mu_a, \mu'_s) - \mathcal{M}_{i,j}$, J and H are the Jacobian and the Hessian of the operator $\Gamma_{i,j}$, respectively. J is given by $J = J_{(i,j)}(m) = \left(\frac{\Gamma_{i,j}}{\partial \mu_a}(m), \frac{\Gamma_{i,j}}{\partial \mu'_s}(m) \right)$, $i = 1, \dots, N_d$, $j = 1, \dots, N_s$, $m = 1, \dots, N_e$ as in (2.7a). For the computation of H , see [21].

Taking the vanishing gradient point $x = (\delta \mu_a, \delta \mu'_s) \in V_{N_e}^{\mu_a} \times V_{N_e}^{\mu'_s}$ of the quadratic form $\frac{1}{2} x^t F''(\mu_a, \mu'_s) x + x^t F'(\mu_a, \mu'_s)$ in (2.12), we obtain

$$F''(\mu_a, \mu'_s)(\delta \mu_a, \delta \mu'_s) = -F'(\mu_a, \mu'_s). \quad (2.14)$$

Using (2.13a), we get

$$[J^t(\mu_a, \mu'_s)J(\mu_a, \mu'_s) + H(\mu_a, \mu'_s)b + \alpha \Lambda''](\delta \mu_a, \delta \mu'_s) = -[J(\mu_a, \mu'_s)^t b + \alpha \Lambda']. \quad (2.15)$$

Thus, if $\delta \mu_a$ and $\delta \mu'_s$ are sufficiently small, the trust region method can be used to solve (2.12) at each iteration without considering the scaling matrix D .

We discuss in section 3.2 how we apply the two-level multiplicative DD method to solve the optimization problem in (2.9) and (2.10) by the trust region method.

3. Two-level domain decomposition methods for diffuse optical tomography

In this section, we describe the two-level domain decomposition methods considered in this paper, as applied to the forward and inverse problems. For simplicity and notational clarity, we will describe our notation and approach for the two-dimensional optical domain $\Omega = [a, b] \times [c, d] \subset \mathbb{R}^2$ and bilinear finite elements. Its extension to the three-dimensional domain is straightforward, by appropriate definition of operators and function spaces.

Let Ω^h denote the domain Ω that is uniformly divided by N_x times in the x -axis direction and N_y times in the y -axis direction. Thus, Ω^h has $N_n = (N_x + 1) \times (N_y + 1)$ nodes and $N_e = N_x \times N_y$ elements. We shall call Ω^h with $(N_x/2 + 1) \times (N_y/2 + 1)$ nodes and $N_x/2 \times N_y/2$ elements, the coarse level of Ω^h , assuming N_x and N_y are even.

Let Ω^h be decomposed into disjoint union of d sub-domains Ω_l , $l = 1, \dots, d$ such that

$$\Omega^h = \bigcup_{l=1}^d \Omega_l. \quad (3.16)$$

(3.16) describes the non-overlapping domain decomposition. For the overlapping domain decomposition, we define Ω_l^w , $l = 1, \dots, d$; an extension of Ω_l , recursively for all non-negative integers w as follows: $\Omega_l^0 = \Omega_l$, and Ω_l^w is the union of Ω_l^{w-1} and its adjacent elements in contact with the boundary of Ω_l^{w-1} , where w will be called the width of the overlapping region. Thus, the overlapping domain decomposition is given by

$$\Omega^h = \bigcup_{l=1}^d \Omega_l^w. \quad (3.17)$$

Figure 1 illustrates an overlapping and a non-overlapping domain decomposition for two sub-domains. Table 1 lists the acronyms and explanations for the algorithms developed in this paper.

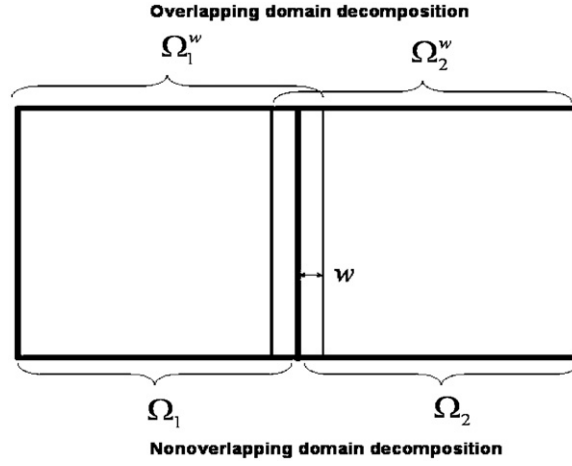


Figure 1. Overlapping domain decomposition and nonoverlapping domain decomposition.

Table 1. The acronyms and explanations of the algorithms.

non-DDM	non-domain decomposition method –Trust region method for the inverse solver using (2.9) and (2.10). and finite element method for the forward solver without using domain decomposition and multigrid methods
MODDM	Multiplicative overlapping domain decomposition method
TMODDM	Two-level multiplicative overlapping domain decomposition method –The forward solver : Multiplicative Schwarz method with two-grid preconditioner
MSDM	Multiplicative space decomposition method
TMSDM	Two-level multiplicative space decomposition method –The inverse solver : Multiplicative Schwarz method with coarse-level initialization using (2.9) and (2.10).

3.1. Two-level multiplicative overlapping domain decomposition method for the forward problem

The forward problem is defined by the boundary value problem (2.1), which is approximated by the finite element formulation (2.5). In this work, we apply a two-level multiplicative overlapping domain decomposition method (TMODDM) to solve (2.5) in an attempt to reduce the computational complexity of the forward problem. In this context, the multi-level structure in TMODDM functions to speed up the convergence, while DD lets us formulate the forward problem as a sequence of smaller-sized problems, thereby reducing the computational requirements. Each sweep of TMODDM involves two steps: the *coarse-level correction* and the *sub-domain correction*. In the following discussion, we describe these steps in detail.

We list the notation and explanation for the variables used in Algorithm TMODDM in table 2.

3.1.1. The coarse-level correction: By formulating a smaller-sized problem on the coarse grid Ω^H , the coarse-level correction step provides an approximation to the error in the optical

Table 2. The notations used in Algorithm TMODDM.

Φ_j^0	Initial guess for the photon density for the j th source
$\Phi_j^{n-1+\frac{1}{d+1}}$	The update of Φ_j^{n-1} by coarse-level correction at the n th sweep of TMODDM
$\Phi_j^{n-1+\frac{p+1}{d+1}}$	The update of $\Phi_j^{(n-1)+\frac{1}{d+1}}$ after p successive sub-domain corrections on $\cup_{k=1}^p \Omega_k^w$ at the n th sweep of TMODDM

density estimate, which in turn is used to update the optical density on Ω^h . The coarse-level correction step can be explained in detail as follows:

Let Φ^n denote the current solution update for the optical density Φ on Ω^h after the n th sweep of TMODDM. The coarse-level correction in the $(n+1)$ th sweep starts with computing the residual [11] on the fine grid Ω^h :

$$r_h \leftarrow \left(K + C + \frac{1}{2a} A \right)_h \Phi^n - f, \quad (3.18)$$

and restricting it onto the coarse grid Ω^H :

$$r_H \leftarrow R(r_h), \quad (3.19)$$

where $R : \mathbb{R}^{(N_x+1) \times (N_y+1)} \rightarrow \mathbb{R}^{(N_x/2+1) \times (N_y/2+1)}$ is the restriction operator. In this work, we use the full weighting restriction operator [39], which performs a nine-point weighted averaging. An approximation to the error in the solution update Φ^n can be obtained by solving the defect equation [39] formulated on Ω^H :

$$\left(K + C + \frac{1}{2a} A \right)_H e_H = r_H. \quad (3.20)$$

Then, the solution of (3.20) is used to update Φ^n , which completes the coarse-level correction:

$$\Phi^{n+\frac{1}{d+1}} \leftarrow \Phi^n + P(e_H), \quad (3.21)$$

where $P : \mathbb{R}^{(N_x/2+1) \times (N_y/2+1)} \rightarrow \mathbb{R}^{(N_x+1) \times (N_y+1)}$ is the prolongation operator. In this work, we use a bilinear prolongation operator [11].

3.1.2. Sub-domain correction. Following the coarse grid correction step, the sub-domain correction is performed on the fine grid Ω^h , by employing a multiplicative overlapping domain decomposition method (MODDM). In this step, the boundary value problem (2.1) is redefined on each of the overlapping sub-domains with appropriate boundary conditions. Then, the solution of the boundary value problem formulated on each sub-domain is used to update the optical density. In the following, we present the details of the sub-domain correction.

Let $\Phi^{n+\frac{p}{d+1}}$ be the current optical density estimate, obtained by updating $\Phi^{n+\frac{1}{d+1}}$ with the solutions of the boundary value problems formulated on the sub-domains $\Omega_1^w, \Omega_2^w, \dots, \Omega_{p-1}^w$. Then, the boundary value problem on the sub-domain Ω_p^w is formulated as

$$-\nabla \cdot (\kappa \nabla v) + \left(\mu_a + \frac{i\omega}{c} \right) v = q \quad \text{in} \quad \Omega_p^w \quad (3.22a)$$

$$v + 2a\kappa \frac{\partial v}{\partial \nu} = 0 \quad \text{on} \quad \partial \Omega_p^w \cap \partial \Omega, \quad (3.22b)$$

$$v = \Phi^{n+\frac{p}{d+1}} \quad \text{on} \quad \partial \Omega_p^w \setminus \partial \Omega. \quad (3.22c)$$

Then, the solution of (3.22a) is used to obtain the new optical density estimate on Ω as follows:

$$\Phi^{n+\frac{p+1}{d+1}} = \begin{cases} v & \text{in } \Omega_p^w \\ \Phi^{n+\frac{p}{d+1}} & \text{in } \Omega \setminus \overline{\Omega_p^w}. \end{cases} \quad (3.23)$$

Recursive application of this procedure for the rest of the sub-domains $\Omega_l^w : l = p+1, p+2, \dots, d$ completes the sub-domain correction step and results in the optical density update Φ^{n+1} for the next TMODDM sweep. We refer to the pseudo-code in algorithm 1 for a summary of the coarse-level correction and sub-domain correction steps in TMODDM.

3.2. Two-level multiplicative overlapping space decomposition method for the inverse problem

In this work, we apply a two-level multiplicative overlapping space decomposition method (TMSDM) to solve the inverse problem in (2.9). We use the term ‘space decomposition’ to distinguish the DD method developed for the optimization problem (2.9) from TMODDM described in section 3.1. Although both methods involve domain decomposition; in the forward problem, the DD method is applied on a partial differential equation, whereas in the inverse problem, it is applied to an optimization problem.

In the forward problem, we obtain the value of the photon density at each node, whereas in the inverse problem, we are interested in the constant value of the optical coefficients on each element. Note that this is a direct consequence of the different discretization schemes followed in the forward and inverse problems. Even though TMSDM can be applied for any overlapping domain decomposition, in this work, we use the same domain decomposition in both forward and inverse problems to avoid introducing new notation.

Algorithm 1 TMODDM

N_s : The number of sources.
 N_d : The number of detectors.
 M_F : The maximum number of sub-domain correction sweeps.
for $j = 1, \dots, N_s + N_d$ **do**
 Initialize Φ_j^0 .
 for $n = 1, \dots, M_F$
 Start coarse-level correction
 $r_h^j \leftarrow (K + C + \frac{1}{2a}A)_h \Phi_j^{n-1} - f^j$, {Compute the residual}
 $r_H^j \leftarrow R(r_h^j)$ Restrict the residual
 $e_H^j \leftarrow (K + C + \frac{1}{2a}A)_H^{-1} r_H^j$, {Compute the error on Ω^H }
 $\Phi_j^{n-1+\frac{1}{d+1}} \leftarrow \Phi_j^{n-1} + P(e_H^j)$ {Update the photon density}
 end coarse-level correction
 for $l = 1, \dots, d$ **do**
 Update $\Phi_j^{n-1+\frac{l+1}{d+1}}$ at Ω_l^w by (3.22) and (3.23) {Sub-domain correction}
 end for
 end for
end for
 Compute $\Gamma_{i,j}$ and $\frac{\partial \Gamma_{i,j}}{\partial \mu_a}(m)$, $\frac{\partial \Gamma_{i,j}}{\partial \mu_s}(m)$, $m = 1, \dots, N_e$ using (2.4) and (2.7).
 {Post-processing}

Table 3. The notations used in Algorithm TMSDM.

μ^0	Initial guess for the optical coefficients $\mu = (\mu_a, \mu'_s)$
$\mu^{n-1+\frac{1}{d+1}}$	The update of μ^{n-1} by the coarse-level inverse solver at the n th sweep of TMSDM
$\mu^{n-1+\frac{p+1}{d+1}}$	The update of $\mu^{(n-1)+\frac{1}{d+1}}$ after p successive sub-domain corrections on $\cup_{k=1}^p \Omega_k^w$ at the n th sweep of TMSDM

TMSDM consists of two steps: *Coarse-level initiation* and *sub-domain correction*. The coarse-level initiation step provides an initial guess for the fine level, by solving (2.9) on the coarse level. The sub-domain correction involves the minimization of (2.9) on the fine level, iteratively on each sub-domain using a multiplicative space decomposition method (MSDM). In the following, we present the details of coarse-level initiation and sub-domain correction.

We list the notation and explanation for the variables used in algorithm TMSDM in table 3.

3.2.1. Coarse-level initiation: By solving a smaller sized minimization problem formulated on the coarse grid Ω^H , the coarse-level initiation provides a computationally viable approximation for the optical coefficient estimates. This approximation is then used as an initial guess at the first sweep of the sub-domain correction step. In theorem 1, we show that the local convergence of the sub-domain correction step under the condition that the initial guess is sufficiently close to the solution. Therefore, the coarse-level initiation is motivated to achieve the convergence of the sub-domain correction. The coarse-level initiation step can be described as follows:

Let $(\mu_a, \mu'_s)^0$ denote the initial guess for the optical coefficients on Ω^h for the optical coefficients (μ_a, μ'_s) . The coarse-level initiation starts with downsampling $(\mu_a, \mu'_s)^0$ onto the coarse grid Ω^H :

$$(\mu_a, \mu'_s)_H^0 \leftarrow D((\mu_a, \mu'_s)^0), \quad (3.24)$$

where the downsampling operator $D : \mathbb{R}^{N_e} \rightarrow \mathbb{R}^{N_e/4}$ is defined by

$$D(h)(m_x, m_y) = \frac{1}{4}[h(2m_x - 1, 2m_y - 1) + h(2m_x - 1, 2m_y) + h(2m_x, 2m_y - 1) + h(2m_x, 2m_y)], \quad (3.25)$$

for $1 \leq m_x \leq N_x/2$, $1 \leq m_y \leq N_y/2$, $h \in \mathbb{R}^{N_e}$, where $N_e/4 = N_x/2 \times N_y/2$ is the number of elements on the coarse level. Then, we formulate the inverse problem on the coarse grid with the initial guess $(\mu_a, \mu'_s)_H^0$ and seek a solution to the following minimization problem:

$$(\mu_a, \mu'_s)_H^{\frac{1}{d+1}} = \underset{(\eta, v) \in V_{N_e/4}^{\mu_a} \times V_{N_e/4}^{\mu'_s}}{\operatorname{argmin}} F_H(\eta, v), \quad (3.26)$$

where $V_{N_e/4}^y = \{\eta \in V^y | \eta \text{ is constant at each } T_m, m = 1, \dots, N_e/4\}$ for $y = \mu_a, \mu_s$ and $F_H : V_{N_e/4}^{\mu_a} \times V_{N_e/4}^{\mu'_s} \rightarrow \mathbb{R}$ is given by

$$F_H(\eta, v) = \frac{1}{2} \sum_{j=1}^{N_s} \sum_{i=1}^{N_d} (\Gamma_{i,j}(\eta, v) - \mathcal{M}_{i,j})^2 + \alpha \Lambda_H(\eta, v),$$

and $\Lambda_H : V_{N_e/4}^{\mu_a} \times V_{N_e/4}^{\mu'_s} \rightarrow \mathbb{R}^+ \cup \{0\}$. Then, the initial guess $(\mu_a, \mu'_s)_H^{\frac{1}{d+1}}$ for the sub-domain correction step is obtained by upsampling $(\mu_a, \mu'_s)_H^0$ to the fine grid Ω^h :

$$(\mu_a, \mu'_s)_H^{\frac{1}{d+1}} \leftarrow U((\mu_a, \mu'_s)_H^0), \quad (3.27)$$

where the upsampling operator $U : \mathbb{R}^{N_x/2 \times N_y/2} \rightarrow \mathbb{R}^{N_x \times N_y}$ in (3.27) is the bilinear prolongation operator.

3.2.2. Sub-domain correction: Following the coarse grid initiation step, the sub-domain correction is performed on the fine grid Ω^h . In this step, the inverse problem (2.9) is solved by successively minimizing the objective functional in (2.9) with respect to the unknown optical coefficients on each sub-domain. Thus, the optimization problem (2.9) is decomposed into a sequence of smaller minimization problems, using MSDM.

Before we give the details of the sub-domain correction step, we first introduce some notation. Recall that $(\eta, \nu) \in V_{N_e}^{\mu_a} \times V_{N_e}^{\mu'_s}$. Then, for each $l = 1, \dots, d$, we can decompose (η, ν) into orthogonal components as follows:

$$(\eta, \nu)_l = \begin{cases} (\eta, \nu) & \text{in } \Omega_l^w \\ (0, 0) & \text{in } \Omega \setminus \overline{\Omega}_l^w, \end{cases} \quad (3.28)$$

and

$$(\eta, \nu)_{l'} = \begin{cases} (0, 0) & \text{in } \Omega_l^w \\ (\eta, \nu) & \text{in } \Omega \setminus \overline{\Omega}_l^w, \end{cases} \quad (3.29)$$

such that $(\eta, \nu) = (\eta, \nu)_l + (\eta, \nu)_{l'}$.

The first sub-domain correction sweep is initiated by the update $(\mu_a, \mu'_s)^{\frac{1}{d+1}}$ provided by the coarse-level initiation. Let $(\mu_a, \mu'_s)^{n+\frac{p}{d+1}}$ be the estimate for the optical coefficients in the $(n+1)$ th sub-domain correction sweep, obtained by updating $(\mu_a, \mu'_s)^{n+\frac{1}{d+1}}$ with the solution estimates obtained on the sub-domains $\Omega_1^w, \Omega_2^w, \dots, \Omega_{p-1}^w$. Then, the inverse problem on the sub-domain Ω_p^w reads

$$(\mu_a, \mu'_s) = \underset{(\eta, \nu) \in V_{N_e}^{\mu_a} \times V_{N_e}^{\mu'_s}}{\operatorname{argmin}} F((\eta, \nu)_p + (\eta, \nu)_{p'}), \quad (3.30)$$

subject to

$$(\eta, \nu)_{p'} = (\mu_a, \mu'_s)^{n+\frac{p}{d+1}}_{p'},$$

where $F(\eta, \nu)$ is given by (2.10). Thus, the minimization is performed over only (η, ν) on Ω_p^w . Then, the solution of (3.30) is used to obtain the new optical coefficients update on Ω as follows:

$$(\mu_a, \mu'_s)^{n+\frac{p+1}{d+1}} = \begin{cases} (\mu_a, \mu'_s)_p & \text{in } \Omega_p^w \\ (\mu_a, \mu'_s)^{n+\frac{p}{d+1}}_{p'} & \text{in } \Omega \setminus \overline{\Omega}_p^w. \end{cases} \quad (3.31)$$

Successive application of this procedure for the rest of the sub-domains $\Omega_l^w : l = p+1, p+2, \dots, d$ completes the $(n+1)$ th sweep of the sub-domain correction step and results in the optical coefficient update $(\mu_a, \mu'_s)^{n+1}$ for the next sub-domain correction sweep. We refer to the pseudo-code in algorithm 2 for a summary of the coarse-level initiation and sub-domain correction steps in TMSDM.

3.3. Convergence of TMODDM and TMSDM

Assume that the mesh size of the finite element formulation is $O(h)$ and that the sub-domains are of diameter $O(H)$ and the width of the overlapping region is $O(\delta H)$, where $0 \leq \delta < 1$. Then the following convergence behaviour is known for algorithm TMODDM (see section 2.5 in [33]).

- (a) Convergence is poor if $\delta = 0$, but improves rapidly as δ increases.

- (b) If δ is fixed, the number of sub-domain correction sweeps required for convergence is bounded independent of h , H and H/h .
- (c) The number of sub-domain correction sweeps required for convergence is roughly half of that needed for the additive Schwarz method.

Algorithm 2 TMSDM

d : The number of sub-domains.

M_U : The maximum number of sub-domain correction sweeps.

Initialize μ^0 on Ω^h .

Start coarse-level initiation

$$(\mu_a, \mu'_s)_H^n \leftarrow D((\mu_a, \mu'_s)^n)$$

$$\text{Solve } (\mu_a, \mu'_s)_H^{n/(d+1)} = \arg \min_{(\eta, v) \in V_{N_e/4}^{\mu_a} \times V_{N_e/4}^{\mu'_s}} F_H(\eta, v)$$

$$(\mu_a, \mu'_s)_H^{n+\frac{1}{d+1}} \leftarrow U((\mu_a, \mu'_s)_H^{n+\frac{1}{d+1}})$$

end coarse-level initiation

for $n = 1, \dots, M_U$ **do**

for $l = 1, \dots, d$ **do**

$$(\mu_a, \mu'_s) = \arg \min_{(\eta, v) \in V_{N_e}^{\mu_a, l} \times V_{N_e}^{\mu'_s, l}} F(\eta, v)$$

$$\text{subject to } (\eta, v)_{l'} = (\mu_a, \mu'_s)_{l'}^{n+\frac{l}{d+1}}$$

 Update the optical coefficients by (3.31)

end for

end for

Therefore, in terms of convergence, multiplicative Schwarz algorithms are more advantageous as compared to additive Schwarz algorithms. This follows from the fact that the multiplicative Schwarz algorithms take the advantage of immediate use of the solution update in the successive neighbouring sub-problem. On the other hand, in additive Schwarz algorithms, one computes the solutions to the localized sub-problems independent of each other and uses the solution updates in the following sub-domain correction sweep. We refer to [31] and [33] for a detailed discussion of the Schwarz algorithms.

The local linear convergence of Algorithm MSDM is shown below, using the results in [5].

Theorem 1. Let Λ be the regularization operator given in (2.11), and Λ' and Λ'' denote the first- and second-order Fréchet derivatives of Λ . Assume that there is a positive constant C_Λ such that $y^t \Lambda'' y \geq C_\Lambda y^t y$ for all $y \in V_{N_e}^{\mu_a} \times V_{N_e}^{\mu'_s}$.

Let $(\mu_a, \mu'_s)^n$ be the n th step MSDM approximation of (μ_a, μ'_s) . Assume that

$$\|(\mu_a, \mu'_s) - (\mu_a, \mu'_s)^q\|_{V_{N_e}^{\mu_a} \times V_{N_e}^{\mu'_s}} \leq \frac{\alpha C_\Lambda}{C_H C_J}, \quad (q = 0, \dots, n). \quad (3.32)$$

Then,

$$\|(\mu_a, \mu'_s)^n - (\mu_a, \mu'_s)\|_{V_{N_e}^{\mu_a} \times V_{N_e}^{\mu'_s}} \leq \left(\frac{8}{9}\right)^n \frac{\alpha^2 C_\Lambda}{C_H^2 C_J} [C_\Lambda C_J + \tilde{C}_\Lambda C_H], \quad (3.33)$$

where $\tilde{C}_\Lambda = \|\Lambda'\|_{V_{N_e}^{\mu_a} \times V_{N_e}^{\mu'_s} \rightarrow \mathbb{R}}$ and C_J, C_H are positive constants such that

$$\|J(\mu_a, \mu'_s)\|_{V_{N_e}^{\mu_a} \times V_{N_e}^{\mu'_s} \rightarrow l^2} \leq C_J, \quad (3.34a)$$

$$\|H(\mu_a, \mu'_s)\|_{V_{N_e}^{\mu_a} \times V_{N_e}^{\mu'_s} \rightarrow l^2} \leq C_H. \quad (3.34b)$$

Proof. See the appendix for the proof of theorem 1.

Note that C_J and C_H depend on the frequency ω . For the multi-frequency measurement case with N_ω frequencies $\omega_1, \dots, \omega_{N_\omega}$, let

$$C_J = \max_{i=1, \dots, N_\omega} C_J^{\omega_i}, \quad C_H = \max_{i=1, \dots, N_\omega} C_H^{\omega_i}, \quad (3.35)$$

where $C_J^{\omega_i}$ and $C_H^{\omega_i}$ are the frequency-dependent norm bounds. Then, theorem 1 can be extended to multi-frequency measurement case in a straightforward manner, by replacing the norm bounds in (3.34a) and (3.34b) by the bounds given in (3.35).

For the general Tikhonov regularizer, Λ is chosen as

$$\Lambda(\eta, v) = \|L_1(\eta - \eta^*)\|_{V_{N_e}^{\mu_a}}^2 + \|L_2(v - v^*)\|_{V_{N_e}^{\mu'_s}}^2.$$

Therefore, if L_1 and L_2 are positive definite, the assumption of $y^t \Lambda'' y \geq C_\Lambda y^t y$ in theorem 1 holds since

$$(\eta, v)^t \Lambda''(\eta, v) = \eta^t L_1 \eta + v^t L_2 v.$$

Clearly, this assumption holds for the zeroth-order Tikhonov regularization. For the appropriate choice of the discrete approximation of the differential operator, first-order Tikhonov regularizer also satisfies the assumption in theorem 1.

Note that in [21], we have shown that the first- and second-order Fréchet derivatives of the coefficient-to-measurement operator with respect to (μ_a, μ'_s) exist and are bounded. Similarly, J and H , being finite approximation to the first- and second-order Fréchet derivatives, satisfy (3.34a) and (3.34b). \square

3.4. Computational cost of the algorithms

In this subsection, the computational cost of the proposed algorithms is analysed. We will call, the method solving (2.5) and (2.15) without any domain decomposition, the non-DD method and compare it with the proposed methods.

The system matrices for each equation are $2N_n \times 2N_n$ and $2N_e \times 2N_e$, respectively. Assume that we require $O(N_n^q)$ and $O(N_e^q)$ ($1 \leq q \leq 3$) floating point operations for each equation with the non-DD method. Note that for a full nonzero matrix, $q = 3$ and for a diagonal matrix, $q = 1$. Suppose that we use d sub-domains with equal nodes and elements for the proposed algorithms.

The coarse-level computation needs 4^{-q} times (in two dimensions) or 8^{-q} times (in three dimensions) the computations required on the fine level computation for the forward and inverse solvers. Thus, if we neglect the coarse-level computation, the computational cost of algorithm MODDM is $M_F d^{1-q}$ (for one computer) and $M_F d^{-q}$ (for d parallel computers) times that of the non-DD method, where M_F is the maximum number of sub-domain correction sweeps. Recall that M_F is the maximum sweep of all sub-domain corrections followed by the coarse grid correction. It is well known that for a given M_F , the convergence behaviour of TMODDM is independent of N_n , d and N_n/d (see (a)–(c) below subsection 3.3). Furthermore TMODDM has good convergence behaviour and it has better convergence behaviour for smaller M_F as compared to MODDM. In this work, we have chosen $M_F = 3$ when TMODDM is used in the inverse solver in section 4.2. This analysis shows that by using multiple sub-domains, algorithm TMODDM can achieve significant reduction in computational requirements.

Table 4. The comparison of the computational costs for the non-DD method, TMSDM on one, d , and d^2 computers. q is a constant between 1 and 3 depending on the sparsity of the system matrix. In the table, N_n is the number of nodes, N_e is the number of elements, d is the number of sub-domains, M_F is the number of sweeps for the forward solver and M_U is the number of sweeps for the inverse solver.

Method	Computational cost	
	Forward solver	Inverse solver
non-DDM	$O(N_n^q)$	$O(N_e^q)$
TMSDM on 1 computer	$M_F d^{1-q} O(N_n^q)$	$M_U d^{1-q} O(N_e^q)$
TMSDM on d computers	$M_F d^{1-q} O(N_n^q)$	$M_U d^{-q} O(N_e^q)$
TMSDM on d^2 computers	$M_F d^{-q} O(N_n^q)$	$M_U d^{-q} O(N_e^q)$

The computational cost of algorithm TMSDM with algorithm TMODDM as the forward solver, and the computational cost of the non-DD method are tabulated in table 4, using 1, d and d^2 computers. When d parallel computers are used, the parallel computing is applied to the inverse problem only, whereas when d^2 computers are used, the parallel computing is applied to both the inverse and forward problems. Note that this comparison for the inverse solver is based on the assumption that the speed of data communication between parallel computers is sufficiently fast. Parallel computation is not treated in this paper, but the proposed algorithms combined with the parallel computing is expected to provide more efficient results.

4. Numerical simulations

In this section, we demonstrate the performance of the algorithms TMODDM and TMSDM using simulated optical data. In section 4.1, we conduct a series of experiments to test and compare the performance of TMODDM to that of the one-level DD method. In section 4.2, we test TMSDM in a number of experiments, where we consider μ_a -only, μ'_s -only and simultaneous μ_a and μ'_s reconstructions. For the summary of method descriptions, we refer to table 1.

In our experiments, we set the angular frequency $\omega = 2\pi \times 100$ MHz, and $a = 1$, except for the simultaneous absorption and reduced scattering imaging case, where we use two frequencies: $\omega_1 = 300$ MHz and $\omega_2 = 500$ MHz. Note that for the μ_a -only simulation, zero-mean Gaussian noise with standard deviation equal to 1% of the average of the measurements was added to the measurements. Similarly, for the μ_s -only case, we added zero-mean Gaussian noise with standard deviation equal to 0.5% of the average of the measurements. For the simultaneous μ_a and μ'_s imaging, we considered additive zero-mean Gaussian noise with standard deviation equal to 5% of the average of the measurements. For the inverse problem formulation, we chose the following zeroth-order Tikhonov regularizer with the regularization parameter $\alpha = 10^{-2}$:

$$\Lambda(\eta, v) = \|\eta\|_{V_{N_e}^{\mu_a}}^2 + \|v\|_{V_{N_e}^{\mu'_s}}^2, \quad (4.36)$$

for $\eta \in V_{N_e}^{\mu_a}$ and $v \in V_{N_e}^{\mu'_s}$.

4.1. Algorithm TMODDM

In this experiment, we evaluate the performance of TMODDM, for an optical medium whose absorption and scattering coefficient distributions are shown in figures 2(a) and (b),

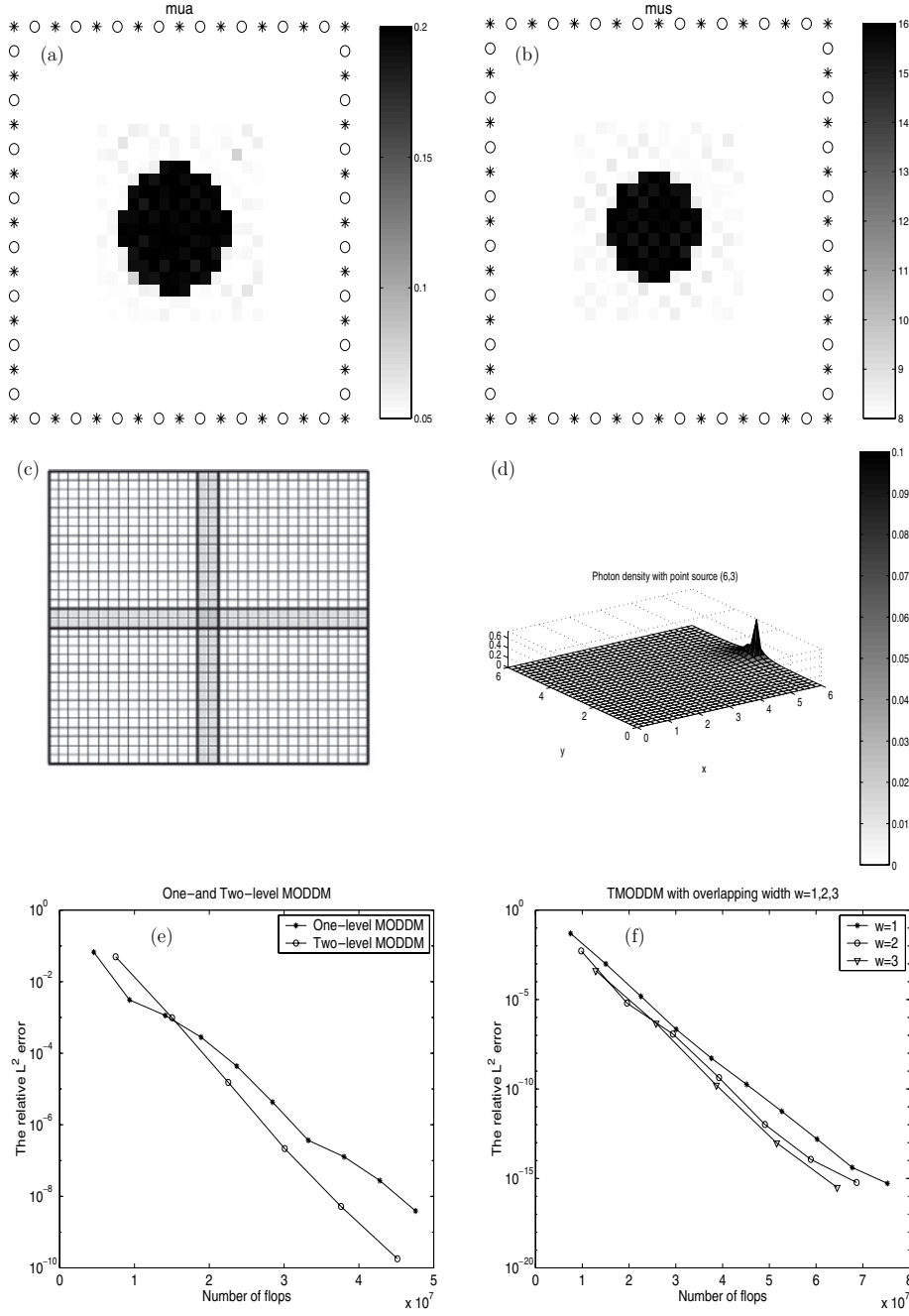


Figure 2. (a) The original μ_a image. The white region represents background tissue with μ_a value of 0.05 cm^{-1} , and the black region represents an anomaly with μ_a value of 0.2 cm^{-1} . (b) The original μ'_s image. The white region represents background tissue with μ'_s value of 8 cm^{-1} , and the black region represents an anomaly with μ'_s value of 16 cm^{-1} . (c) 2×2 domain decomposition of $\Omega = [0, 6] \times [0, 6]$. (d) The LINPACK solution of the frequency-domain diffusion equation for a point source located at $(6, 3)$. (e) Relative L_2 error versus number of floating point operations for one and two-level MODDM. (f) Relative L_2 error versus number of floating point operations for TMODDM with domain decompositions with the overlap region width $w = 1, 2$ and 3 pixels.

respectively. The black region in figure 2(a) shows an anomaly with absorption coefficient $\mu_a = 0.2 \text{ cm}^{-1}$, where the background has an absorption coefficient $\mu_a = 0.05 \text{ cm}^{-1}$. Figure 2(b) shows the reduced scattering coefficient of the same medium, where the black region and the background have reduced scattering coefficients $\mu'_s = 16$ and $\mu'_s = 8 \text{ cm}^{-1}$, respectively. We divide the square domain $\Omega = [0, 6] \times [0, 6] \text{ cm}^2$ into 32×32 uniform pixels. Next, we decompose the domain into four overlapping sub-domains with $2/3 \text{ cm}$ of overlap region, as shown in figure 2(c).

We consider the solution of the diffusion equation (2.1) for a point source located at $(6, 3)$ and compare the performance of TMODDM and the one-level DD method (MODDM) using the following relative $L^2(\Omega)$ error:

$$\frac{\|\Phi^A - \Phi^L\|_{L^2(\Omega)}}{\|\Phi^L\|_{L^2(\Omega)}}, \quad (4.37)$$

where Φ^L is the LINPACK solution of (2.5), and Φ^A is either the TMODDM or MODDM solution. Figure 2(d) shows the LINPACK solution for the point source located at $(6, 3)$. Figure 2(e) shows the relative $L^2(\Omega)$ error versus the number of floating point operations for TMODDM and MODDM. We observe that TMODDM converges faster than the one-level MODDM, with a smaller number of floating point operations.

Next, to show the effect of overlap width on the performance of TMODDM, we consider three cases where the overlap region consists of 1, 2 and 3 pixels, respectively. Figure 2(f) shows the relative $L^2(\Omega)$ error versus the number of floating point operations for each overlap width. We see that the convergence improves as the width gets larger. This verifies the convergence result stated in (a) below subsection 3.3.

4.2. Algorithm TMSDM

In this section, we evaluate the performance of TMSDM in two sets of experiments using simulated data. In the first experiment, we consider μ_a -only and μ'_s -only reconstructions and compare TMSDM to the non-DD method. In the second experiment, we consider simultaneous reconstruction of μ_a and μ'_s using TMSDM and compare the performance to that of the non-DD method. For the description of the non-DD method, we refer to table 1.

For the forward solver, we use TMODDM with the maximum number of sub-domain correction sweeps M_F set to 3. In order to evaluate the performance of the inverse solvers and compare TMSDM to the non-DD method, we define the following signal-to-noise-ratio (SNR):

$$\text{SNR} = 20 \log_{10} \frac{\|y\|_{L^2(\Omega)}}{\|y^A - y\|_{L^2(\Omega)}}, \quad (4.38)$$

where y^A is the actual optical coefficient (either μ_a or μ'_s) and y denotes the reconstructed optical coefficients, obtained by using either TMSDM or the non-DD method.

4.2.1. Experiment 1. In this experiment, we consider two cases. In the first one, we assume that the reduced scattering coefficient of the medium is known and set it to 8 cm^{-1} , and we reconstruct the absorption coefficient of the medium. Figure 3(a) shows the circular heterogeneity with $\mu_a = 0.20 \text{ cm}^{-1}$ embedded in a background with $\mu_a = 0.05 \text{ cm}^{-1}$.

In the second case, we assume that the absorption coefficient of the medium is known and is set to $\mu_a = 0.05 \text{ cm}^{-1}$ and we reconstruct the reduced scattering image. Figure 4(a) shows the circular heterogeneity with $\mu'_s = 16 \text{ cm}^{-1}$ embedded in a background with $\mu'_s = 8 \text{ cm}^{-1}$.

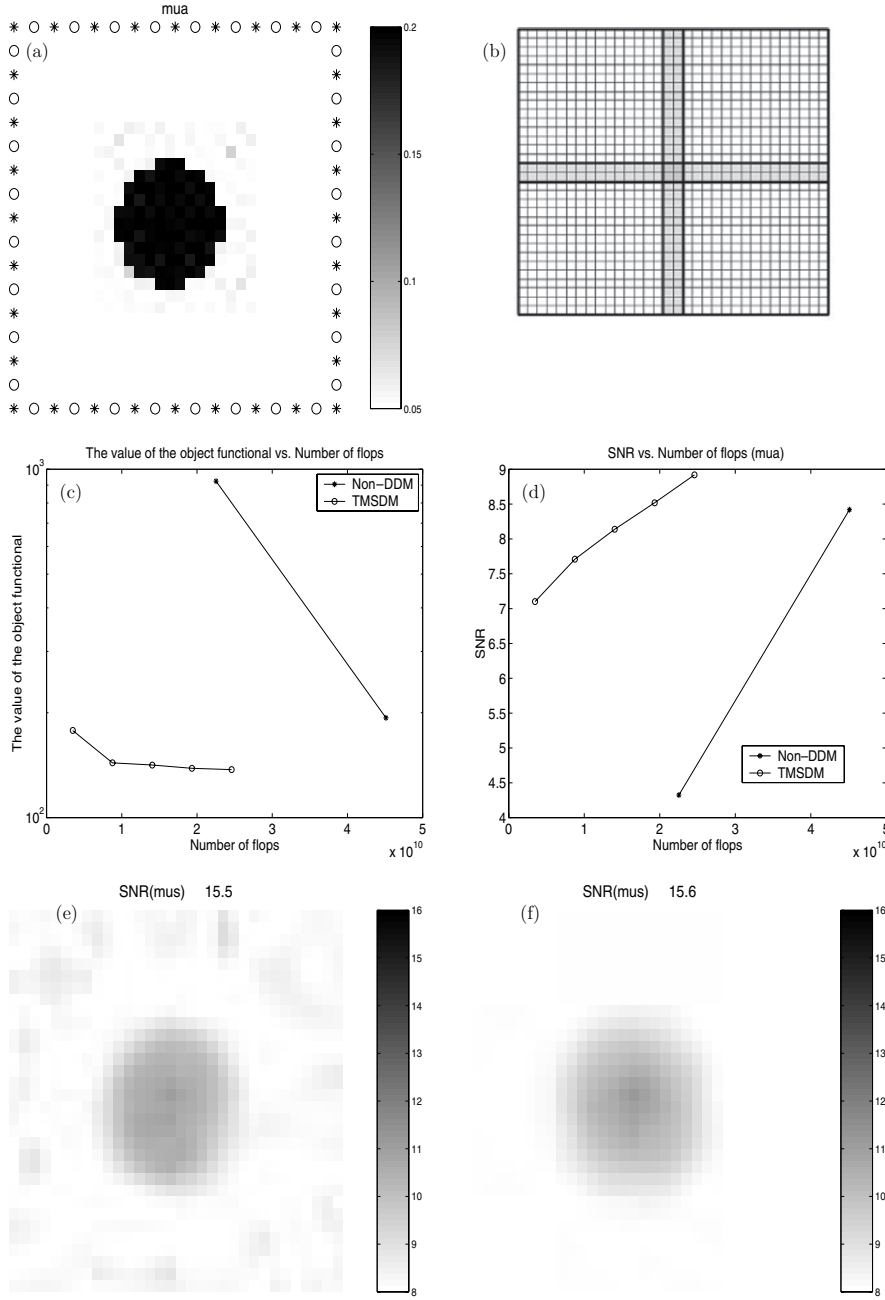


Figure 3. The set-up and the results regarding the μ_a -only reconstruction. (a) The original μ_a image and the source-detector configuration. The white region represents background tissue with μ_a value of 0.05 cm^{-1} , and the black region represents an anomaly with μ_a value of 0.2 cm^{-1} . (b) The 2×2 domain decomposition and uniform 32×32 discretization of Ω . (c) The value of the objective functional versus the number of floating point operations of the non-DD method and TMSDM. (d) The SNR versus the number of floating point operations of the non-DD method and TMSDM. (e) The absorption image reconstruction by the non-DD method after 12.893×10^9 number of floating point operations, with SNR = 8.174. (f) The reconstruction by TMSDM after 8.561×10^9 number of floating point operations with SNR = 9.955.

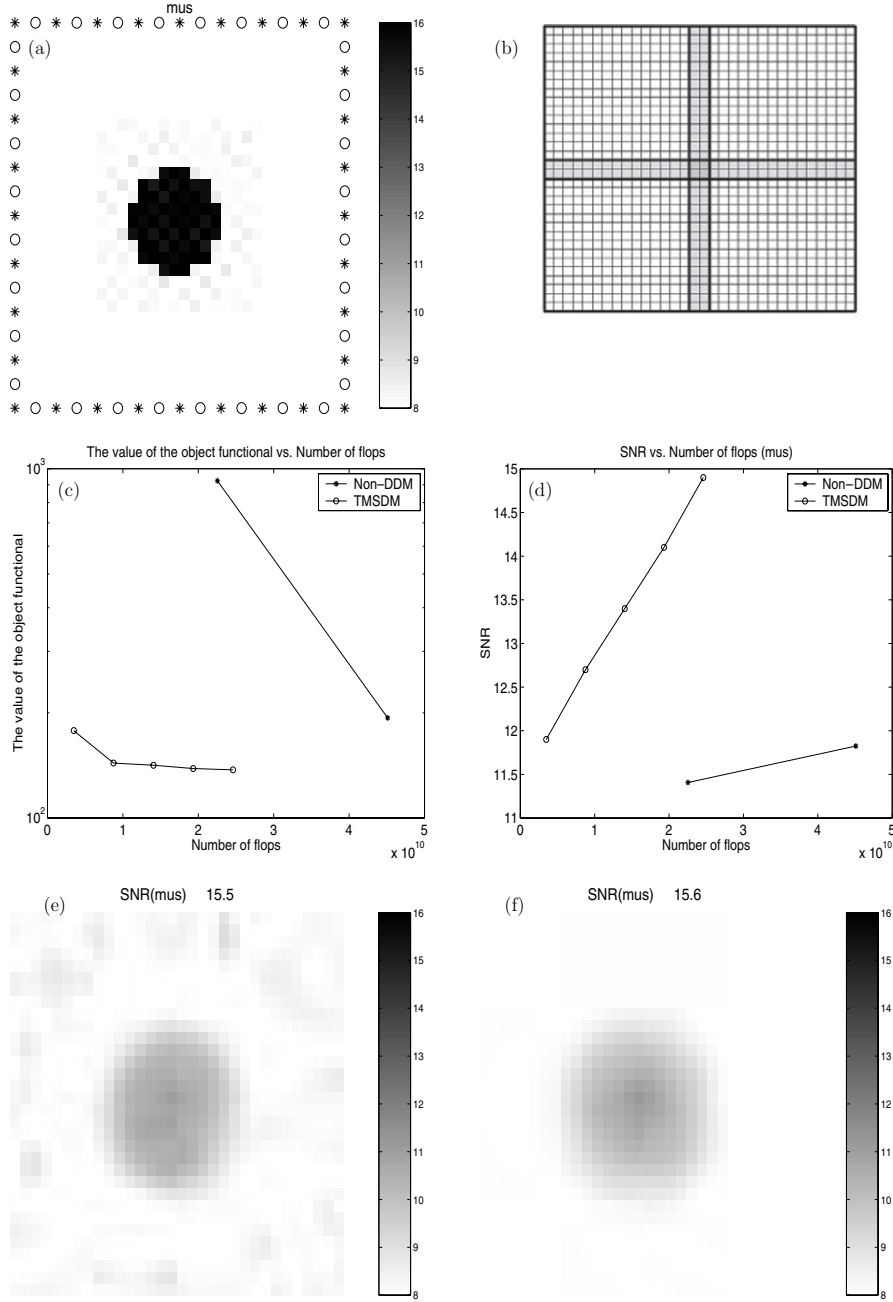


Figure 4. The set-up and the results regarding the μ_a -only reconstruction. (a) The original μ_s' image and the source-detector configuration. The white region represents background tissue with μ_s' value of 8 cm^{-1} , and the black region represents an anomaly with μ_s' value of 16 cm^{-1} . (b) The 2×2 domain decomposition and uniform 32×32 discretization of Ω . (c) The value of the objective functional versus the number of floating point operations of the non-DD method and TMSDM. (d) The SNR versus the number of floating point operations of the non-DD method and TMSDM. (e) The reduced scattering image reconstruction by the non-DD method after 13.165×10^9 number of floating point operations, with SNR = 15.5. (f) The reconstruction by TMSDM after 8.373×10^9 number of floating point operations with SNR = 15.6.

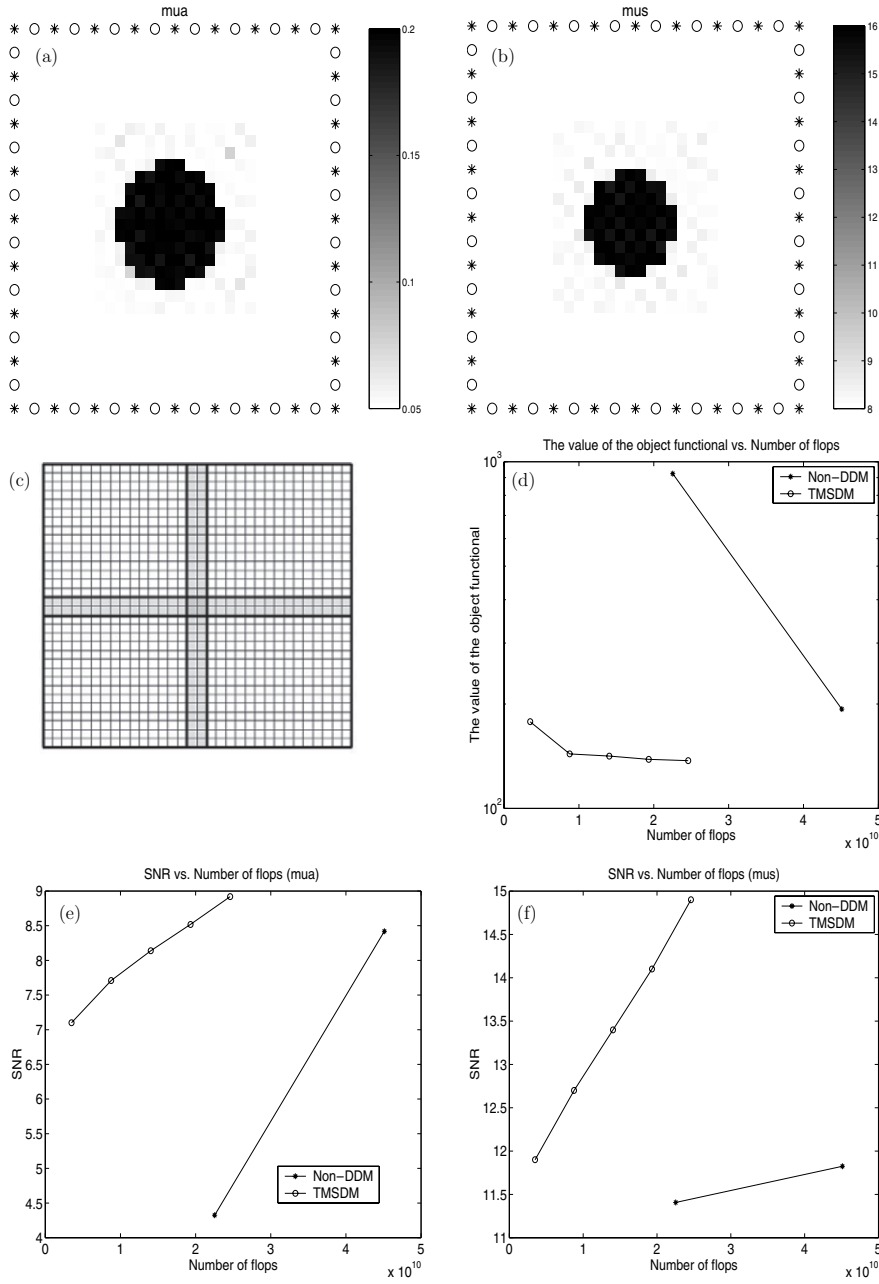


Figure 5. The set-up and the results regarding the simultaneous μ_a and μ_s reconstruction. (a) The original μ_a image and the source-detector configuration. The white region represents background tissue with μ_a value of 0.05 cm^{-1} , and the black region represents an anomaly with μ_a value of 0.2 cm^{-1} . (b) The original μ_s image. The white region represents background tissue with μ_s value of 8 cm^{-1} , and the black region represents an anomaly with μ_s value of 16 cm^{-1} . (c) The 2×2 domain decomposition and uniform 32×32 discretization of Ω . (d) The value of the objective functional versus the number of floating point operations of non-DD method and TMSDM. (e) The SNR for the absorption coefficient reconstruction versus the number of floating point operations of non-DD method and TMSDM. (f) The SNR for the reduced scattering coefficient reconstruction versus the number of floating point operations of non-DD method and TMSDM.

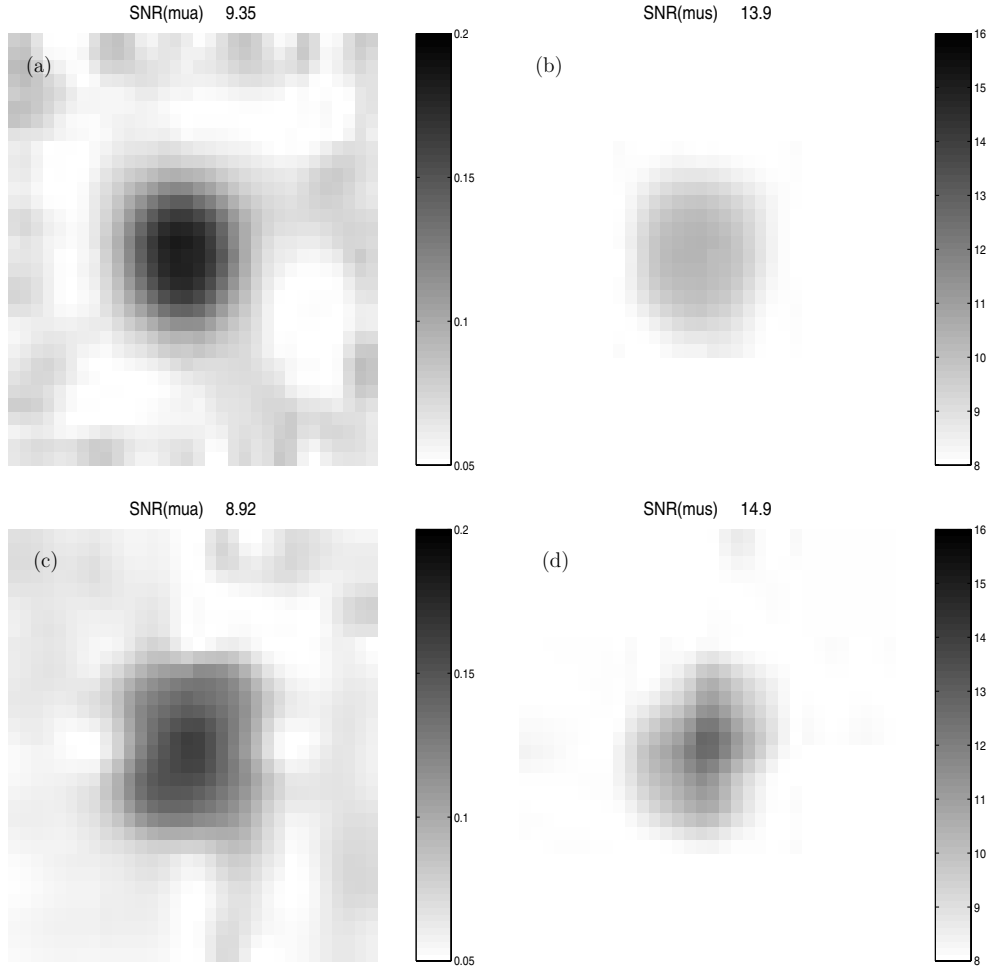


Figure 6. The simultaneous reconstruction results of the absorption and reduced scattering coefficients shown in figures 5(a)–(b). (a),(b): the simultaneous reconstruction of the absorption and reduced scattering coefficients by using the non-DD method after 6.780×10^{10} number of floating point operations with $\text{SNR}(\mu_a) = 9.346$ and $\text{SNR}(\mu'_s) = 13.935$. (c),(d): the simultaneous reconstruction of the absorption and reduced scattering coefficients by using TMSDM after 2.459×10^{10} number of floating point operations, with $\text{SNR}(\mu_a) = 8.920$ and $\text{SNR}(\mu'_s) = 14.899$.

Figures 3(c)–(d) and figures 4(c)–(d) show the value of the objective functional and the SNR versus the number of floating point operations. Figures 3(e), 4(e) and figures 3(f), 4(f) show the reconstructed images using non-DD and TMSDM methods, respectively.

Figures 3–4(c) show that at a given number of floating point operations, TMSDM achieves a lower objective functional value as compared to the non-DD method. Similarly, figures 3–4(d) show that at a given number of floating point operations, TMSDM achieves a higher SNR value.

For the μ'_a -only imaging, the reconstructed images shown in figures 3(e)–(f) indicate that TMSDM provides qualitatively and quantitatively better results as compared to the non-DD method. Note that the reconstructed μ_a image using TMSDM was obtained after 8.561×10^9

floating point operations, while the image using the non-DD method was obtained after 12.893×10^9 floating point operations. Similarly figures 4(e)–(f) show the reconstructed μ'_s images obtained after 13.165×10^9 and 8.373×10^9 floating point operations, by using the non-DD method and TMSDM, respectively. Similar to the μ_a -only imaging case, these images indicate that TMSDM outperforms the non-DD method.

4.2.2. Experiment 2. In this experiment, we test the performance of TMSDM in the simultaneous reconstruction of absorption and reduced scattering images and show the convergence of the algorithm experimentally.

Figure 5(a) shows an inclusion with $\mu_a = 0.20 \text{ cm}^{-1}$ in a background with $\mu_a = 0.05 \text{ cm}^{-1}$. Figure 5(b) shows the reduced scattering coefficient of the same medium, where the circular inclusion corresponding to an object with $\mu'_s = 16 \text{ cm}^{-1}$ is embedded in a background with $\mu'_s = 8 \text{ cm}^{-1}$. Figure 5(c) shows the domain decomposition with uniform discretization for the forward and inverse problems.

Figure 5(d) shows the value of the objective functional versus the number of floating point operations for both TMSDM and the non-DD method. We see that TMSDM achieves a lower objective functional value at a lower number of floating point operations.

Figures 5(e) and (f) show the SNR value achieved by TMSDM and the non-DD method versus the number of floating point operations, respectively for absorption and reduced scattering images. These images indicate that TMSDM outperforms the non-DD method, especially for the reduced scattering image. The reconstructed images shown in figure 6 are consistent with the performance numbers given in figures 5(d)–(e) and (f). We note that the images reconstructed by using TMSDM are obtained in 2.459×10^{10} number of floating point operations, while the images obtained by using the non-DD method require 6.780×10^{10} number of floating point operations.

5. Conclusion

In this work, we developed two-level overlapping domain decomposition algorithms to address the computational complexity of the forward and inverse problems associated with DOT imaging. We used the frequency-domain diffusion equation to model NIR light propagation. In order to address the ill-posed nature of the inverse problem, we used a nonlinear least-squares formulation with a general Tikhonov regularization term to recover both the absorption and scattering coefficients.

In the forward problem, we employed an overlapping domain decomposition algorithm with a two-grid preconditioner (TMODDM), and for the nonlinear inverse problem, we used an overlapping space decomposition algorithm with a coarse-level initiation (TMSDM). We proved the local convergence of the TMSDM method under the conditions that lead to the strict local convexity of the objective functional formulated for the inverse problem. For notational brevity, we described both DD algorithms for a 2D bounded optical domain and uniform discretization. Nevertheless, the extension of the algorithm for the 3D case and adaptive discretization is straightforward. This requires replacing the 2D finite elements with 3D finite elements and definition of 3D restriction (downsampling) and prolongation (upsampling) operators for the two-level algorithms.

Note that in our inverse problem solver, measurements from all source-detector pairs are used for each sub-domain. This accounts for the contribution of all sources to the boundary data. Therefore, this scheme does not impose any constraints on how the image domain is decomposed into sub-domains.

We analysed the computational complexity of both algorithms and demonstrated their performance in three different numerical simulations, where we considered simultaneous absorption and reduced scattering coefficient reconstruction as well as absorption only and reduced scattering only reconstructions. Our study shows that TMODDM provides lower relative error than the one-level MODDM for the same floating point operations and the relative error becomes much lower as the width of the overlapping region grows. Similarly, TMSDM provides lower objective functional values and higher SNR than the non-DD method for the same number of floating point operations, in all experiments including the simultaneous absorption and reduced scattering reconstruction. If parallel computers are used, the computational efficiency of TMSDM is expected to be further enhanced.

Finally, the local convergence properties of the algorithms do not change when they are implemented only for a region of interest (ROI). Therefore, if an ROI is identified either by *a priori* information provided by a secondary imaging modality such as magnetic resonance or x-ray; or by *a posteriori* information obtained from the coarse-level solution, the optical coefficients can be updated only in the sub-domains covering the ROI, providing further reduction in computational requirements.

Acknowledgments

This material is based upon work supported by NSF-BES-0353160, ONR-N00014-04-1-0694 and US Army Medical Research-W81XWH-04-1-0559. Any opinions, findings and conclusions or recommendations expressed in this material are those of the authors and do not necessarily reflect the views of the National Science Foundation. Various portions of this research were supported by the Center for Subsurface Sensing and Imaging Systems, under the Engineering Research Centers Program of the National Science Foundation (Award Number EEC-9986821), and Rensselaer Polytechnic Institute.

Appendix A. The proof of theorem 1

Lemma 1. Let $\mu = (\mu_a, \mu_s)$ and $\tilde{\mu} = \mu + \delta\mu$, $\delta\mu = (\delta\mu_a, \delta\mu_s)$. If $\|\delta\mu\|_{V_{Ne}^{\mu_a} \times V_{Ne}^{\mu_s}} \leq \frac{\epsilon + \alpha C_\Delta}{C_H C_J}$ for some $\epsilon > 0$, then F'' satisfies

$$\epsilon \|\delta\mu\|_{V_{Ne}^{\mu_a} \times V_{Ne}^{\mu_s}} \leq (\delta\mu)^t F''(\mu) (\delta\mu). \quad (\text{A.1})$$

Proof. Let G and \tilde{G} be Green's function for the optical coefficients μ and $\tilde{\mu}$, respectively. Then, we get

$$\begin{aligned} |b|_{l^2} &= \left| \log \left(\frac{1}{2a} \tilde{G}(i : j) \right) - \log \left(\frac{1}{2a} G(i : j) \right) \right|_{l^2} = \left| \log \left(\frac{|\tilde{G}(i : j)|}{|G(i : j)|} \right) \right|_{l^2} \\ &= \log \left(1 + \frac{|\mathcal{R}\tilde{G}(i : j)|}{|G(i : j)|} \right) \leq \frac{|\mathcal{R}\tilde{G}(i : j)|}{|G(i : j)|} \leq C_J \|\delta\mu\|_{V_{Ne}^{\mu_a} \times V_{Ne}^{\mu_s}}, \end{aligned}$$

where $\mathcal{R} = \mathcal{R}_1 + \mathcal{R}_2$ and

$$\begin{aligned} \mathcal{R}_1 \psi(r) &= \int_{\Omega} G(r, r') \psi(r') dr', \\ \mathcal{R}_2 \psi(r) &= \int_{\Omega} \nabla G(r, r') \cdot \nabla \psi(r') dr'. \end{aligned}$$

For the norm boundedness of \mathcal{R} , see [21].

Therefore, using (2.13), (3.34), and (A.2), we get

$$\delta\mu^t F'' \delta\mu = (J\delta\mu)^t (J\delta\mu) + \delta\mu^t H b \delta\mu + \alpha \delta\mu^t \Lambda'' \delta\mu \quad (\text{A.2})$$

$$\geq (J\delta\mu)^t (J\delta\mu) + \alpha \delta\mu^t \Lambda'' \delta\mu - C_H \delta\mu^t \delta\mu |b| \quad (\text{A.3})$$

$$\geq (\alpha C_\Lambda - C_H C_J |\delta\mu|) \delta\mu^t \delta\mu. \quad (\text{A.4})$$

Thus, we have proved the lemma. \square

The inequality (A.1) is called the local strong convexity. With this property and the theorem in [5], we will prove theorem 1.

Proof of theorem 1. The proof of theorem 1 is based on the proof in theorem 3.1 [5]. Let $\mu = (\mu_a, \mu'_s)$ and $\delta\mu = (\delta\mu_a, \delta\mu'_s)$. Let the restrictions of $V_{N_e}^y$, $y = \mu_a, \mu'_s$ to the non-overlapping and overlapping sub-domain Ω_p be $W_{N_e}^{p,y}$ and $V_{N_e}^{p,y}$ for $p = 1, \dots, d$, respectively, such that

$$W_{N_e}^{y,p} = \{x \in V_{N_e}^y | x = 0 \text{ on } \Omega \setminus \overline{\Omega_p}\}, \quad (\text{A.5})$$

$$V_{N_e}^{y,p} = \{x \in V_{N_e}^y | x = 0 \text{ on } \Omega \setminus \overline{\Omega_p^w}\}, \quad (\text{A.6})$$

where $y = \mu_a, \mu'_s$. Then, $W_{N_e}^{y,p}$, $p = 1, \dots, d$ are mutually disjoint, $W_{N_e}^{y,p} \subset V_{N_e}^{y,p}$, and

$$V_{N_e}^y = V_{N_e}^{y,1} + \dots + V_{N_e}^{y,d} = W_{N_e}^{y,1} + \dots + W_{N_e}^{y,d}.$$

Since we did not consider the coarse-level correction step in this theorem, we will use p and d instead of $p+1$ and $d+1$ in (3.31). Let μ^n be the solution of MSDM after n sweeps of sub-domain correction and $\mu^{n+\frac{p}{d}}$ be the solution obtained by updating μ^n with the solution estimates obtained on the sub-domain $\Omega_1^w, \dots, \Omega_p^w$ ($p \leq d$). Define

$$z_p^n = \begin{cases} \mu - \mu^{n+\frac{p}{d}} & \text{in } \Omega_p \\ (0, 0) & \text{in } \Omega \setminus \overline{\Omega_p} \end{cases}$$

and $e^{n+\frac{p}{d}} = \mu^{n+\frac{p}{d}} - \mu^{n+\frac{p-1}{d}} \in V_{N_e}^{\mu_a,p} \times V_{N_e}^{\mu'_s,p}$. Then, $z_p^n \in W_{N_e}^{\mu_a,p} \times W_{N_e}^{\mu'_s,p}$ and we obtain

$$\mu - \mu^n = \sum_{p=1}^d z_p^n, \quad \|\mu - \mu^n\|_{V_{N_e}^{\mu_a} \times V_{N_e}^{\mu'_s}} = \left(\sum_{p=1}^d \|z_p^n\|_{V_{N_e}^{\mu_a} \times V_{N_e}^{\mu'_s}}^2 \right)^{1/2} \quad (\text{A.7})$$

and

$$e^{n+\frac{p}{d}} = \underset{v_p \in V_{N_e}^{\mu_a,p} \times V_{N_e}^{\mu'_s,p}}{\operatorname{argmin}} F(\mu^{n+\frac{p-1}{d}} + v_p), \quad (\text{A.8})$$

(A.8) implies that

$$\langle F'(\mu^{n+\frac{p-1}{d}} + e^{n+\frac{p}{d}}), v_p - e^{n+\frac{p}{d}} \rangle \geq 0 \text{ for all } v_p \in V_{N_e}^{\mu_a,p} \times V_{N_e}^{\mu'_s,p} \quad (\text{A.9})$$

where $\langle \cdot, \cdot \rangle$ is l^2 inner product in the space $V_{N_e}^{\mu_a,p} \times V_{N_e}^{\mu'_s,p}$. Using (A.1) and Taylor expansion for F , we get

$$F(w) - F(v) \geq \langle F'(v), w - v \rangle + \frac{\epsilon}{2} \|w - v\|_{V_{N_e}^{\mu_a} \times V_{N_e}^{\mu'_s}}^2, \quad (\text{A.10})$$

for all $v, w \in V_{N_e}^{\mu_a} \times V_{N_e}^{\mu'_s}$ such that $\|v - w\|_{V_{N_e}^{\mu_a} \times V_{N_e}^{\mu'_s}} \leq \frac{\epsilon + \alpha C_\Lambda}{C_F^2}$. Inserting $w = \mu^{n+\frac{p-1}{d}}$ and $v = \mu^{n+\frac{p}{d}}$ in (A.10) and using (A.9) with $v_p = 0$, we get

$$F(\mu^{n+\frac{p-1}{d}}) - F(\mu^{n+\frac{p}{d}}) \geq \frac{\epsilon}{2} \|e^{n+\frac{p}{d}}\|_{V_{N_e}^{\mu_a,p} \times V_{N_e}^{\mu'_s,p}}^2 \geq 0$$

and

$$\begin{aligned} F(\mu^n) - F(\mu^{n+1}) &\geq \sum_{p=1}^d (F(\mu^{n+\frac{p-1}{d}}) - F(\mu^{n+\frac{p}{d}})) \\ &\geq \frac{\epsilon}{2} \sum_{p=1}^d \|e^{n+\frac{p}{d}}\|_{V_{N_e}^{\mu_a, p} \times V_{N_e}^{\mu'_s, p}}^2 \geq 0. \end{aligned} \quad (\text{A.11})$$

Since $\mu = \operatorname{argmin}_{v \in V_{N_e}^{\mu_a} \times V_{N_e}^{\mu'_s}} F(v)$, we get

$$\langle F'(\mu), v - \mu \rangle \geq 0 \text{ for all } v \in V_{N_e}^{\mu_a} \times V_{N_e}^{\mu'_s}, \quad (\text{A.12})$$

as in (A.8). Inserting $w = \mu^n$ and $v = \mu$ into (A.10) and using (A.12), we get

$$\begin{aligned} F(\mu^n) - F(\mu) &= \langle F'(\mu), \mu^n - \mu \rangle + \frac{\epsilon}{2} \|\mu^n - \mu\|_{V_{N_e}^{\mu_a} \times V_{N_e}^{\mu'_s}}^2 \\ &\geq \frac{\epsilon}{2} \|\mu^n - \mu\|_{V_{N_e}^{\mu_a} \times V_{N_e}^{\mu'_s}}^2 \geq 0. \end{aligned} \quad (\text{A.13})$$

Finally, we obtain

$$\begin{aligned} 0 &\leq F(\mu^{n+1}) - F(\mu) \leq \langle F'(\mu^{n+1}), \mu^{n+1} - \mu \rangle \text{ (using (A.10))} \\ &= \left\langle F'(\mu^{n+1}), \sum_{p=1}^d e^{n+\frac{p}{d}} + \mu^n - \mu \right\rangle = \sum_{p=1}^d \langle F'(\mu^{n+1}), e^{n+\frac{p}{d}} - z_p^n \rangle \\ &\leq \sum_{p=1}^d \langle F'(\mu^{n+1}) - F'(\mu^{n+\frac{p}{d}}), e^{n+\frac{p}{d}} - z_p^n \rangle \text{ (using (A.9))} \\ &= \sum_{p=1}^d \sum_{l=p+1}^d \langle F'(\mu^{n+\frac{l}{d}}) - F'(\mu^{n+\frac{l-1}{d}}), e^{n+\frac{p}{d}} - z_p^n \rangle \\ &= \sum_{p=1}^d \sum_{l=p+1}^d \langle F''(y_l^n) e^{n+\frac{l}{d}}, e^{n+\frac{p}{d}} - z_p^n \rangle \end{aligned}$$

for some y_l^n which lies between $\mu^{n+\frac{l}{d}}$ and $\mu^{n+\frac{l-1}{d}}$

$$\begin{aligned} &\leq \epsilon \left(\sum_{l=1}^d \|e^{n+\frac{l}{d}}\|_{V_{N_e}^{\mu_a} \times V_{N_e}^{\mu'_s}}^2 \right)^{1/2} \left(\sum_{p=1}^d \|e^{n+\frac{p}{d}} - z_p^n\|_{V_{N_e}^{\mu_a} \times V_{N_e}^{\mu'_s}}^2 \right)^{1/2} \text{ (using (A.1))} \\ &\leq \epsilon \left[\sum_{l=1}^d \|e^{n+\frac{l}{d}}\|_{V_{N_e}^{\mu_a} \times V_{N_e}^{\mu'_s}}^2 + \left(\sum_{p=1}^d \|e^{n+\frac{p}{d}}\|_{V_{N_e}^{\mu_a} \times V_{N_e}^{\mu'_s}}^2 \right)^{1/2} \left(\sum_{p=1}^d \|z_p^n\|_{V_{N_e}^{\mu_a} \times V_{N_e}^{\mu'_s}}^2 \right)^{1/2} \right] \\ &\leq 2(F(\mu^n) - F(\mu^{n+1})) + 2\sqrt{F(\mu^n) - F(\mu^{n+1})}\sqrt{F(\mu^n) - F(\mu)} \\ &\quad \text{(using (A.7), (A.11) and (A.13)).} \end{aligned}$$

Let $d_n = F(\mu^n) - F(\mu)$, then the above equation and the Cauchy–Schwarz inequality implies

$$\begin{aligned} d_{n+1} &\leq 2(d_n - d_{n+1}) + 2\sqrt{d_n - d_{n+1}}\sqrt{d_n} \\ &\leq \left(2 + \frac{1}{2\eta}\right)(d_n - d_{n+1}) + 2\eta d_n, \end{aligned}$$

for all $\eta > 0$. Thus, we obtain

$$\frac{d_{n+1}}{d_n} \leq \frac{4\eta^2 + 4\eta + 1}{6\eta + 1}. \quad (\text{A.14})$$

The left-hand side of (A.14) takes minimum value $\frac{8}{9} < 1$ when $\eta = \frac{1}{6}$. Thus we have the following successive inequalities:

$$d_n \leq \frac{8}{9} d_{n-1} \leq \left(\frac{8}{9}\right)^2 d_{n-2} \leq \cdots \leq \left(\frac{8}{9}\right)^n d_0. \quad (\text{A.15})$$

Using the mean-value theorem, (2.13a), (3.32), (3.34a) and (A.2), we can estimate d_0 as follows:

$$\begin{aligned} d_0 &= F(\mu^0) - F(\mu) \leq \sup_{0 < \theta < 1} |F'(\theta\mu^0 + (1-\theta)\mu)| |\mu - \mu_0| \\ &\leq C_J^2 |\mu - \mu_0|^2 + \alpha \tilde{C}_\Lambda |\mu - \mu_0| \leq \frac{\alpha^2 C_\Lambda^2}{C_H^2} + \frac{\alpha^2 C_\Lambda \tilde{C}_\Lambda}{C_H C_J}. \end{aligned} \quad (\text{A.16})$$

Using (A.15) and (A.16), we obtain (3.33). \square

References

- [1] Arridge S R 1999 Optical tomography in medical imaging *Inverse Problems* **15** R41–93
- [2] Arridge S R 2001 Methods for the inverse problem in optical tomography *Waves and Imaging Through Complex Media* ed P Sebbah and J-M Tualle (Dordrecht: Kluwer) pp 307–29
- [3] Arridge S R, Schweiger M and Delpy D T 1992 Iterative reconstruction of near-infrared absorption images *Inverse problems in Scattering and Imaging* ed M A Fiddy *Proc. SPIE* 1767 372–83
- [4] Badea L 1991 On the Schwarz alternation method with more than two subdomains for nonlinear monotone problems *SIAM J. Numer. Anal.* **28** 179–204
- [5] Badea L, Tai X-C and Wang J 2003 Convergence rate analysis of a multiplicative Schwarz method for variational inequalities *SIAM J. Numer. Anal.* **41** 1052–73
- [6] Badea L and Wang J 1999 An additive Schwarz method for variational inequalities *Math. Comput.* **69** 1341–54
- [7] Bazaraa M S, Sherali H D and Shetty C M 1993 *Nonlinear Programming, Theory and Algorithms* 2nd edn (New York: Wiley)
- [8] Boag A 2001 A fast multilevel domain decomposition algorithm for radar imaging *IEEE Trans. on Antennas Propag.* **49** 666–71
- [9] Boag A, Bresler Y and Michielssen E 2000 A multilevel domain decomposition algorithm for fast $O(n^2 \log n)$ reprojection of tomographic images *IEEE Trans. Image Process.* **9** 1573–82
- [10] Bramble J, Pasciak J, Wang J and Xu J 1991 Convergence estimates for product iterative methods with applications to domain decomposition *Math. Comp.* **57** 1–21
- [11] Briggs W L 1987 *A Multigrid Tutorial* (Philadelphia: SIAM)
- [12] Byrd R H, Schnabel R B and Shultz G A 1988 Approximate solution of the trust region problem by minimization over two-dimensional subspaces *Math. Program.* **40** 247–63
- [13] Cormick S F 1999 *Multilevel Adaptive Methods for Partial Differential Equations* (Philadelphia: SIAM)
- [14] Eppstein M J and Dougherty D E 1998 Optimal 3-d travel time tomography *Geophys.* **63** 1053–61
- [15] Eppstein M J, Dougherty D E, Hawrysz D J and Sevick-Muraca E M 2001 Three-dimensional Bayesian optical image reconstruction with domain decomposition *IEEE Trans. Med. Imaging* **20** 147–63
- [16] Guven M, Yazici B, Intes X and Chance B 2003 An adaptive multigrid algorithm for region of interest diffuse optical tomography *International Conference in Image Processing Proc. IEEE* **2** 823–6
- [17] Guven M, Yazici B, Intes X and Chance B 2003 An adaptive V-grid algorithm for diffuse optical tomography *Bioengineering Conference (Proc. of IEEE)* pp 95–96
- [18] Isakov V 1990 On uniqueness in the inverse transmission scattering problem *Commun. Partial Diff. Eqns.* **15** 1565–87
- [19] Kaipio J and Somersalo E 2005 *Statistical and Computational Inverse Problems (Applied Mathematical Sciences vol 160)* (New York: Springer)
- [20] Kwon K 2004 Identification of anisotropic anomalous region in inverse problems *Inverse Problems* **20** 1117–36
- [21] Kwon K and Yazıcı B Born expansion and Fréchet derivatives in diffuse optical tomography *in preparation*

See endnote 1

- [22] Kwon K and Sheen D 2002 Anisotropic inverse conductivity and scattering problems *Inverse Problems* **18** 745–56
- [23] Lai C-H, Ierotheou C S, Palansuriya C J and Pericleous K A 2001 Domain decomposition methods for welding problems *12th International Conference on Domain Decomposition Methods Proc. IEEE* **43** 411–20
- [24] Levenberg K 1944 A method of the solution of certain problems in least squares *Q. Appl. Math.* **2** 164–68
- [25] Marquardt D 1979 An algorithm for least-squares estimation of nonlinear parameters CAS-26: *IEEE Trans. Circuits and Systems (Sept., 1979)*
- [26] Oh S, Milstein A B, Bouman C A and Webb K J 2005 A general framework for nonlinear multigrid inversion *IEEE Trans. Image Process.* **14** 125–40
- [27] O’Leary M A, Boas D A, Chance B and Yodh A G 1995 Experimental images of heterogeneous turbid media by frequency-domain diffusing-photon tomography *Opt. Lett.* **20** 426–8
- [28] Palansuriya C J 1999 Domain decomposition based algorithms for inverse problems *PhD Thesis*, University of Greenwich
- [29] Palansuriya C J, Lai C H and Ierotheou C H 1998 A domain decomposition based algorithm for nonlinear 2D inverse heat conduction problems *Contemp. Math.* **218** 515–22
- [30] Pogue B W, Patterson M S, Jiang H and Paulsen K D 1995 Initial assessment of a simple system for frequency domain diffuse optical tomography *Phys. Med. Biol.* **40** 1709–29
- [31] Quarteroni A and Valli A 1999 *Domain Decomposition Methods for Partial Differential Equations* (Oxford: Oxford Science Publications)
- [32] Schwarz H A 1870 *Gesammelte Mathematische Abhandlungen* vol 2 (Berlin: Springer) pp 133–43
- [33] Smith B, Bjørstad P and Gropp W 1996 *Domain Decomposition, Parallel Multilevel Methods for Elliptic Partial Differential Equations* (Cambridge: Cambridge University Press)
- [34] Son I-Y, Guven M, Yazıcı B and Intes X 2003 A 2-level domain decomposition algorithm for inverse diffuse optical tomography *ICIP Proc. IEEE* **2** 823–6
- [35] Sylvester J and Uhlmann G 1987 A global uniqueness theorem for an inverse boundary value problem *Ann. math.* **125** 153–69
- [36] Tai X-C 2003 Rate of convergence for some constraint decomposition methods for nonlinear variational inequalities *Numer. Math.* **93** 755–86
- [37] Tai X-C, Frøen J, Espedal M S and Chan T F 1998 Overlapping domain decomposition and multigrid methods for inverse problems *Contemp. Math.* **218** 523–29
- [38] Tai X-C and Xu J 2001 Global and uniform convergence of subspace correction methods for some convex optimization problems *Math. Comput.* **7** 105–24
- [39] Trottenberg U, Oosterlee C and Schuller A 2001 *Multigrid* (New York: Academic)
- [40] Ye J C, Bouman C A, Millane R P and Webb K J 2001 Nonlinear multigrid algorithms for Bayesian optical diffusion tomography *IEEE Trans. Image Process.* **10** 909–22

Born expansion and Fréchet derivatives in diffuse optical tomography

Kiwoon Kwon[†] and Birsen Yazıcı^{† ‡}

[†] Electrical, Computer, and Systems Engineering, Rensselaer Polytechnic Institute,
110 8th St., Troy, NY 12180, USA

Abstract. The inverse DOT problem involves the inversion of the associated coefficient-to-measurement operator which maps the spatially varying optical coefficients of turbid medium to the boundary measurements. The inversion of the coefficient-to-measurement operator requires the computation of the Fréchet derivative of the coefficient-to-measurement operator. In this work, we derive the Fréchet derivatives of the coefficient-to-measurement operator on appropriate normed spaces, by making use of the relationship between the Fréchet derivatives and Born expansion. In this context, we first analyze the Born expansion, show the conditions which ensure the existence and convergence of the Born expansion, and compute the error in the m -th order Born approximation. Then, we derive the m -th order Fréchet derivatives of the coefficient-to-measurement operator and show the relationship of the Fréchet derivatives to the terms in the Born expansion.

[‡] corresponding author : yazici@ecse.rpi.edu

1. Introduction

Diffuse optical tomography (DOT) in near infrared involves determining the spatially resolved optical properties of a turbid medium from boundary measurements based on a photon propagation model. For deep tissue, frequency domain diffusion equation with Robin boundary condition constitutes a good model for photon propagation. Coefficients of the diffusion equation, namely the absorption and reduced scattering coefficients, represent the optical properties of the medium. As a result, the inverse DOT problem involves the inversion of the associated coefficient-to-measurement operator which maps the coefficients of the diffusion equation to the boundary measurements. The inversion of the coefficient-to-measurement operator calls for the computation of the Fréchet derivative of the coefficient-to-measurement operator. Thus, the Fréchet derivative of the coefficient-to-measurement operator is an integral part of the algorithms developed for DOT imaging.

In this work, we derive the m -th order Fréchet derivative of the coefficient-to-measurement operator in various normed spaces for both the absorption and reduced scattering coefficients. The Fréchet derivative of the coefficient-to-measurement operator is related to the Fréchet derivative of the coefficient-to-solution operator, which can be interpreted as the ratio of the perturbation in the photon density to an infinitesimal perturbation in the optical coefficients. Similarly, the Born expansion in DOT can be regarded as the Neumann series expansion of the perturbed photon density, given in terms of the unperturbed photon density and the perturbation in the optical coefficients. Hence, the Fréchet derivatives and the Born expansion are closely related. In this respect, we first analyze the Born expansion and investigate the conditions which ensure the convergence of the Born expansion. Next, we derive the Fréchet derivative of coefficient-to-solution operator, and then extend our results to the Fréchet derivative of the coefficient-to-measurement operator.

Before we give the technical details of our analysis and results, we will describe how our work differs from the previously reported studies in the general inverse scattering problem and particularly in DOT. In this context, we present an extensive literature survey on Born expansion and Fréchet derivatives, respectively, and give an outline of our analysis and findings regarding the Born expansion and Fréchet derivatives in DOT.

1.1. Born Expansion

In this section, we describe the related work and the contribution of our work in the area of Born expansion.

We consider the following aspects in our Born expansion analysis: First, we study the validity of the Born expansion by deriving bounds of the integral operators in the Born expansion. In this context, we first show the conditions to ensure the existence

of the Born expansion. Second, we show the restrictions on the optical coefficients that guarantee the convergence of the m -th order Born approximation and compute the error in the m -th order Born approximation. Third, we analyze the Born expansion not only for the perturbation of the absorption coefficient but also for the reduced scattering coefficient. Fourth, the analysis of the Born expansion is done for the n -dimension for any $n \geq 2$. Fifth, we summarize the existence and singular properties of the Robin function, which is the kernel of the integral operator for each term in the Born expansion. Note that we use the term *Robin function* for the Green's function of the diffusion equation to stress that the Green's function satisfies the (homogeneous) Robin boundary condition.

Studies on the Born expansion in the area of quantum scattering were initiated with the establishment of the Lippmann-Schwinger equation [9, 22]. The beam of particles of light can be modelled by the Schrödinger equation. Then, the scattered field due to the perturbation in the refractive index can be represented by the Lippmann-Schwinger equation, which is an implicit integral representation of the scattered field solution. Using the Lippmann-Schwinger equation recursively, the formal Neumann series expansion of the scattered field with respect to the incident wave gives the Born expansion. However, in quantum mechanics, there are relatively few systems which are of physical interest and/or can be solved exactly. Therefore, approximation methods such as Born approximation are widely used [4, 30, 32, 34]. We note that acoustic scattering can also be considered as a case of quantum scattering, since the Helmholtz equation is a special case of the Schrödinger equation.

The analysis, in this paper, for the validity of the Born expansion and the error in the Born expansion differs from the analysis in quantum and acoustic scattering [3, 4, 6, 17, 18, 23, 29, 30, 32, 34, 35, 37] in the following aspects: First, in these studies, the scattered wave is considered in an unbounded domain with spatially constant background properties of interest. Thus, the associated Green's function is explicitly known. However, we consider the Robin boundary condition for arbitrary bounded domains and spatially varying background optical coefficients. Therefore, the existence, singularities, and other properties of the Robin function are not known a priori. Although the Green's function of the diffusion equation in specific geometries with specific optical coefficients is known analytically [24, 25, 26, 27], to the best of our knowledge, studies on the existence and singularities of the Robin function for arbitrary geometries in which the Robin function is not known analytically, have not been reported. Thus, we study the singularity properties of the Robin function using [5, 36], based on the definition of the Robin function given in [28]. Second, in quantum and acoustic scattering theory, only the perturbation in the refractive index, which corresponds to the absorption coefficient in DOT, has been considered. In this work, we consider the perturbation with respect to both the absorption and reduced scattering

coefficients. We note that the analysis of the Born expansion for the reduced scattering coefficient requires more sophisticated mathematical machinery as compared to the analysis of the Born expansion for the absorption coefficient. This complication results from the presence of the gradients of the Robin function and the unperturbed photon density in the Born expansion for the reduced scattering coefficient. Third, we establish a relationship between the Born expansion and the Fréchet derivatives of the coefficient-to-solution operator.

1.2. Fréchet derivative

In this section, we describe the related work and the contribution of our paper in the area of Fréchet derivatives.

A number of studies on the derivation of the Fréchet derivatives have been reported in inverse acoustic scattering problem [3, 11, 16, 31] and in electrical impedance tomography [12, 13]. In these studies, Fréchet derivatives are either given by the solution of partial differential equations using weak formulation [3, 11, 12, 16] or by the solution of integral equation systems [13, 31]. Although these studies, for example [3], is potentially applicable to DOT, most researchers in DOT use the perturbation method and the first order Born approximation to approximate the first order Fréchet derivative [2]. The derivation of the first order Fréchet derivative is straightforward; however the higher order terms in the Born expansion are usually discarded regardless of the relative magnitude of the higher order terms with respect to the first order terms. Ye et. al [38] derived the Fréchet derivative of the coefficient-to-measurement operator using the perturbation method without using the first-order Born approximation. However, in that work, the Robin function is assumed to be H^1 bounded, which is not valid. In contrast, in our work, we showed and used the argument that the convolution of the Robin function and any H^1 function is H^1 bounded [5, 36]. Dierkes et. al [7] derived the first order Fréchet derivative for DOT, where a Dirichlet boundary problem with zero source is considered for the derivation, which is different from the model used in this paper.

In this paper, we first derive the Fréchet derivatives of the coefficient-to-solution operator, then we obtain the Fréchet derivatives of the coefficient-to-measurement operator by change of variables. The approach followed in deriving the Fréchet derivatives in this paper differs from the approaches in [2, 3, 7, 11, 12, 13, 16, 31, 38] in the following aspects: First, we compute the Fréchet derivatives of any order. Second, we use various normed spaces for the definition of the Fréchet derivatives, such as Lebesgue space L^p , $1 \leq p \leq \infty$, the first order Sobolev space W^1 , $1 \leq p \leq \infty$, and the weighted Sobolev space $W_{r,\log}^{0,\infty}$ for two dimension and $W_{r,2}^{0,\infty}$ for dimension higher than 2, where r is a point in the domain of interest. Third, we consider both the

absorption and the reduced scattering coefficients for the derivation of the Fréchet derivatives. Fourth, we show that the m -th order Fréchet derivatives are equal to the m -th order terms in the Born expansion up to constant multiples, whereas other approaches [3, 7, 11, 12, 13, 16, 31], do not provide the higher order derivatives. Even though the approaches in [3, 7, 11, 12, 13, 16, 31] can be used to derive the higher order derivatives, the approach presented in this paper has several advantages over the previous approaches: First, we compute the m -th order Fréchet derivatives, which can not be easily derived by the previous approaches, by showing that they are equal to $m!$ times the m -th term in the Born expansion. Although Born expansion is well-known in quantum and acoustic scattering and DOT [3, 6, 17, 18, 23, 25, 29, 35, 37], to the best of our knowledge, there has not been a study to relate the higher order Fréchet derivatives to the terms in Born expansion. Note that the inclusion of the higher order Fréchet derivatives improves the resolution of the reconstructed optical coefficients of DOT [25] and the bounds of the higher order Fréchet derivatives can be utilized in the analysis of the numerical DOT reconstruction algorithms [21]. Second, the recursive structure of the Born expansion makes it possible to bound the m -th order Fréchet derivative in a variety of normed spaces by the m -th multiple of the bound of the first order Fréchet derivative.

The rest of our paper is organized as follows: In section 2, we provide a mathematical formulation of DOT. The definition, existence, and singular properties of the Robin function are given in Section 3. The validity of the Born expansion and the error analysis due to the m -th order Born approximation is given in Section 4. In Section 5, we show that the Fréchet derivatives of coefficient-to-solution operator are given by the terms in the Born expansion. Section 6 summarizes our results and conclusion. The paper concludes with two appendices providing proofs for Lemmas 3.3 and 4.6.

2. Photon Diffusion Equation in Frequency Domain

We model the propagation of light in bounded turbid media by the photon diffusion equation with Robin boundary condition. In the frequency domain, the photon diffusion equation is given by:

$$-\nabla \cdot (\kappa \nabla \Phi) + \left(\mu_a + \frac{i\omega}{c}\right) \Phi = q \quad \text{in } \Omega \quad (2.1a)$$

$$\Phi + 2a\nu \cdot (\kappa \nabla \Phi) = 0 \quad \text{on } \partial\Omega \quad (2.1b)$$

where Ω is a Lipschitz domain in \mathbb{R}^n , $n = 2, \dots$, $\partial\Omega$ is its boundary, c is the speed of light, ω is the angular frequency of the source q , ν is the unit outward normal vector on the boundary, Φ is the photon density, and μ_a, μ'_s , and $\kappa = \frac{1}{3(\mu_a + \mu'_s)}$ are the absorption,

reduced scattering, and diffusion coefficients, respectively, and the constant a accounts for the the refraction index mismatch at the boundary, where we assume a is a constant and κ, μ_a, μ'_s are scalar functions satisfying

$$0 < L \leq \kappa, \mu_a, \mu'_s, a \leq U. \quad (2.2)$$

for some positive constants L and U .

Let us define the partial differential operators \mathcal{M} and \mathcal{N} defined on the function space on $H^1(\Omega)$ and $H^{1/2}(\partial\Omega)$, respectively, as follows:

$$\mathcal{M}\Psi = -\nabla \cdot (\kappa \nabla \Psi) + (\mu_a + \frac{i\omega}{c})\Psi \text{ for } \Psi \in H^1(\Omega), \quad (2.3a)$$

$$\mathcal{N}\Upsilon = \Upsilon + 2a\nu \cdot (\kappa \nabla \Upsilon) \text{ for } \Upsilon \in H^{1/2}(\partial\Omega). \quad (2.3b)$$

Then, (2.1) is represented by

$$\mathcal{M}\Phi = q \text{ in } \Omega \quad (2.4a)$$

$$\mathcal{N}\Phi = 0 \text{ in } \partial\Omega. \quad (2.4b)$$

If the partial differential operator is with respect to r , we will use the notation $\mathcal{M}_r, \mathcal{N}_r$ along with \mathcal{M} and \mathcal{N} .

In the following, we show the existence and uniqueness of the weak solution of (2.1).

Proposition 2.1 Let $q \in H^{-1}(\Omega)$. Then there is a unique weak solution $\Phi \in H^1(\Omega)$ satisfying (2.1).

Proof By multiplying both sides of (2.1a) with the complex conjugate \bar{v} of $v \in H^1(\Omega)$, integrating over Ω , and using integration by parts and (2.1b), we get the following weak formulation:

$$\begin{aligned} b(\Phi, v) &= l(v), \\ b(u, v) &= \int_{\Omega} \kappa \nabla u \cdot \nabla \bar{v} + \int_{\Omega} (\mu_a + \frac{i\omega}{c}) u \bar{v} + \frac{1}{2a} \int_{\partial\Omega} u \bar{v}, \\ l(v) &= \int_{\Omega} q \bar{v}, \end{aligned} \quad (2.5)$$

where \bar{c} is the complex conjugate for the complex number $c \in \mathbb{C}$. The sesquilinear form $b : H^1(\Omega) \times H^1(\Omega) \rightarrow \mathbb{C}$, for complex number space \mathbb{C} , satisfies

$$\Re(b(u, u)) \geq L \|\nabla u\|_{L^2(\Omega)}^2 \geq CL \|u\|_{H^1(\Omega)}^2, \quad (2.6a)$$

$$\begin{aligned} |b(u, v)| &\leq \left(U + \frac{\omega}{c}\right) \|u\|_{H^1(\Omega)} \|v\|_{H^1(\Omega)} + \frac{1}{2a} \|u\|_{L^2(\partial\Omega)} \|v\|_{L^2(\partial\Omega)} \\ &\leq \left(U + \frac{\omega}{c} + \frac{1}{2a}\right) \|u\|_{H^1(\Omega)} \|v\|_{H^1(\Omega)}, \end{aligned} \quad (2.6b)$$

$$|l(v)| \leq \|q\|_{H^{-1}(\Omega)} \|v\|_{H^1(\Omega)}, \quad (2.6c)$$

where $\Re(z)$ stands for the real part of complex valued function z . The last inequality in (2.6a) comes from Poincare lemma and the last inequality in (2.6b) comes from the trace formula. Using (2.6), there is a unique solution of (2.5) by Lax-Milgram lemma [10]. \square

In the rest of this paper, we will consider two cases i) $q \in H^{-1}(\Omega)$, and ii) q is a Dirac delta function, i.e. $q = \delta(\cdot - r_0), r_0 \in \Omega$. Proposition 2.1 shows that when $q \in H^{-1}(\Omega)$, we get $\Phi \in H^1(\Omega)$. The solution of (2.1) when $q = \delta(\cdot - r^0)$ is called the Robin function. Dirac Delta function is not contained in $H^{-1}(\Omega)$, since it is contained in $H^s(\Omega)$ if and only if $s < -\frac{n}{2}$ by [8]. Thus, we can not conclude from Proposition 2.1 that the Robin function is contained in $H^1(\Omega)$. Rigorous definitions of the Dirac Delta function and the Robin function require the use of distribution theory [14, 15]. To avoid technicalities involved in the distribution theory, we shall follow the concepts in [28] and use Levi functions to develop a rigorous definition of the Robin function.

3. The Robin function

The solution of (2.3a) when $q(\cdot) = \delta(\cdot - r^0)$ is called the Green, Neumann, or Robin function depending on whether the operator \mathcal{N} is $\Phi, \kappa \frac{\partial \Phi}{\partial \nu}$, or (2.3b), respectively. Sometimes Green, Neumann, and Robin functions are simply called the Green function without any regard to the boundary conditions. In this paper, however, we will use the term Robin function.

First, we introduce the following function H which is associated with the definition of Levi functions and the Robin function.

$$H(r, r') = \begin{cases} \frac{1}{(n-2)\omega_n \kappa(r')} |r - r'|^{2-n} & n \geq 3 \\ \frac{1}{\omega_2 \kappa(r')} \log\left(\frac{2d}{|r - r'|}\right) & n = 2, \end{cases} \quad (3.7)$$

where $r, r' \in \mathbb{R}^n$, ω_n is the hypersurface area of the unit sphere in \mathbb{R}^n , and $d = \sup_{r^1, r^2 \in \Omega} |r^1 - r^2|$. The function H satisfies

$$\nabla_r \cdot (\kappa(r') \nabla_r H(r, r')) = 0 \text{ for } r \in \Omega \setminus \{r'\}. \quad (3.8)$$

We will discuss other relevant properties of the function H at the end of Section 3.1, after introducing some function spaces containing $H(r, \cdot)$ and $H(\cdot, r)$.

3.1. Function spaces

In this section, we will introduce Sobolev spaces and weighted Sobolev spaces and show the boundedness of the function H , which is closely related to the boundedness of the Robin function. To simplify our notation, for the rest of this paper, we will drop Ω from the notation of the function spaces. For example, we will use L^1 instead of $L^1(\Omega)$ for

integrable functions on Ω . Let us define multi index $\beta = (\beta_1, \beta_2, \dots, \beta_n)$ for nonnegative integers $\beta_i, i = 1, \dots, n$, such that $|\beta| = \beta_1 + \beta_2 + \dots + \beta_n$, and $D^\beta \phi = \frac{\partial^{|\beta|}}{\partial^{\beta_1} r_1 \partial^{\beta_2} r_2 \dots \partial^{\beta_n} r_n}$.

In the following, we introduce the Sobolev spaces and the associated norms given by [1]:

$$\begin{aligned} L^p &= \{\phi \in L^1 \mid \|\phi\|_{L^p} := \left(\int_{\Omega} |\phi|^p \right)^{1/p} \leq \infty\}, \\ W^{k,p} &= \{\phi \in L^p \mid \|\phi\|_{W^{k,p}} := \left(\sum_{l=0}^k \sum_{|\beta|=l} \|D^\beta \phi\|_{L^p}^p \right)^{1/p} \leq \infty\} \end{aligned}$$

where $k = 1, 2, \dots, p \geq 1$ and

$$\begin{aligned} L^\infty &= \{\phi \in L^1 \mid \|\phi\|_{L^\infty} = \sup \phi \leq \infty\}, \\ W^{k,\infty} &= \{\phi \in L^\infty \mid \|\phi\|_{W^{k,\infty}} = \max_{l=0,\dots,k} \max_{|\beta|=l} \|D^\beta \phi\|_{L^\infty} \leq \infty\}. \end{aligned}$$

$W^{k,p}$ and $W^{k,\infty}$ are Banach spaces and $W^{k,\infty} \subset W^{k,p} \subset W^{k,q} \subset W^{k,1}$ for $p \geq q \geq 1$, since Ω is bounded. In particular, $W^{k,2}$ is a Hilbert space and we denote it by H^k and $W^{0,p} := L^p$ is called Lebesgue space.

Similarly, the weighted Sobolev spaces $W_{r_0,\alpha}^{k,\infty}$ and $W_{r_0,\log}^{k,\infty}$, for $r_0 \in \Omega$, a real number α , and the associated norms are given by:

$$W_{r_0,\alpha}^{k,\infty} = \{\phi \mid \|\phi\|_{W_{r_0,\alpha}^{k,\infty}} := \max_{l=0,\dots,k} \max_{|\beta|=l} \| |r - r_0|^{n-\alpha+l} D^\beta \phi \|_{L^\infty} < \infty\} \quad (3.9a)$$

$$\begin{aligned} W_{r_0,\log}^{k,\infty} &= \{\phi \mid \|\phi\|_{W_{r_0,\log}^{k,\infty}} \\ &:= \max \left(\max_{i=1,\dots,n} \left\| \frac{\partial \phi}{\partial r_i} \right\|_{W_{r_0,n}^{k-1,\infty}}, \left\| \frac{\phi(\cdot)}{\log(2d/|\cdot - r_0|)} \right\|_{L^\infty} \right) < \infty\} \quad (3.9b) \end{aligned}$$

Then, the following holds for $W_{r_0,\alpha}^{k,\infty}$, $W_{r_0,\log}^{k,\infty}$ and the Sobolev spaces:

$$\begin{aligned} W^{k,\infty} &\subset W_{r_0,\log}^{k,\infty}, \\ W_{r_0,\alpha}^{k,\infty} &\not\subset W^{k,1}, \text{ if } \alpha - k \leq 0, \\ W^{k,\infty} &\subset W_{r_0,\alpha}^{k,\infty} \subset W^{k,1}, \text{ if } \alpha - k > 0, \\ W^{k,\infty} &= W_{r_0,\alpha}^{k,\infty}, \text{ if } \alpha - k \geq n, \end{aligned}$$

for $k = 0, 1, 2, \dots$.

The following proposition shows that $W_{r_0,\alpha}^{k,\infty}$ and $W_{r_0,\log}^{k,\infty}$ are Banach spaces.

Proposition 3.1 $W_{r_0,\alpha}^{k,\infty}$ and $W_{r_0,\log}^{k,\infty}$ for $k = 0, 1, 2, \dots$ are Banach spaces with norms given in (3.9a) and (3.9b), respectively.

Proof We can verify that $\|\cdot\|_{W_{r_0,\alpha}^{k,\infty}}$ is a norm by using the definition of the norm $\|\cdot\|_{W^{k,\infty}}$ as follows: Let $\phi \in W_{r_0,\alpha}^{k,\infty}$, then $(r - r_0)^{n-\alpha+|\beta|} D^\beta \phi(r) \in L^\infty$ for $|\beta| \leq k$. Thus, triangular inequality in $W_{r_0,\alpha}^{k,\infty}$ comes from the triangular property in L^∞ . If $\|\phi\|_{W_{r_0,\alpha}^{k,\infty}} = 0$, then $\phi(r) = 0$ for $r \neq r_0$, which means that $\phi = 0$ almost everywhere in Ω . $\|c\phi\|_{W_{r_0,\alpha}^{k,\infty}} = |c| \|\phi\|_{W_{r_0,\alpha}^{k,\infty}}$ can be derived in a straightforward manner. Thus, $W_{r_0,\alpha}^{k,\infty}$ is a normed space. Assume that $\{\phi_p\}_{p=1,\dots}$ is a Cauchy sequence in $W_{r_0,\alpha}^{k,\infty}$, that is, $\{(r - r_0)^{n-\alpha} \phi_p\}_{p=1,\dots} \in W^{k,\infty}$. Since $W^{k,\infty}$ is a Banach space, there is a convergent subsequence $\{\phi_{p_l}\}_{l=1,\dots}$ and $\psi \in W^{k,\infty}$ such that $\|(r - r_0)^{n-\alpha} \phi_{p_l} - \psi\|_{W^{k,\infty}} \rightarrow 0$ as $l \rightarrow \infty$, i.e. $\|\phi_{p_l} - (r - r_0)^{\alpha-n} \psi\|_{W_{r_0,\alpha}^{k,\infty}} \rightarrow 0$ as $l \rightarrow \infty$. Since $(r - r_0)^{\alpha-n} \psi \in W_{r_0,\alpha}^{k,\infty}$, we have proved that $W_{r_0,\alpha}^{k,\infty}$ is complete, and thus is a Banach space. Using a similar argument, it is straightforward to prove that $W_{r_0,\log}^{k,\infty}$ are Banach spaces using $\log(\frac{2d}{|r-r_0|}) \geq \log 2$ for all $r, r_0 \in \Omega$. \square

For further information about the weighted Sobolev spaces, see [20]. Noting that $H(r', \cdot)$ has singularities only at r' with order $O(|\cdot - r'|^{2-n})$, we get the following properties of the function $H(\cdot, r')$:

$$H(\cdot, r') \in C^\infty(\mathbb{R}^n \setminus \{r'\}), \quad (3.10a)$$

$$H(\cdot, r') \in W^{k,p} \text{ if and only if } 1 \leq p < \frac{n}{n+k-2}, \quad (3.10b)$$

$$H(\cdot, r') \in W_{r',2}^{2,\infty}, \quad n = 3, 4, \dots, \quad (3.10c)$$

$$H(\cdot, r') \in W_{r',\log}^{2,\infty}, \quad n = 2, \quad (3.10d)$$

$$\frac{\partial H(\cdot, r')}{\partial r_i} \in W_{r',1}^{0,\infty}, \quad i = 1, \dots, n, \quad (3.10e)$$

$$\frac{\partial^2 H(\cdot, r')}{\partial r_i \partial r_j} \in W_{r',0}^{0,\infty}, \quad i, j = 1, \dots, n. \quad (3.10f)$$

Following (3.10b), we can write

$$H(\cdot, r') \in L^p \quad \text{if and only if } 1 \leq p < \infty \text{ when } n = 2 \quad (3.11a)$$

$$H(\cdot, r') \in W^{1,p} \quad \text{if and only if } 1 \leq p < 2 \text{ when } n = 2 \quad (3.11b)$$

$$H(\cdot, r') \in L^p \quad \text{if and only if } 1 \leq p < 3 \text{ when } n = 3 \quad (3.11c)$$

$$H(\cdot, r') \in W^{1,p} \quad \text{if and only if } 1 \leq p < \frac{3}{2} \text{ when } n = 3 \quad (3.11d)$$

$$H(\cdot, r') \notin W^{2,p} \quad \text{for } n = 2, 3, \dots \quad (3.11e)$$

By simple computation, we can obtain the following bounds for H instead of (3.10c)-(3.10f):

$$\|H(\cdot, r)\|_{W_{r,2}^{0,\infty}}, \|H(r, \cdot)\|_{W_{r,2}^{0,\infty}} \leq \frac{1}{(n-2)\omega_n L} \quad \text{if } n = 3, 4, \dots \quad (3.12a)$$

$$\|H(\cdot, r)\|_{W_{r, \log}^{0, \infty}}, \|H(r, \cdot)\|_{W_{r, \log}^{0, \infty}} \leq \frac{1}{\omega_2 L} \quad \text{if } n = 2 \quad (3.12b)$$

$$\left\| \frac{\partial H(\cdot, r')}{\partial r_i} \right\|_{W_{r', 1}^{0, \infty}}, \left\| \frac{\partial H(r', \cdot)}{\partial r_i} \right\|_{W_{r', 1}^{0, \infty}} \leq \frac{1}{\omega_n L} \quad (3.12c)$$

$$\left\| \frac{\partial^2 H(\cdot, r')}{\partial r_i \partial r_j} \right\|_{W_{r', 0}^{0, \infty}}, \left\| \frac{\partial^2 H(r', \cdot)}{\partial r_i \partial r_j} \right\|_{W_{r', 0}^{0, \infty}} \leq \frac{n}{\omega_n L} \quad (3.12d)$$

for all $i, j = 1, \dots, n$. Note that if κ is sufficiently smooth, (3.10) and (3.12) hold for $H(r, \cdot)$ as well.

3.2. Levi function and Robin function

In this section, we provide precise definitions of the Robin function and investigate the properties of the Robin function. To do that, the definitions and properties of the Levi function will be introduced following the approaches in [28].

Definition 3.2. [Levi function] A function $L(r, r'), r, r' \in \Omega$ is called a *Levi function* if $L(\cdot, r') \in C^2(\Omega \setminus \{r'\})$, and $L(\cdot, r') - H(\cdot, r') \in W_{r', 2+\lambda}^{2, \infty}$ for some constant $\lambda > 0$, where λ is the order of the Levi function.

Note that $H(r, r')$ is a Levi function, and $H(r', r)$ is also a Levi function of order 1 if $\kappa \in W^{2, \infty}$. Thus, if $L(r, r')$ is a Levi function of order λ , then $L(r', r)$ a Levi function of order $\min(\lambda, 1)$. Before introducing the properties of the Levi function in the following lemma, let us state some known results.

Let $K(r, \cdot) \in W_{r, \alpha}^{0, \infty}, \alpha > 0$ and

$$u(r) = \int_{\Omega} K(r, r') \phi(r') dr'.$$

Then the following facts are known:

- When $K(r, \cdot) \in W_{r, \alpha}^{0, \infty}, \alpha > 0$, there exists a constant $C_1 = C_1(\alpha, p, q)$ which depends on α, p and q such that the following holds [36]:

$$\|u\|_{L^q} \leq C_1(\alpha, p, q) \sup_{r \in \Omega} \|K(r, \cdot)\|_{W_{r, \alpha}^{0, \infty}} \|\phi\|_{L^p} \quad (3.13)$$

for $0 < \alpha < \frac{n}{p} \leq \alpha + \frac{n}{q}$.

If K is a Levi function, then we can take $\alpha \leq 2$ for $n \geq 3$ and $\alpha < 2$ for $n = 2$, and if K is a derivative of a Levi function, we can take $\alpha \leq 1$. However, if K is a second derivative of a Levi function, we must choose $\alpha \leq 0$ and hence can not use (3.13).

- When the kernel K is a Levi function and $p \leq \frac{n}{2}$, the maximum value of q in (3.13) is taken as follows :

$$\|u\|_{L^{\frac{np}{n-2p}}} \leq C_1(2, p) \sup_{r \in \Omega} \|K(r, \cdot)\|_{W_{r,2}^{0,\infty}} \|\phi\|_{L^p} \quad \text{for } p < \frac{n}{2} \quad (3.14a)$$

$$\|u\|_{L^{\frac{n}{\epsilon}}} \leq \tilde{C}_1(\epsilon) d^\epsilon \sup_{r \in \Omega} \|K(r, \cdot)\|_{W_{r,2-\epsilon}^{0,\infty}} \|\phi\|_{L^p} \quad \text{for } p = \frac{n}{2} \quad (3.14b)$$

by taking $\alpha = 2$ for $p < \frac{n}{2}$ and $\alpha = 2 - \epsilon$ for $p = \frac{n}{2}$ where ϵ is some constant between 0 and 2, $C_1(\alpha, p) = C_1(\alpha, p, \frac{np}{n-\alpha p})$, and $\tilde{C}_1(\epsilon) = C_1(\alpha - \epsilon, \frac{n}{2}, \frac{n}{\epsilon})$.

- When K is a Levi function and $p > \frac{n}{2}$, we have the following inequality:

$$\|u\|_{C^0} \leq C_2(p) \sup_{r \in \Omega} \|K(r, \cdot)\|_{W_{r,2}^{0,\infty}} \|\phi\|_{L^p} \quad \text{for } p > \frac{n}{2}, \quad (3.15)$$

where $C_2(p)$ is a constant depending on p [36].

- When $K = \frac{\partial^2 H}{\partial r_i \partial r_j}$, there exists a constant C_3 [5]:

$$\|u\|_{L^p} \leq \frac{C_3}{L} \|\phi\|_{L^p}. \quad (3.16)$$

Although the constants in this paper may depend on n , we will neglect this dependence on n unless it is needed. Using (3.13) and (3.16), we obtain the following lemma about the properties of the Levi function. Note that these are also the properties of the Robin function.

Lemma 3.3 Let $L(\cdot, r')$ be a Levi function of order $\lambda > 0$ and assume $\kappa \in C^{0,\lambda}$ and $\partial\Omega \in C^{1,\lambda}$. Let $\psi \in L^p, p \geq 1$ and v be given by

$$v(r) = \int_{\Omega} L(r, r') \psi(r') dr'. \quad (3.17)$$

Then, $\frac{\partial v}{\partial r_i}, i = 1, \dots, n$ are absolutely continuous on one-dimensional line parallel to r_i -axis, $\frac{\partial^2 v}{\partial r_i \partial r_j} \in L^p, i, j = 1, \dots, n$, and the following bounds hold:

$$\|v\|_{L^p} \leq C_1\left(\min\left(\frac{n}{p}, 2\right), p, p\right) \sup_{r \in \Omega} \|L(r, \cdot)\|_{W_{r,2}^{0,\infty}} \|\psi\|_{L^p} \quad n \geq 3, \quad (3.18a)$$

$$\|v\|_{L^p} \leq C_1\left(\min\left(\frac{2}{p}, 2\right) - \epsilon, p, p\right) \sup_{r \in \Omega} \|L(r, \cdot)\|_{W_{r,2}^{0,\infty}} \|\psi\|_{L^p} \quad n = 2, 0 < \epsilon < 2, \quad (3.18b)$$

$$\left\| \frac{\partial v}{\partial r_i} \right\|_{L^p} \leq C_1\left(\min\left(\frac{n}{p}, 1\right), p, p\right) \sup_{r' \in \Omega} \left\| \frac{\partial L(r', \cdot)}{\partial r_i} \right\|_{W_{r',2}^{0,\infty}} \|\psi\|_{L^p} \quad i = 1, \dots, n, \quad (3.18c)$$

$$\left\| \frac{\partial^2 v}{\partial r_i \partial r_j} \right\|_{L^p} \leq \left[C_1(\lambda, p, p) \sup_{r' \in \Omega} \left\| \frac{\partial^2 (L - H)(r', \cdot)}{\partial r_i \partial r_j} \right\| + \frac{C_3}{L} + \frac{1}{nL} \right] \|\psi\|_{L^p} \quad i, j = 1, \dots, n, \quad (3.18d)$$

where C_1 and C_2 are introduced in (3.13) and (3.15), respectively. Furthermore, the following equations hold:

$$\frac{\partial v}{\partial r_i}(r) = \int_{\Omega} \frac{\partial L}{\partial r_i}(r, r') \psi(r') dr', \quad (3.19a)$$

$$\frac{\partial^2 v}{\partial r_i \partial r_j}(r) = -\frac{1}{n\kappa(r)} \psi(r) + \lim_{\epsilon \rightarrow 0} \int_{\Omega \setminus \overline{B(x, \epsilon)}} \frac{\partial^2 L}{\partial r_i \partial r_j}(r, r') \psi(r') dr', \quad (3.19b)$$

$$\mathcal{M}_r v(r) = -\psi(r) + \int_{\Omega} \mathcal{M}_r L(r, r') \psi(r') dr'. \quad (3.19c)$$

If $v \in W^{2,p}$, then

$$\begin{aligned} v(r) &= \int_{\Omega} (v(r') \mathcal{M}_{r'} L(r, r') - \mathcal{M} v(r') L(r, r')) dr' \\ &\quad + \int_{\partial\Omega} (\mathcal{N} v(r') L(r, r') - v(r') \mathcal{N}_r L(r, r')) dS(r'). \end{aligned} \quad (3.20)$$

Proof : See Appendix A. \square

Definition 3.4 [Robin function] A Levi function R of order $\lambda > 0$ which is a solution of the equations

$$\mathcal{M}_r R(r, r') = 0 \text{ for } r \in \Omega \setminus \{r'\} \quad (3.21a)$$

$$\mathcal{N}_r R(r, r') = 0 \text{ for } r \in \partial\Omega \setminus \{r'\} \quad (3.21b)$$

is called a Robin function. Note that \mathcal{M}_r and \mathcal{N}_r are the complex conjugate operators for \mathcal{M}_r and \mathcal{N}_r , respectively.

A few existence theorems of Robin functions can be found in Section 19 and Section 22 in [28]. For the rest of the paper, we assume that the Robin function exists for Ω, κ , and μ_a . Note that if the Robin function exists, it is unique. A Levi function which satisfies (3.21a) but not necessarily (3.21b), is called the fundamental solution. If $\kappa \in C^{2,\lambda}$ and $\mu_a \in C^{0,\lambda}$, there exist fundamental solutions for \mathcal{M} in Ω by Theorem 19.VIII and Section 22 in [28]. However, even though fundamental solutions exist, these solutions are not unique. For example, H is a fundamental solution for (2.1) when $\mu_a = 0$, $\omega = 0$, and κ is a constant.

In the following, we investigate the properties of the Robin function.

Lemma 3.5 Let $R(\cdot, r')$ be a Robin function of order $\lambda > 0$, $\kappa \in C^{0,\lambda}$, and $\partial\Omega \in C^{1,\lambda}$. Let $\psi \in L^p$, $p \geq 1$, and v be given by

$$v(r) = \int_{\Omega} R(r, r') \psi(r') dr'. \quad (3.22)$$

Then (3.18), (3.19), and (3.20) hold replacing the Levi function L with the Robin function R . Furthermore, we get the following equations for v with the Robin function as the kernel:

$$\mathcal{M}_r v(r) = -\psi(r), \quad (3.23a)$$

$$v(r) = -\int_{\Omega} R(r, r') \mathcal{M} v(r') dr' + \int_{\partial\Omega} R(r, r') \mathcal{N} v(r') dS(r'),$$

$$\text{if } v \in W^{2,p}, \quad (3.23b)$$

$$v(r) = \int_{\Omega} R(r, r') q(r') dr' \quad \text{if } v \text{ satisfies (2.4) and } q \in L^p, \quad (3.23c)$$

$$R(r, r') = \overline{R(r', r)}. \quad (3.23d)$$

Proof (3.18), (3.19), and (3.20) hold because a Robin function is also a Levi function. (3.23a) is derived by using the definition of the Robin function and (3.19c). Using (3.20), we derive (3.23b) and (3.23c). (3.23d) is induced from the fact that the adjoint operator of \mathcal{M} is the complex conjugate of \mathcal{M} and Theorem 10.I. in [28]. \square

4. Born expansion

In this section, we first define the Born expansion in the normed spaces introduced in Section 3.1 and discuss the validity of the Born expansion. Next, we compute the error in the m -th order Born approximation using the inequalities developed in Section 3.2. In Section 4.1, we analyze the Born expansion when both the absorption and the diffusion coefficients are perturbed. Similar analysis is applied to the Born expansion when both the absorption and reduced scattering coefficient are perturbed. In Section 4.2., we analyze the Born expansion when the diffusion coefficient is fixed and only the absorption coefficient is perturbed.

Assume that (κ, μ_a) is changed into $(\tilde{\kappa}, \tilde{\mu}_a)$, and let $\delta\kappa = \tilde{\kappa} - \kappa$, $\delta\mu_a = \tilde{\mu}_a - \mu_a$, and $\delta\kappa = 0$ in some neighborhood of $\partial\Omega$. Let the solution of (2.1) for the optical coefficients $(\tilde{\kappa}, \tilde{\mu}_a)$ be $\tilde{\Phi}$ such that

$$-\nabla \cdot (\tilde{\kappa} \nabla \tilde{\Phi}) + (\tilde{\mu}_a + \frac{i\omega}{c}) \tilde{\Phi} = q \quad \text{in } \Omega, \quad (4.24a)$$

$$\tilde{\Phi} + 2a\tilde{\kappa} \frac{\partial \tilde{\Phi}}{\partial \nu} = 0 \quad \text{on } \partial\Omega. \quad (4.24b)$$

Inserting $\tilde{\kappa} = \kappa + \delta\kappa$ and $\tilde{\mu}_a = \mu_a + \delta\mu_a$ into (4.24), we get

$$-\nabla \cdot (\kappa \nabla \tilde{\Phi}) + (\mu_a + \frac{i\omega}{c}) \tilde{\Phi} = q + \nabla \cdot (\delta\kappa \nabla \tilde{\Phi}) - \delta\mu_a \tilde{\Phi} \quad \text{in } \Omega, \quad (4.25a)$$

$$\tilde{\Phi} + 2a\kappa \frac{\partial \tilde{\Phi}}{\partial \nu} = 0 \quad \text{on } \partial\Omega. \quad (4.25b)$$

Using (3.23c), $\tilde{\Phi}$ can be represented by

$$\tilde{\Phi}(r) - \Phi(r) = (\mathcal{R}\tilde{\Phi})(r), \quad (4.26)$$

where

$$\begin{aligned} (\mathcal{R}\Psi)(r) &= \mathcal{R}(\delta\kappa, \delta\mu_a)\Psi(r) = (\mathcal{R}_1\Psi)(r) + (\mathcal{R}_2\Psi)(r), \\ (\mathcal{R}_1\Psi)(r) &= \mathcal{R}_1(\delta\mu_a)\Psi(r) = - \int_{\Omega} \delta\mu_a(r')R(r, r')\Psi(r')dr', \\ (\mathcal{R}_2\Psi)(r) &= \mathcal{R}_2(\delta\kappa)\Psi(r) = - \int_{\Omega} \delta\kappa(r')\nabla R(r, r')\nabla\Psi(r')dr'. \end{aligned}$$

Note that in the derivation of (4.26), (3.23c) was used. Thus, (4.26) holds when $\tilde{\Phi} \in L^p$. Since $H^1 \subset L^2$ and the Robin function is contained in L^p for all $p \geq 1$, ($n = 2$) and $1 \leq p < \frac{n}{n-2}$, ($n \geq 3$), where n is the space dimension, (4.26) holds at least for the Robin function and H^1 functions. Using (4.26) recursively, we obtain the formal Born expansion:

$$\tilde{\Phi} = \Phi^{(0)} + \Phi^{(1)} + \Phi^{(2)} + \dots + \Phi^{(m)} + \tilde{\Phi}^{(m+1)}, \quad (4.27)$$

where

$$\begin{aligned} \Phi^{(0)} &= \Phi, \\ \Phi^{(1)} &= \mathcal{R}\Phi \\ \Phi^{(2)} &= \mathcal{R}\mathcal{R}\Phi \\ &\dots \\ \Phi^{(m)} &= \mathcal{R}^m\Phi \\ \tilde{\Phi}^{(m+1)} &= \mathcal{R}^{m+1}\tilde{\Phi}. \end{aligned}$$

The formal expansion (4.27) exists if and only if $\mathcal{R}^k\Phi, k = 1, \dots, m$ is defined. We provide the following definition related with the expansion (4.27).

Definition 4.1[m-th order representation and infinite order representation with index M]

The integral operator \mathcal{R} has an m -th order representation

$$B_0 \rightarrow B_1 \rightarrow B_2 \rightarrow B_3 \rightarrow \dots \rightarrow B_m. \quad (4.28)$$

if there are normed spaces $B_k, k = 0, 1, \dots, m$ such that $\mathcal{R}(B_{k-1}) \subset B_k$ for all $k = 1, \dots, m$.

We call that the operator \mathcal{R} has an infinite order representation with an index M

$$B_0 \rightarrow B_1 \rightarrow B_2 \rightarrow B_3 \rightarrow \dots \rightarrow B_M \rightarrow B_M \rightarrow \dots \quad (4.29)$$

if there are $M + 1$ normed spaces B_0, B_1, \dots, B_M such that $\mathcal{R}(B_{k-1}) \subset B_k$ for all $k = 1, \dots, M$.

If \mathcal{R} has m -th order representation, we define $E^m\Phi$ and $F^m\Phi$ as follows:

$$E^m\Phi = \Phi^{(0)} + \Phi^{(1)} + \Phi^{(2)} + \dots + \Phi^{(m-1)} + \tilde{\Phi}^{(m)} \quad (4.30a)$$

$$F^m\Phi = \Phi^{(0)} + \Phi^{(1)} + \Phi^{(2)} + \dots + \Phi^{(m-1)} + \Phi^{(m)}. \quad (4.30b)$$

If the operator \mathcal{R} has m -th order representation, then

$$E^1 = E^2 = \dots = E^m, E^m\Phi = \tilde{\Phi}. \quad (4.31)$$

by (4.27). If \mathcal{R} has infinite order representation with an index M , then (4.31) holds for all $m \geq 1$. If we define $E^\infty\Phi$ as

$$E^\infty\Phi = \Phi^{(0)} + \Phi^{(1)} + \Phi^{(2)} + \dots + \Phi^{(m-1)} + \Phi^{(m)} + \dots, \quad (4.32)$$

then $E^\infty\Phi \in B_M$ and we can easily show that

$$E^\infty = E^1 = \dots = E^m = \dots, E^\infty\Phi = \tilde{\Phi} \quad (4.33)$$

Furthermore, if the operator \mathcal{R} has an infinite order representation, we have the following proposition:

Proposition 4.2 Assume that the operator \mathcal{R} has an infinite order representation with an index M . If $\{F^m\Phi\}_{m=M, M+1, \dots}$ converges, the limit is $E^\infty\Phi \in B_M$. The necessary and sufficient condition for $F^m\Phi, m = M, M+1, \dots$ to converge to $E^\infty\Phi$ is

$$\lim_{k \rightarrow \infty} \left\| \mathcal{R}^{M+k} \tilde{\Phi} \right\|_{B_M} = 0. \quad (4.34)$$

The sufficient condition for (4.34) is

$$\|\mathcal{R}\|_{B_M \rightarrow B_M} < 1. \quad (4.35)$$

Proof Since $E^\infty\Phi - F^m\Phi = E^{m+1}\Phi - F^m\Phi = \mathcal{R}^{m+1}\tilde{\Phi}$, (4.34) is the necessary and sufficient condition for $F^m\Phi$ to converge to $E^\infty\Phi$. If $\|\mathcal{R}\|_{B_M \rightarrow B_M} < 1$, then

$$\begin{aligned} \|\mathcal{R}^{M+k}\Phi\|_{B_M} &\leq \|\mathcal{R}^k\|_{B_M \rightarrow B_M} \|\mathcal{R}^M\Phi\|_{B_M} \\ &\leq \|\mathcal{R}\|_{B_M \rightarrow B_M}^k \|\mathcal{R}^M\Phi\|_{B_M} \rightarrow 0 \text{ as } k \rightarrow \infty. \end{aligned} \quad (4.36)$$

□

Definition 4.3 [m -th order Born approximation and (m -th order, infinite order) Born expansion] $F^m\Phi$ is called the m -th order Born approximation and $E^m\Phi, E^\infty\Phi$ are called the m -th order and infinite order Born expansion, respectively. $E^m\Phi, E^\infty\Phi$ is just called Born expansion, since they are equal by (4.33).

Using Proposition 4.2, we investigate the following questions about Born expansion and Born approximation:

- When does the infinite order Born expansion E^∞ exist? In other words, is there an infinite order representation with an index M for the operator \mathcal{R} such that

$$B_0 \rightarrow B_1 \rightarrow B_2 \rightarrow B_3 \rightarrow \cdots \rightarrow B_M \rightarrow B_M \rightarrow \cdots \quad (4.37)$$

as in (4.29).

- Assume that there exists an infinite order representation with an index M (4.37) for the operator \mathcal{R} . By Proposition 4.2, (4.34) and (4.35) are the necessary and sufficient condition and the sufficient condition, respectively, for the Born approximations F^m to converge to the Born expansion E^∞ . Then, what are the conditions on $\delta\mu_a$ and/or $\delta\kappa$ for the operator \mathcal{R} to satisfy (4.35)?
- Assume that F^m converges to E^∞ . Then, what is the error in the m -th order Born approximation ($m = 1, 2, \dots$), that is, what is the norm bound for $\tilde{\Phi}^{(m+1)} = E^\infty - F^m$?

Although it is possible to compute the error in the Born approximation when E^∞ does not exist or F^m does not converge to E^∞ , we will treat the case when E^∞ exists and F^m converges to E^∞ . In the following sections, we first relate \mathcal{R} to the infinite order representation, then we argue about the condition on the optical coefficients for the norm of \mathcal{R} to be less than 1. Finally, we compute the error in the m -th order Born approximation with respect to the Born expansion.

4.1. The Born expansion when both the diffusion and absorption coefficients are perturbed

In this section, we treat the Born expansion when both the diffusion and absorption coefficients are perturbed. By Proposition 4.2, we need to define the operator \mathcal{R} recursively to define the Born expansion, which requires the definition for $\nabla\mathcal{R}$. The kernel of the integral operator $\nabla\mathcal{R}_1$ is the derivative of Robin function which is a weakly singular kernel and contained in $W_{r_0,1}^{0,\infty}$. However, the kernel of $\nabla\mathcal{R}_2$ is the second derivative of Robin function which is a hyper singular kernel and is not integrable. Note that the treatment of integral operators with hyper singular kernels is more difficult as compared to the treatment of integral operators with weak singular kernels [19].

To do a quantitative analysis, we first define the following bounds for the Robin function

$$S(n) := \sup_{r \in \Omega} \|R(r, \cdot)\|_{W_{r,2}^{1,\infty}}, n \geq 3, \quad (4.38a)$$

$$S(n) := \sup_{r \in \Omega} \|R(r, \cdot)\|_{W_{r,\log}^{1,\infty}}, n = 2, \quad (4.38b)$$

$$T(n) := \sup_{r \in \Omega} \|(R - H)(r, \cdot)\|_{W_{r,2}^{2,\infty}}. \quad (4.38c)$$

Lemma 4.4 \mathcal{R}_1 and \mathcal{R}_2 are bounded with respect to $W^{1,p}$ norm:

$$\|\mathcal{R}_1\|_{W^{1,p} \rightarrow W^{1,p}} \leq C_4 \|\delta\mu_a\|_{L^\infty}, \quad (4.39a)$$

$$\|\mathcal{R}_2\|_{W^{1,p} \rightarrow W^{1,p}} \leq C_5 \|\delta\kappa\|_{L^\infty}, \quad (4.39b)$$

where

$$C_4 = S(n) \max \left(C_1(\min(\frac{n}{p}, 2), p, p), C_1(\min(\frac{n}{p}, 1), p, p) \right) \quad n \geq 3, \quad (4.40a)$$

$$C_4 = S(n) \max \left(C_1(2 - \epsilon, p, p), C_1(\min(\frac{2}{p}, 1), p, p) \right) \quad n = 2, 0 < \epsilon < 2 \quad (4.40b)$$

$$C_5 = C_1(\min(\frac{n}{p}, 1), p, p)S(n) + C_1(\lambda, p, p)T(n) + \frac{C_3 n^2}{L} + \frac{n}{L}. \quad (4.40c)$$

Proof Let $\psi \in W^{1,p}$, then by (3.18a), (3.18b), and (3.18c),

$$\left\| \int_{\Omega} R(r, r') \delta\mu_a(r') \psi(r') dr' \right\|_{L^p} \leq C_1(\min(n/p, 2), p, p) \|R(r, \cdot)\|_{L^p} \|\delta\mu_a\|_{L^\infty} \|\psi\|_{L^p} \quad n \geq 3, \quad (4.41a)$$

$$\left\| \int_{\Omega} R(r, r') \delta\mu_a(r') \psi(r') dr' \right\|_{L^p} \leq C_1(2/p - \epsilon, p, p) \|R(r, \cdot)\|_{L^p} \|\delta\mu_a\|_{L^\infty} \|\psi\|_{L^p} \quad n = 2, 0 < \epsilon < 2, \quad (4.41b)$$

$$\left\| \int_{\Omega} \frac{\partial R(r, r')}{\partial r_i} \delta\mu_a(r') \psi(r') dr' \right\|_{L^p} \leq C_1(\min(n/p, 1), p, p) \left\| \frac{\partial R(r, \cdot)}{\partial r_i} \right\|_{L^p} \|\delta\mu_a\|_{L^\infty} \|\psi\|_{L^p} \quad i = 1, \dots, n. \quad (4.41c)$$

(4.39a) is derived from (4.41) by defining C_4 as in (4.40a) and (4.40b). Using (3.18c), (3.18d), and (3.23d), we get

$$\begin{aligned} & \left\| \int_{\Omega} \frac{\partial R(r, r')}{\partial r'_i} \delta\kappa(r') \frac{\partial \psi(r')}{\partial r'_i} dr' \right\|_{L^p} = \left\| \int_{\Omega} \frac{\partial \bar{R}(r', r)}{\partial r'_i} \delta\kappa(r') \frac{\partial \psi(r')}{\partial r'_i} dr' \right\|_{L^p} \\ & \leq C_1(\min(n/p, 1), p, p) \left\| \frac{\partial R(r, \cdot)}{\partial r_i} \right\|_{L^p} \|\delta\kappa\|_{L^\infty} \|\psi\|_{W^{1,p}} \quad n \geq 3, i = 1, \dots, n, \end{aligned} \quad (4.42a)$$

$$\begin{aligned} & \left\| \int_{\Omega} \frac{\partial R(r, r')}{\partial r'_i} \delta\kappa(r') \frac{\partial \psi(r')}{\partial r'_i} dr' \right\|_{L^p} \leq C_1(2/p - \epsilon, p, p) \|R(r, \cdot)\|_{L^p} \|\delta\kappa\|_{L^\infty} \|\psi\|_{W^{1,p}} \\ & \quad n = 2, 0 < \epsilon < 2, i = 1, 2, \end{aligned} \quad (4.42b)$$

$$\begin{aligned} & \left\| \int_{\Omega} \frac{\partial^2 R(r, r')}{\partial r'_i \partial r'_j} \delta\kappa(r') \psi(r') dr' \right\|_{L^p} = \left\| \int_{\Omega} \frac{\partial^2 R(r, r')}{\partial r_i \partial r_j} \delta\kappa(r') \psi(r') dr' \right\|_{L^p} \\ & \leq \|\delta\kappa\|_{L^\infty} \|\psi\|_{W^{1,p}} \left(C_1(\min(\frac{n}{p}, 1), p, p)S(n) + C_1(\lambda, p, p)T(n) + \frac{C_3 n^2}{L} + \frac{n}{L} \right). \end{aligned} \quad (4.42c)$$

Using (4.42) and defining C_5 as in (4.40c), we get (4.39b). \square

Using Lemma 4.4, we state and prove the following results about Born expansion and Born approximation when both the absorption and reduced scattering coefficients are perturbed.

Theorem 4.5 The integral operator \mathcal{R} has an infinite order representation with the index $M = 1$ as follows:

$$W^{1,p} \rightarrow W^{1,p} \rightarrow W^{1,p} \rightarrow \dots \quad (4.43)$$

If

$$C_4 \|\delta\mu_a\|_\infty + C_5 \|\delta\kappa\|_\infty < 1 \quad (4.44)$$

holds, then $E^\infty \Phi$ exists for the representation given in (4.43) and the m -th order Born approximation $F^m \Phi$ converges to $E^\infty \Phi$ for $\Phi \in W^{1,p}$. Furthermore, the error between $\tilde{\Phi} = E^\infty \Phi$ and $F^{m-1} \Phi$ is given as follows:

$$\left\| \tilde{\Phi} - F^{m-1} \Phi \right\|_{W^{1,p}} \leq (C_4 \|\delta\mu_a\|_\infty + C_5 \|\delta\kappa\|_\infty)^m \left\| \tilde{\Phi} \right\|_{W^{1,p}}. \quad (4.45)$$

Proof From (4.39), we derive

$$\|\mathcal{R}\|_{W^{1,p} \rightarrow W^{1,p}} \leq C_4 \|\delta\mu_a\|_{L^\infty} + C_5 \|\delta\kappa\|_{L^\infty}. \quad (4.46)$$

Hence (4.43) holds and (4.44) is the sufficient condition for E^∞ to exist by Proposition 4.2. (4.45) holds using (4.46) and the following inequality:

$$\tilde{\Phi} - F^{m-1} \Phi = \tilde{\Phi}^{(m)} = \mathcal{R}^m \Phi.$$

\square

4.2. Born expansion when only the absorption coefficient is perturbed

In this section, we will study the Born expansion and the Born approximation when $\delta\kappa = 0$ and $\delta\mu_a \neq 0$. When $\delta\kappa = 0$, the analysis given in Theorem 4.5 holds. Furthermore, we can say more about the Born expansion. Since $\mathcal{R} = \mathcal{R}_1$, we do not need to treat the second or first derivative of Robin function as the kernel of the integral operator \mathcal{R} .

Before analyzing the Born expansion in the normed spaces in $L^p, p \geq 1$, L^∞ , $W_{r_0, \log}^{0, \infty}(n = 2)$, and $W_{r_0, 2}^{0, \infty}(n \geq 3)$ for $r_0 \in \Omega$, we first state some inequalities:

Lemma 4.6 Let $0 < \alpha_1, \alpha_2 < n$ and $r^1, r^2 \in \Omega$, then

$$i) \quad \int_{\Omega} \log(2d/|r^1 - r'|) dr' \leq (\log(2) + 1)\omega_2 d, \quad n = 2, \quad (4.47a)$$

$$ii) \quad \int_{\Omega} |r^1 - r'|^{\alpha_1 - n} dr' \leq \omega_n \frac{d^{\alpha_1}}{\alpha_1}, \quad (4.47b)$$

$$iii) \quad \int_{\Omega} \log(2d/|r^1 - r'|) \log(2d/|r^2 - r'|) dr' \leq C_6 \omega_2 d^2, \quad n = 2, \quad (4.47c)$$

$$iv) \quad \int_{\Omega} |r^1 - r'|^{\alpha_1 - n} |r' - r^2|^{\alpha_2 - n} dr', \\ \leq C_7(\alpha_1, \alpha_2) \omega_n |r^1 - r^2|^{\alpha_1 + \alpha_2 - n} \quad \text{if } \alpha_1 + \alpha_2 < n, \quad (4.47d)$$

$$\leq C_8(\alpha_1, \alpha_2) \omega_n \log(2d/|r^1 - r^2|) \quad \text{if } \alpha_1 + \alpha_2 = n, \quad (4.47e)$$

$$\leq C_7(\alpha_1, \alpha_2) \omega_n d^{\alpha_1 + \alpha_2 - n} \quad \text{if } \alpha_1 + \alpha_2 > n \quad (4.47f)$$

$$v) \quad \int_{\Omega} |r^1 - r'|^{\alpha_1 - n} \log(2d/|r' - r^2|) dr' \leq C_9(\alpha_1) \omega_n d^{\alpha_1}, \quad (4.47g)$$

where

$$C_6 \leq \frac{1}{4}(6(\log 2)^2 + 2 \log 2 \log 3 + \log 3 - \log 2 - 1) < 1, \\ C_7(\alpha_1, \alpha_2) = 2^{n - \alpha_1 - \alpha_2} \left[\frac{3^{n - \max(\alpha_1, \alpha_2)}}{n - \alpha_1 - \alpha_2} + \frac{1}{\alpha_1} + \frac{1}{\alpha_2} \right], \\ C_8(\alpha_1, \alpha_2) = \left[3^{n - \max(\alpha_1, \alpha_2)} + \frac{1}{\alpha_1 \log 2} + \frac{1}{\alpha_2 \log 2} \right], \\ C_9(\alpha_1) = \frac{\log 4}{\alpha_1 2^{\alpha_1}} + \frac{\log 4 + \frac{1}{n}}{n 2^{\alpha_1}} + \frac{\log 6 + \frac{1}{\alpha_1}}{\alpha_1}.$$

Proof See Appendix B. \square

To do a quantitative analysis, let us define the following bounds for the Robin function

$$U(n) := \sup_{r \in \Omega} \|R(r, \cdot)\|_{W_{r,2}^{0,\infty}}, n \geq 3 \quad (4.48a)$$

$$U(n) := \sup_{r \in \Omega} \|R(r, \cdot)\|_{W_{r,\log}^{0,\infty}}, n = 2 \quad (4.48b)$$

$$U(n, \epsilon) := \sup_{r \in \Omega} \|R(r, \cdot)\|_{W_{r,2-\epsilon}^{0,\infty}}, n \geq 3, 0 < \epsilon < 2. \quad (4.48c)$$

With the aid of Lemma 4.6, we are able to state and prove the following inequalities for the integral operator \mathcal{R}_1 .

Lemma 4.7 We have the following norm bounds for the integral operator \mathcal{R}_1 :

$$i) \quad \|\mathcal{R}_1\|_{L^p \rightarrow L^p} \leq C_1 \left(\min \left(\frac{n}{p}, 2 \right), p, p \right) U(n) \|\delta \mu_a\|_{L^\infty} \quad n \geq 3, \quad (4.49a)$$

$$i) \quad \|\mathcal{R}_1\|_{L^p \rightarrow L^p} \leq C_1 \left(\frac{2}{p} - \epsilon, p, p \right) U(n) \|\delta\mu_a\|_{L^\infty} \quad n = 2, 0 < \epsilon < 2, \quad (4.49b)$$

$$iii) \quad \|\mathcal{R}_1\|_{L^\infty \rightarrow L^\infty} \leq C_{10} \omega_n U(n) \|\delta\mu_a\|_{L^\infty}, \quad (4.49c)$$

$$iv) \quad \|\mathcal{R}_1\|_{W_{r,2}^{0,\infty} \rightarrow W_{r,2}^{0,\infty}} \leq C_7(2, 2) \omega_n U(n) \|\delta\mu_a\|_\infty \quad n = 3, 5, 6, \dots, \quad (4.49d)$$

$$v) \quad \|\mathcal{R}_1\|_{W_{r,2}^{0,\infty} \rightarrow W_{r,2}^{0,\infty}} \leq C_8(2, 2) \omega_4 U(4) \|\delta\mu_a\|_\infty \quad n = 4, \quad (4.49e)$$

$$vi) \quad \|\mathcal{R}_1\|_{W_{r,\log}^{0,\infty} \rightarrow W_{r,\log}^{0,\infty}} \leq C_6 \log 2 \omega_2 U(2) \|\delta\mu_a\|_\infty \quad n = 2, \quad (4.49f)$$

where the constant C_{10} is given by

$$C_{10} = (\log 2 + 1)d, \quad n = 2 \quad (4.50a)$$

$$C_{10} = \frac{d^2}{2}, \quad n \geq 3 \quad (4.50b)$$

Proof (4.49a) and (4.49c) result from (3.18a) and (3.18b), respectively. (4.49c) is derived from (4.47a) for two-dimension and (4.47b) for n -dimension ($n \geq 3$) with $\alpha_1 = 2$. (4.49d) is obtained by (4.47d) and (4.47f) and using $|r_1 - r_2| \leq d$ for all $r_1, r_2 \in \Omega$. Similarly, (4.49e) and (4.49d) are derived from (4.47e) and (4.47g), respectively. \square .

By using Lemma 4.7, we give the following theorem about Born expansion and Born approximation :

Theorem 4.8 The integral operator $\mathcal{R} = \mathcal{R}_1$ has the following infinite order representation with an index $M = 1$ such that

$$L^p \rightarrow L^p \rightarrow L^p \rightarrow L^p \rightarrow \dots, \quad p \geq 1, \quad (4.51a)$$

$$L^\infty \rightarrow L^\infty \rightarrow L^\infty \rightarrow L^\infty \rightarrow \dots, \quad (4.51b)$$

$$W_{r,2}^{0,\infty} \rightarrow W_{r,2}^{0,\infty} \rightarrow W_{r,2}^{0,\infty} \rightarrow \dots, \quad n \geq 3, \quad (4.51c)$$

$$W_{r,\log}^{0,\infty} \rightarrow W_{r,\log}^{0,\infty} \rightarrow W_{r,\log}^{0,\infty} \rightarrow W_{r,\log}^{0,\infty} \rightarrow \dots \quad n = 2. \quad (4.51d)$$

Given the normed space $B = L^p(p \geq 1), L^\infty, W_{r,2}^{0,\infty}$, or $W_{r,\log}^{0,\infty}$, define a constant $C_{11} = C_{11}(B)$ depending on the normed space B as follows:

$$C_{11} = C_{11}(B) = \begin{cases} C_1(\min(\frac{n}{p}, 2), p, p)U(n) & \text{if } B = L^p \text{ and } n \geq 3, \\ C_1(\frac{2}{p} - \epsilon, p, p)U(2) & \text{if } B = L^p, n = 2, \\ C_{10}\omega_n U(n) & \text{if } B = L^\infty, \\ C_7(2, 2)\omega_n U(n) & \text{if } B = W_{r,2}^{0,\infty} \text{ and } n = 3, 5, 6, \dots, \\ C_8(2, 2)\omega_4 U(4) & \text{if } B = W_{r,2}^{0,\infty} \text{ and } n = 4, \\ C_6 \log 2 \omega_2 U(2) & \text{if } B = W_{r,\log}^{0,\infty} \text{ and } n = 2, \end{cases}$$

where $0 < \epsilon < 2$ and $r \in \Omega$. If the following condition

$$\|\delta\mu_a\|_\infty < \frac{1}{C_{11}(B)} \quad (4.52)$$

holds, then $E^\infty \Phi$ exists for each representation given in (4.51) and the m -th order Born approximation $F^m \Phi$ converges to $E^\infty \Phi$ for $\Phi \in B$. Furthermore, the error between $\tilde{\Phi} = E^\infty \Phi$ and $F^{m-1} \Phi$ is given by:

$$\left\| \tilde{\Phi} - F^{m-1} \Phi \right\|_B \leq (C_{11}(B) \|\delta\mu_a\|_\infty)^m \left\| \tilde{\Phi} \right\|_B. \quad (4.53)$$

The proof of Theorem 4.8 is obtained by Proposition 4.2 and Lemma 4.7, which is similar to the proof of Theorem 4.5. In Theorem 4.5 and Theorem 4.8, the same normed space is used for the infinite order representations with an index $M = 1$. However, the following theorem is another kind of infinite order representation for the operator \mathcal{R} with an index $M \neq 1$.

Theorem 4.9 The operator \mathcal{R} has the following infinite order representations with index $M \geq 2$ and $B_M = C^0$, where C^0 is the normed space of continuous functions having the norm $\|\cdot\|_{L^\infty}$:

$$L^\infty \rightarrow C^0 \rightarrow C^0 \rightarrow C^0 \rightarrow C^0 \rightarrow C^0 \rightarrow \dots \quad \text{for } n = 2, 3, 4, \dots, \quad (4.54a)$$

$$L^{\frac{n}{2k}} \rightarrow L^{\frac{n}{2(k-1)}} \rightarrow \dots \rightarrow L^{n/2} \rightarrow L^{\frac{n}{\epsilon}} \rightarrow C^0 \rightarrow C^0 \rightarrow \dots$$

$$\text{if } 1 \leq p = \frac{n}{2k} \text{ and } k \text{ is an positive integer,} \quad (4.54b)$$

$$L^p \rightarrow L^{\frac{np}{n-2p}} \rightarrow \dots \rightarrow L^{\frac{np}{n-2lp}} \rightarrow C^0 \rightarrow C^0 \rightarrow \dots$$

$$\text{for } l = \left[\frac{n-2p}{2p} \right] \geq 0 \text{ if } 1 \leq p \neq \frac{n}{2k} \text{ and } k \text{ is an positive integer,} \quad (4.54c)$$

$$W_{r_0,2}^{0,\infty} \rightarrow W_{r_0,4}^{0,\infty} \rightarrow \dots \rightarrow W_{r_0,n-2}^{0,\infty} \rightarrow W_{r_0,\log}^{0,\infty} \rightarrow C^0 \rightarrow C^0 \rightarrow \dots$$

$$\text{for } n = 2, 4, 6, \dots, \quad (4.54d)$$

$$W_{r_0,2}^{0,\infty} \rightarrow W_{r_0,4}^{0,\infty} \rightarrow \dots \rightarrow W_{r_0,n-1}^{0,\infty} \rightarrow C^0 \rightarrow C^0 \rightarrow \dots \text{ for } n = 3, 5, 7, \dots \quad (4.54e)$$

Let the normed space $B = L^\infty, L^p (p \geq 1), W_{r_0,2}^{0,\infty} (n \geq 3), W_{r_0,\log}^{0,\infty} (n = 2)$. If the condition

$$\|\delta\mu_a\|_{L^\infty} < \frac{1}{C_{10}\omega_n U(n)} \quad (4.55)$$

holds, then $E^\infty \Phi$ exists for each representation given in (4.54) and $F^m \Phi$ converges to $E^\infty \Phi$ for $\Phi \in B$. The bounds for the error between the $(m-1)$ -th order Born approximation and $\tilde{\Phi} = E^\infty \Phi$ are given by:

$$i) \quad \left\| \tilde{\Phi} - F^{m-1} \Phi \right\|_{C^0} \leq (C_{10}\omega_n U(n) \|\delta\mu_a\|_{L^\infty})^m \left\| \tilde{\Phi} \right\|_{L^\infty}, \quad (4.56a)$$

$$ii) \quad \left\| \tilde{\Phi} - F^{m-1} \Phi \right\|_{L^{\frac{np}{n-2mp}}} \leq C_{12}(m, n, p) (U(n) \|\delta\mu_a\|_{L^\infty})^m \left\| \tilde{\Phi} \right\|_{L^p},$$

$$\text{if } m \leq \frac{n-2p}{2p} \quad \left(\frac{np}{n-2mp} \leq \frac{n}{2} \right). \quad (4.56b)$$

$$iii) \quad \left\| \tilde{\Phi} - F^{m-1} \Phi \right\|_{L^{\frac{n}{\epsilon}}} \leq C_{12}(m, n, p) C_{13}(\epsilon, n) (U(n) \|\delta\mu_a\|_{L^\infty})^m \left\| \tilde{\Phi} \right\|_{L^p},$$

$$\text{if } m-1 = \frac{n-2p}{2p} \text{ is an integer,} \quad (4.56c)$$

$$\begin{aligned} iv) \quad \left\| \tilde{\Phi} - F^{m-1}\Phi \right\|_{C^0} &\leq C_{12} \left(\frac{n-2p}{2p}, p, n \right) C_{13} C_2 \left(\frac{n}{\epsilon} \right) (C_{10}\omega_n)^{m-\frac{n-2p}{2p}-1} \\ &\quad \cdot (U(n) \|\delta\mu_a\|_{L^\infty})^m \left\| \tilde{\Phi} \right\|_{L^p}, \\ &\text{if } \frac{n-2p}{2p} \text{ is an integer and } m > \frac{n-2p}{2p}, \end{aligned} \quad (4.56d)$$

$$\begin{aligned} v) \quad \left\| \tilde{\Phi} - F^{m-1}\Phi \right\|_{C^0} &\leq C_{12} \left(\left[\frac{n-2p}{2p} \right], p, n \right) (C_{10}\omega_n)^{m-\left[\frac{n-2p}{2p} \right]} \\ &\quad \cdot (U(n) \|\delta\mu_a\|_{L^\infty})^m \left\| \tilde{\Phi} \right\|_{L^\infty}, \\ &\text{if } \frac{n-2p}{2p} \text{ is not an integer and } m > \frac{n-2p}{2p}, \end{aligned} \quad (4.56e)$$

$$\begin{aligned} vi) \quad \left\| \tilde{\Phi} - F^{m-1}\Phi \right\|_{W_{r_0, 2m+2}^{0, \infty}} &\leq \Pi_{i=1}^m C_7(2, 2i) (\omega_n U(n) \|\delta\mu_a\|_\infty)^m \left\| \tilde{\Phi} \right\|_{W_{r_0, 2}^{0, \infty}}, \\ &\text{if } 2m+2 < n, \end{aligned} \quad (4.56f)$$

$$\begin{aligned} vii) \quad \left\| \tilde{\Phi} - F^{m-1}\Phi \right\|_{W_{r_0}^{0, \infty}} &\leq \Pi_{i=1}^{m-1} C_7(2, 2i) C_8(2, n-2) (\omega_n U(n) \|\delta\mu_a\|_\infty)^m \left\| \tilde{\Phi} \right\|_{W_{r_0, 2}^{0, \infty}}, \\ &\text{if } 2m+2 = n, \end{aligned} \quad (4.56g)$$

$$\begin{aligned} viii) \quad \left\| \tilde{\Phi} - F^{m-1}\Phi \right\|_{C^0} &\leq \frac{C_6 d}{\log 2 + 1} ((\log 2 + 1) d \omega_2 U(n) \|\delta\mu_a\|_\infty)^m \left\| \tilde{\Phi} \right\|_{W_{r_0}^{0, \infty}}, \\ &\text{if } n = 2, \end{aligned} \quad (4.56h)$$

$$\begin{aligned} ix) \quad \left\| \tilde{\Phi} - F^{m-1}\Phi \right\|_{C^0} &\leq \Pi_{i=1}^{\frac{n-2}{2}} C_7(2, 2i) C_8(2, n-2) C_9(2) d^2 (C_{10}\omega_n)^{m-\frac{n}{2}} \\ &\quad \cdot (\omega_n U(n) \|\delta\mu_a\|_\infty)^m \left\| \tilde{\Phi} \right\|_{W_{r_0, 2}^{0, \infty}}, \\ &\text{if } n \text{ is even and } 2m+2 > n \geq 4, \end{aligned} \quad (4.56i)$$

$$\begin{aligned} x) \quad \left\| \tilde{\Phi} - F^{m-1}\Phi \right\|_{C^0} &\leq \Pi_{i=1}^{\frac{n-1}{2}} C_7(2, 2i) d (C_{10}\omega_n)^{m-\frac{n-1}{2}} (\omega_n U(n) \|\delta\mu_a\|_\infty)^m \left\| \tilde{\Phi} \right\|_{W_{r_0, 2}^{0, \infty}}, \\ &\text{if } n \text{ is odd and } 2m+2 > n, \end{aligned} \quad (4.56j)$$

where C_2 is defined in (3.15); C_6, C_7, C_8 , and C_9 are defined in Lemma 4.6; C_{10} is defined in Lemma 4.7; and the constants C_{12} and C_{13} are given by

$$\begin{aligned} C_{12}(m, p, n) &= \Pi_{i=1}^m C_1(2, \frac{np}{n-2ip}) \\ C_{13}(\epsilon, n) &= \tilde{C}_1(\epsilon) d^\epsilon \frac{U(n, \epsilon)}{U(n)}. \end{aligned}$$

Proof From (4.47a), (4.47b), (3.15), and using $L^\infty \subset L^p$ for all $p \geq 1$, we get (4.56a) through the sequence of image function spaces (4.54a). From (3.14), (3.15), and (4.56b),

we get (4.56b)-(4.56e) from (4.54b) and (4.54c). From (4.47c)-(4.47g) and (4.56b), we get (4.56f)-(4.56j) by (4.54d) and (4.54e). The sufficient condition (4.55) results from (4.49c). \square

Thus, by Theorem 4.8 and Theorem 4.9, we have investigated the three questions related to the Born expansion and the Born approximation when only the absorption coefficient is perturbed.

We now focus on the conditions (4.52) and (4.55). $C_6, C_7(2, 2)(n = 3, 5, 6, \dots), C_8(2, 2)(n = 4)$, and C_{10} can be estimated by

$$C_6 \leq 1, \quad (4.57a)$$

$$C_7(2, 2) \leq 2^{n-4} \left[\frac{3^{n-2}}{n-4} + 1 \right], \quad n = 3, 5, 6, 7, \dots, \quad (4.57b)$$

$$C_8(2, 2) \leq 9 + \frac{1}{\log 2} \leq 11, \quad n = 4, \quad (4.57c)$$

$$C_{10} \leq 1.7d, \quad n = 2, \quad (4.57d)$$

$$C_{10} \leq \frac{d^2}{2}, \quad n \geq 3. \quad (4.57e)$$

If we neglect the lower order term $R - H$, then the approximation of $U(n)$ is as follows:

$$U(n) \approx \sup_{r \in \Omega} |r - r_0|^{n-2} |H(r, r_0)| \leq \frac{1}{(n-2)\omega_n L}, \quad n \geq 3 \quad (4.58)$$

$$U(n) \approx \sup_{r \in \Omega} |H(r, r_0)| / \log(|r - r_0|/2d) \leq \frac{1}{\omega_n L}, \quad n = 2 \quad (4.59)$$

Using (4.57) and (4.58), the conditions (4.52) and (4.55) for the m -th order Born approximation to converge to the Born expansion can be changed as follows :

$$\|\delta\mu_a\|_{L^\infty} \leq \frac{L}{1.7d}, \quad n = 2 \text{ for (4.51b) and (4.54) }, \quad (4.60a)$$

$$\|\delta\mu_a\|_{L^\infty} \leq \frac{2(n-2)L}{d^2} \quad n \geq 3 \text{ for (4.51b) and (4.54) }, \quad (4.60b)$$

$$\|\delta\mu_a\|_{L^\infty} \leq \frac{(n-2)(n-4)L}{2^{n-4}(3^{n-2} + n - 4)} \quad n = 3, 5, 6, \dots, \text{ for (4.51c) }, \quad (4.60c)$$

$$\|\delta\mu_a\|_{L^\infty} \leq \frac{2L}{11} \quad n = 4, \text{ for (4.51c) }, \quad (4.60d)$$

$$\|\delta\mu_a\|_{L^\infty} \leq \frac{L}{\log 2} \quad n = 2, \text{ for (4.51d) }. \quad (4.60e)$$

Note that all conditions in (4.60) depend on L , which is the lower bound of κ . Given the bound of C_1 , a similar analysis can be obtained for the representation (4.51a) of the Born expansion.

5. The Fréchet derivatives

In this section, we derive the Fréchet derivatives of the coefficient-to-solution and the coefficient-to-measurement operators. We use the relationship between the Fréchet derivatives and the Born expansion. We consider the cases where the Born expansion has the infinite order representation with index $M = 1$ such that

$$B \rightarrow B \rightarrow B \rightarrow \dots \quad (5.61)$$

where $B = W^{1,p}$ when both the diffusion and absorption coefficients are perturbed (Theorem 4.5) and $B = L^p, L^\infty, W_{r,2}^{0,\infty}$, or $W_{r,\log}^{0,\infty}$ when only the absorption coefficient is perturbed (Theorem 4.8).

We first state the definition of the Fréchet derivative for operators defined on Banach spaces.

Let B_1 and B_2 be Banach spaces and $BL(B_1, B_2)$ be the Banach space of bounded linear operators from B_1 to B_2 with the norm

$$\|Q\| = \sup_{x \in B_1 \setminus \{0\}} \frac{\|Qx\|_{B_2}}{\|x\|_{B_1}}, Q \in BL(B_1, B_2). \quad (5.62)$$

Definition 5.1 [The (first order) Fréchet derivative] Let $P : S \subset B_1 \rightarrow B_2$ be an operator from a open set S of Banach space B_1 into a Banach space B_2 . Then, P is called Fréchet differentiable for $x \in S$, if there is a continuous linear operator $Q : B_1 \rightarrow B_2$ such that

$$\lim_{\|\delta x\|_{B_1} \rightarrow 0} \frac{\|P(x + \delta x) - [P(x) + Q(\delta x)]\|_{B_2}}{\|\delta x\|_{B_1}} = 0. \quad (5.63)$$

The linear operator Q is called the first order Fréchet derivative, or simply the Fréchet derivative of P and denoted by $P'(x)$.

Definition 5.2 [The second order Fréchet derivative] Let $P'(x)$ be the Fréchet derivative of $P : S \subset B_1 \rightarrow B_2$ for each $x \in S$. Then $P' : S \subset B_1 \rightarrow BL(B_1, B_2)$. If P' is Fréchet differentiable at x , we denote it by

$$P''(x) : B_1 \rightarrow BL(B_1, B_2), \quad (5.64)$$

and call it the second order Fréchet derivative or Hessian of P at x .

Definition 5.3 [The m -th order Fréchet derivative] Higher order Fréchet derivatives are defined recursively, for $m = 3, \dots$ by $P^{(m)}(x) : B_1 \rightarrow BL(B_1^{m-1}, B_2)$ such that

$$\lim_{\|\delta x\|_{B_1} \rightarrow 0} \frac{\|P^{(m-1)}(x + \delta x) - [P^{(m-1)}(x) + P^{(m)}(x)\delta x]\|_{BL(B_1^{m-2}, B_2)}}{\|\delta x\|_{B_1}} = 0, \quad (5.65)$$

where $BL(B_1^1, B_2) = BL(B_1, B_2)$ and $BL(B_1^m, B_2) = BL(B_1, BL(B_1^{m-1}, B_2))$.

We can also view $P^{(m)}(x)$ as a mapping from B_1^m , the Cartesian product of B_1 with itself m times, to B_2 . Let us denote the image of $P^{(m)}(x)$ at m -tuples $(\delta x_1, \delta x_2, \dots, \delta x_m) \in B_1^m$ by $P^{(m)}(x)[\delta x_1, \delta x_2, \dots, \delta x_m]$ and $P^{(m)}(x; \delta x) := P^{(m)}(x)[\delta x, \delta x, \dots, \delta x]$.

5.1. The Frechet derivatives of the coefficient-to-solution operator

Let us define the coefficient-to-solution operator $\Psi : G \rightarrow B$ such that $\Psi(x) = \Phi$, where $\Phi \in B$ is the solution of (2.1) and x, G, B are given by:

$$G = L^\infty \times L^\infty, \quad B = W^{1,p}, \text{ when } x = (\kappa, \mu_a), \quad (5.66a)$$

$$G = L^\infty, \quad B = W^{1,p}, \text{ when } x = \kappa \text{ and } \mu_a \text{ is fixed}, \quad (5.66b)$$

$$G = L^\infty, \quad B = L^p, L^\infty, W_{r,2}^{0,\infty}, \text{ or } W_{r,\log}^{0,\infty}, \quad (5.66c)$$

when $x = \mu_a$ and κ is fixed.

Let x be given. In Section 4, $\mathcal{R}^m = \mathcal{R}^m(\delta x)$ is treated as a bounded linear operator in $BL(B, B)$ mapping $\Phi \in B$ to $\mathcal{R}^m(\delta x)\Phi \in B$ with a given δx . However, in this section, we will interpret $\mathcal{R}^m = \mathcal{R}^m(\cdot)\Phi$ as an operator in $BL(G^m, B)$ from $(\delta x_1, \dots, \delta x_m) \in G^m$ with a given Φ such that

$$\mathcal{R}^m(\delta x_1, \delta x_2, \dots, \delta x_m)\Phi = \mathcal{R}(\delta x_1)\mathcal{R}(\delta x_2) \cdots \mathcal{R}(\delta x_m)\Phi. \quad (5.67)$$

Then, by a similar analysis as in Theorem 4.5 and Theorem 4.8, we can show that the operator $\mathcal{R}^m\Phi$ is bounded for the operator norm from G^m into B such that

$$\|\mathcal{R}^m[\delta x_1, \dots, \delta x_m]\Phi\|_{G^m \rightarrow B} \leq C_{14} \|\delta x_1\|_G \cdots \|\delta x_m\|_G \|\Phi\|_B. \quad (5.68)$$

where $C_{14} = \max(C_4, C_5), C_5$, and $C_{11}(B)$ depending on the case (5.66a), (5.66b), and (5.66c), respectively, by Theorem 4.5 and Theorem 4.8. Note that in the Born expansion, the m -th order term is given by $\mathcal{R}^m(\delta x)\Phi$.

Theorem 5.4. The m -th order Fréchet derivatives of the coefficient-to-solution operator Ψ are contained in $BL(G^m, B)$ and are given by

$$\frac{\partial^m \Psi}{\partial x^m} = m! \mathcal{R}^m \Phi \text{ when } x = (\kappa, \mu_a) \quad (5.69a)$$

$$\frac{\partial^m \Psi}{\partial \mu_a^k \kappa^{m-k}} = m! \mathcal{R}_1^k \mathcal{R}_2^{m-k} \Phi. \quad (5.69b)$$

Proof We will prove (5.69) first. Assume $x = (\kappa, \mu_a)$. Inserting $m = 2$ in (5.68), we get

$$\begin{aligned} \|\Psi(x + \delta x) - (\Psi(x) + \mathcal{R}(\delta x)\Phi)\|_B &= \|\tilde{\Phi} - (\Phi + \mathcal{R}(\delta x)\Phi)\|_B \\ &= \|\mathcal{R}^2(\delta x)\tilde{\Phi}\|_B \leq \|\tilde{\Phi}\|_B C_{14}^2 \|\delta x\|_G^2, \end{aligned} \quad (5.70)$$

for all $\delta x \in G$ and $\Phi \in B$. By the definition of the Fréchet derivative in (5.63), we get $\frac{\partial \Psi}{\partial x} = \mathcal{R}\Phi$. In this proof, we use $\mathcal{R}[x]$ instead of \mathcal{R} , when it is needed to stress that the Robin function, which is the kernel of the integral operator \mathcal{R} , depends on x .

Next, we will prove that $\frac{\partial^m \Psi}{\partial x^m} = m! \mathcal{R}^m \Phi$, $m \geq 2$, by induction. Let us assume $\frac{\partial^k \Psi}{\partial x^k} = k! \mathcal{R}^k \Phi$ for an integer $k \leq m$. Then by the definition given in (5.65)

$$\frac{\partial^{k-1} \Psi}{\partial x^{k-1}}(x + \delta x) = \frac{\partial^{k-1} \Psi}{\partial x^{k-1}}(x) + \frac{\partial^{k-1} \Psi}{\partial x^{k-1}} \delta x + o_{k-1}(\|\delta x\|_G) \quad (5.71)$$

or equivalently,

$$\mathcal{R}^{(k-1)}[x + \delta x]\Phi = \mathcal{R}^{(k-1)}[x]\Phi + k\mathcal{R}^{(k)}[x]\delta x\Phi + o_{k-1}(\|\delta x\|_G), \quad (5.72)$$

for all $k \leq m$. Here $\psi = o_{k-1}(\|\delta x\|_G)$ means that $\lim_{\|\delta x\|_G \rightarrow 0} \frac{\|\psi\|_{BL(G^{k-1}, W^1, p)}}{\|\delta x\|_G} = 0$. Then using (5.68) and (5.72)

$$\begin{aligned} \frac{\partial^{m-1} \Psi}{\partial x^{m-1}}(x + \delta x) &= (m-1)! \mathcal{R}^{m-1}[x + \delta x]\Phi \\ &= (m-1)! (\mathcal{R}[x] + \mathcal{R}^2[x]\delta x + o_1(\|\delta x\|_G)) \mathcal{R}^{m-2}[x + \delta x]\Phi \\ &= (m-1)! (\mathcal{R}[x] + \mathcal{R}^2[x]\delta x + o_1(\|\delta x\|_G)) \\ &\quad \cdot (\mathcal{R}^{m-2}[x]\Phi + (m-1)\mathcal{R}^{m-1}[x]\delta x\Phi + o_{m-2}(\|\delta x\|_G)) \\ &= (m-1)! \mathcal{R}^{m-1}[x]\Phi + m! \mathcal{R}^m[x]\delta x\Phi + o_m(\|\delta x\|_G) \\ &= \frac{\partial^{m-1} \Psi}{\partial x^{m-1}}(x) + m! \mathcal{R}^m[x]\delta x\Phi + o_m(\|\delta x\|_G). \end{aligned} \quad (5.73)$$

Using the definition of the higher order derivatives (5.65), we get $\frac{\partial^m \Psi}{\partial x^m}(x) = m! \mathcal{R}^m[x]\Phi$. Hence, by induction argument, we have proved (5.69a). With a similar argument and noting that \mathcal{R}_1 is independent of $\delta\kappa$ and that \mathcal{R}_2 is independent of $\delta\mu_a$, we prove (5.69b). \square

If P is m -times continuously differentiable on S , and $P^{(m)}(x)$ is integrable between any two points in S , then the Taylor's theorem holds: For any $x, x + \delta x \in S$, we have

$$P(x + \delta x) = P(x) + \sum_{i=1}^{m-1} \frac{P^{(i)}(x)}{i!} \delta x^i + E_m(x + \delta x, x; P), \quad (5.74)$$

where

$$\|E_m(x + \delta x, x; P)\|_{B_2} \leq \frac{\|\delta x\|_{B_1}^m}{m!} \sup_{\theta \in [0,1]} \|P^{(m)}(x + \theta\delta x)\|_{BL(B_1^{(m)}, B_2)}. \quad (5.75)$$

Although the statement and the proof are similar to the Taylor's theorem in Euclidean space, we must consider each term with respect to the operators between Banach spaces. For the proof of (5.74), see [33]. If another operator Q is m -times differentiable, $E_m(x + \delta x, x; Q) \leq C \|\delta x\|_{B_1}^m$, and $P(x) = Q(x)$, then we can show that

$$P^{(i)}(x) = Q^{(i)}(x), i = 0, \dots, m-1. \quad (5.76)$$

Let $T^m := P(x) + \sum_{i=1}^m \frac{P^{(i)}(x)}{i!} \delta x^i$ be the m -th order Taylor expansion. Then from Lemma 4.3 and (5.76), we conclude that the m -th order Born approximation is the same as the m -th order Taylor expansion, i.e. $T^m = F^m$. This fact can be used as another proof of Theorem 5.4.

5.2. The Fréchet derivatives of coefficient-to-measurement operator

In this section, we compute the Fréchet derivatives of the coefficient-to-measurement operator Γ .

Given the photon density function Φ , which is the solution of (2.1), different type of boundary data can be measured. Let f be any function from complex space \mathbb{C} to \mathbb{C} and let $\Gamma = f(\Psi)$. The Fréchet derivatives of the coefficient-to-measurement operator Γ can be computed using the Fréchet derivatives of the coefficient-to-solution operator Ψ by using change of variables as follows:

$$\begin{aligned} \Gamma' &= f'(\Psi)\Psi' = f'(\Psi)\mathcal{R}\Phi \\ \Gamma'' &= f''(\Psi)(\Psi')^2 + f'(\Psi)\Psi'' = f''(\Psi)(\mathcal{R}\Phi)^2 + 2f'(\Psi)\mathcal{R}^2\Phi \end{aligned}$$

and

$$f(\Psi)^{(m)} = \sum_{i=1}^m f^{(i)}(\Psi) A_{m,i}(\mathcal{R}\Phi, \mathcal{R}^2\Phi, \dots, \mathcal{R}^{(m)}\Phi), m \geq 3,$$

where $A_{m,i}$ is a polynomial of degree m and $A_{m,i}(x_1, \dots, x_m)$ is a linear combination of monomials $\Pi_{l=1}^m x_l^{j_l}$ with $\sum_{l=1}^m j_l = m$, if f is m times differentiable.

Most widely used functions for f are

$$f(x) = \Re(x) \quad (5.77a)$$

$$f(x) = \Re(\log x) \quad (5.77b)$$

for some complex number x . (5.77a) is called the Born measurement and (5.77b) is called Rytov measurement.

In the case of the Born measurements, $\Gamma^{(m)} = m!\Re(\mathcal{R}^m\Phi)$, and in the case of Rytov measurement, the first and second order Fréchet derivatives are given by

$$\Gamma' = \Re\left(\frac{\mathcal{R}\Phi}{\Phi}\right) \quad (5.78a)$$

$$\Gamma'' = \Re\left(\frac{-(\mathcal{R}\Phi)^2}{\Phi^2} + \frac{2\mathcal{R}^2\Phi}{\Phi}\right). \quad (5.78b)$$

In [21], we have proved the local convergence of a method which we call Two-level Multiplicative Space Decomposition Method for DOT image reconstruction. In the proof of the convergence, we have assumed that the second order Fréchet derivative of coefficient-to-measurement operator is bounded, when Rytov measurements are used. By using (5.70) and (5.78b), the second order Fréchet derivative is bounded by

$$\|\Gamma''\|_{G^2 \rightarrow W^{1,p}} \leq 3C_{14}^2. \quad (5.79)$$

6. Conclusion

In this paper, we derived the Born expansion and Frechet derivatives for the diffuse optical tomography for arbitrary domains with Robin type boundary conditions. To define valid Born expansion, we introduced sequences of appropriate normed spaces such as Lebesgue spaces, Sobolev spaces, and weighted Sobolev spaces. We derived sufficient conditions on the perturbation in the diffusion and absorption coefficients for the convergence of the Born expansion in n dimensions, ($n \geq 2$). We computed bounds for the error in the m -th order Born approximation. Next, we showed that the m -th order Frechet derivatives of the coefficient-to-solution operator is equal to the $m!$ times the m -th corresponding term in the Born expansion.

Although we only consider the boundary value problem (2.1) with Robin boundary conditions, the analysis introduced in this paper can be easily extended to the general second order elliptic partial differential equations with other boundary conditions.

Acknowledgments

This material is based upon work supported by ONR-N00014-04-1-0694, and US Army Medical Research-W81XWH-04-1-0559. Any opinions, findings, and conclusions or recommendations expressed in this material are those of the authors and do not necessarily reflect the views of the National Science Foundation. Various portions of this research were supported by the Center for Subsurface Sensing and Imaging Systems, under the Engineering Research Centers Program of the National Science Foundation (Award Number EEC-9986821), and Rensselaer Polytechnic Institute.

References

- [1] R. A. Adams. *Sobolev spaces*. Academic Press [A subsidiary of Harcourt Brace Jovanovich, Publishers], New York-London, 1975. Pure and Applied Mathematics, Vol. 65.
- [2] S. R. Arridge. Optical tomography in medical imaging. *Inverse Problems*, 15:R41–93, 1999.
- [3] G. Bao and P. Li. Inverse medium scattering for the Helmholtz equation at fixed frequency. *Inverse Problems*, 21(5):1621–1641, 2005.
- [4] D. R. Bates. *Quantum theory I. Elements*. Academic Press, 1961.

- [5] A. P. Calderon and A. Zygmund. On the existence of certain singular integrals. *Acta. Math.*, 88:85–139, 1952.
- [6] B. Chen and J. J. Stamnes. Validity of diffraction tomography based on the first born and the first rytov approximations. *Applied optics*, 37:2996–3006, 1998.
- [7] T. Dierkes, O. Dorn, F. Natterer, V. Palamodov, and H. Sielschott. Fréchet derivatives for some bilinear inverse problems. *SIAM journal on applied mathematics*, 62:2092–2113, 2002.
- [8] G. B. Folland. *Introduction to partial differential equations*. Princeton University Press, second edition, 1995.
- [9] M. Gell-Mann and M. L. Goldberger. The formal theory of scattering. *Physical Review*, 91:398–408, 1953.
- [10] D. Gilbarg and N. S. Trudinger. *Elliptic partial differential equations of second order*. Springer-Verlag, 1983.
- [11] F. Hettlich. Fréchet derivatives in inverse obstacle scattering. *Inverse Problems*, 11(2):371–382, 1995.
- [12] F. Hettlich and W. Rundell. The determination of a discontinuity in a conductivity from a single boundary measurement. *Inverse Problems*, 14(1):67–82, 1998.
- [13] B. Hofmann. A denseness theorem with an application to a two-dimensional inverse potential refraction problem. *SIAM J. Math. Anal.*, 30(4):896–911 (electronic), 1999.
- [14] L. Hörmander. *The analysis of linear partial differential operators. I*. Classics in Mathematics. Springer-Verlag, Berlin, 2003. Distribution theory and Fourier analysis, Reprint of the second (1990) edition [Springer, Berlin; MR1065993 (91m:35001a)].
- [15] L. Hörmander. *The analysis of linear partial differential operators. II*. Classics in Mathematics. Springer-Verlag, Berlin, 2005. Differential operators with constant coefficients, Reprint of the 1983 original.
- [16] A. Kirsch. The domain derivative and two applications in inverse scattering theory. *Inverse Problems*, 9(1):81–96, 1993.
- [17] W. Kohn. The validity of Born expansions. *Physical Review*, 87:539–540, 1952.
- [18] W. Kohn. On the convergence of Born expansions. *Reviews of modern physics*, 26:292–310, 1954.
- [19] Rainer Kress. On the numerical solution of a hypersingular integral equation in scattering theory. *J. Comput. Appl. Math.*, 61, 1995.
- [20] A. Kufner. *Weighted Sobolev Spaces*. Wiley, 1985. Second edition.
- [21] K. Kwon, B. Yazıcı, and M. Guven. Two-level domain decomposition methods for diffuse optical tomography. submitted to *Inverse Problems*.
- [22] B. A. Lippmann and J. Schwinger. Variational principles for scattering processes I. *Physical Review*, 79:469–480, 1950.
- [23] I. Manning. Error and convergence bounds for the Born expansion. *Physical Review*, 139:B495–B500, 1965.
- [24] V. A. Markel, V. Mital, and J. C. Schotland. Inverse problem in optical diffusion tomography III : Inversion formulas and singular value decomposition. *J. Opt. Soc. Am. A*, 20:890–, 2003.
- [25] V. A. Markel, J. A. O’Sullivan, and J. C. Schotland. Inverse problem in optical diffusion tomography. IV. nonlinear inversion formula. *J. Opt. Soc. Am. A*, 20:903–912, 2003.
- [26] V. A. Markel and J. C. Schotland. Inverse problem in optical diffusion tomography I :Fourier-Laplace inversion formulas. *J. Opt. Soc. Am. A*, 18:1336–, 2001.
- [27] V. A. Markel and J. C. Schotland. Inverse problem in optical diffusion tomography II : Role of boundary conditions. *J. Opt. Soc. Am. A*, 19:558–, 2002.
- [28] C. Miranda. *Partial Differential equations of elliptic type*. Springer-Verlag, 1970.
- [29] F. Natterer. An error bound for the Born approximation. *Inverse Problems*, 20(2):447–452, 2004.
- [30] M. S. Pindzola and F. J. Robicheaux. Time-dependent born-series calculations of three-body

- scattering systems. *Physical Review A*, 64.
- [31] R. Potthast. Fréchet differentiability of boundary integral operators in inverse acoustic scattering. *Inverse Problems*, 10(2):431–447, 1994.
 - [32] H. Rabitz. Born series for potential scattering. *Physical Review A*, 5:620–627, 1972.
 - [33] L. B. Rall. *Computational Solution of Nonlinear Operator Equations*. John Wiley & Sons, 1969.
 - [34] T. H. Rihan. Modified distorted-wave Born series. *Physical Review*, 164:1247–1252, 1967.
 - [35] L. I. Schiff. *Quantum mechanics*. McGraw-Hill, 1968.
 - [36] S. L. Sobolev. *Applications of functional analysis in mathematical physics*. Translated from the Russian by F. E. Browder. Translations of Mathematical Monographs, Vol. 7. American Mathematical Society, Providence, R.I., 1963.
 - [37] V. I. Tatarski. *Wave propagation in a turbulent medium*. McGraw-Hill, 1961.
 - [38] J. C. Ye, K. J. Webb, R. P. Millane, and T. J. Downar. Modified distorted born iterative method with an approximate fréchet derivative for optical diffusion tomography. *J. Opt. Soc. Am. A*, 16:1814–1826, 1999.

Appendix A. Proof of Lemma 3.3

Using $W_{r,\alpha}^{0,\infty} \subset W_{r,\alpha-\epsilon}^{0,\infty}$ for all $0 \leq \epsilon < \alpha$, $L(r, \cdot) \in W_{r,2-\epsilon}^{0,\infty}$ and inserting $q = p$ to (3.13), we get (3.18a) with $C_1(\min(\frac{n}{p} - \epsilon, 2 - \epsilon), p, p)$. Using $\frac{\partial L(r', \cdot)}{\partial r_i} \in W_{r',1}^{0,\infty}$ and inserting $q = p$ we get (3.19a) and (3.18c) with the constant $C_1(\min(\frac{n}{p}, 1), p, p)$.

We start to prove (3.19b) and (3.18d) by defining

$$v_{i,\delta}(r) := \int_{\Omega \setminus \overline{B}(r,\delta)} \frac{\partial H(r, r')}{\partial r_i} \psi(r') dr'. \quad (\text{A.1})$$

Taking the derivative of $v_{i,\delta}$, we get

$$\frac{\partial v_{i,\delta}}{\partial r_j}(r) = \int_{\Omega \setminus \overline{B}(r,\delta)} \frac{\partial^2 H(r, r')}{\partial r_i \partial r_j} \psi(r') dr' - \int_{\partial B(r,\delta)} \frac{\partial H(r, r')}{\partial r_i} \psi(r') \nu_j^\delta dS(r') \quad (\text{A.2a})$$

$$= \psi(r) \int_{\partial B(r,\delta)} \frac{\partial H(r, r')}{\partial r_i} \nu_j^\delta dS(r') + \int_{\Omega \setminus \overline{B}(r,\delta)} \frac{\partial^2 H(r, r')}{\partial r_i \partial r_j} \psi(r') dr' \quad (\text{A.2b})$$

$$- \int_{\partial B(r,\delta)} \left[\frac{\partial H(r, r')}{\partial r_i} \psi(r') + \frac{\partial H(r', r)}{\partial r_i} \psi(r) \right] \nu_j^\delta dS(r'), \quad (\text{A.2c})$$

where ν_j^Ω and ν_j^δ are the j -th component of the outer normal vector with respect to $\partial\Omega$ and $\partial B(r, \delta)$, respectively. Let us assume $\psi \in C^{0,\lambda}$. Using $\frac{\partial(H(r', \cdot) + H(\cdot, r'))}{\partial r_i} r_j \in W_{r',1+\lambda}^{0,\infty}$ the integral in (A.2c) is bounded by

$$\begin{aligned} & \left| \int_{\partial B(r,\delta)} \left[\frac{\partial H(r, r')}{\partial r_i} \psi(r') + \frac{\partial H(r', r)}{\partial r_i} \psi(r) \right] \nu_j^\delta dS(r') \right| \\ & \leq \int_{\partial B(r,\delta)} \left| \frac{\partial(H(r, r') + H(r', r))}{\partial r_i} \psi(r') \right| dS(r') \\ & \quad + \int_{\partial B(r,\delta)} \left| \frac{\partial H(r', r)}{\partial r_i} \right| |\psi(r') - \psi(r)| dS(r') \\ & \leq \frac{\delta^\lambda}{\lambda} \omega_n \|\psi\|_{C^{0,\lambda}} \left[\frac{\|\kappa\|_{C^{0,\lambda}}}{nL^2} + \frac{1}{nL} \right]. \end{aligned} \quad (\text{A.3})$$

Thus, by (A.3), the integral in (A.2c) goes to zero as δ goes to zero for $\psi \in C^{0,\lambda}$. And the first integral in (A.2b) is $-\psi(r) \frac{1}{n\kappa(r)}$. Letting δ go to zero, we get

$$\begin{aligned} \frac{\partial^2 v}{\partial r_i \partial r_j}(r) &= \int_{\Omega} \frac{\partial^2 (L - H)(r, r')}{\partial r_i \partial r_j} \psi(r') dr' + \lim_{\delta \rightarrow 0} \frac{\partial v_{i,\delta}}{\partial r_j}(r) \\ &= \int_{\Omega} \frac{\partial^2 (L - H)(r, r')}{\partial r_i \partial r_j} \psi(r') dr' + \int_{\Omega} \frac{\partial^2 H(r, r')}{\partial r_i \partial r_j} \psi(r') dr' - \frac{\psi(r)}{n\kappa(r)}. \end{aligned} \quad (\text{A.4})$$

The second integral of the righthand side of (A.4) is bounded in the sense of (3.16). Thus, we proved (3.19b). We prove (3.18d) using (3.13), (3.16), and (A.4).

$$\left\| \frac{\partial^2 v}{\partial r_i \partial r_j} \right\|_{L^p} \leq C_1(\lambda, p, p) \|\psi\|_{L^p} \sup_{r' \in \Omega} \left\| \frac{\partial^2 (L - H)(r', \cdot)}{\partial r_i \partial r_j} \right\|$$

$$+\frac{C_3}{L} \|\psi\|_{L^p} + \frac{1}{nL} \|\psi\|_{L^p} \quad (\text{A.5a})$$

Thus, we proved (3.18d) for $\psi \in C^{0,\lambda}$. Extension of (3.18d) when $\phi \in L^p$ can be found in [5, 28].

(3.19c) follows from (3.19a) and (3.19b). To prove (3.20), using Stokes theorem in $\Omega \setminus B(r, \delta)$, we get

$$\begin{aligned} & \int_{\Omega \setminus B(r, \delta)} [v(r') \mathcal{M}_{r'} L(r, r') - L(r, r') \mathcal{M}_{r'} v(r')] dr' \\ &= \int_{\partial \Omega} [v(r') \mathcal{N}_{r'} L(r, r') - L(r, r') \mathcal{N}_{r'} v(r')] dS(r') \\ & \quad - \int_{\partial B(r, \delta)} \left[v(r') \kappa(r') \frac{\partial L(r, r')}{\partial \nu}(r') - L(r, r') \kappa(r') \frac{\partial v}{\partial \nu}(r') \right] dS(r'). \end{aligned} \quad (\text{A.6})$$

Since $v \in W^{2,p}(\Omega)$, $v \in W^{2-\frac{1}{p},p}(\partial \Omega)$ by trace formula, each term of the second integral of the righthand side of (A.6) has the following asymptotic behavior:

$$\left| \int_{\partial B(r, \delta)} L(r, r') \kappa(r') \frac{\partial v}{\partial \nu}(r') dS(r') \right| \leq U \|L(r, \cdot)\|_{W_{r,2}^{0,\infty}} \|v\|_{W^{2,p}} \quad (\text{A.7a})$$

$$\begin{aligned} & \left| \int_{\partial B(r, \delta)} v(r') \kappa(r') \frac{\partial(L-H)(r, r')}{\partial \nu}(r') dS(r') \right| \\ & \leq U \|v\|_{W^{2,p}} \left\| \frac{\partial(L-H)(r, \cdot)}{\partial r'_i} \right\|_{W_{r,1+\lambda}^{0,\infty}} \delta^\lambda \end{aligned} \quad (\text{A.7b})$$

$$\begin{aligned} & \int_{\partial B(r, \delta)} v(r') \kappa(r') \frac{\partial H(r, r')}{\partial \nu}(r') dS(r') \\ &= \int_{\partial B(r, 1)} v \left(\delta \frac{r' - r}{|r' - r|} \right) dS \left(\frac{r' - r}{|r' - r|} \right). \end{aligned} \quad (\text{A.7c})$$

(A.7a) and (A.7b) go to 0 as δ goes to 0 and (A.7c) goes to $v(r)$ as δ goes to 0 by the mean value theorem. Thus letting $\delta \rightarrow 0$ and combining (A.6) and (A.7), we get (3.20) interpreting the first term in (A.6) as in the sense of (3.16). \square

Appendix B. Proof of Lemma 4.6

(4.47a) and (4.47b) are obtained easily using spherical coordinates with respect to r^1 . Let us divide Ω into three regions depending on two points r^1 and r^2 :

$$\begin{aligned} \Omega_{r^1} &= \{r' \in \Omega \mid |r' - r^1| \leq \frac{|r^1 - r^2|}{2}\} \\ \Omega_{r^2} &= \{r' \in \Omega \mid |r' - r^2| \leq \frac{|r^1 - r^2|}{2}\} \\ \Omega_c &= \{r' \in \Omega \mid |r' - r^1| > \frac{|r^1 - r^2|}{2}, |r' - r^2| > \frac{|r^1 - r^2|}{2}\}. \end{aligned}$$

Consider the equation (4.47c), which is decomposed as

$$\begin{aligned}
& \int_{\Omega} \log(2d/|r^1 - r'|) \log(2d/|r^2 - r'|) dr' \\
&= \int_{\Omega_{r^1}} \log(2d/|r^1 - r'|) \log(2d/|r^2 - r'|) dr' \\
&+ \int_{\Omega_{r^2}} \log(2d/|r^1 - r'|) \log(2d/|r^2 - r'|) dr' \\
&+ \int_{\Omega_c} \log(2d/|r^1 - r'|) \log(2d/|r^2 - r'|) dr'. \tag{B.1}
\end{aligned}$$

Next, consider the first term in the righthand side of (B.1). If $r' \in \Omega_{r^1}$, then $|r' - r^2| \geq \frac{|r^1 - r^2|}{2}$. Using this result and by change of variables with respect to the spherical coordinates centered at r^1 , we get

$$\begin{aligned}
& \int_{\Omega_{r^1}} \log(2d/|r^1 - r'|) \log(2d/|r' - r^2|) dr' \\
&\leq \omega_2 \log(4d/|r^1 - r^2|) \int_0^{\frac{|r^1 - r^2|}{2}} \rho \log(2d/\rho) d\rho \\
&\leq \frac{\omega_2}{16} \log(4d/|r^1 - r^2|) |r^1 - r^2|^2 [2 \log(4d/|r^1 - r^2|) + 1]. \tag{B.2}
\end{aligned}$$

Likewise,

$$\begin{aligned}
& \int_{\Omega_{r^2}} \log(2d/|r^1 - r'|) \log(2d/|r' - r^2|) dr' \\
&\leq \frac{\omega_2}{16} \log(4d/|r^1 - r^2|) |r^1 - r^2|^2 [2 \log(4d/|r^1 - r^2|) + 1]. \tag{B.3}
\end{aligned}$$

If $r' \in \Omega_c$, then $|r^1 - r'| \geq \frac{|r' - r^2|}{3}$. Using this fact and by change of variables with respect to spherical coordinates centered at r^2 , we get

$$\begin{aligned}
& \int_{\Omega_c} \log(2d/|r^1 - r'|) \log(2d/|r' - r^2|) dr' \\
&\leq \int_{\Omega_c} \log(6d/|r' - r^2|) \log(2d/|r' - r^2|) dr' \\
&\leq \omega_2 \int_0^d (\log 3 \log(2d/\rho) + (\log(2d/\rho))^2) \rho d\rho \\
&\leq \omega_2 d^2 \left[\frac{1}{2} (\log 2)^2 + \frac{1}{4} (\log 3 - 1)(2 \log 2 + 1) \right]. \tag{B.4}
\end{aligned}$$

Inserting (B.2), (B.3), (B.4) into (B.1), we get (4.47c).

Returning to (4.47b), (4.47d), and (4.47e), we get

$$\int_{\Omega} |r^1 - r'|^{\alpha_1 - n} |r' - r^2|^{\alpha_2 - n} dr' = \int_{\Omega_{r^1}} |r^1 - r'|^{\alpha_1 - n} |r' - r^2|^{\alpha_2 - n} dr'$$

$$\begin{aligned}
& + \int_{\Omega_{r_2}} |r^1 - r'|^{\alpha_1-n} |r' - r^2|^{\alpha_2-n} dr' \\
& + \int_{\Omega_c} |r^1 - r'|^{\alpha_1-n} |r' - r^2|^{\alpha_2-n} dr',
\end{aligned} \tag{B.5}$$

where each term in the righthand side of (B.5) is bounded by

$$\begin{aligned}
& \int_{\Omega_{r_1}} |r^1 - r'|^{\alpha_1-n} |r' - r^2|^{\alpha_2-n} dr' \\
& \leq 2^{n-\alpha_2} |r^1 - r^2|^{\alpha_2-n} \int_{\Omega_{r_1}} |r^1 - r'|^{\alpha_1-n} dr' \\
& \leq 2^{n-\alpha_2} |r^1 - r^2|^{\alpha_2-n} \int_0^{|r^1-r^2|/2} \rho^{\alpha_1-n} \rho^{n-1} \omega_n d\rho \\
& = \frac{\omega_n}{\alpha_1} 2^{n-\alpha_1-\alpha_2} |r^1 - r^2|^{\alpha_1+\alpha_2-n}.
\end{aligned} \tag{B.6}$$

Likewise

$$\int_{\Omega_{r_2}} |r^1 - r'|^{\alpha_1-n} |r' - r^2|^{\alpha_2-n} dr' \leq \frac{\omega_n}{\alpha_2} 2^{n-\alpha_1-\alpha_2} |r^1 - r^2|^{\alpha_1+\alpha_2-n}. \tag{B.7}$$

Suppose that $\alpha_1 + \alpha_2 < n$, then

$$\begin{aligned}
& \int_{\Omega_c} |r^1 - r'|^{\alpha_1-n} |r' - r^2|^{\alpha_2-n} dr' \\
& \leq 3^{n-\alpha_1} \int_{\Omega_c} |r' - r^2|^{\alpha_1+\alpha_2-2n} dr' \\
& \leq 3^{n-\alpha_1} \int_{|r^1-r^2|/2}^{\infty} \rho^{\alpha_1+\alpha_2-2n} \rho^{n-1} \omega_n d\rho \\
& \leq 3^{n-\alpha_1} 2^{n-\alpha_1-\alpha_2} |r^1 - r^2|^{\alpha_1+\alpha_2-n} \frac{\omega_n}{n - \alpha_1 + \alpha_2}.
\end{aligned} \tag{B.8}$$

Inserting (B.6), (B.7), (B.8) into (B.5) and considering the symmetry of r^1 and r^2 for (B.8), we get (4.47d). (4.47e) and (4.47f) is derived by modifying the integral area for the third integral in (B.8) into $\int_{|r^1-r^2|}^d \cdot$ and $\int_0^d \cdot$, respectively. Finally, (4.47g) is computed in a similar way as follows:

$$\begin{aligned}
& \left| \int_{\Omega} |r^1 - r'|^{\alpha_1-n} \log(2d/|r' - r^2|) dr' \right| \leq \int_{\Omega_{r_1}} |r^1 - r'|^{\alpha_1-n} |\log(2d/|r' - r^2|)| dr' \\
& + \int_{\Omega_{r_2}} |r^1 - r'|^{\alpha_1-n} |\log(2d/|r' - r^2|)| dr' + \int_{\Omega_c} |r^1 - r'|^{\alpha_1-n} |\log(2d/|r' - r^2|)| dr' \\
& \leq \omega_n \log(4d/|r^1 - r^2|) \frac{|r^1 - r^2|^{\alpha_1}}{\alpha_1 2^{\alpha_1}} + \omega_n \frac{|r^1 - r^2|^{\alpha_1}}{2^{\alpha_1} n} \left(\log(4d/|r^1 - r^2|) + \frac{1}{n} \right) \\
& + \omega_n \frac{d^{\alpha_1}}{\alpha_1} \left(\log(6) + \frac{1}{\alpha_1} \right) \leq \omega_n d^{\alpha_1} C_7(\alpha_1).
\end{aligned}$$

Effect of discretization error and adaptive mesh generation in diffuse optical absorption imaging

Murat Guven[†], Birsen Yazici^{†‡}, Kiwoon Kwon[†], Eldar Giladi^{*},
Xavier Intes[§]

[†] Electrical, Computer, and Systems Engineering Department, Rensselaer
Polytechnic Institute, Troy, NY, USA

^{*} Department of Mathematical Sciences, Rensselaer Polytechnic Institute, Troy, NY,
USA

[§] ART Advanced Research Technologies, Quebec, Canada

Abstract.

In Diffuse Optical Tomography (DOT), the discretization error in the numerical solutions of the forward and inverse problems results in error in the reconstructed optical images. In practice, this error can not be avoided, but can be reduced by appropriate discretization. In this work, we analyze the error in the reconstructed optical absorption images, resulting from the discretization of the forward and inverse problems. We show that the error due to the discretization of each problem is bounded by the discretization error in the corresponding problem solution, scaled spatially by the solutions of both problems. Based on this error analysis, we develop adaptive discretization schemes for the forward and inverse problems in order to reduce the error in the reconstructed images. This approach leads to adaptively refined composite meshes that yield the desired level of imaging accuracy while minimizing the computational complexity.

1. Introduction

Imaging in Diffuse Optical Tomography (DOT) is comprised of two interdependent stages which seek solutions to the forward and inverse problems. The forward problem is associated with describing the NIR light propagation, while the objective of the inverse problem is to estimate the unknown optical parameters from boundary measurements [3].

There are a variety of factors that affect the accuracy of the DOT imaging, such as model mismatch (due to light propagation model and/or linearization of the inverse problem), measurement noise, discretization, numerical algorithm efficiency, and inverse problem formulation. In this work, we present an error analysis to show the effect of the discretization error on the accuracy of the reconstructed optical absorption images. Our

[‡] corresponding author : yazici@ecse.rpi.edu

analysis identifies several factors which influence the extent to which the discretization error impacts the accuracy of the reconstructed images. For example; the mutual dependence of forward and inverse problems, the number of sources and detectors and their configuration, and the formulation of the inverse problem. In particular, our error analysis reveals that one has to consider the inherent dependence of the inverse problem solution on the solution of the forward problem in order to develop an effective discretization scheme for each problem. In this context, based on the presented error analysis, we propose adaptive discretization schemes for the forward and inverse problems which ensure stable image reconstructions and reduce the error in the reconstructed optical images resulting from discretization.

There has been extensive research on error estimation and adaptive mesh refinement, however most of the efforts have concentrated on the estimation of discretization error in the solutions of partial differential equations (PDEs) [6, 2, 7, 8, 26, 28]. On the contrary, relatively little has been published in the area of parameter estimation problems governed by PDEs; see for example [24, 10, 23, 9] for *a posteriori* error estimates and/or adaptive mesh refinement strategies in parameter estimation problems. In the area of DOT, Arridge *et al* showed that approximation errors resulting from the discretization of the forward problem can lead to significant degradation in the quality of the reconstructed images [4]. In that work, the error in the reconstructed images is minimized using an enhanced imaging model that treats this additional approximation error within the Bayesian framework. To address the optical image degradation due to discretization, several investigators have reported on adaptive discretization schemes for the forward and inverse problems, yet an analysis regarding the error in the reconstructed optical images, resulting from discretization has not been reported so far. In [12], Eppstein *et al* proposed a “data driven zonation” scheme, which can be viewed as an adaptive discretization algorithm, for fluorescence imaging. We presented a region-of-interest (ROI) imaging scheme for DOT [15], which employed a multi-level algorithm on a nonuniform grid. The non-uniform grid is designed so as to provide finer spatial resolution for the ROI which corresponds to the tumor region as indicated by *a priori* anatomical image. Torregrossa *et al* proposed an *a priori* non-uniform mesh design which provides high resolution at the heterogeneities and near boundary regions [27]. In that work, the mesh refinement is independent of the source-detector configuration and the location of the heterogeneities. Gu *et al* proposed a dual mesh strategy, in which, a relatively fine uniform mesh is considered for the forward problem discretization and a coarse uniform mesh is generated for the inverse problem discretization [14]. In the same study, an adaptive refinement scheme was proposed for the inverse problem discretization, but no adaptive refinement was considered for the solution of the forward problem. Huang and Zhu also presented a dual-mesh strategy which makes use of *a priori* ultrasound information [16]. In that work, the dual mesh is

a coarse mesh for the background tissue and a relatively fine mesh for the heterogeneity, similar to the approach in [15]. In fluorescence imaging, Joshi *et al* used a dual adaptive mesh strategy to discretize the inverse problem and the associated coupled diffusion equations, where the refinement criterion is based on *a posteriori* discretization error estimates [19]. Note that in all these studies [12, 15, 27, 14, 16, 19], the mesh refinement criteria considered for the inverse (forward) problem disregard the impact of the solution of the forward (inverse) problem.

In this work, we model the forward problem by the frequency-domain diffusion equation. As for the inverse problem, we focus on the estimation of the absorption coefficient. We consider the linear integral equation resulting from the iterative linearization of the inverse problem based on Born approximation and use zeroth order Tikhonov regularization to address the ill-posedness of the resulting integral equation. We use finite elements with piecewise linear Lagrange basis functions to discretize the forward and inverse problems and analyze the effect of the discretization of each problem on the reconstructed optical absorption image. Our analysis describes the dependence of the image quality on the optical image properties, the configuration of the source and detectors, and the regularization parameter, in addition to the discretization error in the solution of each problem. In this respect, we separately show the effect of the discretization of the forward and inverse problems. Hence, we first consider the impact of the inverse problem discretization when there is no discretization error in the solution of the forward problem, and provide a bound for the resulting error in the reconstructed optical image. Next, we analyze the effect of the forward problem discretization on the accuracy of the reconstructed image without discretizing the inverse problem, and obtain another bound for the resulting error in the reconstructed optical image. We see that each error bound comprises the discretization error in the corresponding problem solution, scaled spatially by the solutions of both problems. This is a direct consequence of the fact that the inverse problem solution depends on the model defined by the forward problem. Finally, based on the two error bounds provided by the error analysis, we propose a practical adaptive discretization scheme for the forward and inverse problems, respectively. We remark that the mesh refinement criterion for each problem comprises the discretization error in the corresponding problem solution, scaled spatially by the solutions of both problems. Thus, the proposed adaptive mesh generation algorithms address the interdependence between the forward and inverse problems and the source-detector configuration as well. This makes the proposed adaptive discretization algorithms different from the previous approaches [12, 15, 27, 14, 16, 19]. The simulation experiments validate the implications of our error analysis and show that the proposed mesh generation algorithms significantly improve the accuracy of the reconstructed optical images while keeping the number of unknowns in the forward and inverse problems within the allowable limits.

The outline of this paper is as follows: Section 2 defines the forward and inverse problems. In Section 3, we discuss the discretization of the forward and inverse problems. In Section 4, we present two theorems that summarize the impact of discretization on the accuracy of the reconstructed optical images. In Section 5, we introduce the adaptive mesh generation algorithms for the solution of the forward and inverse problems. In Section 6, we present our experimental results, which is followed by the Conclusion section. The Appendix includes results regarding the boundedness and compactness of the forward operator and the proof for the convergence of the inverse problem discretization.

2. Forward and Inverse Problems

In this section, we describe the model for NIR light propagation and define the forward and inverse DOT problems. Table 1 provides a list of the notation used throughout the paper.

2.1. Forward Problem

We use the following boundary value problem to model the NIR light propagation in a bounded domain $\Omega \subset \mathbb{R}^3$:

$$-\nabla \cdot D(\mathbf{x})\nabla g_j + (\mu_a(\mathbf{x}) + \frac{i\omega}{c})g_j = Q_j(\mathbf{x}) \quad \mathbf{x} \in \Omega, \quad (2.1)$$

$$g_j + 2aD(\mathbf{x})\frac{\partial g_j}{\partial n} = 0 \quad \mathbf{x} \in \partial\Omega, \quad (2.2)$$

where $Q_j(\mathbf{x})$ is the point source located at \mathbf{x}_s^j , $D(\mathbf{x})$ is the diffusion coefficient, $\mu_a(\mathbf{x})$ is the absorption coefficient, ω is the modulation frequency of the source, c is the speed of the light and $a = (1 + R)/(1 - R)$ where R is a parameter governing the internal reflection at the boundary $\partial\Omega$. Note that we assume the diffusion coefficient is isotropic. For the general anisotropic material, see [20].

The adjoint problem associated with (2.1)-(2.2) is given by the following boundary value problem [3]:

$$-\nabla \cdot D(\mathbf{x})\nabla g_i^* + (\mu_a(\mathbf{x}) - \frac{i\omega}{c})g_i^* = 0 \quad \mathbf{x} \in \Omega, \quad (2.3)$$

$$g_i^* + 2aD(\mathbf{x})\frac{\partial g_i^*}{\partial n} = Q_i^*(\mathbf{x}) \quad \mathbf{x} \in \partial\Omega, \quad (2.4)$$

where $Q_i^*(\mathbf{x})$ is the adjoint source located at \mathbf{x}_d^i . In this work, we approximate the point source Q_j in (2.1) and the adjoint source Q_i^* in (2.4) by Gaussian functions with sufficiently low variance, whose centers are located at \mathbf{x}_s^j and \mathbf{x}_d^i , respectively.

Table 1. Index of notation.

Notation	Explanation
$g(\mathbf{x}, \mathbf{x}_s^j) = g_j(\mathbf{x}) = g_j$	Solution of the diffusion equation for the j^{th} point source located at $\mathbf{x} = \mathbf{x}_s^j$
$g^*(\mathbf{x}, \mathbf{x}_d^i) = g_i^*(\mathbf{x}) = g_i^*$	Solution of the adjoint problem for the i^{th} adjoint source located at $\mathbf{x} = \mathbf{x}_d^i$
$G_j(\mathbf{x}) = G_j$	Finite element approximation of $g_j(\mathbf{x})$
$G_i^*(\mathbf{x}) = G_i^*$	Finite element approximation of $g_i^*(\mathbf{x})$
$e_j(\mathbf{x}) = e_j$	The discretization error in the finite element approximation of $g(\mathbf{x}, \mathbf{x}_s^j)$
$e_i^*(\mathbf{x}) = e_i^*$	The discretization error in the finite element approximation of $g^*(\mathbf{x}, \mathbf{x}_d^i)$
$\alpha(\mathbf{x}) = \alpha$	Small perturbation over the background $\mu_a(\mathbf{x})$
$\Gamma(\mathbf{x}_d^i, \mathbf{x}_s^j) = \Gamma(i, j) = \Gamma_{ij}$	Differential measurement at the i^{th} detector due to the j^{th} source
$A_a : L^\infty \rightarrow \mathbb{C}^{N_d \times N_s}$	The integral operator mapping $\alpha(\mathbf{x})$ to Γ_{ij}
$A_a^* : \mathbb{C}^{N_d \times N_s} \rightarrow L^1$	The adjoint of A_a
$H(\mathbf{x}_s^j, \mathbf{x}_d^i; \mathbf{x})$	The kernel of A_a
$H^*(\mathbf{x}; \mathbf{x}_s^j, \mathbf{x}_d^i)$	The kernel of A_a^*
γ	$A_a^* \Gamma_{ij}$
λ	The regularization parameter
$\alpha^\lambda(\mathbf{x}) = \alpha^\lambda$	Solution of the regularized inverse problem
$\overline{f(\mathbf{x})}$	The complex conjugate of $f(\mathbf{x})$
$\ f(\mathbf{x})\ _0$	The L^2 (or H^0) norm of $f(\mathbf{x})$ over the domain Ω
$\ f(\mathbf{x})\ _p$	The H^p norm of $f(\mathbf{x})$ over the domain Ω
$\ f(\mathbf{x})\ _\infty$	The L^∞ norm of $f(\mathbf{x})$ over the domain Ω
$\ f(\mathbf{x})\ _{L^p(\Omega)}$	The L^p norm of $f(\mathbf{x})$ over the domain Ω
$\ f(\mathbf{x})\ _{0,m}$	The L^2 (or H^0) norm of $f(\mathbf{x})$ over the m^{th} finite element Ω_m
$\ f(\mathbf{x})\ _{p,m}$	The H^p norm of $f(\mathbf{x})$ over the m^{th} finite element Ω_m
$\ f(\mathbf{x})\ _{\infty,m}$	The L^∞ norm of $f(\mathbf{x})$ over the m^{th} finite element Ω_m

For the solution of the forward problem, we consider the variational problem formulations of (2.1)-(2.2) and (2.3)-(2.4):

$$\int_{\Omega} \overline{\nabla \psi} \cdot D \nabla g_j + \overline{\psi} \left((\mu_a + \frac{j\omega}{c}) g_j - Q_j \right) + \int_{\partial\Omega} \overline{\psi} \frac{1}{2a} g_j = 0, \quad (2.5)$$

where $\overline{\psi} \in H^1$ is a test function. Equivalently, we can express (2.5) using the sesquilinear

form:

$$b(\psi, g_j) := A(\psi, g_j) + \langle \psi, \frac{1}{2a} g_j \rangle = (\psi, Q_j), \quad (2.6)$$

where

$$\begin{aligned} A(\psi, g_j) &:= \int_{\Omega} \overline{\nabla \psi} \cdot D \nabla g_j + (\mu_a + \frac{j\omega}{c}) \overline{\psi} g_j, \\ (\psi, Q_j) &:= \int_{\Omega} \overline{\psi} Q_j, \\ \langle \psi, \frac{1}{2a} g_j \rangle &:= \frac{1}{2a} \int_{\partial\Omega} \overline{\psi} g_j. \end{aligned}$$

Similarly, the variational problem for (2.3)-(2.4) can be formulated as:

$$b^*(\psi, g_i^*) := A(\psi, g_i^*) + \langle \psi, \frac{1}{2a} g_i^* \rangle = \langle \psi, \frac{1}{2a} Q_i^* \rangle, \quad (2.7)$$

where in $A(\psi, g_i^*)$, ω is replaced by $-\omega$.

The sesquilinear forms $b(\psi, g_j)$, $b^*(\psi, g_i^*)$ are continuous and positive definite [17]. As a result, the variational problems (2.6) and (2.7) have unique solutions, which follows from the Lax-Milgram Lemma [11]. Furthermore, the solutions g_j and g_i^* of the variational problems (2.6) and (2.7) belong to H^1 , which results from the H^1 boundedness of the Gaussian function that approximates the point source Q_j and the adjoint source Q_i^* [17]. Assuming $D(\mathbf{x}), \mu_a(\mathbf{x}) \in C^2(\Omega)$ and noting that $Q_j, Q_i^* \in H^1$; the solutions g_j, g_i^* satisfy $g_j, g_i^* \in H_{loc}^3(\Omega)$ (Chapter 6.3, Theorem 2 in [13]). This last condition implies (Chapter 5.6, Theorem 6 in [13])

$$g_j, g_i^* \in C^1(\Omega). \quad (2.8)$$

2.2. Inverse Problem

In this work, we focus on the estimation of the absorption coefficient; therefore we assume $D(\mathbf{x})$ is known. To address the nonlinear nature of the inverse DOT problem, we consider an iterative algorithm based on repetitive linearization of the inverse problem using first order Born approximation [3]. As a result, at each linearization step, the following linear integral equation relates the differential optical measurements to a small perturbation $\alpha(\mathbf{x})$ on the absorption coefficient $\mu_a(\mathbf{x})$:

$$\Gamma(\mathbf{x}_d^i, \mathbf{x}_s^j) = - \int_{\Omega} \overline{g^*(\mathbf{x}, \mathbf{x}_d^i)} g(\mathbf{x}, \mathbf{x}_s^j) \alpha(\mathbf{x}) d\mathbf{x} \quad (2.9)$$

$$\begin{aligned} &= \int_{\Omega} H(\mathbf{x}_s^j, \mathbf{x}_d^i; \mathbf{x}) \alpha(\mathbf{x}) d\mathbf{x} \\ &= A_a \alpha, \end{aligned} \quad (2.10)$$

where $\mathbf{x}_d^i, i = 1, \dots, N_d$ and $\mathbf{x}_s^j, j = 1, \dots, N_s$ are respectively the detector and source positions, $H(\mathbf{x}_s^j, \mathbf{x}_d^i; \mathbf{x}) = -\overline{g^*(\mathbf{x}, \mathbf{x}_d^i)} g(\mathbf{x}, \mathbf{x}_s^j)$ is the kernel of the integral operator

$A_a : L^\infty \rightarrow \mathbb{C}^{N_d \times N_s}$, $g(\mathbf{x}, \mathbf{x}_s^j)$ is the solution of (2.6), $g^*(\mathbf{x}, \mathbf{x}_d^i)$ is the solution of (2.7), and $\Gamma(\mathbf{x}_d^i, \mathbf{x}_s^j)$ represents the differential measurement at the i^{th} detector due to the j^{th} source. Note that approximating Q_i^* in (2.4) by a Gaussian function centered at \mathbf{x}_d^i implies that $\Gamma(\mathbf{x}_d^i, \mathbf{x}_s^j)$ corresponds to the scattered optical field evaluated at \mathbf{x}_d^i , after filtering it by that Gaussian function. Thus, the Gaussian approximation of the adjoint source models the finite size of the detectors. Similarly, approximating Q_j in (2.1) by a Gaussian function models the finite beam of the source.

Let g_j and g_i^* in (2.9) be the solutions of (2.6) and (2.7), respectively. Then, the linear operator $A_a : L^\infty \rightarrow \mathbb{C}^{N_d \times N_s}$ defined by (2.9) is compact and bounded by (see Appendix A and Appendix B)

$$\|A_a\|_{L^\infty \rightarrow l^1} \leq N_d N_s \max_i \|g_i^*\|_0 \max_j \|g_j\|_0. \quad (2.11)$$

For the given solution space L^∞ for α , the compactness of the linear operator A_a implies the ill-posedness of (2.9). Hence, we regularize (2.9) with a zeroth order Tikhonov regularization. This yields the following equation which defines our inverse problem at each linearization step:

$$\gamma = A_a^* \Gamma_{ij} = (A_a^* A_a + \lambda I) \alpha^\lambda \quad (2.12)$$

$$= K \alpha^\lambda, \quad (2.13)$$

where $\lambda > 0$ and α^λ is an approximation to α . In this representation, $A_a^* : \mathbb{C}^{N_d \times N_s} \rightarrow L^1$ is the adjoint of A_a and I is the identity operator.

Let $A = A_a^* A_a$, then $A : L^\infty \rightarrow L^1$ is defined as follows:

$$\begin{aligned} (A\alpha)(\mathbf{x}) &= \sum_{i,j}^{N_d, N_s} H^*(\mathbf{x}; \mathbf{x}_s^j, \mathbf{x}_d^i) \int_{\Omega} H(\mathbf{x}_s^j, \mathbf{x}_d^i; \mathbf{x}) \alpha(\mathbf{x}) d\mathbf{x} \\ &= \int_{\Omega} \kappa(\mathbf{x}, \mathbf{x}) \alpha(\mathbf{x}) d\mathbf{x}, \end{aligned} \quad (2.14)$$

where $\kappa(\mathbf{x}, \mathbf{x})$ stands for the kernel of the integral operator A and is given by

$$\kappa(\mathbf{x}, \mathbf{x}) = \sum_{i,j}^{N_d, N_s} H^*(\mathbf{x}; \mathbf{x}_s^j, \mathbf{x}_d^i) H(\mathbf{x}_s^j, \mathbf{x}_d^i; \mathbf{x}), \quad (2.15)$$

and $H^*(\mathbf{x}; \mathbf{x}_s^j, \mathbf{x}_d^i)$ is the kernel of the adjoint operator A_a^* given by:

$$(A_a^* \beta)(\mathbf{x}) = \sum_{i,j}^{N_d, N_s} H^*(\mathbf{x}; \mathbf{x}_s^j, \mathbf{x}_d^i) \beta(\mathbf{x}_d^i, \mathbf{x}_s^j) = \sum_{i,j}^{N_d, N_s} -g^*(\mathbf{x}, \mathbf{x}_d^i) \overline{g(\mathbf{x}, \mathbf{x}_s^j)} \beta(\mathbf{x}_d^i, \mathbf{x}_s^j), \quad (2.16)$$

for all $\beta \in \mathbb{C}^{N_d \times N_s}$.

Having defined the adjoint integral operator, we note that the operator $A = A_a^* A_a : L^\infty \rightarrow L^1$ is compact and that the operator $K : L^\infty \rightarrow L^1$ is bounded by $\|K\| \leq \|A_a\|^2 + \lambda$. In this work, we assume that the solution $\alpha^\lambda \in L^\infty$ also satisfies $\alpha^\lambda \in H^1$. For the rest of the paper, we will denote L^∞ and L^1 by X and Y , respectively.

3. Discretization of the Inverse and Forward Problems

In this section, we outline the discretization of the inverse and forward problems.

3.1. Inverse Problem Discretization

In practice, we seek a finite-dimensional approximation to the solution of the inverse problem (2.13) at each linearization step. Therefore, we discretize (2.13) by projecting it onto a finite dimensional subspace.

Let $X_n \in X$ and $Y_n \in Y$ denote a sequence of finite-dimensional subspaces of dimension n , spanned by piecewise linear Lagrange basis functions $\{L_1, \dots, L_n\}$, and $\{\mathbf{x}_p\}$, $p = 1, \dots, n$, be the set of collocation points on Ω . Then, the projection operator $P_n : Y \rightarrow Y_n$ associated with the collocation method is defined by

$$P_n f(\mathbf{x}) = \sum_{p=1}^n f(\mathbf{x}_p) L_p(\mathbf{x}), \quad \mathbf{x} \in \Omega, \quad (3.17)$$

for all $f(\mathbf{x}) \in Y$.

The collocation method approximates the solution of (2.13) by an element $\alpha_n^\lambda \in X_n$ satisfying

$$(K\alpha_n^\lambda)(\mathbf{x}_l) = \gamma(\mathbf{x}_l), \quad l = 1, \dots, n. \quad (3.18)$$

Using the piecewise linear Lagrange basis functions $L_p(\mathbf{x})$ for X_n , we express α_n^λ as

$$\alpha_n^\lambda(\mathbf{x}) = \sum_{p=1}^n a_p L_p(\mathbf{x}). \quad (3.19)$$

Then, projection by collocation method for the operator K yields

$$\lambda a_l + \sum_{p=1}^n a_p \int_{\Omega} \kappa(\mathbf{x}_l, \mathbf{x}) L_p(\mathbf{x}) d\mathbf{x} = \gamma(\mathbf{x}_l), \quad l = 1, \dots, n, \quad (3.20)$$

which is equivalent to

$$P_n K \alpha_n^\lambda = P_n \gamma. \quad (3.21)$$

3.2. Forward Problem Discretization

In this section, we consider the finite element discretization of (2.6) and (2.7), and use their solutions to approximate $H(\mathbf{x}_s^j, \mathbf{x}_d^i; \mathbf{x})$ and $H^*(\mathbf{x}; \mathbf{x}_s^j, \mathbf{x}_d^i)$. As a result, we obtain finite dimensional approximations to K and γ .

Let $L_k(\mathbf{x})$ be the piecewise linear Lagrange basis functions. Replacing ψ and g_j in (2.6) with their finite-dimensional counterparts $\Psi = \sum_{k=1}^{N_j} p_k L_k(\mathbf{x})$, $G_j =$

$\sum_{k=1}^{N_j} c_k L_k(\mathbf{x})$; and replacing ψ and g_i^* in (2.7) with $\Psi = \sum_{k=1}^{N_i} p_k L_k(\mathbf{x})$, $G_i^* = \sum_{k=1}^{N_i} d_k L_k(\mathbf{x})$ yields the matrix equations:

$$\mathbf{S}\mathbf{c}_j = \mathbf{q}_j, \quad (3.22)$$

$$\mathbf{S}^*\mathbf{d}_i = \mathbf{q}_i^*, \quad (3.23)$$

for $\mathbf{c}_j = [c_1, c_2, \dots, c_{N_j}]^T$ and $\mathbf{d}_i = [d_1, d_2, \dots, d_{N_i}]^T$. Here \mathbf{S} and \mathbf{S}^* are the finite element matrices and \mathbf{q}_j and \mathbf{q}_i^* are the load vectors resulting from the finite element discretization of (2.6) and (2.7). Note that for each source (detector), the dimension of the finite element solution G_j (G_i^*) can be different, therefore N_j (N_i) may vary.

The H^1 boundedness of the solutions g_j and g_i^* implies that the discretization error e_j and e_i^* in G_j and G_i^* on the m^{th} finite element is bounded. A bound for e_j and e_i^* can be found by using the interpolation error estimates (Theorem 4.4.4 in [11]):

$$\|e_j\|_{0,m} \leq C\|g_j\|_{1,m} h_m^j, \quad (3.24)$$

$$\|e_i^*\|_{0,m} \leq C\|g_i^*\|_{1,m} h_m^i, \quad (3.25)$$

where C is a positive constant and h_m^j (h_m^i) is the diameter of the smallest ball containing the m^{th} finite element.

3.3. Discretization of the Inverse Problem with Operator Approximations

Substituting the finite element approximations G_j and G_i^* in (2.14) and (2.16), and using the resulting finite-dimensional operator approximations in (3.21), we obtain the following linear system in terms of $\tilde{\alpha}_n^\lambda$ which approximates α^λ :

$$P_n \tilde{K} \tilde{\alpha}_n^\lambda = P_n \tilde{\gamma}. \quad (3.26)$$

In (3.26), the operator $\tilde{K} : X \rightarrow Y$ is the finite dimensional approximation of K in (2.13) and $P_n \tilde{K} : X_n \rightarrow Y_n$. Similarly,

$$\tilde{\gamma} = \tilde{A}_a^* \Gamma, \quad (3.27)$$

where \tilde{A}_a^* is the approximation to the adjoint operator A_a^* , obtained by substituting G_j and G_i^* in (2.16).

4. Discretization-based Error Analysis

As a result of the discretization of the forward and inverse problems, the reconstructed image $\tilde{\alpha}_n^\lambda$ in (3.26) is an approximation to the actual image α^λ . Thus, the accuracy of the reconstructed image depends on the error incurred by the discretization of the forward and inverse problems.

In this section, we analyze the effect of the discretization of the forward and inverse problems on the accuracy of DOT imaging. The analysis is carried out based on the inverse problem at each linearization defined by (2.13) and the associated kernel $\kappa(\mathbf{x}, \mathbf{x})$.

In this work, we follow an approach which allows us to separately analyze the effect of the discretization of each problem on the accuracy of the reconstructed optical image. In this respect, we first consider the impact of projection (i.e. inverse problem discretization) by collocation method when the associated kernel $\kappa(\mathbf{x}, \mathbf{x})$ in (2.13) is exact. Next, we explore the case in which the kernel is replaced by its finite-dimensional approximation (i.e. degenerate kernel) and analyze the effect of the forward problem discretization on the accuracy of the reconstructed image without projecting (2.13).

Our analysis reveals that even the kernel is exact, the accuracy of the solution approximation α_n^λ in (3.21) resulting from the inverse problem discretization depends on the kernel $\kappa(\mathbf{x}, \mathbf{x})$ of the integral operator. Likewise, the error in the reconstructed optical image due to the discretization of the forward problem is a function of the inverse problem solution. These results suggest that the discretization of the inverse and forward problems can not be considered independent of each other.

4.1. Case 1: The kernel $\kappa(\mathbf{x}, \mathbf{x})$ is exact

In this section, we show the effect of projection on the optical imaging accuracy. In the analysis, we assume that the kernel $\kappa(\mathbf{x}, \mathbf{x})$ is exact. We first prove the convergence of the projection method for the operator K , and then analyze the effect of projection on the imaging accuracy.

Clearly, the inverse operator $K^{-1} : Y \rightarrow X$ exists since K is positive definite for $\lambda > 0$. Furthermore, by the compactness of A and Riesz Theorem, the inverse operator K^{-1} is bounded by

$$\|K^{-1}\| \leq \frac{1}{\lambda}. \quad (4.28)$$

Lemma: Projection by collocation method for the operator $K : X \rightarrow Y$ converges.

Specifically, the operators $P_n K : X_n \rightarrow Y_n$ are invertible and $(P_n K)^{-1} P_n K \alpha^\lambda \rightarrow \alpha^\lambda$, $n \rightarrow \infty$. Furthermore,

$$\|(P_n K)^{-1} P_n K\|_{X \rightarrow Y_n} \leq C_M \frac{\|K\|}{\lambda} \quad (4.29)$$

for some $C_M > 0$ independent of n .

Proof. See Appendix C. □

Based on the Lemma, the following theorem provides an upper bound for $\|\alpha^\lambda - \alpha_n^\lambda\|_{L^1(\Omega)}$, where α_n^λ is the solution of (3.21):

Theorem 1: Let $\{\Omega_m\}$ denote a set of finite elements for $m = 1, \dots, N_\Delta$, such that $\bigcup_{m=1}^{N_\Delta} \Omega_m = \Omega$ and h_m be the diameter of the smallest ball that contains the m^{th} element. Then,

$$\|\alpha^\lambda - \alpha_n^\lambda\|_{L^1(\Omega)} \leq C \sqrt{V_\Omega} \|I - T_n\|_{Y \rightarrow X_n} \sum_{m=1}^{N_\Delta} \|\alpha^\lambda\|_{1,m} h_m$$

$$+ \frac{C}{\lambda} \|T_n\|_{Y \rightarrow X_n} \max_{i,j} \|g_i^* g_j\|_{L^1(\Omega)} \sum_{m=1}^{N_\Delta} \sum_{i,j}^{N_d, N_s} \|g_i^* g_j\|_{0,m} \|\alpha^\lambda\|_{1,m} h_m,$$

where C is a positive constant, V_Ω is the volume of Ω and $T_n : Y \rightarrow X_n$ is a uniformly bounded operator given by $T_n = [I + \frac{1}{\lambda} P_n A]^{-1} P_n$.

Proof.

$$\begin{aligned} \alpha^\lambda - \alpha_n^\lambda &= [I - (P_n K)^{-1} P_n K] \alpha^\lambda \\ &= [I - (P_n K)^{-1} P_n K] (\alpha^\lambda - \psi) \end{aligned} \quad (4.30)$$

since $[I - (P_n K)^{-1} P_n K] \psi = 0$, where $\psi \in X_n$ is the interpolant of α^λ . Using (C.3),

$$\begin{aligned} [I - (P_n K)^{-1} P_n K] &= I - [I + \frac{1}{\lambda} P_n A]^{-1} \frac{1}{\lambda} P_n K \\ &= I - T_n \frac{1}{\lambda} K, \end{aligned} \quad (4.31)$$

where $T_n = [I + \frac{1}{\lambda} P_n A]^{-1} P_n$ is a uniformly bounded operator (see Appendix C). We use K defined by (2.13) and (4.31) in (4.30) to obtain

$$\alpha^\lambda - \alpha_n^\lambda = (I - T_n) (\alpha^\lambda - \psi) - \frac{T_n}{\lambda} A (\alpha^\lambda - \psi). \quad (4.32)$$

Then we use the definition of A in (4.32) and find

$$\alpha^\lambda - \alpha_n^\lambda = (I - T_n) (\alpha^\lambda - \psi) - \frac{T_n}{\lambda} \int_{\Omega} \kappa(\mathbf{x}, \dot{\mathbf{x}}) (\alpha^\lambda - \psi)(\dot{\mathbf{x}}) d\dot{\mathbf{x}}. \quad (4.33)$$

This leads to

$$\begin{aligned} \|\alpha^\lambda - \alpha_n^\lambda\|_{L^1(\Omega)} &\leq \|I - T_n\|_{Y \rightarrow X_n} \|\alpha^\lambda - \psi\|_{L^1(\Omega)} \\ &\quad + \frac{1}{\lambda} \|T_n\|_{Y \rightarrow X_n} \left\| \int_{\Omega} \kappa(\mathbf{x}, \dot{\mathbf{x}}) (\alpha^\lambda - \psi)(\dot{\mathbf{x}}) d\dot{\mathbf{x}} \right\|_{L^1(\Omega)} \\ &\leq \sqrt{V_\Omega} \|I - T_n\|_{Y \rightarrow X_n} \|\alpha^\lambda - \psi\|_0 \\ &\quad + \frac{1}{\lambda} \|T_n\|_{Y \rightarrow X_n} \int_{\Omega} d\mathbf{x} \int_{\Omega} |\kappa(\mathbf{x}, \dot{\mathbf{x}}) (\alpha^\lambda - \psi)(\dot{\mathbf{x}})| d\dot{\mathbf{x}}, \end{aligned} \quad (4.34)$$

The second term in (4.34) can then be rewritten as:

$$\begin{aligned} &\frac{1}{\lambda} \|T_n\|_{Y \rightarrow X_n} \int_{\Omega} d\mathbf{x} \int_{\Omega} |\kappa(\mathbf{x}, \dot{\mathbf{x}}) (\alpha^\lambda - \psi)(\dot{\mathbf{x}})| d\dot{\mathbf{x}} \\ &= \frac{1}{\lambda} \|T_n\|_{Y \rightarrow X_n} \int_{\Omega} d\mathbf{x} \left(\sum_{m=1}^{N_\Delta} \int_{\Omega_m} |\kappa(\mathbf{x}, \dot{\mathbf{x}}) (\alpha^\lambda - \psi)(\dot{\mathbf{x}})| d\dot{\mathbf{x}} \right). \end{aligned} \quad (4.35)$$

Let $e_\alpha = \alpha^\lambda - \psi$ be the interpolation error. Then, using (2.15),

$$\sum_{m=1}^{N_\Delta} \int_{\Omega_m} |\kappa(\mathbf{x}, \dot{\mathbf{x}}) e_\alpha(\dot{\mathbf{x}})| d\dot{\mathbf{x}} \quad (4.36)$$

$$= \sum_{m=1}^{N_\Delta} \int_{\Omega_m} \left| \sum_{i,j}^{N_d, N_s} g_i^*(\mathbf{x}) \overline{g_j(\mathbf{x})} g_i^*(\hat{\mathbf{x}}) g_j(\hat{\mathbf{x}}) e_\alpha(\hat{\mathbf{x}}) \right| d\hat{\mathbf{x}} \quad (4.37)$$

$$\begin{aligned} &\leq \sum_{m=1}^{N_\Delta} \sum_{i,j}^{N_d, N_s} |g_i^*(\mathbf{x}) g_j(\mathbf{x})| \int_{\Omega_m} |g_i^*(\hat{\mathbf{x}}) g_j(\hat{\mathbf{x}})| |e_\alpha(\hat{\mathbf{x}})| d\hat{\mathbf{x}} \\ &\leq \sum_{m=1}^{N_\Delta} \sum_{i,j}^{N_d, N_s} |g_i^*(\mathbf{x}) g_j(\mathbf{x})| \|g_i^*(\hat{\mathbf{x}}) g_j(\hat{\mathbf{x}})\|_{0,m} \|e_\alpha(\hat{\mathbf{x}})\|_{0,m}, \end{aligned} \quad (4.38)$$

where (4.38) follows from the Schwarz' inequality. Note that $g_i^* g_j \in L^2$ since $g_i^*, g_j \in L^\infty$ by (2.8).

We now use (4.35) and (4.38) to obtain

$$\begin{aligned} &\frac{1}{\lambda} \|T_n\|_{Y \rightarrow X_n} \int_{\Omega} d\mathbf{x} \left(\int_{\Omega} |\kappa(\mathbf{x}, \hat{\mathbf{x}}) (\alpha^\lambda - \psi)| d\hat{\mathbf{x}} \right) \\ &\leq \frac{1}{\lambda} \|T_n\|_{Y \rightarrow X_n} \int_{\Omega} d\mathbf{x} \\ &\quad \times \sum_{m=1}^{N_\Delta} \sum_{i,j}^{N_d, N_s} |g_i^*(\mathbf{x}) g_j(\mathbf{x})| \|g_i^*(\hat{\mathbf{x}}) g_j(\hat{\mathbf{x}})\|_{0,m} \|e_\alpha(\hat{\mathbf{x}})\|_{0,m}. \end{aligned} \quad (4.39)$$

Using the bound (4.39) in (4.34) and substituting the interpolation error bound [11]

$$\|e_\alpha\|_{0,m} \leq C \|\alpha^\lambda\|_{1,m} h_m, \quad (4.40)$$

we obtain

$$\begin{aligned} \|\alpha^\lambda - \alpha_n^\lambda\|_{L^1(\Omega)} &\leq C \sqrt{V_\Omega} \|I - T_n\|_{Y \rightarrow X_n} \sum_{m=1}^{N_\Delta} \|\alpha^\lambda\|_{1,m} h_m \\ &+ \frac{C}{\lambda} \|T_n\|_{Y \rightarrow X_n} \sum_{m=1}^{N_\Delta} \sum_{i,j}^{N_d, N_s} \|g_i^* g_j\|_{L^1(\Omega)} \|g_i^* g_j\|_{0,m} \|\alpha^\lambda\|_{1,m} h_m \\ &\leq C \sqrt{V_\Omega} \|I - T_n\|_{Y \rightarrow X_n} \sum_{m=1}^{N_\Delta} \|\alpha^\lambda\|_{1,m} h_m \\ &+ \frac{C}{\lambda} \|T_n\|_{Y \rightarrow X_n} \max_{i,j} \|g_i^* g_j\|_{L^1(\Omega)} \sum_{m=1}^{N_\Delta} \sum_{i,j}^{N_d, N_s} \|g_i^* g_j\|_{0,m} \|\alpha^\lambda\|_{1,m} h_m. \end{aligned} \quad (4.41)$$

□

Remarks: (i) Theorem 1 shows the spatial dependence of the inverse problem discretization on the forward problem solution.

(ii) The first term in (4.41) suggests that the mesh of the inverse problem be refined where $\|\alpha^\lambda\|_1$ is large.

- (iii) The second term in (4.41) shows that the term $\|\alpha^\lambda\|_{1,m}$ is scaled spatially by $\|g_i^* g_j\|_{0,m}$. Thus, the effect of the interpolation error e_α in the inverse problem solution is scaled by the solution of the forward problem.
- (iv) The regularization parameter affects the bound on $\|\alpha^\lambda - \alpha_n^\lambda\|_{L^1(\Omega)}$.
- (v) Increasing the number of sources and detectors will increase the bound on $\|\alpha^\lambda - \alpha_n^\lambda\|_{L^1(\Omega)}$.

4.2. Case 2: The kernel is degenerate

In this section, we first derive approximate upper bounds for the approximation errors $\|\tilde{K} - K\|$ and $\|\tilde{\gamma} - \gamma\|$, which result from the discretization of the forward problem. Then, we show the effect of these approximation errors on the accuracy of the reconstructed optical image. For notational convenience, we will drop the subscripts on the norms $\|\cdot\|$ where necessary.

The operator $K : X \rightarrow Y$ is bounded with a bounded inverse $K^{-1} : Y \rightarrow X$. By the finite element approximation of the associated kernel, the sequence of bounded linear finite-dimensional operators \tilde{K} is norm convergent $\|\tilde{K} - K\| \rightarrow 0$; $N_j, N_i \rightarrow \infty$, for $j = 1, \dots, N_s$ and $i = 1, \dots, N_d$, and

$$\|\tilde{K}^{-1}\| < 1/\lambda, \quad (4.42)$$

which can be obtained analogous to (4.28).

In the following, we derive an explicit approximation to the error $\|\tilde{K} - K\|$ in terms of the associated kernel and the discretization error in the kernel approximation. The result is then used to compute the error in the reconstructed optical image due to $\|\tilde{K} - K\|$.

By definition,

$$\|(A_a - \tilde{A}_a)\alpha\|_{l^1} = \sum_{i,j}^{N_d, N_s} \left| \int_{\Omega} (\overline{g_i^*(\mathbf{x})} g_j(\mathbf{x}) - \overline{G_i^*(\mathbf{x})} G_j(\mathbf{x})) \alpha(\mathbf{x}) d\mathbf{x} \right|, \quad (4.43)$$

where G_i^*, G_j are finite element approximations to g_i^* and g_j , respectively. We can expand $\overline{g_i^*} g_j - \overline{G_i^*} G_j$ as

$$\overline{g_i^*} g_j - \overline{G_i^*} G_j = \overline{e_i^*} e_j + G_j \overline{e_i^*} + \overline{G_i^*} e_j, \quad (4.44)$$

where $e_i^* = g_i^* - G_i^*$ and $e_j = g_j - G_j$. Replacing G_i^* and G_j respectively with $g_i^* - e_i^*$ and $g_j - e_j$, we get

$$\begin{aligned} \overline{g_i^*} g_j - \overline{G_i^*} G_j &= g_j \overline{e_i^*} + \overline{g_i^*} e_j - \overline{e_i^*} e_j \\ &\approx g_j \overline{e_i^*} + \overline{g_i^*} e_j, \end{aligned} \quad (4.45)$$

where we neglect the term $\overline{e_i^*} e_j$.

We can express $\tilde{K} - K$ as

$$\tilde{K} - K = A_a^* A_a - \tilde{A}_a^* \tilde{A}_a. \quad (4.46)$$

Following a similar approach as above,

$$A_a^* A_a - \tilde{A}_a^* \tilde{A}_a = (A_a^* - \tilde{A}_a^*)(A_a - \tilde{A}_a) + \tilde{A}_a^*(A_a - \tilde{A}_a) + (A_a^* - \tilde{A}_a^*)\tilde{A}_a. \quad (4.47)$$

As a result, the following condition holds:

$$\|\tilde{K} - K\| \leq \|(A_a^* - \tilde{A}_a^*)(A_a - \tilde{A}_a)\| + \|\tilde{A}_a^*(A_a - \tilde{A}_a) + (A_a^* - \tilde{A}_a^*)\tilde{A}_a\|. \quad (4.48)$$

Since $\tilde{A}_a = -(A_a - \tilde{A}_a) + A_a$, (4.48) can be rewritten as

$$\begin{aligned} \|\tilde{K} - K\| &= \|A_a^* A_a - \tilde{A}_a^* \tilde{A}_a\| \\ &\leq \|(A_a^* - \tilde{A}_a^*)(A_a - \tilde{A}_a)\| + 2\|A_a^*(A_a - \tilde{A}_a)\| \\ &\approx 2\|A_a^*(A_a - \tilde{A}_a)\|, \end{aligned} \quad (4.49)$$

where we neglect the term $\|(A_a^* - \tilde{A}_a^*)(A_a - \tilde{A}_a)\|$.

Similarly, $\|\tilde{\gamma} - \gamma\|$ can be interpreted as

$$\begin{aligned} \|\tilde{\gamma} - \gamma\|_{L^1(\Omega)} &= \int_{\Omega} \left| \sum_{i,j}^{N_d, N_s} (g_i^*(\mathbf{x}) \overline{g_j(\mathbf{x})} - G_i^*(\mathbf{x}) \overline{G_j(\mathbf{x})}) \Gamma(\mathbf{x}_d^i, \mathbf{x}_s^j) \right| d\mathbf{x} \\ &\approx \int_{\Omega} \left| \sum_{i,j}^{N_d, N_s} (e_i^*(\mathbf{x}) \overline{g_j(\mathbf{x})} + g_i^*(\mathbf{x}) \overline{e_j(\mathbf{x})}) \Gamma(i, j) \right| d\mathbf{x}, \end{aligned} \quad (4.50)$$

where the error in Γ due to discretization is neglected and the last approximation is derived similar to (4.45).

We now analyze the effect of the forward problem discretization on the accuracy of the reconstructed optical image. Let $\tilde{\alpha}^\lambda$ be the solution of

$$\tilde{K} \tilde{\alpha}^\lambda = \tilde{\gamma}, \quad (4.51)$$

where \tilde{K} and $\tilde{\gamma}$ are the finite dimensional approximations to K and γ , respectively. Then, by Theorem 10.1 in [21], the error in the solution $\tilde{\alpha}^\lambda$ with respect to the actual solution α^λ is bounded by

$$\|\alpha^\lambda - \tilde{\alpha}^\lambda\| \leq \frac{1}{\lambda} \left\{ \|(\tilde{K} - K)\alpha^\lambda\| + \|\tilde{\gamma} - \gamma\| \right\}. \quad (4.52)$$

In the next theorem, we will expand the terms in (4.52) to show explicitly the effect of the forward problem discretization on the accuracy of the inverse problem solution.

Theorem 2: Let h_m^i and h_m^j be the diameter of the smallest ball that contains the m^{th} element in the finite element solutions G_i^* and G_j , respectively. Then, a bound for the error in the solution $\tilde{\alpha}^\lambda$ due to operator approximation \tilde{K} is given:

$$\begin{aligned} \|\alpha^\lambda - \tilde{\alpha}^\lambda\|_{L^1(\Omega)} &\leq \frac{C}{\lambda} \max_{i,j} \|g_i^* g_j\|_{L^1(\Omega)} \\ &\times \left(\sum_{m=1}^{N_\Delta} \sum_{i,j}^{N_d, N_s} \left(2\|g_j \alpha^\lambda\|_{0,m} + \|\alpha\|_\infty \|g_j\|_{0,m} \right) \|g_i^*\|_{1,m} h_m^i \right. \\ &\left. + \sum_{m=1}^{N_\Delta} \sum_{i,j}^{N_d, N_s} \left(2\|g_i^* \alpha^\lambda\|_{0,m} + \|\alpha\|_\infty \|g_i^*\|_{0,m} \right) \|g_j\|_{1,m} h_m^j \right), \end{aligned} \quad (4.53)$$

where C is a positive constant.

Proof. Using (4.49), (4.43), and (4.45), we can write

$$\begin{aligned}
& \|(\tilde{K} - K)\alpha^\lambda\|_{L^1(\Omega)} \approx 2\|A_a^*(A_a - \tilde{A}_a)\alpha^\lambda\|_{L^1(\Omega)} \\
& = 2\left\| \sum_{i,j}^{N_d, N_s} g_i^*(\mathbf{x}) \overline{g_j(\mathbf{x})} \int_{\Omega} \left(g_j(\mathbf{x}) \overline{e_i^*(\mathbf{x})} + \overline{g_i^*(\mathbf{x})} e_j(\mathbf{x}) \right) \alpha^\lambda(\mathbf{x}) d\mathbf{x} \right\|_{L^1(\Omega)} \\
& \leq 2 \max_{i,j} \|g_i^* g_j\|_{L^1(\Omega)} \sum_{i,j}^{N_d, N_s} \int_{\Omega} \left| \left(g_j(\mathbf{x}) \overline{e_i^*(\mathbf{x})} + \overline{g_i^*(\mathbf{x})} e_j(\mathbf{x}) \right) \alpha^\lambda(\mathbf{x}) \right| d\mathbf{x}. \tag{4.54}
\end{aligned}$$

An upper bound for the integral in (4.54) can be obtained as follows:

$$\begin{aligned}
& \int_{\Omega} \left| \left(g_j(\mathbf{x}) \overline{e_i^*(\mathbf{x})} + \overline{g_i^*(\mathbf{x})} e_j(\mathbf{x}) \right) \alpha^\lambda(\mathbf{x}) \right| d\mathbf{x} \\
& \leq \sum_{m=1}^{N_{\Delta}} \|e_i^*\|_{0,m} \|g_j \alpha^\lambda\|_{0,m} + \|e_j\|_{0,m} \|g_i^* \alpha^\lambda\|_{0,m}. \tag{4.55}
\end{aligned}$$

Note that $g_j \alpha^\lambda \in L^2$ since $|g_j \alpha^\lambda| \leq |g_j| |\alpha^\lambda|$. Similarly, $g_i^* \alpha^\lambda \in L^2$ since $|g_i^* \alpha^\lambda| \leq |g_i^*| |\alpha^\lambda|$. Using (4.55) in (4.54),

$$\begin{aligned}
& \|(\tilde{K} - K)\alpha^\lambda\|_{L^1(\Omega)} \\
& \leq 2 \max_{i,j} \|g_i^* g_j\|_{L^1(\Omega)} \sum_{m=1}^{N_{\Delta}} \sum_{i,j}^{N_d, N_s} \|e_i^*\|_{0,m} \|g_j \alpha^\lambda\|_{0,m} + \|e_j\|_{0,m} \|g_i^* \alpha^\lambda\|_{0,m}. \tag{4.56}
\end{aligned}$$

To compute an upper bound for $\|\tilde{\gamma} - \gamma\|$, we first write

$$\begin{aligned}
& \int_{\Omega} \left| \sum_{i,j}^{N_d, N_s} \left(e_i^*(\mathbf{x}) \overline{g_j(\mathbf{x})} + \overline{g_i^*(\mathbf{x})} e_j(\mathbf{x}) \right) \Gamma(i, j) \right| d\mathbf{x} \\
& \leq \max_{i,j} |\Gamma(i, j)| \int_{\Omega} \sum_{i,j}^{N_d, N_s} |e_i^*(\mathbf{x}) \overline{g_j(\mathbf{x})} + \overline{g_i^*(\mathbf{x})} e_j(\mathbf{x})| d\mathbf{x} \\
& \leq \max_{i,j} |\Gamma(i, j)| \sum_{m=1}^{N_{\Delta}} \sum_{i,j}^{N_d, N_s} \left(\|e_i^*\|_{0,m} \|g_j\|_{0,m} + \|g_i^*\|_{0,m} \|e_j\|_{0,m} \right). \tag{4.57}
\end{aligned}$$

Noting (2.9),

$$\max_{i,j} |\Gamma(i, j)| \leq \max_{i,j} \|g_i^* g_j\|_{L^1(\Omega)} \|\alpha\|_{\infty}, \tag{4.58}$$

which leads to

$$\begin{aligned}
& \max_{i,j} |\Gamma(i, j)| \sum_{m=1}^{N_{\Delta}} \sum_{i,j}^{N_d, N_s} \left(\|e_i^*\|_{0,m} \|g_j\|_{0,m} + \|g_i^*\|_{0,m} \|e_j\|_{0,m} \right) \\
& \leq \max_{i,j} \|g_i^* g_j\|_{L^1(\Omega)} \|\alpha\|_{\infty} \left(\sum_{m=1}^{N_{\Delta}} \sum_{i,j}^{N_d, N_s} \|e_i^*\|_{0,m} \|g_j\|_{0,m} + \|g_i^*\|_{0,m} \|e_j\|_{0,m} \right). \tag{4.59}
\end{aligned}$$

We now use (4.56), (4.59), the corresponding discretization error estimates (3.24)-(3.25), and (4.52) to obtain (4.53). \square

- Remarks:** (i) Theorem 2 suggests the use of meshes designed individually for the solutions G_j , $j = 1, \dots, N_j$ and G_i^* , $i = 1, \dots, N_i$.
- (ii) Theorem 2 states explicitly the effect of the forward problem discretization on the accuracy of the inverse problem solution. In this context, Theorem 2 suggests a discretization scheme for the forward problem, where the discretization criterion is based on the inverse problem solution accuracy, rather than the accuracy of the forward problem solution.
- (iii) For each source, when solving for G_j , h_m^j has to be kept small where $(2\|g_i^* \alpha^\lambda\|_{0,m} + \|\alpha\|_\infty \|g_i^*\|_{0,m}) \|g_j\|_{1,m}$ is large. Note that $\|g_j\|_{1,m}$ will be large on the elements close to the j^{th} source.
- (iv) For each detector, when solving for G_i^* , h_m^i has to be kept small where $(2\|g_j \alpha^\lambda\|_{0,m} + \|\alpha\|_\infty \|g_j\|_{0,m}) \|g_i^*\|_{1,m}$ is large. Note that $\|g_i^*\|_{1,m}$ will be large on the elements close to the i^{th} detector.
- (v) $|g_j|$ and $|g_i^*|$ are higher close to the sources and detectors, respectively. Therefore, h_m^j has to be small around the j^{th} source and around all detectors, where α^λ is nonzero. Likewise, h_m^i has to be small around the i^{th} detector and around all sources, where α^λ is nonzero.
- (vi) If α^λ is nonzero on the whole domain Ω , then the error may become higher depending on the magnitude of $|g_j|$ and $|g_i^*|$.
- (vii) The regularization parameter affects the bound on $\|\alpha^\lambda - \tilde{\alpha}^\lambda\|_{L^1(\Omega)}$.
- (viii) Increasing the number of sources and detectors increases the bound on $\|\alpha^\lambda - \tilde{\alpha}^\lambda\|_{L^1(\Omega)}$.

4.3. Iterative Born Approximation

In this section, we explore the error in the inverse problem solution within an iterative linearization approach.

The error analysis presented in this paper covers the error which results from the discretization of the forward and inverse problems. If α is sufficiently low, then one iteration suffices to solve the inverse problem and the error analysis discussed above applies. When iterative linearization is considered to address the nonlinearity of the inverse problem, we can make use of the error analysis at each linearized step as follows: At the end of the $(r-1)^{th}$ linearization step, the absorption coefficient estimate is given by $\hat{\mu}_a^{(r-1)}(\mathbf{x}) = \mu_a^{(0)}(\mathbf{x}) + \sum_{t=1}^{r-1} \tilde{\alpha}_{n(t)}^\lambda$, where $\tilde{\alpha}_{n(t)}^\lambda$ has an error due to discretization with respect to the actual solution $\alpha_{(t)}^\lambda$. In the next linearization, an error on the new solution update $\hat{\mu}_a^{(r)}(\mathbf{x})$ will be introduced due to:

- (i) projection,

- (ii) the error $(\tilde{K} - K)^{(r-1)}$ in the operator $(\tilde{K})^{(r-1)}$ and the error $(\tilde{\gamma} - \gamma)^{(r-1)}$ in $(\tilde{\gamma})^{(r-1)}$ resulting from forward problem discretization, and
- (iii) the errors in $(\tilde{K})^{(r-1)}$ and $(\tilde{\gamma})^{(r-1)}$ due to error in G_j and G_i^* resulting from the error in $\hat{\mu}_a^{(r-1)}(\mathbf{x})$.

As a result, the error in $\hat{\mu}_a^{(r)}(\mathbf{x})$ at the r^{th} iteration is bounded by:

$$\|\mu_a(\mathbf{x}) - \hat{\mu}_a^{(r)}(\mathbf{x})\| = \left\| \sum_{t=1}^r \alpha_{(t)}^\lambda - \tilde{\alpha}_{n(t)}^\lambda \right\| \leq \sum_{t=1}^r \|\alpha_{(t)}^\lambda - \tilde{\alpha}_{n(t)}^\lambda\|, \quad (4.60)$$

assuming that the background absorption $\mu_a^{(0)}(\mathbf{x})$ is approximated accurately.

5. Adaptive mesh generation

In this section, we first discuss the adaptive mesh design for the discretization of the forward and inverse problems based on Theorems 1 and 2, such that the resulting error in the reconstructed optical image due to each discretization is below a preset bound. Next, we present practical adaptive mesh generation algorithms for the forward and inverse problems, respectively.

5.1. Adaptive Mesh Generation for the Forward Problem

Let the mesh parameter h_m^j for g_j for $j = 1, \dots, N_s$ and the mesh parameter h_m^i for g_i^* for $i = 1, \dots, N_d$ be chosen so that:

$$h_m^j \leq \frac{\epsilon_f}{\sum_i^{N_d} (2\|g_i^* \alpha^\lambda\|_{0,m} + \|\alpha\|_\infty \|g_i^*\|_{0,m}) \|g_j\|_{1,m}} = B_j, \quad (5.61)$$

$$h_m^i \leq \frac{\epsilon_f}{\sum_j^{N_s} (2\|g_j \alpha^\lambda\|_{0,m} + \|\alpha\|_\infty \|g_j\|_{0,m}) \|g_i^*\|_{1,m}} = B_i^*, \quad (5.62)$$

where the tolerance ϵ_f will be defined later. Then, by Theorem 2, the error in the reconstructed image due to the forward problem discretization is bounded by:

$$\frac{C}{\lambda} \max_{i,j} \|g_i^*(\mathbf{x}) g_j(\mathbf{x})\|_{L^1(\Omega)} N_\Delta (N_d + N_s) \epsilon_f = \tilde{\epsilon}^f, \quad (5.63)$$

where C is a positive constant and $\tilde{\epsilon}^f$ is the total allowable error in the reconstructed optical image due to the forward problem discretization. Equation (5.63) implies the following value for ϵ_f :

$$\epsilon_f = \frac{\lambda \tilde{\epsilon}^f}{C(N_d + N_s) N_\Delta \max_{i,j} \|g_i^*(\mathbf{x}) g_j(\mathbf{x})\|_{L^1(\Omega)}}. \quad (5.64)$$

In practice, B_j and B_i^* in (5.61)-(5.62) can not be computed since α , α^λ , g_j , and g_i^* are unknown. However, B_j and B_i^* can be estimated by using approximations for the functions involved in these bounds, based on either *a priori* information or on the

recent forward and inverse problem solution updates. Then, the elements whose mesh parameter h_m^j (h_m^i) exceeds B_j (B_i^*) can be determined and refined to satisfy (5.61)-(5.62).

Algorithm 1 outlines the adaptive mesh generation algorithm for the forward problem in the form of a pseudocode. The algorithm is performed for each source and detector before the linearization of the inverse problem and it yields a family of adaptively refined meshes with conforming elements. We use Rivara's algorithm [25] for refinement.

Algorithm 1 The pseudocode for the mesh generation algorithm for the forward problem, prior to the linearization of the inverse problem.

```

◇ Generate an initial uniform mesh  $(\Delta, N_\Delta)$ ,  $\Delta = \bigcup_{m=1}^{N_\Delta} \{\Delta_m\}$ 
◇ Set  $\epsilon^f$ 
◇ Initialize the set of marked elements:  $M_e \leftarrow \{\}$ 
◇  $flag = True$ 
  while  $flag = True$ 
    for each element  $\Delta_m \in \Delta$  with mesh parameter  $h_m^j$  ( $h_m^i$ )
      if first linearization
        . Use analytical solutions for  $g_j$  and  $g_i^*$  and a priori anatomical
          information about  $\alpha$  to compute the bound  $B_j$  in (5.61) ( $B_i^*$  in (5.62))
      else
        . Use current solution updates  $G_j$  and  $G_i^*$  and  $\tilde{\alpha}_n^\lambda$ 
          to compute  $B_j$  in (5.61) ( $B_i^*$  in (5.62))
      end
      if  $h_m^j > B_j$  ( $h_m^i > B_i^*$ )
        .  $M_e \leftarrow M_e \cup \{\Delta_m\}$ 
      end
    end
  end

  if  $M_e \neq \{\}$ 
    . Refine the marked elements and update the mesh  $\Delta$ 
    .  $M_e \leftarrow \{\}$ 
  else
    .  $flag = False$ 
  end
end
◇ Solve for  $G_j$  ( $G_i^*$ ).

```

In practice, after the first sweep of refinement, one can compute the bound B_j and B_i^* only for the new elements. We note that for the initial mesh design, we use a model problem to compute the terms in the error bound relevant to the forward problem solution (see Appendix D). If there is no *a priori* information, α^λ can be assumed to be spatially constant at the first linearization step. After the first linearization, the norms in B_j and B_i^* relevant to g_j and g_i^* are not expected to change significantly. In this context, the terms $\|g_j \alpha^\lambda\|_{0,m}$, $\|g_i^* \alpha^\lambda\|_{0,m}$ in (5.61) and (5.62) can be bounded by $\|g_j\|_{0,m} \|\alpha^\lambda\|_{\infty,m}$ and $\|g_i^*\|_{0,m} \|\alpha^\lambda\|_{\infty,m}$, respectively. Therefore, one can store the norms $\|g_j\|_{0,m}$ and $\|g_i^*\|_{0,m}$ at the end of the first mesh generation, and update B_j and B_i^* in the following mesh generations by using these stored values and the updated $\|\alpha^\lambda\|_{\infty,m}$ values.

In case ϵ_f (ϵ_f^*) can not be chosen in prior, we consider a posterior approach, set $\epsilon_f = 1$ ($\epsilon_f^* = 1$), and compute h_m^j/B_j (h_m^i/B_i^*) on each element, which is used as the indicator for refinement. Then, the elements with indicator value exceeding the average h_m^j/B_j (h_m^i/B_i^*) quantity are marked for refinement. We note that in this case, the algorithm has to be stopped when the number of nodes in the mesh exceeds the allowable number of nodes.

5.2. Adaptive mesh generation for the inverse problem:

Let the mesh parameter h_m for the solution of the inverse problem be defined as follows:

$$h_m \leq \epsilon_{inv} / \left(\sqrt{V_\Omega} \|I - T_n\|_{Y \rightarrow X_n} \|\alpha^\lambda\|_{1,m} + \frac{1}{\lambda} \|T_n\|_{Y \rightarrow X_n} \times \max_{i,j} \|g_i^*(\mathbf{x}) g_j(\mathbf{x})\|_{L^1(\Omega)} \sum_{i,j}^{N_d, N_s} \|g_i^*(\mathbf{x}) g_j(\mathbf{x})\|_{0,m} \|\alpha^\lambda\|_{1,m} \right) = B_{inv}. \quad (5.65)$$

Then, by Theorem 1, the error in the reconstructed image due to inverse problem discretization is bounded by

$$CN_\Delta \epsilon_{inv} = \tilde{\epsilon}^{inv}, \quad (5.66)$$

where C is a positive constant and $\tilde{\epsilon}^{inv}$ is the total allowable error in the reconstructed optical image due to inverse problem discretization.

We present the pseudocode for our adaptive mesh generation algorithm used at each linearization of the inverse problem in Algorithm 2. Similar to the forward problem discretization, we use Rivara's algorithm [25] for the refinement of the elements.

In practice, B_{inv} in (5.65) can not be computed since α^λ , g_j , g_i^* , and T_n are unknown. Similar to the approach described in Section 5.1, we can compute an estimate for B_{inv} by using the uniform boundedness of the operator T_n (See Appendix C) and by using approximate values for the functions involved in B_{inv} . In this context, we use either *a priori* information or the recent forward and inverse problem solution updates

Algorithm 2 The pseudocode for the mesh generation algorithm at every linearization step of the inverse problem.

```

  ◇ Generate an initial uniform mesh  $(\Delta, N_\Delta)$ ,  $\Delta = \bigcup_{m=1}^{N_\Delta} \{\Delta_m\}$ 
  ◇ Set  $\epsilon_{inv}$ 
  ◇ Initialize the set of marked elements:  $M_e \leftarrow \{\}$ 
  ◇  $flag = True$ 
  while  $flag = True$ 
    for each element  $\Delta_m \in \Delta$  with mesh parameter  $h_m$ 
      if first linearization
        . Use current solution updates  $G_j$  and  $G_i^*$  and a priori information
          about  $\alpha$  to compute  $B_{inv}$  in (5.65)
      else
        . Use current solution updates  $G_j$  and  $G_i^*$  and  $\tilde{\alpha}_n^\lambda$ 
          to compute  $B_{inv}$  in (5.65)
      end
      if  $h_m > B_{inv}$ 
        .  $M_e \leftarrow M_e \cup \{\Delta_m\}$ 
      end
    end

    if  $M_e \neq \{\}$ 
      . Refine the marked elements and update the mesh  $\Delta$ 
      .  $M_e \leftarrow \{\}$ 
    else
      .  $flag = False$ 
    end
  end
  ◇ Solve for  $\tilde{\alpha}_n^\lambda$ .

```

to calculate (5.65) on each element. Then, the elements with the mesh parameter $h_m > B_{inv}$ are determined and refined to satisfy (5.65).

In order to save computations, after the first sweep of refinement, one can compute the bound B_{inv} only for the new elements. Furthermore, similar to the approach described in Section 5.1, the term $\|g_i^*(\mathbf{x})g_j(\mathbf{x})\|_{0,m}$ in (5.65) can be stored after the first mesh generation and can be used in the following mesh generations. In this context, the bound B_{inv} can be updated by using only the updated $\|\alpha^\lambda\|_{\infty,m}$ value.

Note that, in practice, one of the two terms in the denominator of B_{inv} will be dominant depending on the value of λ . Thus, we consider only the dominant term for

the computation of B_{inv} . In case ϵ_f can not be chosen in prior, we consider a posterior approach, set $\epsilon_{inv} = 1$ and compute $\|\alpha^\lambda\|_{1,m} h_m$ or $\sum_{i,j}^{N_d, N_s} \|g_i^*(\mathbf{x}) g_j(\mathbf{x})\|_{0,m} \|\alpha^\lambda\|_{1,m} h_m$ on each element, which are used as refinement indicators. Then, the elements with indicator value which exceeds the average indicator value are refined. In this case, the algorithm has to be stopped when the number of nodes in the mesh exceeds the allowable number of nodes.

6. Numerical Experiments

We conduct a series of numerical experiments to demonstrate the implications of Theorems 1 and 2, and to present the effectiveness of the proposed adaptive mesh generation algorithms. We perform our experiments in 2D for ease of comparison and image quality appraisals.

In the first simulation, we consider a series of image reconstructions to show the effectiveness of the proposed adaptive mesh generation algorithms. In this context, we compare the images reconstructed by using uniform meshes for the forward and inverse problems to the images reconstructed by using adaptive meshes which are designed based on Theorems 1 and 2.

In the second simulation, we show the effect of the heterogeneity size on the accuracy of the reconstructed absorption images. Next, we demonstrate how this error can be addressed by the proposed adaptive discretization schemes.

In the final simulation study, we demonstrate the implication of Theorem 2 and show that meshes generated for the forward problem by using discretization error estimates which disregard the interaction between the solutions g_j and g_i^* and α^λ can lead to unstable image reconstructions. We note that the proposed adaptive mesh generation algorithm for the forward problem addresses this problem.

Note that in all experiments, we use triangular finite elements with piecewise linear Lagrange basis functions and we apply Gaussian elimination method to solve the forward problem (3.22)-(3.23) and the linearized inverse problem (3.26).

6.1. Simulation Study 1

In this simulation study, we consider the geometry shown in Figure 1(a). We simulate the optical data by solving the diffusion equation at $\omega = 0$ on a fine uniform grid with 61 nodes along x and y directions, where the refractive index mismatch parameter $a = 3$. 11 sources and 11 detectors are evenly spaced on the bottom and top edges of the square, respectively. The diffusion coefficient $D(\mathbf{x}) = 0.0410$ is assumed to be constant. The circular heterogeneity with absorption coefficient $\mu_a = 0.2 \text{ cm}^{-1}$ is embedded in an optically homogeneous background with $\mu_a = 0.04 \text{ cm}^{-1}$.

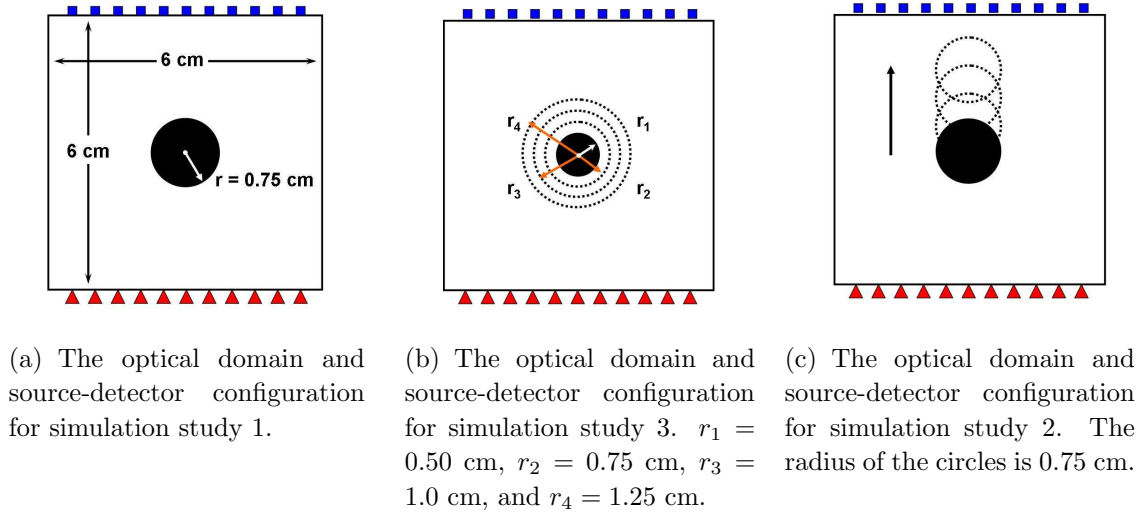


Figure 1. The setups used for the simulation studies 1, 2, and 3. The squares and triangles denote the detectors and sources, respectively.

In order to obtain a series of of absorption imaging problems using the same setup, we consider 5 values for the background absorption value. Then, for each imaging problem, we consider three mesh scenarios: Uniform mesh for both forward and inverse problems; adaptive mesh for the forward problem and uniform mesh for the inverse problem; and adaptive meshes for both forward and inverse problems. We refer to Table 2 for a brief outline of the first simulation study.

Table 2. The mesh scenarios and the background μ_a values in simulation study 1.

Mesh (Forward)	Mesh (Inverse)	Background μ_a (cm ⁻¹)
Uniform	Uniform	0.032, 0.036, 0.040, 0.044, 0.050
Adaptive	Uniform	0.032, 0.036, 0.040, 0.044, 0.050
Adaptive	Adaptive	0.032, 0.036, 0.040, 0.044, 0.050

The uniform mesh used for the forward problem discretization has 625 nodes and is shown in Figure 2(a). The uniform mesh for the inverse problem has 313 nodes and is shown in Figure 2(b). We use the algorithms described in Sections 5.1 and 5.2 to generate the adaptive meshes for the forward and inverse problems. The number of nodes in each of the adaptive meshes used for the forward problem does not exceed 750. An example for the adaptive mesh generated for a source located at (1.0, 0) is shown in Figure 2(c). For an example, the adaptive mesh for the inverse problem generated for the case where the background $\mu_a = 0.050$ cm⁻¹ has 418 nodes and is shown in Figure 2(d).

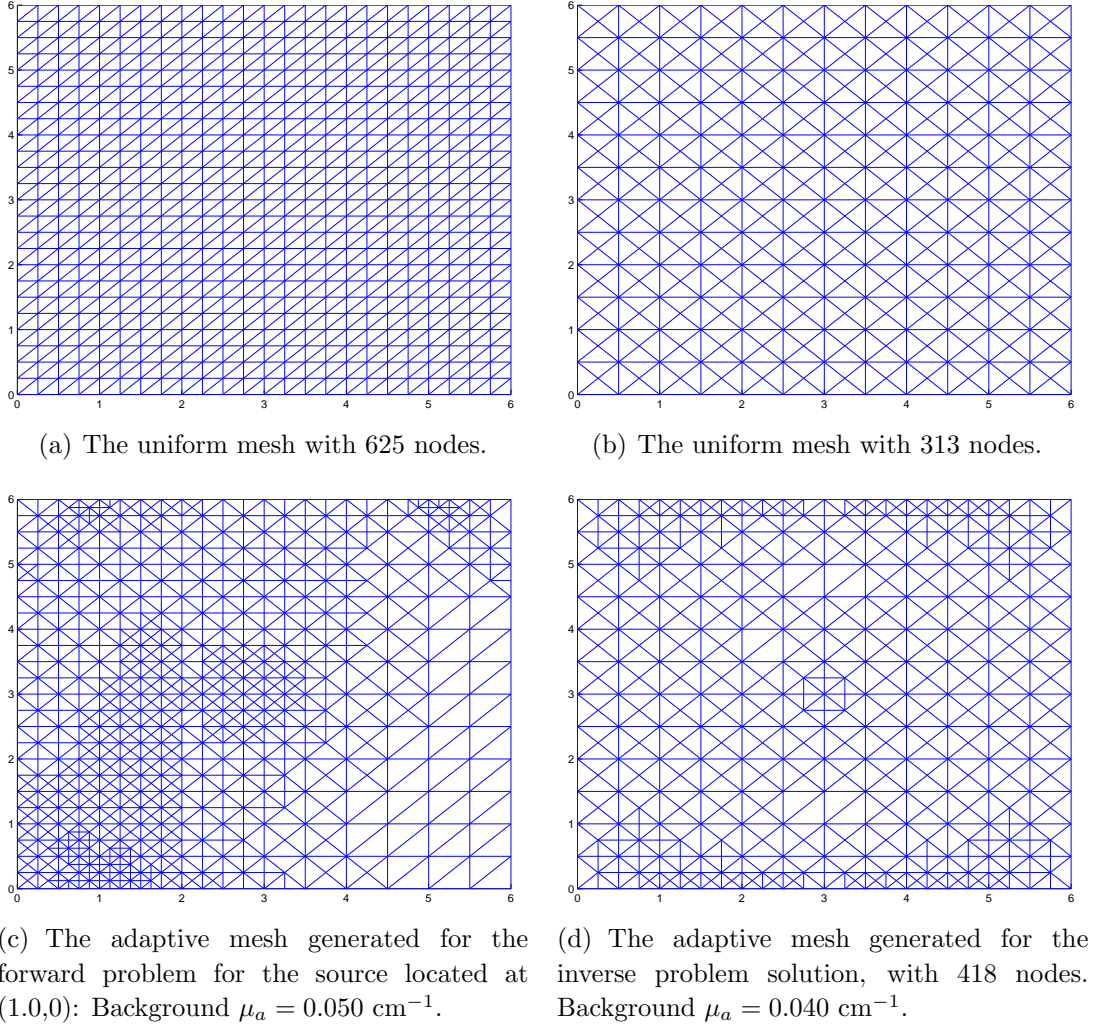


Figure 2. Examples of meshes used in the first simulation study.

For the inverse problem, we set the regularization parameter λ to 10^{-7} in all experiments. We consider the image reconstructed by using fine uniform meshes (61×61 nodes for the forward problem and 61×61 nodes for the inverse problem) as the reference image, which is assumed to possess no error due to discretization. We compute the error $\|\alpha^\lambda - \tilde{\alpha}_n^\lambda\|_{L^1(\Omega)}$ for each image reconstruction and tabulate the results in Table 3. We see that the error in the images reconstructed by using uniform meshes for both forward and inverse problems is significantly reduced by the use of adaptively refined meshes. A similar behavior is observed for all choices of background absorption value.

We present image reconstructions in Figures 3 and 4 for the two extreme cases, where the background absorption value is equal to 0.032 and 0.050 cm^{-1} , respectively. Figures 3(a) and 4(a) display the reference images used to compute the error values given in Table 3. Figures 3(c) and 3(d) show that the optical heterogeneity is resolved

Table 3. The error $\|\alpha^\lambda - \tilde{\alpha}_n^\lambda\|_{L^1(\Omega)}$ for each experiment described in the simulation study 1 and Table 2. The first column shows the type of the meshes used in the forward and inverse problems, respectively. The unit of background μ_a is cm^{-1} .

	Background μ_a :	0.032	0.036	0.040	0.044	0.050
Uniform-Uniform	$\ \alpha^\lambda - \tilde{\alpha}_n^\lambda\ _{L^1(\Omega)} :$	0.2325	0.2559	0.2773	0.2932	0.3013
Adaptive-Uniform	$\ \alpha^\lambda - \tilde{\alpha}_n^\lambda\ _{L^1(\Omega)} :$	0.1238	0.1139	0.1166	0.1209	0.1278
Adaptive-Adaptive	$\ \alpha^\lambda - \tilde{\alpha}_n^\lambda\ _{L^1(\Omega)} :$	0.1043	0.0997	0.0998	0.1003	0.1009

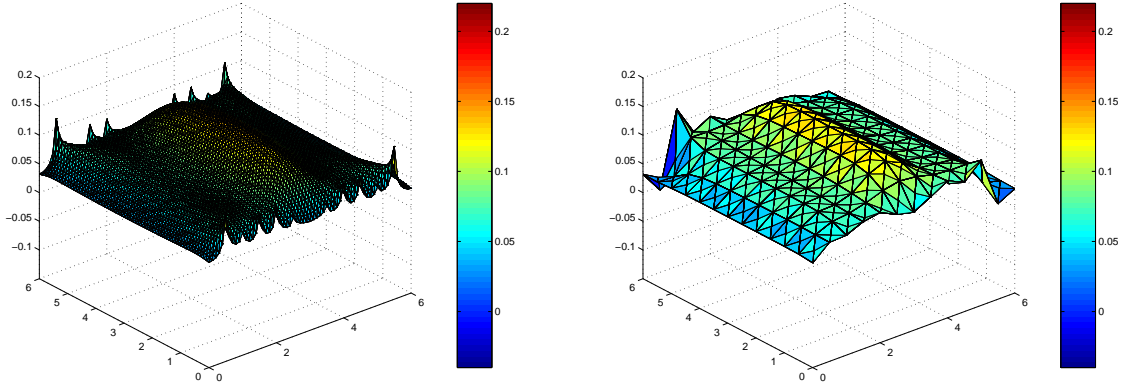
better by using adaptive meshes as compared to the reconstructed image obtained by using uniform meshes, which is shown in Figure 3(b). These results are consistent with the error values given in Table 3. A similar trend is seen in Figures 4(c) and 4(d). Note that the number of nodes in the adaptive meshes is almost equal to the number of nodes that the uniform meshes have. In Figure 5, we show the cross-sectional views from the reconstructed images. We see that the use of coarse uniform meshes fails to resolve the circular heterogeneity especially for the case in which the background $\mu_a = 0.032 \text{ cm}^{-1}$.

6.2. Simulation Study 2

In this study, we consider the geometry shown in Figure 1(b). To simulate the optical data, we use the same source-detector configuration considered in the first simulation study. We simulate the optical data by solving the diffusion equation at $\omega = 0$ on a fine uniform grid with 61 nodes along x and y directions, where the refractive index mismatch parameter $a = 3$. The diffusion coefficient $D(\mathbf{x})$ is assumed to be constant and $D(\mathbf{x}) = 0.0410 \text{ cm}$.

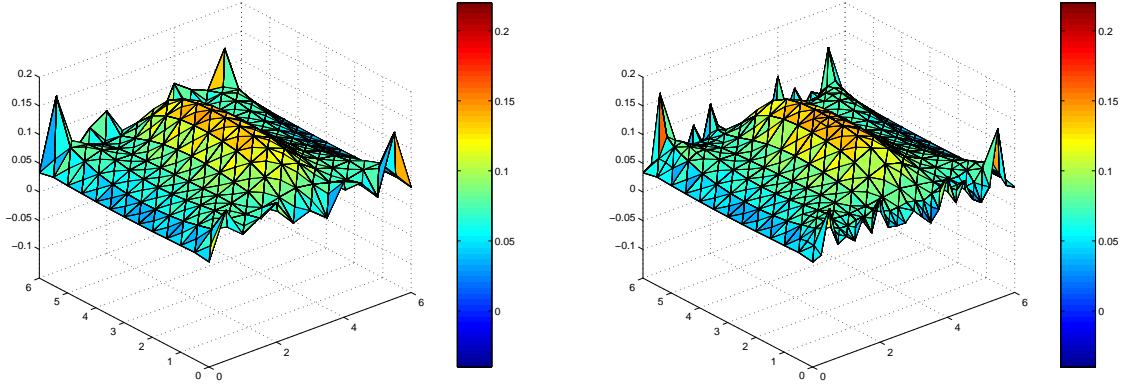
We consider 4 different radii for the circular heterogeneity with $\mu_a = 0.20 \text{ cm}^{-1}$ embedded in a background with $\mu_a = 0.040 \text{ cm}^{-1}$ as shown in Figure 1(b). For each case, we compute the error for different mesh scenarios, similar to the first simulation study: Uniform mesh for both forward and inverse problems; adaptive mesh for the forward problem and uniform mesh for the inverse problem; and adaptive meshes for both forward and inverse problems. The adaptive meshes for this simulation study were generated based on Theorems 1 and 2, and the mesh generation algorithms described in the first simulation study and Section 5. The uniform meshes used for the forward and inverse problems are identical to those used in the first simulation study. We note that the number of nodes in the adaptive meshes generated for the forward and inverse problems is close to the number of nodes in the corresponding uniform meshes.

In Table 4, we tabulate the error norm $\|\alpha^\lambda - \tilde{\alpha}_n^\lambda\|$ obtained for each heterogeneity size with different mesh choices. Table 4 shows that the error increases with increasing



(a) The optical absorption image used as the reference for error computations.

(b) The reconstructed absorption image using the uniform mesh in Figure 2(a) for the forward, and the uniform mesh in Figure 2(b) for the inverse problem.



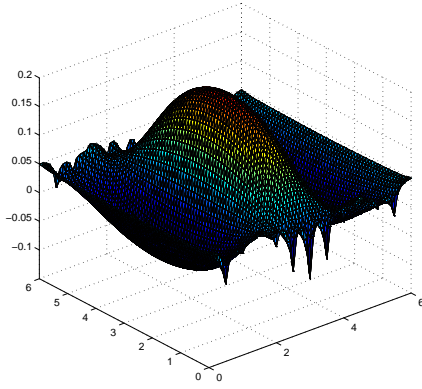
(c) The reconstructed absorption image using an adaptive mesh for the forward, and the uniform mesh in Figure 2(b) for the inverse problem.

(d) The reconstructed absorption image using an adaptive mesh for the forward, and the adaptive mesh in Figure 2(d) for the inverse problem.

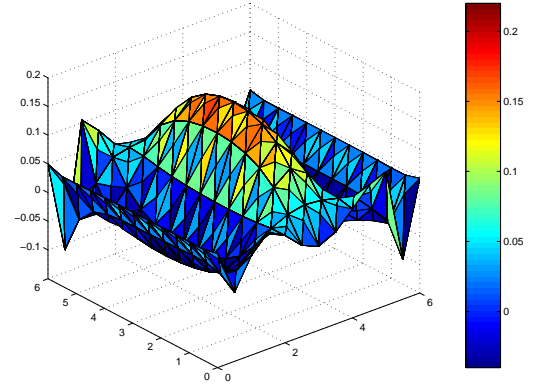
Figure 3. The reconstruction results of simulation study 1, with the background $\mu_a = 0.032 \text{ cm}^{-1}$.

heterogeneity size. We see that the reduction in the error as a result of using adaptive meshes is more significant for smaller sized heterogeneities. However, further reduction in the error norm $\|\alpha^\lambda - \tilde{\alpha}_n^\lambda\|$ is possible by increasing the number of nodes in the meshes.

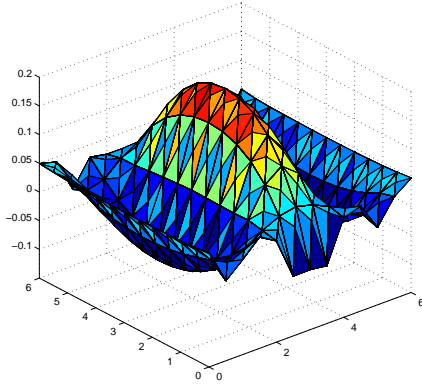
For brevity, we only show the reconstruction results for the extreme cases: $r = 0.5 \text{ cm}$ and $r = 1.25 \text{ cm}$. We note that the regularization parameter $\lambda = 5 \times 10^{-9}$ in all reconstructions. Figures 6(a) and 6(b) show the images used as the reference images α^λ in the calculation of the error norms $\|\alpha^\lambda - \tilde{\alpha}_n^\lambda\|$ listed in Table 4. Figures 6(e)-6(f) show that the adaptive meshes reduce the artifacts as compared to the images reconstructed



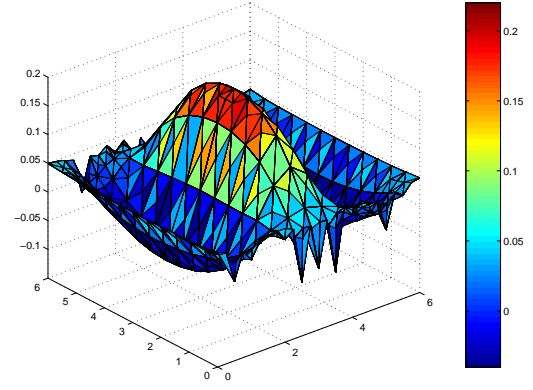
(a) The optical absorption image used as the reference for error computations.



(b) The reconstructed absorption image using the uniform mesh in Figure 2(a) for the forward, and the uniform mesh in Figure 2(b) for the inverse problem.



(c) The reconstructed absorption image using an adaptive mesh for the forward, and the uniform mesh in Figure 2(b) for the inverse problem.



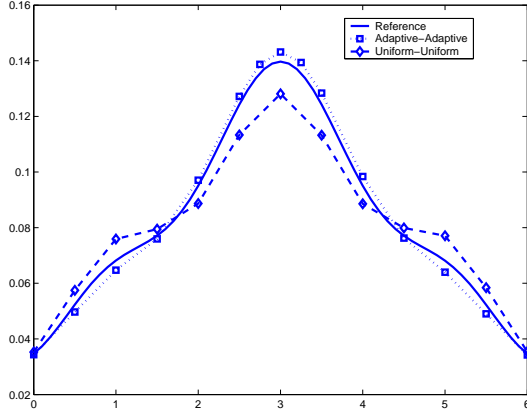
(d) The reconstructed absorption image using an adaptive mesh for the forward, and the adaptive mesh in Figure 2(d) for the inverse problem.

Figure 4. The results of simulation study 1, with the background $\mu_a = 0.050 \text{ cm}^{-1}$.

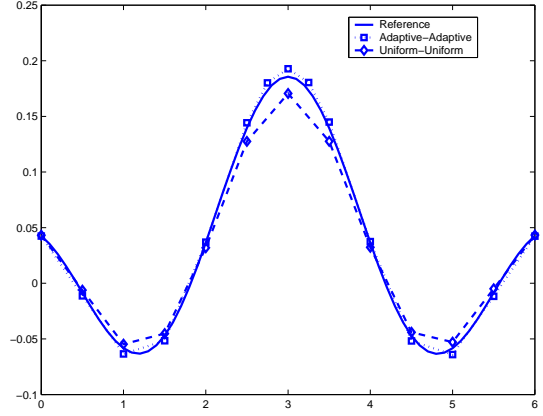
by using uniform meshes, which are shown in Figures 6(c)-6(d).

6.3. Simulation Study 3

In this simulation study, we consider the geometry shown in Figure 1(c). The center of the circular heterogeneity is moved vertically towards the detector side to see the effect on the imaging accuracy. Next, we show how the error in the reconstructed images due to discretization can be addressed by using appropriate meshes for the solutions of the forward and inverse problems. In this context, we compare the results obtained by using 1) uniform meshes, 2) the adaptive meshes generated using conventional *a priori*



(a) The cross-sectional cuts taken from Figures 3(a), 3(b), and 3(d), along x direction at $y = 3$. The solid, square, and diamond lines correspond to the cross-sectional cuts taken from the images shown in Figures 3(a), 3(d), and 3(b), respectively.



(b) The cross-sectional cuts taken from Figures 4(a), 4(b), and 4(d), along x direction at $y = 3$. The solid, square, and diamond lines correspond to the cross-sectional cuts taken from the images shown in Figures 4(a), 4(d), and 4(b), respectively.

Figure 5. The cross-sectional views from the reconstructed images in simulation study 1, corresponding to the cases where the background $\mu_a = 0.032$ and $\mu_a = 0.050 \text{ cm}^{-1}$, respectively.

Table 4. The L^1 norm of α^λ and the error $\|\alpha^\lambda - \tilde{\alpha}_n^\lambda\|_{L^1(\Omega)}$ for each experiment described in the simulation study 2. The first column shows the type of the meshes used in the forward and inverse problems, respectively. The radius of the circular heterogeneity is given in cm .

Radius:		0.50	0.75	1.0	1.25
$\ \alpha^\lambda\ _{L^1(\Omega)}:$		0.7196	1.3760	1.4759	1.7817
Uniform-Uniform	$\ \alpha^\lambda - \tilde{\alpha}_n^\lambda\ _{L^1(\Omega)}:$	0.5622	0.5706	0.5850	0.6337
Adaptive-Uniform	$\ \alpha^\lambda - \tilde{\alpha}_n^\lambda\ _{L^1(\Omega)}:$	0.2153	0.2776	0.3766	0.5113
Adaptive-Adaptive	$\ \alpha^\lambda - \tilde{\alpha}_n^\lambda\ _{L^1(\Omega)}:$	0.2020	0.2630	0.3592	0.5034

discretization error estimates, and 3) the adaptive meshes proposed in this study. By conventional error estimates, we mean the *a priori* discretization error estimates (3.24) and (3.25) for the solution of the forward problem, and the *a priori* interpolation error estimate (4.40) for the solution of the inverse problem.

To simulate the optical data, we use the same source-detector configuration considered in the first simulation study. We simulate the optical data by solving the diffusion equation at $\omega = 0$ on a fine uniform grid with 61 nodes along x and y

directions, where the refractive index mismatch parameter $a = 3$. We note that, in all reconstructions, the background absorption value is set to $\mu_a = 0.04 \text{ cm}^{-1}$ and the diffusion coefficient $D(\mathbf{x})$ is assumed to be constant and $D(\mathbf{x}) = 0.0410 \text{ cm}$.

The uniform meshes used in this simulation study are identical to the ones used in simulation studies 1 and 2. Sample meshes for the forward problem solution using the conventional and the proposed adaptive meshing strategies are shown in Figures 7(a)-7(b) and Figures 8(c) and 8(d), respectively. We see that the conventional adaptive mesh generation strategy leads to meshes refined around only sources or detectors, but not both. In contrast, Figures 8(c) and 8(d) show that the proposed strategy results in adaptive meshes refined around sources, detectors, and the heterogeneity as well. This observation is consistent with Theorem 2. The adaptive mesh for the inverse problem solution, which was generated using the *a priori* interpolation error estimate (4.40) is shown in Figure 8(f). Note that the mesh was generated for the case where the circular heterogeneity was centered at $(3.0, 3.5)$. The mesh generated based on Theorem 1 (Figure 8(e)) provides higher resolution close to the sources and detectors as compared to the mesh shown in Figure 8(f), which is merely refined around the heterogeneity.

In this simulation study, we consider 4 different positions for the center of the circular heterogeneity with radius 0.75 cm, along y -axis: center at $(3.0, 3.0)$, $(3.0, 3.5)$, $(3.0, 4.0)$, and $(3.0, 4.5)$, respectively. Similar to the previous simulations, we compute the error in the reconstructed images for all cases, and compare the error values attained by different meshing strategies. Finally we present the reconstructed images obtained by using different mesh strategies corresponding to the case where the circular inclusion is centered at $(3.0, 3.5)$ and $(3.0, 4.0)$.

Using the meshes for the forward problem discretization (see Figures 7(a)-7(b)) which were generated by using the conventional *a priori* discretization error estimates (3.24)-(3.25) leads to the image reconstructions shown in Figures 7(c) and 7(d), where the regularization parameter $\lambda = 10^{-8}$. We observe that the finite-dimensional operator does not provide a stable solution. We note that using an adaptive mesh for the inverse problem solution does not change the outcome (Figure 7(d)). Note also that the meshes generated by using the conventional *a priori* discretization error estimates (3.24)-(3.25) are sufficient to provide accurate finite element approximations to the actual solutions g_j and g_i^* . Therefore, the unstable reconstructions can be attributed to the errors $K - \tilde{K}$ and $\gamma - \tilde{\gamma}$, due to inappropriate discretization as noted by Theorem 2. In consistence with Theorem 2, this observation suggests that solving the forward problem accurately does not necessarily imply that approximate operator \tilde{K} and $\tilde{\gamma}$ are error-free. Therefore, in order to address such problems, one has to follow a discretization scheme based on Theorem 2 for the solution of the forward problem, which takes into account the interaction between the solutions of the diffusion equation and the associated adjoint problem, as described in Section 5.1.

In order to suppress the severe artifacts observed in Figures 7(c) and 7(d), we increased the regularization parameter and set $\lambda = 10^{-6}$. The resulting images are shown in Figures 7(e) and 7(f). As noted by Theorems 1 and 2, increasing the regularization parameter reduces the error in the reconstructed images. However, increasing the regularization parameter will also compromise the image quality and lead to over-smoothed images. In order to address the instability issue without degrading the image quality by using high regularization parameters, we modified the adaptive mesh generation method that lead to the meshes shown in Figures 7(a)-7(b). In this context, for the first 2 refinements, we used the proposed mesh generation algorithm based on Theorem 2 to generate an initial adaptive mesh; and for the next 2 refinements, we used the conventional error estimates (3.24)-(3.25). Following this modification, the samples of the resulting adaptive meshes are shown in Figures 8(a) and 8(b). For a comparison, we also present in Figures 8(c)-8(d), the adaptive meshes generated by using the proposed adaptive mesh generation algorithms as described in Section 5.1. We observe that the meshes shown in Figures 8(c)-8(d), indicate further refinement around sources, detectors and the circular heterogeneity as compared with the adaptive meshes shown in Figures 8(a) and 8(b).

Examples of the adaptive meshes generated for the inverse problem based on Theorem 1 and the conventional *a priori* interpolation estimate (4.40) are shown in Figures 8(e) and 8(f), respectively. We observe that the adaptive mesh shown in Figure 8(e) provides higher resolution around sources and detectors as compared to the adaptive mesh shown 8(f).

We note that the uniform meshes used in this simulation study are identical to those used in the previous simulation studies.

In order to compare the performance of the conventional and proposed adaptive mesh strategies, we perform 4 experiments and compute the error in the reconstructed optical absorption images. For each experiment we consider 5 different mesh strategies and refer to Table 5 for the description of these experiments.

We show the reconstructed optical absorption images for the two cases in Figures 9 and 10, corresponding to the circular heterogeneity centered at (3.0,3.5) and (3.0,4.0), respectively. Figures 9(a) and 10(a) show the reference absorption image reconstructions which are used to compute the error in the reconstructed optical images.

Figure 9(b) shows the image reconstructed using coarse uniform meshes for both the forward and inverse problems, for the case where the circular inclusion is centered at (3.0,3.5) where the regularization parameter was set to $\lambda = 10^{-8}$. With the same value of the regularization parameter, Figures 9(c) and 9(e) show the images obtained by using the adaptive meshes based on Theorems 2 and 1, respectively. We observe the improvements especially around the boundaries. Using the conventional adaptive meshes for the forward problem solution, which were modified around sources and

Table 5. The relevant parameters in the experiments 1-5 in simulation study 3. The acronym “Conv.” implies that the corresponding mesh was generated using the conventional *a priori* discretization error estimates (3.24)-(3.25) for the forward problem solution, and the conventional *a priori* interpolation error estimate (4.40) for the inverse problem solution. The acronym “Prop.” refers to the adaptive meshes generated by using the proposed adaptive mesh generation algorithms based on Theorems 1 and 2, for the inverse and forward problem solutions, respectively. The last column in the table shows the coordinates of the center of the circular heterogeneity, considered in each experiment.

	Mesh (Forward)	Mesh (Inverse)	Center at:
Exp. 1	Uniform	Uniform	[(3.0,3.0), (3.0,3.5), (3.0,4.0), (3.0,4.5)]
Exp. 2	Adaptive (Conv.)	Uniform	[(3.0,3.0), (3.0,3.5), (3.0,4.0), (3.0,4.5)]
Exp. 3	Adaptive (Conv.)	Adaptive (Conv.)	[(3.0,3.0), (3.0,3.5), (3.0,4.0), (3.0,4.5)]
Exp. 4	Adaptive (Prop.)	Uniform	[(3.0,3.0), (3.0,3.5), (3.0,4.0), (3.0,4.5)]
Exp. 5	Adaptive (Prop.)	Adaptive (Prop.)	[(3.0,3.0), (3.0,3.5), (3.0,4.0), (3.0,4.5)]

detectors as noted before, we ran into a similar instability problem. Therefore, in order to obtain better reconstructions with the conventional adaptive meshes, we set the regularization parameter $\lambda = 10^{-7}$ in the corresponding inverse problem formulations. The resulting reconstructed images are shown in Figures 9(d) and 9(f). In this case, we observe that the use of conventional adaptive meshes for the forward and inverse problems does not improve the image quality as compared to the reconstructed image shown in Figure 9(b), which is obtained by using coarse uniform meshes.

We observe similar results for the case where the circular inclusion is centered at (3.0,4.0). We note that the regularization parameter is set to $\lambda = 10^{-8}$ for all reconstructions except for the reconstructions obtained by using conventional adaptive meshes, in which case $\lambda = 10^{-7}$. Figures 9 show the reconstructed images corresponding to all meshing strategies.

Table 6 shows the error norm computations for all cases. The error values are consistent with Figures 9 and 10. In all cases, the proposed adaptive meshes significantly reduce the error in the reconstructed images. Furthermore, the image quality is enhanced by merely appropriate discretization, without having to increase the regularization parameter. In contrast, the conventional adaptive meshes perform worse than uniform meshes even though a higher regularization parameter is used.

7. Conclusion

In this work, we presented an error analysis to show the relationship between the error in the reconstructed optical absorption images and the discretization of the forward

Table 6. The error $\|\alpha^\lambda - \tilde{\alpha}_n^\lambda\|_{L^1(\Omega)}$ for each experiment described in the simulation study 3. The first column shows the type of the meshes used in the forward and inverse problems, respectively. The superscript ‘C’ denotes that the corresponding adaptive mesh generation is based on conventional *a priori* error estimates.

	Radius at:	(3.0,3.0)	(3.0,3.5)	(3.0,4.0)	(3.0,4.5)
Uniform-Uniform	$\ \alpha^\lambda - \tilde{\alpha}_n^\lambda\ _{L^1(\Omega)}:$	0.4539	0.4606	0.4733	0.4956
Adaptive-Uniform	$\ \alpha^\lambda - \tilde{\alpha}_n^\lambda\ _{L^1(\Omega)}:$	0.2690	0.2695	0.2634	0.2507
Adaptive-Adaptive	$\ \alpha^\lambda - \tilde{\alpha}_n^\lambda\ _{L^1(\Omega)}:$	0.2433	0.2455	0.2459	0.2434
Adaptive-Uniform	$\ \alpha^\lambda - \tilde{\alpha}_n^{\lambda,C}\ _{L^1(\Omega)}:$	0.7989	0.7596	0.7072	0.6418
Adaptive-Adaptive	$\ \alpha^\lambda - \tilde{\alpha}_n^{\lambda,C}\ _{L^1(\Omega)}:$	0.8011	0.7614	0.7070	0.6351

and inverse problems. We summarized the implications of the error analysis in two theorems and proposed novel adaptive mesh generation algorithms for the forward and inverse problems. The theorems provide an insight into the impact of forward and inverse problem discretizations on the accuracy of the reconstructed optical absorption images. These theorems show that the error in the reconstructed optical image due to the discretization of each problem is bounded by roughly the multiplication of the discretization error in the corresponding solution and the solution of the other problem. Theorem 2 shows that solving the diffusion equation and the associated adjoint problem accurately may not ensure small values for $\|\tilde{K} - K\|$ and $\|\gamma - \tilde{\gamma}\|$, which may lead to large errors in the reconstructed optical images, depending on the value of the regularization parameter as well.

Based on the error analysis, we provided two practical adaptive mesh generation algorithms, one for the forward and one for the inverse problem, which take the interdependence between the two problems into account. Our simulation experiments showed that the proposed mesh generation algorithms significantly improve the accuracy of the reconstructed optical images while keeping the number of unknowns in the forward and inverse problems within the allowable limits. Furthermore, in our simulation studies, we showed that the adaptive mesh generation algorithms based on conventional error estimates may lead to high error in the reconstructed images.

The error analysis presented in this work can be extended to show the effect of the discretization error on the accuracy of simultaneous reconstruction of scattering and absorption coefficients. Our future work will focus on the error in the simultaneous reconstruction of scattering and absorption, resulting from the discretization of the forward and inverse problem. Note that the error analysis introduced in this paper is not limited to DOT, and can easily be adapted for similar inverse parameter estimation

problems.

Acknowledgments

This material is based upon work supported by NSF-BES-0353160, ONR-N00014-04-1-0694, and US Army Medical Research-W81XWH-04-1-0559. Any opinions, findings, and conclusions or recommendations expressed in this material are those of the authors and do not necessarily reflect the views of the National Science Foundation. Various portions of this research were supported by the Center for Subsurface Sensing and Imaging Systems, under the Engineering Research Centers Program of the National Science Foundation (Award Number EEC-9986821), and Rensselaer Polytechnic Institute.

Appendix

Appendix A. Boundedness of A_a

$$\|A_a \alpha\|_{l^1} = \sum_{i,j}^{N_d, N_s} \left| \int_{\Omega} H(\mathbf{x}_s^j, \mathbf{x}_d^i; \mathbf{x}) \alpha(\mathbf{x}) d\mathbf{x} \right|. \quad (\text{A.1})$$

We can write the following inequality:

$$\begin{aligned} \|A_a \alpha\|_{l^1} &\leq \sum_{i,j}^{N_d, N_s} \int_{\Omega} |H(\mathbf{x}_s^j, \mathbf{x}_d^i; \mathbf{x}) \alpha(\mathbf{x})| d\mathbf{x} \\ &\leq \left(\sum_{i,j}^{N_d, N_s} \int_{\Omega} |H(\mathbf{x}_s^j, \mathbf{x}_d^i; \mathbf{x})| d\mathbf{x} \right) \|\alpha(\mathbf{x})\|_{\infty}. \end{aligned} \quad (\text{A.2})$$

Using Schwarz' inequality, we can write an upper bound for the summation as follows:

$$\begin{aligned} \sum_{i,j}^{N_d, N_s} \int_{\Omega} |H(\mathbf{x}_s^j, \mathbf{x}_d^i; \mathbf{x})| d\mathbf{x} &= \sum_{i,j}^{N_d, N_s} \|g^*(\mathbf{x}; \mathbf{x}_d^i) g(\mathbf{x}; \mathbf{x}_s^j)\|_{L^1(\Omega)} \\ &\leq \sum_{i,j}^{N_d, N_s} \|g^*(\mathbf{x}; \mathbf{x}_d^i)\|_0 \|g(\mathbf{x}; \mathbf{x}_s^j)\|_0 \\ &\leq N_d N_s \max_i \|g_i^*\|_0 \max_j \|g_j\|_0, \end{aligned} \quad (\text{A.3})$$

which leads to

$$\|A_a \alpha\|_{l^1} \leq N_d N_s \max_i \|g_i^*\|_0 \max_j \|g_j\|_0 \|\alpha\|_{\infty}.$$

Therefore an upper bound for the norm of A_a is given by

$$\|A_a\|_{L^{\infty}(\Omega) \rightarrow l^1} \leq N_d N_s \max_i \|g_i^*\|_0 \max_j \|g_j\|_0. \quad (\text{A.4})$$

The boundedness of g_j and g_i^* imply that A_a is bounded. \square

Note that for actual Dirac-delta source and Dirac-delta adjoint source, g_j and g_i^* are also bounded such that $g_j, g_i^* \in L^2(\Omega)$ [22].

Appendix B. Compactness of A_a

A_a is bounded by (A.4). Furthermore A_a maps the infinite dimensional subspace L^{∞} to a finite-dimensional subspace $\mathbb{C}^{N_d \times N_s}$, that is the range $R(A_a)$ of A_a satisfies $R(A_a) \in \mathbb{C}^{N_d \times N_s}$ due to the finite number of sources and detectors. As a result, A_a is compact [21]. The inverse problem is ill-posed as a consequence of compactness [21]. \square

Appendix C. Proof of the Lemma

The identity operator I is a bounded operator with bounded inverse and $(P_n I)^{-1} = I : Y_n \rightarrow Y_n$. Furthermore $\|P_n\|$ is bounded [5]

$$\|P_n\| = \max_{\mathbf{x} \in \Omega} \sum_{k=1}^n |L_k(\mathbf{x})|, \quad (\text{C.1})$$

where $L_k(\mathbf{x})$ are the piecewise linear Lagrange basis functions. $A = A_a^* A_a$ is bounded and compact, and $K = \lambda I + A$ is injective. As a result, by Theorem 13.7 in [21], the projection method also converges for $K = \lambda I + A$. Convergence of projection for K implies $(P_n K)^{-1} P_n K \alpha^\lambda \rightarrow \alpha^\lambda$, $n \rightarrow \infty$ for $(P_n K)^{-1} P_n K : X \rightarrow X_n$ [21].

It follows from the proof of Theorem 13.7 in [21] that $[I + \frac{1}{\lambda} P_n A]^{-1} : Y_n \rightarrow X_n$ exists and is uniformly bounded for all sufficiently large n . Then from $P_n K = \lambda P_n [I + \frac{1}{\lambda} P_n A] = \lambda [I + \frac{1}{\lambda} P_n A]$, it follows that $P_n K : X_n \rightarrow Y_n$ is invertible for all sufficiently large n with the inverse given by

$$(P_n K)^{-1} = [I + \frac{1}{\lambda} P_n A]^{-1} \frac{1}{\lambda}. \quad (\text{C.2})$$

As a result we can write $(P_n K)^{-1} P_n K$ as follows:

$$(P_n K)^{-1} P_n K = [I + \frac{1}{\lambda} P_n A]^{-1} \frac{1}{\lambda} P_n K. \quad (\text{C.3})$$

Thus,

$$\|(P_n K)^{-1} P_n K\|_{X \rightarrow X_n} \leq C_M \frac{\|K\|}{\lambda} \quad (\text{C.4})$$

using the fact that $(I + \frac{1}{\lambda} P_n A)^{-1}$ is uniformly bounded, that is $\|(I + \frac{1}{\lambda} P_n A)^{-1}\|_{Y_n \rightarrow X_n} \leq C_M$ where $C_M > 0$ is independent of n and $\|P_n\|_{Y \rightarrow Y_n} = 1$ for piecewise linear Lagrange basis functions. \square

Appendix D. Solution of the Model Problem

In order to initialize the adaptive mesh for the solution of the forward problem (provided $D(\mathbf{x}) = \bar{D}$ and $\mu_a(\mathbf{x}) = \bar{\mu}_a$ are spatially constant), we use an analytical solution to compute the estimates of g_j and g_i^* . To derive an analytical 2D solution, we use polar coordinates to rewrite (2.1):

$$\frac{1}{\rho} \frac{\partial}{\partial \rho} \left(\rho \frac{\partial g}{\partial \rho} \right) + \frac{1}{\rho} \frac{\partial}{\partial \theta} \left(\rho \frac{\partial g}{\partial \theta} \right) + K_\Omega^2 g = - \frac{4\pi}{\rho} \frac{\delta(\rho - \rho_s) \delta(\theta - \theta_s)}{D},$$

where we consider an unbounded domain, model the source by a Dirac-delta function and $K_\Omega^2 = -(\mu_a c + j\omega)/cD$. Then the solution is given by [18]

$$g(\rho, \rho_s; \theta, \theta_s) = \frac{4}{D\pi} \left\{ \frac{1}{2} I_0(k_\Omega \rho_{<}) K_0(k_\Omega \rho_{>}) + \sum_{m=1}^{\infty} \cos[m(\theta - \theta_s)] I_m(k_\Omega \rho_{<}) K_m(k_\Omega \rho_{>}) \right\},$$

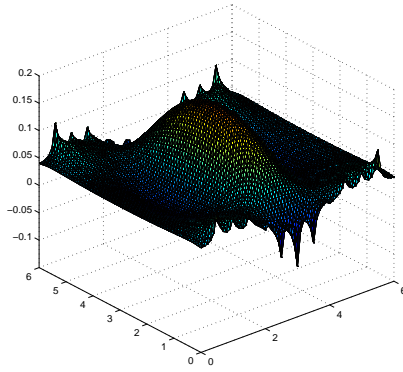
where I_m and K_m are the modified Bessel functions of the first and second kind, respectively [1] and $k_\Omega = \sqrt{-K_\Omega^2}$.

The solution of the problem in 3D can be derived in a similar manner [18, 29].

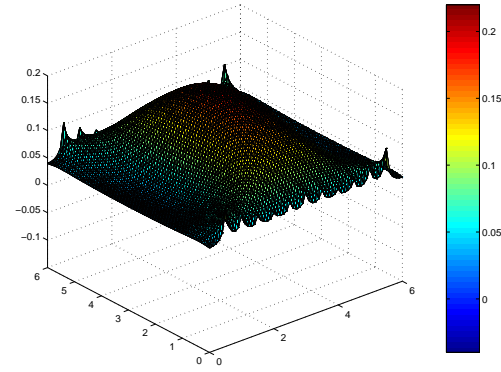
References

- [1] M. Abramowitz and I. A. Stegun. *Handbook of Mathematical Functions*. Dover, 1968.
- [2] M. Ainsworth and J. T. Oden. A unified approach to a posteriori error estimation using elemental residual methods. *Numerische Mathematik*, 65:23–50, 1993.
- [3] S. R. Arridge. Optical tomography in medical imaging. *Inverse Problems*, 15:R41–93, 1999.
- [4] S. R. Arridge, J. P. Kaipio, V. Kolehmainen, M. Schweiger, E. Somersalo, T. Tarvainen, and M. Vauhkonen. Approximation errors and model reduction with an application in optical diffusion tomography. *Inverse Problems*, 22:175–195, 2006.
- [5] K. Atkinson and H. Weimin. *Theoretical Numerical Analysis A Functional Analysis Framework*. Springer Verlag, 2001.
- [6] I. Babuška and W. C. Rheinboldt. Error estimates for adaptive finite element computations. *SIAM Journal on Numerical Analysis*, 15:736–754, 1978.
- [7] I. Babuška, O. C. Zienkiewicz, J. Gago, and E. R. de A. Oliveira. *Accuracy Estimates and Adaptive Refinements in Finite Element Computations*. John Wiley and Sons, 1986.
- [8] R. E. Bank and A. Weiser. Some a posteriori error estimators for elliptic partial differential equations. *Mathematics of Computation*, 44:283–301, 1985.
- [9] L. Beilina. *Adaptive Hybrid FEM/FDM Methods for Inverse Scattering Problems*. PhD thesis, Chalmers University of Technology, 2002.
- [10] J. G. Brankov, Y. Yang, and M. N. Wernick. Tomographic image reconstruction based on a content-adaptive mesh model. *IEEE Transactions on Medical Imaging*, 23(2):202–212, 2004.
- [11] S. C. Brenner and L. R. Scott. *The Mathematical Theory of Finite Element Methods*. Springer Verlag, 2002.
- [12] M. J. Eppstein, D. E. Dougherty, D. J. Hawrysz, and E. M. Sevick-Muraca. Three-dimensional Bayesian optical image reconstruction with domain decomposition. *IEEE Trans. on Medical Imaging*, 20(3):147–163, 2001.
- [13] L. C. Evans. *Partial Differential Equations*. American Mathematical Society, 1998.
- [14] X. Gu, Y. Xu, and H. Jiang. Mesh-based enhancement schemes in diffuse optical tomography. *Medical Physics*, 30(5):861–869, 2003.
- [15] M. Guven, B. Yazici, X. Intes, and B. Chance. An adaptive multigrid algorithm for region of interest diffuse optical tomography. In *International Conference in Image Processing*, volume 2 of *Proc. of IEEE*, pages 823–826, 2003.
- [16] M. Huang and Q. Zhu. Dual-mesh optical tomography reconstruction method with a depth correction that uses a priori ultrasound information. *Applied Optics*, 43(8):1654–1662, 2004.
- [17] F. Ihlenburg. *Finite Element Analysis of Acoustic Scattering*. Springer Verlag, 1998.
- [18] J. D. Jackson. *Classical Electrodynamics*. John Wiley and Sons, 1962.
- [19] A. Joshi, W. Bangerth, and E. M. Sevick-Muraca. Adaptive finite element based tomography for fluorescence optical imaging in tissue. *Optics Express*, 12(22):5402–5417, 2004.
- [20] J. Kaipio and E. Somersalo. *Statistical and computational inverse problems*, volume 160 of *Applied Mathematical Sciences*. Springer-Verlag, New York, 2005.
- [21] R. Kress. *Linear Integral Equations*. Springer Verlag, 1999.
- [22] K. Kwon and B. Yazıcı. Born expansion and Fréchet derivatives in diffuse optical tomography. In preparation.
- [23] R. Li, W. Liu, H. Ma, and T. Tang. Adaptive finite element approximation for distributed elliptic optimal control problems. *SIAM Journal on Control and Optimization*, 41:1321–1349, 2002.
- [24] M. Molinari, S. J. Cox, B. H. Blott, and G. J. Daniell. Adaptive mesh refinement techniques for electrical impedance tomography. *Physiological Measurement*, 22:91–96, 2001.
- [25] M. C. Rivara. Mesh refinement processes based on the generalized bisection of simplices. *SIAM*

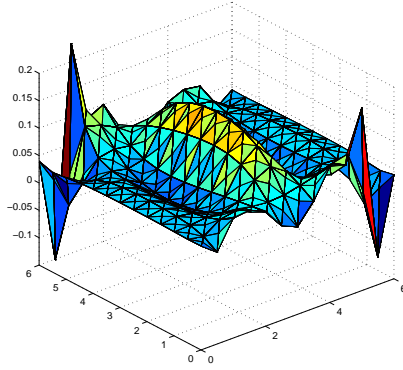
- Journal on Numerical Analysis*, 21(3):604–613, 1984.
- [26] T. Strouboulis and K. A. Hogue. Recent experiences with error estimation and adaptivity, part i: review of error estimators for scalar elliptic problems. *Computer Methods in Applied Mechanics and Engineering*, 97:399–436, 1992.
 - [27] M. Torregrossa, C. V. Zint, and P. Poulet. Image reconstruction in optical tomography: mesh influence. In *IV International Workshop, Computational Problems of Electrical Engineering*, pages 183–186, 2002.
 - [28] R. Verfurth. *A Review of A Posteriori Error Estimation and Adaptive Mesh Refinement Techniques*. Teubner-Wiley, 1996.
 - [29] S. Walker, D. A. Boas, and E. Gratton. Photon density waves scattered from cylindrical inhomogeneities: theory and experiments. *Applied Optics*, 37(10):1935–1944, 1998.



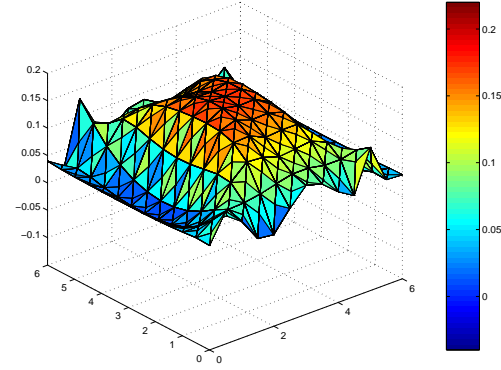
(a) The optical absorption image used as the reference for error computations. The image corresponds to the reconstruction of the circular heterogeneity of radius 0.5 cm.



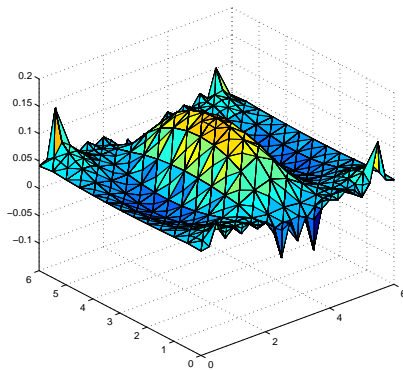
(b) The optical absorption image used as the reference for error computations. The image corresponds to the reconstruction of the circular heterogeneity of radius 1.25 cm.



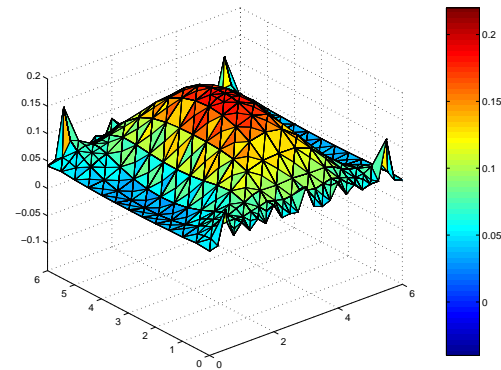
(c) The reconstructed absorption image using the uniform mesh in Figure 2(a) for the forward, and the uniform mesh in Figure 2(b) for the inverse problem.



(d) The reconstructed absorption image using the uniform mesh in Figure 2(a) for the forward, and the uniform mesh in Figure 2(b) for the inverse problem.

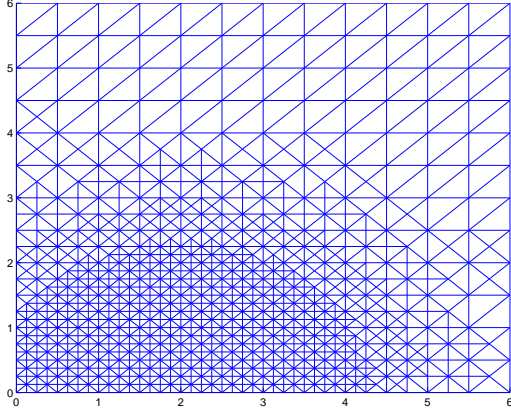


(e) The reconstructed absorption image using adaptive meshes for both the forward and the inverse problems.

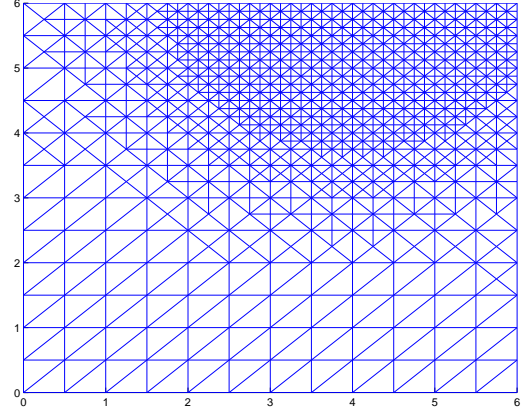


(f) The reconstructed absorption image using an adaptive mesh for both the forward and the inverse problems.

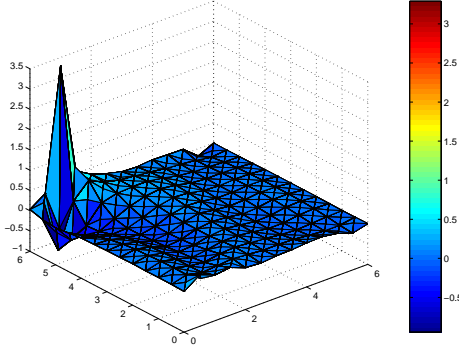
Figure 6. The results of simulation study 2. The left and right columns show the reconstructed images regarding the optical heterogeneity with radius 0.50 cm, and 1.25 cm, respectively. The background $\mu_a = 0.040 \text{ cm}^{-1}$ in all of the reconstructions. The reference images shown in (a) and (b) are obtained using a uniform mesh with 61×61 nodes in both the forward and inverse problems.



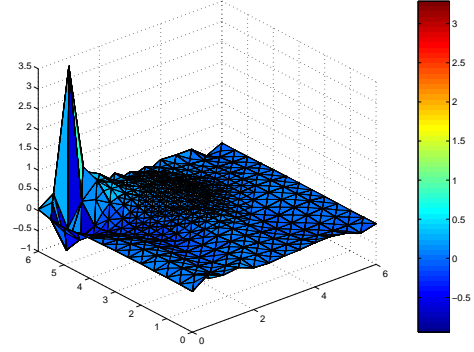
(a) The adaptive mesh with 865 nodes for the forward problem solution for the source located at (2.0,0), generated based on the conventional *a priori* error estimate (3.24).



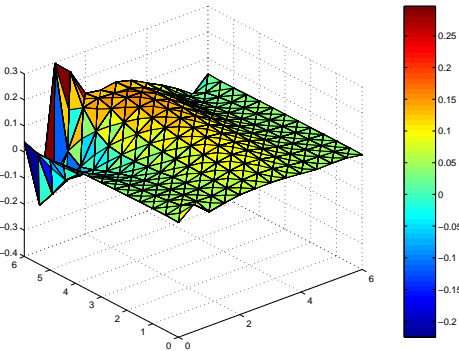
(b) The adaptive mesh with 865 nodes for the forward problem solution for the detector located at (4.0,6.0), generated based on the conventional *a priori* error estimate (3.25).



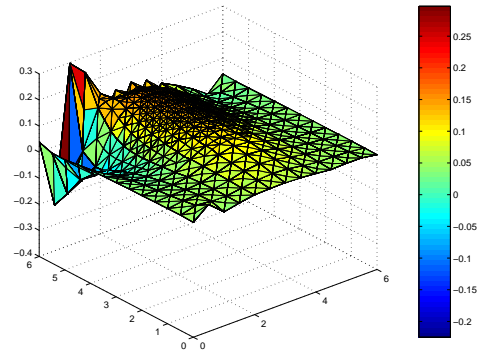
(c) The reconstructed optical image using adaptive mesh for the forward and uniform mesh for the inverse problem. $\lambda = 10^{-8}$.



(d) The reconstructed optical image using adaptive meshes for both the forward and inverse problems. $\lambda = 10^{-8}$.

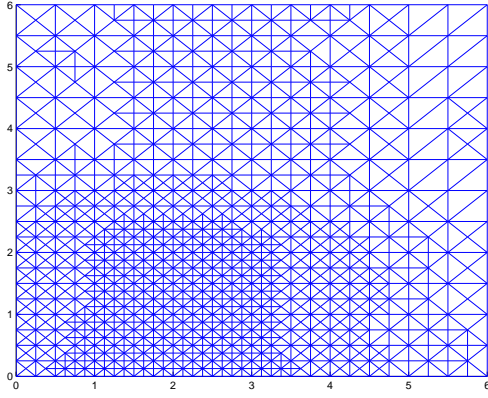


(e) The reconstructed optical image using adaptive mesh for the forward and uniform mesh for the inverse problem. $\lambda = 10^{-6}$.

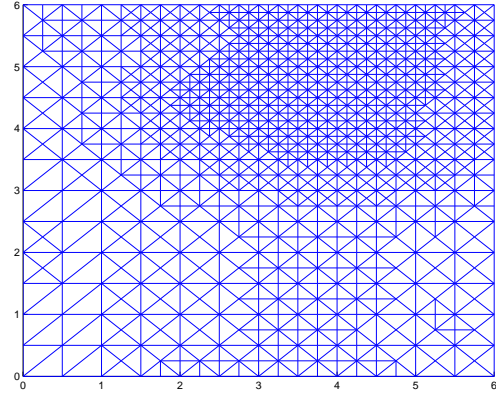


(f) The reconstructed optical image using adaptive meshes for both the forward and inverse problems. $\lambda = 10^{-6}$.

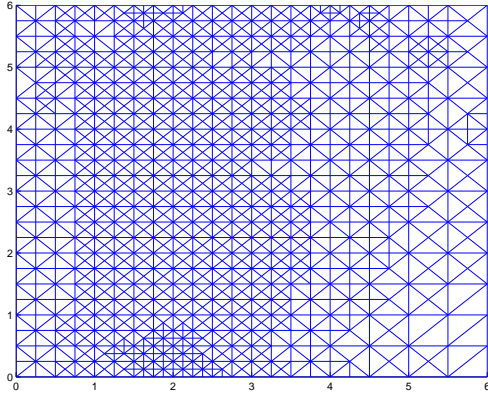
Figure 7. (a)-(b) Samples of adaptive meshes in the third simulation study, generated by using the conventional error estimates (3.24) and (3.25), which led to unstable optical image reconstruction shown in (c) to (f), for the circular heterogeneity centered at (3.0, 3.5). (c)-(d) The unstable optical image reconstructions in the third simulation study, obtained by using the adaptive meshes for the forward problem solution whose examples are shown in (a)-(b). $\lambda = 10^{-8}$. (e)-(f) The unstable optical image reconstructions in the third simulation study, obtained by using the adaptive meshes for the forward problem solution whose examples are shown in (a)-(b). λ was set to 10^{-6} to suppress the significantly large artifacts observed in (c)-(d).



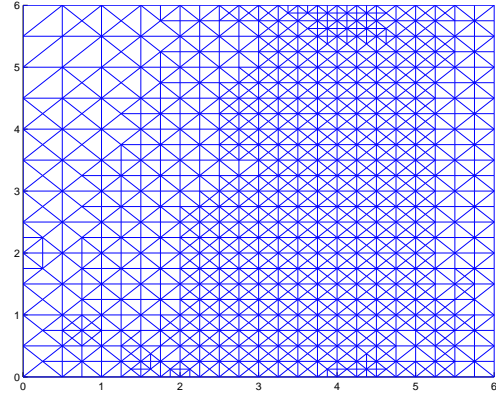
(a) The adaptive mesh with 942 nodes for the forward problem solution for the source located at $(2.0, 0)$, obtained by refining the adaptive mesh shown in Figure 7(a) around the detectors.



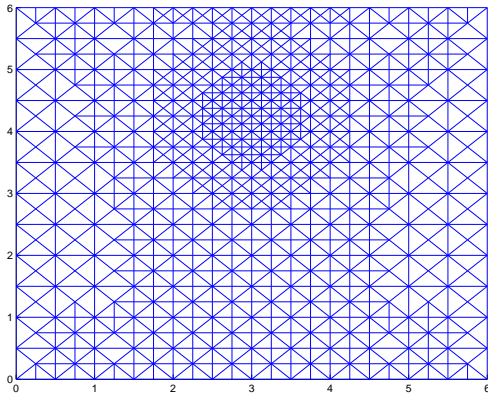
(b) The adaptive mesh with 955 nodes for the forward problem solution for the detector located at $(4.0, 6.0)$, obtained by refining the adaptive mesh shown in Figure 7(b) around the sources.



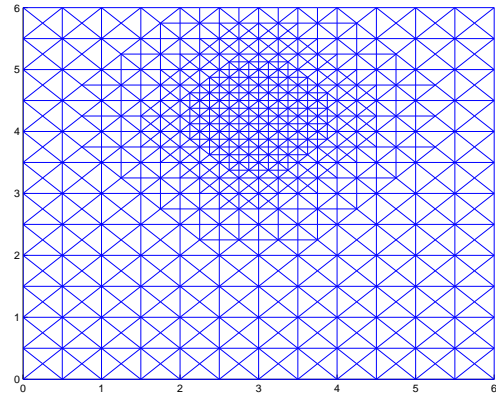
(c) The adaptive mesh with 895 nodes for the forward problem solution for the source located at $(2.0, 0)$, generated based on Theorem 2.



(d) The adaptive mesh with 896 nodes for the forward problem solution for the detector located at $(4.0, 6.0)$, generated based on Theorem 2.

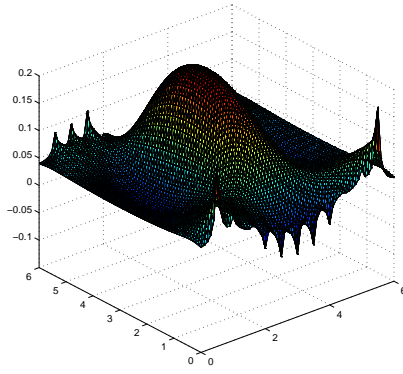


(e) The adaptive mesh with 691 nodes for the inverse problem solution, generated based on Theorem 1.

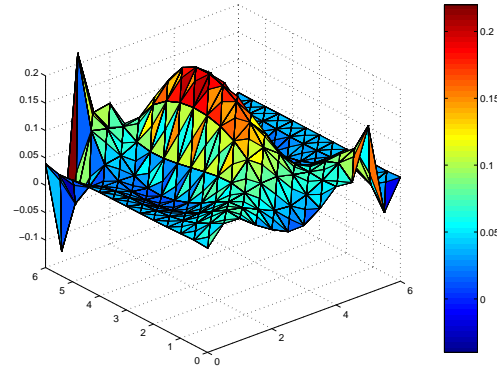


(f) The adaptive mesh with 609 nodes for the inverse problem solution, generated based on conventional error estimates.

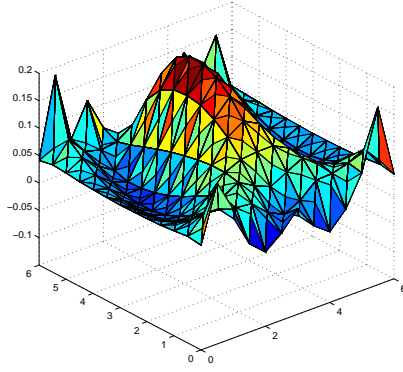
Figure 8. Samples of adaptive meshes used in the third simulation study, which led to the optical image reconstructions shown in Figure 10. The meshes were generated for the circular heterogeneity centered at $(3.0, 4.5)$.



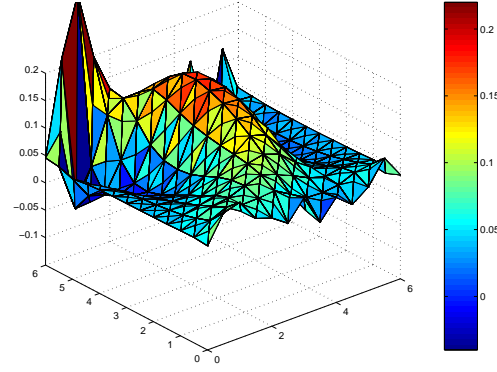
(a) The absorption image used as the reference in the error computations.



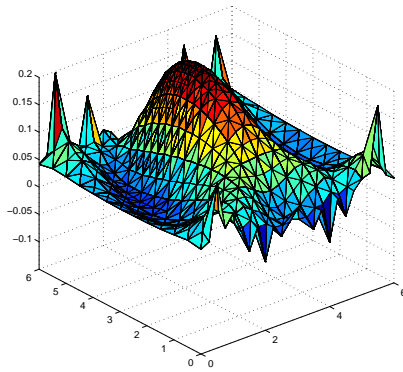
(b) The reconstructed absorption image using the uniform mesh in Figure 2(a) for the forward, and the uniform mesh in Figure 2(b) for the inverse problem.



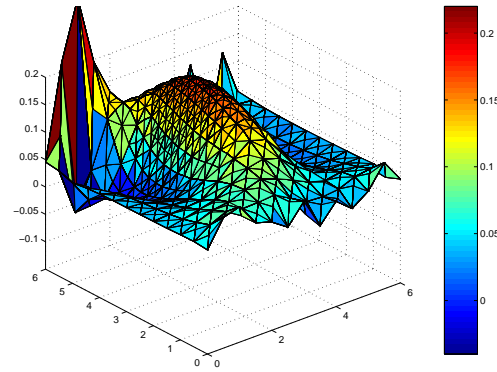
(c) The reconstructed absorption image using adaptive meshes based on Theorem 2 for the forward, and the uniform mesh in Figure 2(b) for the inverse problem.



(d) The reconstructed absorption image using adaptive meshes based on *a priori* error estimates (3.24) and (3.25) for the forward, and the uniform mesh in Figure 2(b) for the inverse problem.

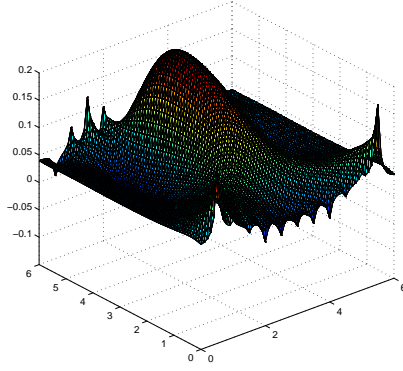


(e) The reconstructed absorption image using adaptive meshes based on Theorem 2 for the forward, and using the adaptive mesh based on Theorem 1 for the inverse problem.

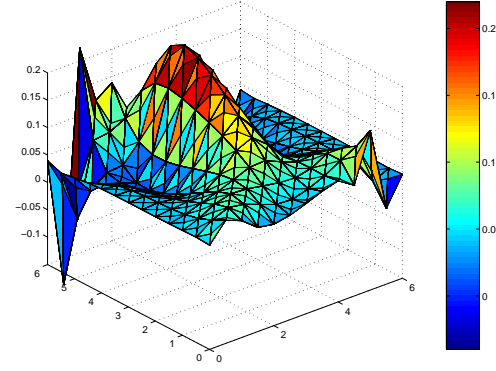


(f) The reconstructed absorption image using adaptive meshes based on *a priori* error estimates (3.24) and (3.25) for the forward, and the interpolation error estimate (4.40) for the inverse problem.

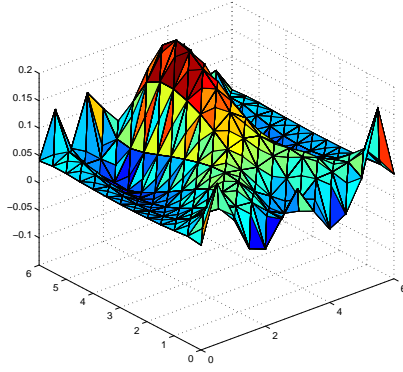
Figure 9. The reconstructed optical images regarding the circular heterogeneity centered at $(3.0, 3.5)$.



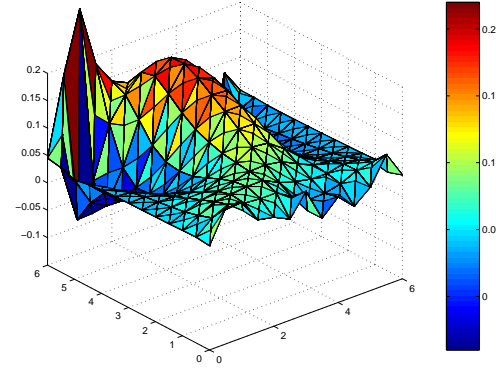
(a) The absorption image used as the reference in the error computations.



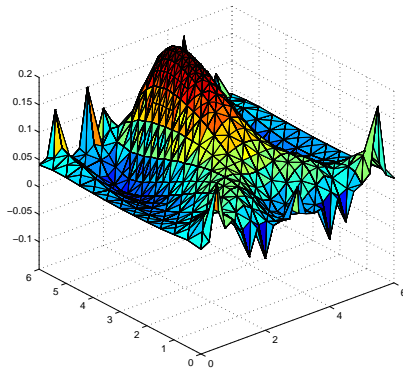
(b) The reconstructed absorption image using the uniform mesh in Figure 2(a) for the forward, and the uniform mesh in Figure 2(b) for the inverse problem.



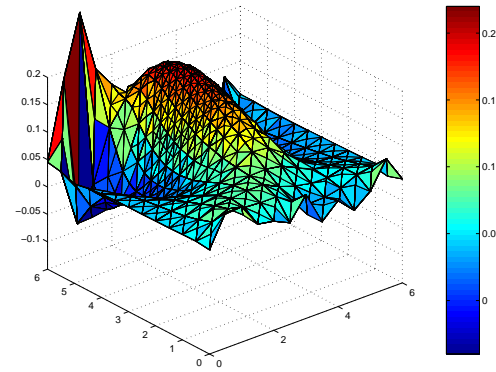
(c) The reconstructed absorption image using adaptive meshes based on Theorem 2 for the forward, and the uniform mesh in Figure 2(b) for the inverse problem.



(d) The reconstructed absorption image using adaptive meshes based on *a priori* error estimates (3.24) and (3.25) for the forward, and the uniform mesh in Figure 2(b) for the inverse problem.



(e) The reconstructed absorption image using adaptive meshes based on Theorem 2 for the forward, and the adaptive mesh based on Theorem 1 for the inverse problem.



(f) The reconstructed absorption image using adaptive meshes based on *a priori* error estimates (3.24) and (3.25) for the forward, and the interpolation error estimate (4.40) for the inverse problem.

Figure 10. The reconstructed optical images regarding the circular heterogeneity centered at $(3.0, 4.0)$.